UNIVERSITY OF LEEDS

Numerical Simulations of Shock-Cloud Interactions

Robertas Alūzas

School of Physics and Astronomy

University of Leeds

Submitted in accordance with
the requirements for the degree of

Doctor of Philosophy

September 2014

The candidate confirms that the work submitted is his own, except where work which has formed part of jointly authored publications has been included. The contribution of the candidate and the other authors of this work has been explicitly indicated. The candidate confirms that appropriate credit has been given within this thesis where reference has been made to the work of others.

Preface

Within this thesis, some chapters have been based on work presented in the following jointly authored publications:

I. "Numerical simulations of shocks encountering clumpy regions", **R. Alūzas**, J.M. Pittard, T.W. Hartquist, S.A.E.G. Falle, R. Langton, 2012, MNRAS, 425, 2212.

II. "Numerical simulations of a shock interacting with multiple magnetized clouds", **R. Alūzas**, J.M. Pittard, S.A.E.G. Falle, T.W. Hartquist, 2014, MNRAS, 444, 971.

Paper I forms the basis of Chapter 3. The hydrodynamical code used to perform the simulations in this Chapter was written and developed by S.A.E.G. Falle. Routines setting up the initial conditions for the particular problem were written by J.M. Pittard. The primary author (R. Alūzas) was responsible for small modifications to the code enabling finite regions and to track the shock position. Preliminary low resolution simulations of clumpy regions were performed by R. Langton. The primary author performed the higher resolution simulations, analyzed the data and wrote the initial draft of the publication before incorporating the comments from co-authors in the final draft.

Paper II forms the basis of Chapter 4. The simulations and analysis were carried out by the primary author. The primary author has developed the Python routines used to analyze the data, wrote the initial draft of the publication and then incorporated comments from co-authors in the final draft.

Acknowledgements

This thesis is greatly indebted to the guidance of Julian Pittard. The process involved an excessive amount of red pen but was enjoyable nevertheless. Thanks also go out to Tom Hartquist for sharing his wisdom and Sam Falle for sharing his code.

A queue of people are responsible for getting me here. I would like to thank the academic staff at the University of Leeds, course mates Chris and Mark, classmates Donatas and Dovydas and my cousin Kristina for challenging me throughout the years. The earliest intellectual endeavours I can remember were at the houses of my grandparents and for that I am grateful too.

A glass of *Verdita* goes out to fellow PhD students and my friends for making the last four years such great fun. In particular to Hazel and Jonny, who might not realise it, but without them the experience would have been very different.

My parents and sister deserve unlimited gratitude for a number of things, but most of all for always being there for me, despite the distance. Finally, to my partner, Živilė, for sharing this journey and keeping me sane in the final year.

To all of you, I say,

Ačiū

Abstract

This Thesis presents numerical simulations of shocks interacting with regions containing multiple individual clouds. Firstly, the hydrodynamic interaction is presented. It is the first study to include 100s of clouds in a clumpy region which 'mass-load' the flow. The 'mass-loading' reduces the Mach number of the shock and leads to the formation of a dense shell. In cases in which the 'mass-loading' is sufficient the flow slows enough that the shock degenerates into a wave. The shock does not decelerate below a minimum velocity determined by properties of the region. Despite the turbulence generated behind the shock, the initial mass loss from the clouds is weaker. Nevertheless, the shell is found to regulate the cloud lifetimes such that all clouds are destroyed in similar time. The one exception occurs when a few high density clouds are distributed among lower density ones.

Secondly, 2D adiabatic magnetohydrodynamic simulations of a shock interacting with groups of two or three cylindrical clouds are presented. We find (i) some clouds are stretched along their field lines, whereas others are confined by their field lines; (ii) upstream clouds may accelerate past downstream clouds; (iii) clouds may also change their relative positions transverse to the direction of shock propagation as they 'slingshot' past each other; (iv) downstream clouds may be offered some

protection from the oncoming flow as a result of being in the lee of an upstream cloud; (v) the cycle of cloud compression and re-expansion is generally weaker when there are nearby neighbouring clouds.

This small-scale study helps to interpret the behaviour of systems with 100s of clouds. Infinitely wide regions can be interpreted via interactions between individual clouds, but in regions of finite width shocks driven from the sides of the region have different field-flow orientations - individual clouds can experience evolving field morphology.

Abbreviations

AMR	Adaptive Mesh Refinement
CMZ	Central Molecular Zone
CNM	Cold Neutral Medium
DM	Dispersion Measure
EM	Emission Measure
GMC	Giant Molecular Cloud
HIM	Hot Ionized Medium
IR	Infrared
ISM	Interstellar Medium
ISRF	Interstellar Radiation Field
KH	Kelvin-Helmholtz
MHD	Magnetohydrodynamic
PAH	Polycyclic Aromatic Hydrocarbon
PE	Photoelectric Effect
RH	Rankine-Hugoniot
RT	Rayleigh-Taylor
SN	Supernova
SNR	Supernova Remnant
UV	Ultraviolet
WIM	Warm Ionized Medium
WNM	Warm Neutral Medium

Contents

List of Figures

LIST OF FIGURES

LIST OF FIGURES

List of Tables

LIST OF TABLES

Space. It seems to go on and on forever. But then you get to the end and a gorilla starts throwing barrels at you.

Phillip J. Fry, 1999

Chapter 1

Introduction

The Milky Way galaxy (the Galaxy[1]) is thought to be a typical barred spiral galaxy (Blitz & Spergel 1991). It consists of a bulge in the Galactic Center, a bar and a disk composed of spiral arms. Furthermore, there is a spherical distribution of globular clusters of old stars in the halo. It is by studying the apparent size and brightness of these clusters that Trumpler (1930) observed that clusters diminish in apparent brightness faster than in apparent size, suggesting that light is absorbed along the way, now known to be due to interstellar dust (see Sec. 1.1.1.4). The existence of gas was already known from spectroscopy. Hartmann (1904) discovered absorption lines in a spectroscopic binary system which were stationary, unlike the lines originating from the stars themselves which move as the stars orbit each other. Furthermore, such stationary lines were found to have distinct velocities, revealing the presence of multiple individual clouds (e.g. Adams 1949).

The tenous matter filling the space between stars in the Galactic disk is now called the Interstellar Medium (ISM). It is composed of gas and dust and makes up

[1]Upper case G is used to distinguish our galaxy.

10–15% of the total mass in the Galactic disk (Ferrière 2001). Stars are formed out of it and shape it throughout their lifetimes and in their death. In the following Section the composition of the ISM is described. In Section 1.2 the physics governing the structure of the ISM is introduced. Sec. 1.3 highlights the connection to the evolution of stars. Finally, Sec 1.4 overviews the existing literature on interactions between shocks and clouds.

1.1 The Interstellar Medium

Most of the work on the ISM relies on observations within our Galaxy. These observations can be supplemented by the outside view of its large scale distribution in other spiral galaxies, particularly M31 (e.g. Bajaja & Shane 1982; Corbelli *et al.* 2010) and M33 which has a favorable inclinition permitting surveys of molecular clouds (Rosolowsky *et al.* 2003; Fukui & Kawamura 2010). While our Galaxy is a typical spiral galaxy, it is worth mentioning alternatives where the ISM can be very different. Elliptical galaxies, such as M32 or M87 are largely devoid of ISM. In all but a handfull of elliptical galaxies star formation has ceased a long time ago (Huang & Gu 2009; Combes *et al.* 2007). Irregular galaxies can contain a lot of ISM. In particular the Large Magellanic Cloud which is relatively nearby and has significantly different conditions is a good test to the theories. Blitz *et al.* (2007) find that the empirical relations Larson (1981) found for the Milky Way hold in other local group galaxies. However, the Luminosity - Radius relationship, while retaining the same index of power law, has a different constant of proportionality implying that Giant Molecular Clouds (GMCs, see Sec. 1.1.1.1) have constant surface density within a galaxy, but its value can vary between the galaxies.

Table 1.1: Components of the interstellar gas. Typical values are given where, T is temperature, n is number density of hydrogen nuclei near the Sun, and z is the scale height at the solar radius.

Component	T (K)	n (cm^{-3})	z (pc)
Molecular	10–20	10^2–10^6	81
Cold Atomic[a]	40–100	20–50	150
Warm Atomic[a]	6000–10000	0.2–0.5	400
Warm Ionized[b]	∼8000	0.2–0.5	180
H II regions[c]	7000–10000	10–10^6	70
Hot Ionized	$\sim 10^6$	~ 0.0065	1000–5000

Based on Ferrière (2001) and supplemented with:
[a] Kalberla & Kerp (2009), [b] Gaensler *et al.* (2008)
and [c] Tielens (2005).

Dark matter is now know to be an important component of galaxies. It dominates the total mass of the galaxy, contributes to the gravitational potential and sets the galactic rotation curve. Galactic models (e.g. Fujimoto *et al.* 2014) need to include a dark matter potential, but in general it is the observed distribution of the gas that is used to understand the shape of the dark matter (Olling & Merrifield 2000) or even to test alternative theories (Sánchez-Salcedo *et al.* 2008) rather than the other way round.

1.1.1 Phases of the ISM

It is customary to split the ISM into phases. The properties of these phases are summarized in Table 1.1. The main distinction that is used to separate the phases is the state of hydrogen. Molecular and cold atomic phases exist as cold clouds within a more tenous, warmer medium. They occupy only 1-2% of the volume but make up half of the total mass of the ISM.

Most of the numbers in Table 1.1 are taken from Ferrière (2001) with some supplementary, more up to date sources.

1.1.1.1 The molecular medium

Molecular clouds make up the densest phase of the ISM. Most of the molecular mass is contained within GMCs. Their masses lie in the range of 10^4–$10^6\,M_\odot$, with the average number density of order $100\,cm^{-3}$ (McKee & Ostriker 2007). Within them a lot of substructure exists, so that the typical density within a GMC is closer to $3000\,cm^{-3}$. The origin of this substructure is an active area of research though turbulence in particular is believed to play a very important role (Hennebelle & Falgarone 2012). All present day star formation is thought to occur in GMCs, particularly in the dense cores (Fukui & Kawamura 2010).

The scale height of molecular gas is low and so it is found predominantly in the disk. Moreover, within our Galaxy it is observed that most of the molecular gas resides in the inner 0.4 kpc and in the ring between 3.5 kpc and 7 kpc (the Sun is at 8.5 kpc from the Galactic Centre) (Ferrière 2001).

The formation of H_2 in the gas phase is unlikely under the interstellar conditions. Formation rate is greatly enhanced by interstellar dust particles (Sec. 1.1.1.4), which act as a catalyst. A hydrogen atom is attracted to the dust and sticks to its surface. Another hydrogen atom, also attracted to the dust, then either sticks to the first one forming a H_2 molecule or sticks to the surface of the dust grain. The atoms on the grain surface can then move along with the possibility of colliding and forming a molecule. Once formed, molecules are easily dissociated by ultraviolet (UV) photons so molecular clouds reside in the halo of atomic gas shielding it. In particular, for the UV radiation field in the solar region a column density

of $N_{\rm H} \simeq 2 \times 10^{20}$ cm^{-2} of atomic gas is needed to shield H_2 and a higher value, $N_{\rm H} \simeq 1.4 \times 10^{21}$ cm^{-2}, for the next most abundant molecule, CO (McKee & Ostriker 2007).

The H_2 molecule has no dipole moment. Its lowest energy transition is in the infrared (IR). However, its main lines occur in the UV which require high temperatures to excite. They are also difficult to observe due to absorption by the interstellar dust and Earth's atmosphere. Direct observations of H_2 are possible in absorption with satellites such as the *Far Ultraviolet Spectroscopic Explorer* (FUSE) (e.g. Rachford *et al.* 2002). The next most abundant molecule, CO, has transitions in radio wavelengths which can be observed from the ground and are used to trace the molecular gas. To obtain the column density of H_2 a conversion factor is used

$$X_{\rm CO} = \frac{N_{\rm H_2}}{W_{\rm CO}} \simeq 2 \times 10^{20}\,{\rm cm^{-2}}({\rm K\,km\,s^{-1}})^{-1}, \tag{1.1}$$

where $N_{\rm H_2}$ is the column density of molecular hydrogen in cm^{-2} and $W_{\rm CO}$ is the integrated intensity of the $^{12}C^{18}O$ $J = 1 \rightarrow 0$ transition line in observational units of K km s^{-1}. A summary of current knowledge of this conversion factor and its limitations is given in Bolatto *et al.* (2013). They claim that this value is accurate to within 30% in the Galactic disk, but can vary significantly in different enviroments, being higher at low metallicity, and lower in starburst regions and some galactic centres. Other limitations include regions of molecular hydrogen that are not sufficiently shielded for CO to exist (Wolfire *et al.* 2010). Observations of CO reveal that the molecular gas is very cold, around 10-20 K.

1.1.1.2 The atomic medium

Unlike molecular hydrogen, atomic hydrogen (H I) is directly observable. Its electronic transitions from the Lyman series fall exclusively in the UV which cannot be observed from the ground but were first observed by Morton (1967) with a spectrograph on a rocket. Fortunately (for ground observations), the "hyperfine" structure of hydrogen gives rise to a 21 cm radio line, which is used to map H I in the Galaxy. A review by Kalberla & Kerp (2009) summarizes the current knowledge of the distrubution and dynamics of H I in the Galaxy, some of which is presented below.

Taking into account the heating and cooling processes and typical pressures (see Sec. 1.2), Field *et al.* (1969) proposed that H I gas has two thermally stable phases, which are referred to as the Cold Neutral Medium (CNM) and the Warm Neutral Medium (WNM). The CNM has temperatures $\lesssim$300 K (typically 40–100 K) and is found as clouds on scales from parsecs down to tens of astronomical units. The distribution is often filamentary or sheetlike (Heiles & Troland 2003). The WNM has a diffuse distribution, is found in every direction (i.e. it has a 100% area filling fraction), and has a temperature $\gtrsim$5000 K (typically 6000–10000 K). The densities of these two phases in the vicinity of the Sun are 20–50 cm^{-3} and 0.2–0.5 cm^{-3} respectively. These phases are able to exist in pressure equilibrium. However, about half of the H I in the disk is found to be thermally unstable, in the transient range $300 \lesssim T \lesssim 5000$ K.

The values given in Table 1.1 refer to the midplane density and the scale height at the location of the Sun. The average midplane density decreases exponentially with radius, but the scale height increases. Hence the atomic disk of the Milky Way

is highly flared, consistent with a lower gravitational component in the vertical direction.

All GMCs posses atomic envelopes of comparable mass (Blitz 1990), also molecular cores form quickly in atomic clouds of sufficient column density (Bergin *et al.* 2004). The formation of molecular clouds proceeds through condensation of atomic clouds rather than coalescence of molecular material (Elmegreen 1993).

1.1.1.3 The ionized medium

Massive O and B stars emit strong radiation above 13.6 eV, and are thus able to ionize hydrogen around them. These regions are called H II regions[1]. In a homogeneous medium such regions would have a well defined sharp boundary where ionization balances recombination (see Strömgren sphere in Sec .1.3.1.1). In a clumpy medium some radiation may escape.

The recombination rate of hydrogen is proportional to n_H and n_e and hence scales as $\approx n_e^2$. A number of lines are emitted, in particular the H_α line (the *Balmer* line between the energy levels of $n = 3$ and $n = 2$) in the red part of the visible spectrum[2]. Transitions between higher levels produce faint radio lines. The integrated intensity of these lines is then directly proportional to the emission measure (EM),

$$\mathrm{EM} = \int n_e^2 ds. \tag{1.2}$$

where ds is a line of sight through the H II region.

[1]While H II refers to ionized hydrogen in general, H II regions refer specifically to photoionized regions around massive stars.

[2]After excluding the recombinations directly into the $n = 1$ level, which produce an ionizing photon, about 50% of the remaining recombination cascades involve $n = 3$ to $n = 2$ transition

Unfortunately, like all optical and shorter wavelengths, H_α lines suffer from interstellar extinction and can only probe the structure within a cylinder of radius 2-3 kpc around the Sun. Another method that is unaffected by interstellar extinction is the observations of signals from pulsars. Electromagnetic waves interact with free electrons with longer wavelengths being delayed more. The spread in arrival times is directly proportional to the column density of free electrons, called the dispersion measure,

$$\mathrm{DM} = \int_0^L n_e ds, \tag{1.3}$$

where L is the distance to the pulsar.

With distances to pulsars independently calibrated, DM measures (supported by H_α observations) reveal two components to the ionized medium: the H II regions which are confined to the disk and a diffuse, widespread component which is not associated with any individual star (Reynolds 1990). The temperature of these regions is regulated to ∼8000 K, and the number density of hydrogen is 0.2–0.5 cm^{-3}, similar to the WNM. These two ionized components are collectively referred to as the Warm Ionized Medium (WIM). The vertical structure of the diffuse WIM is summarized in Gaensler *et al.* (2008).

The power required to maintain diffuse WIM is ∼15% of the total power of the ionizing radiation from OB stars (Domgörgen & Mathis 1994). Dove *et al.* (2000) calculate that a comparable fraction of photons from OB associations is indeed capable of escaping the atomic layer of the smooth Galactic disk (equivalent to WNM). The effect of a distribution of cold clouds (CNM) is dependent on geometry. Cylindrical clouds reduce the fraction of escaping photons while spherical

clouds increase the fraction.

UV observations also reveal the presence of highly ionized species, such as O^{5+}(O VI) and N^{4+} (N V). Their very high ionization potentials (114 and 77 eV respectively) make photoionization very unlikely, implying collisional excitation at high temperatures. Measured linewidths also support the view that the temperature of such gas is $\sim 10^6$ K. The presence of this coronal component, also called Hot Ionized Medium (HIM), has been theorized to provide the pressure needed to confine high-altitude clouds (Spitzer 1956). The Local Bubble around the Sun is in fact such a region with a hydrogen density $\approx 0.0065\,\mathrm{cm}^{-3}$ (Snowden *et al.* 1998). The region extends 100 pc in the plane of the disk and potentially up to the Galactic halo in the vertical direction (Welsh *et al.* 2010). These regions are believed to be created by supernova (SN) explosions (see Sec. 1.3.1.2). The Local Bubble was likely blown up by a SN in the Scorpius-Centaurus OB Association roughly 2–3 Myr ago (Fields *et al.* 2005; Farhang *et al.* 2014; Frisch *et al.* 2011).

1.1.1.4 Dust

As already mentioned, dust obscures light, particularly at shorter wavelengths which is why radio wavelengths are mainly used to probe the ISM. The spectra of stars are also affected. The wavelength dependent absorption "reddens" their light. The total extinction is defined by $A_\lambda \equiv 2.5\log_{10}(F^0_\lambda/F_\lambda)$ and is dependent on wavelength λ. F_λ is the observed flux and F^0_λ is the expected flux in the absence of extinction, which can be determined from the spectral type of the star. Draine (2003) overviews the observed properties of interstellar dust and possible models to explain them.

The curve of extinction versus wavelength constrains the dust models. The slope

is dependent on the size of the grains and is found to vary for different sight lines. Other features, such as a bump of increased absorption at 217.5 nm constrain the composition of the grains. Two types of grains are proposed. Silicate grains are made up of molecules involving SiO with sizes between 5 nm and 250 nm and a power law distribution $dn/da \propto a^{-3.5}$, where a is the size of the grain (Mathis 1997). Carbonaceous materials can take many forms, such as diamond, graphite or amorphous carbon and also Polycyclic Aromatic Hydrocarbons (PAHs), which are graphite grains with hydrogen on the edges. PAHs in particular are required to account for a number of spectral features. The size distribution is similar to silicate grains, although Draine (2003) proposes a triple peaked distribution to explain the observed features.

The distribution of dust is patchy and follows the distribution of gas. Draine & Li (2007) obtain a dust-to-gas mass ratio of ∼0.01 for the Galaxy, corresponding to all of the refractory elements (such as Mg, Si, Fe), two thirds of C and 20% of O locked up in the dust grains. However even within our Galaxy, a factor of 3 variation in dust-to-gas ratio can be seen (e.g. Burstein 2003).

The grains are an important catalyst in the ISM. Molecules, in particular molecular hydrogen, form on the surfaces of dust grains (Hollenbach & Salpeter 1971; Vidali 2013). Molecular hydrogen can form in the gas phase via the H^- path (McDowell 1961) or via three-body reactions (Palla *et al.* 1983; Bovino *et al.* 2014). The former requires a significant fraction of free electrons, the latter very high densities. These processes are relevant to H_2 formation in the early universe. In the present epoch the dust allows it to form more easily via the Langmuir-Hinshelwood mechanism where hydrogen atoms adsorp to the dust grain and then migrate along the surface until they form H_2 and desorp (Herbst 1995). Under certain conditions

the Eley-Rideal mechanism is also possible where a hydrogen atom in the gas phase reacts directly with a hydrogen atom on the grain surface (Duley 1996; Le Bourlot *et al.* 2012).

Elongated dust grains preferentially absorb light with the **E** vector along their long axis. Grains tend to be aligned with their long axis perpendicular to the magnetic field[1] (Davis & Greenstein 1951; Hoang & Lazarian 2008). This produces polarization of observed starlight which is used to determine the orientation of the magnetic field.

Dust grains are generally charged and in dense regions they are the main source of charge and free electrons. In a strongly magnetized medium with a low ionization fraction dust grains provide the coupling between gas and the magnetic field and set the ambipolar diffusion rate (Draine 2000).

Grains contribute to heating/cooling processes (see Sec. 1.2). In particular, they convert UV starlight into gas heat with a few percent efficiency, which makes it the dominant heating mechanism for the diffuse (Warm Atomic, and Ionized phases in Table 1.1) gas (Draine 2000). If dust is cooler than gas it can cool the gas via collisions (Tielens 2005).

1.1.2 Additional components

1.1.2.1 Magnetic field

The polarization of starlight produced by dust grains aligned with a magnetic field reveals the presence of the magnetic field in the Galaxy (Davis & Greenstein 1951;

[1] Though small grains, carbonaceous grains and grains in dense regions are probably not aligned, and in some cases alignment with long axis parallel to magnetic field may be possible (Lazarian 2007).

Mathewson & Ford 1970). Polarization reveals the orientation of the field perpendicular to the line of sight. The magnetic field strength along the line of sight can be determined from Zeeman splitting (Troland & Heiles 1986; Crutcher 2012, biased towards cold, dense regions), and Faraday Rotation (Rand & Lyne 1994, biased towards ionized regions). Radio synchrotron emission connects the properties of the magnetic field and of cosmic ray electrons (Jansson & Farrar 2012).

Compilations of these results are presented in Ferrière (2001) and Jansson (2010). The magnetic field consists of a large scale regular component and a small scale random component. The total strength in the Solar region is $\sim$6 μG, of which $\sim$1.4 μG comes from the regular component (Beck 2001). The regular component of the magnetic field is oriented along the Galactic disk, and broadly follows the spiral arms, albeit with a smaller pitch angle and potential "magnetic spiral arms" inbetween optical arms. The magnetic field makes at least two reversals in the disk (Rand & Lyne 1994). Such a feature has not been observed in external galaxies.

The magnetic field strength is only weakly correlated with gas density in diffuse regions. Only at number densities in the region of $\sim 10^2$–10^4 cm^{-3} is a meaningful increase in field strength with increasing density observed (Troland & Heiles 1986). The field strength increases towards the Galactic center, reaching $\sim$10 μG at 3 kpc Galactic radius (Beck 2001). Within 200 pc the field is approximately poloidal with a field strength of $\sim$10 μG, reaching up to $\sim$1 mG in filaments and dense clouds (Ferrière 2009).

The vertical component of the regular magnetic field in the disk is 0.2–0.3 μG (Han & Qiao 1994). The magnetic field extends well above the optical disk. The lower limit on its scale height is 1.5 kpc but it could possibly be as high as 6 kpc (Beck 2001).

The ISM is tightly coupled to the magnetic field except for the densest parts of molecular clouds where the ionization fractions are extremely low. The magnetic pressure is significantly larger than the thermal pressure of the ISM, supporting the gas against its own weight on large scales. This can lead to the Parker instability (Parker 1966) and the formation of cloud complexes (Elmegreen 1982). Magnetic fields suppress turbulent motions in the ISM and modify the motion of interstellar clouds. They support molecular clouds delaying their gravitational collapse, but also transport the angular momentum away, allowing protostellar cores to contract (Mouschovias & Paleologou 1979).

Finally, magnetic fields are required to accelerate cosmic rays and to confine them to the Galaxy (see Sec. 1.1.2.2).

1.1.2.2 Cosmic rays

Cosmic rays are very energetic charged particles. They consist mainly of protons but there is also a fraction of helium nuclei, electrons, and heavier nuclei and even trace amounts of antimatter particles: positrons and antiprotons. The relative abundances are close to solar abundances ruling out the majority of exotic sources which have been proposed (Drury 2012). There is an overabundance of light nuclei: Li, Be and B which are produced via spallation in collisions of cosmic rays (particularly C and O nuclei) and matter (Meneguzzi *et al.* 1971). A hint on the origin of cosmic rays comes from the overabundance of ^{22}Ne. Binns *et al.* (2005) find the ratio ^{22}Ne/^{20}Ne to be 5 times higher than that in the solar wind, consistent with origins in the vicinity of Wolf-Rayet stars and OB associations that host them.

Strong *et al.* (2010) calculate the power requirements for the galactic cosmic rays to be $\sim 0.7 \times 10^{34}$ W (in comparison, the total radiative power of all the stars in

the galaxy is of the order of 10^{37} W). Supernovae at an average mechanical energy of 10^{44} J (10^{51} erg) occuring approximately once every 50 years (Diehl *et al.* 2006) provide 6×10^{34} W, enough to power the cosmic rays if there exists a mechanism able to convert ∼10% of the supernova energy into cosmic ray energy.

One such mechanism is *diffuse shock acceleration* (Drury 1983). Cosmic rays move along the magnetic field lines (while gyrating around the line) in the Galaxy and can scatter off inhomogeneities in the field (Fermi 1949). In shock fronts with a magnetic field component parallel to the direction of shock propagation, particles can cross the shock front many times with a net acceleration in each cycle (two shock-crossings) coming from the relative velocity of the upstream and downstream medium[1]. The irregularities in the magnetic field required for scattering to occur are readily produced by turbulence downstream of the shock. Upstream of the shock cosmic rays are travelling faster than the Alfvén-speed and excite Alfvén waves by which they are scattered (Bell 1978).

By scattering off the Alfvén waves cosmic rays exert pressure on the ISM through the magnetic field. Cosmic ray pressure is in rough equipartition with the magnetic field pressure and the dynamical pressure. Ferrière (2001) give a value of ∼9300 $\mathrm{K\,cm^{-3}}$ for the cosmic ray pressure near the Sun. A typical midplane value could be somewhat smaller outside the Local Bubble, but it is significantly higher than the thermal pressure (see Sec. 1.2.3).

Collisions between gas and cosmic rays are rare so cosmic rays are able to penetrate into molecular clouds and are the main source of heating and ionization

[1]Even without the shock fronts a particle is more likely to collide with an oncoming cloud than a receding one resulting in a net acceleration called *stochastic acceleration* (Jones 1994). However the observed energy spectrum and the aforementioned power considerations point to shock origins (Kulsrud 2005).

in dense molecular cores (see Sec. 1.2.1). In collisions pions are produced which decay into γ-rays. The collision rate is proportional to the total gas density so observations of γ-rays (after subracting the H I and H II contribution) can indirectly probe difficult to observe H_2 gas. It is one of the ways to determine the "CO-to-H_2" factor (Bolatto *et al.* 2013) and is also used to detect H_2 gas that is not visible in CO (Grenier *et al.* 2005).

1.1.3 Additional structure

In addition to the disk, the Galaxy is defined by two further structures, the Galactic Centre and the spiral arms.

1.1.3.1 Spiral arms

The spiral arms are density enhancements in the disk caused by density waves (Lin & Shu 1964; Kaplan & Pikelner 1974). Star formation occurs predominantly in the spiral arms (Urquhart *et al.* 2014), as this is where the dense molecular gas is concentrated. The largest scale molecular structures, Giant Molecular Associations, form from diffuse gas collected during their passage through the spiral arm (Molinari *et al.* 2014). In the molecular-gas-rich inner regions of the disk the ratio of molecular gas in the spiral arms to molecular gas in the inter-arm regions is $\sim$3, but in the outer Galaxy this ratio can be as high as 13 as molecular gas there is found almost exclusively in the spiral arms.

Gómez & Cox (2004) model the spiral structure and find that the midplane density varies by a factor of 3 between arms and inter-arm regions, a similar factor to the molecular gas ratio in the inner Galaxy. Cox (2005) remarks that this density

contrast is probably limited to the dense phases of the ISM, while diffuse phases are probably more uniformly distributed in the Galaxy. ISM models with midplane density varying by a factor of 4.1 by Shukurov *et al.* (2004) find a corresponding pressure variation by a factor of 2.8, and a higher scale height in the interarm region. The pressure and density in the interarm regions could also be affected by the vertical motion in the disk initiated by the spiral arms as seen in Gómez & Cox.

1.1.3.2 Galactic center

The central 500 pc is an extreme environment, very different from the rest of the Galaxy. Morris & Serabyn (1996) reviews the structure of the ISM in the Galactic center. The standout feature is a strong concentration of molecular gas within the central 200 pc, referred to as the *central molecular zone* (CMZ). Clouds in the CMZ have high density ($\gtrsim 10^4$ cm^{-3}), high temperature (30–200 K), highly supersonic internal velocity dispersions (15–50 km s^{-1}), and a high volume filling fraction ($f \gtrsim 0.1$) and mass (5–10 $\times$ 10^7 M$_\odot$).

The most massive GMC in the CMZ is Sagittarius B2 (Goldsmith *et al.* 1992). It contains 5–10 $\times$ 10^6 M$_\odot$ and has a diameter of 45 pc. Its volume density is 1800–3500 cm^{-3} peaking to 4–9 $\times$ 10^5 cm^{-3} in a parsec sized core. Another extreme cloud, G0.253 + 0.016 (also known as "the Brick") contains 1–1.5 $\times$ 10^5 M$_\odot$ in a 6 pc sized clump (Longmore *et al.* 2012). Even less extreme clouds, labeled "d", "e" and "f" in Longmore *et al.* (2013) contain $\sim$$10^5$ M$_\odot$ within a diameter of $\sim$7 pc. For comparison, a massive local GMC, the Orion A molecular cloud, contains 1 $\times$ 10^5 M$_\odot$ extended over 45 pc (Wilson *et al.* 2005).

The gas temperature in molecular clouds in the Galactic Center is 50–100 K (Ao *et al.* 2013) (cf. 10–20 K in the disk clouds) while the dust temperature is 14–20 K

(García-Marín *et al.* 2011; Molinari *et al.* 2011). Ao *et al.* (2013) argue that only strong cosmic-ray or turbulent heating can explain the difference. Yusef-Zadeh *et al.* (2013a) also point to cosmic ray heating, in order to explain the methanol abundance. The cosmic ray ionization rate in the Galactic Centre is one to two orders of magnitude greater than in the disk (Yusef-Zadeh *et al.* 2013b).

While the Galaxy is considered typical of the spirals, the CMZ peculiarly appears to be typical of a different class of galaxies. Kruijssen & Longmore (2013) argues that the conditions in the CMZ are very similar to galaxies at high redshift. While temperatures, velocity dispersions and densities are comparable, the star formation rate is lower in the Galactic centre. The cause of this factor ∼10–100 discrepancy is an active area of research (e.g. Kruijssen *et al.* 2013). A possible solution is that the current quiet episode is just a lull between starburst events, and that the rate might substantially pick up within the next 10 Myr or so.

1.2 Physical processes in the ISM

1.2.1 Heating

The ISM is heated by photons from the interstellar radiation field (ISRF) or by charged cosmic ray particles. The origin and composition of CRs has been discussed in Sec. 1.1.2.2. Mathis *et al.* (1983) describe the main components of the ISRF. In optical to near-IR the ISRF is composed of blackbody radiation of individual stars, which itself can be represented as a diluted blackbody. A smaller blackbody component comes from OB stars in the near-UV. A second dominant component comes from the far-IR emission from dust that was heated by massive stars. Stahler &

Palla (2005) identify the cosmic microwave background as an energetically important component in the microwave range. A small X-ray component comes from the HIM (Sec. 1.1.1.3).

Shorter wavelengths are easily absorbed. Soft X-rays from massive stars are confined to their H II regions (Sec. 1.3.1.1), in which X-ray and UV background can be significantly higher due to local sources. In the interiors of dense clouds, the stellar component is absorbed and reemitted by dust in IR.

Cosmic rays, mainly protons, heat the ISM by ionizing H I or H_2.

$$p^+ + H \rightarrow H^+ + e^- + p^+, \tag{1.4}$$

$$p^+ + H_2 \rightarrow H_2^+ + e^- + p^+. \tag{1.5}$$

A single cosmic ray can cause multiple ionizations, each of which produces an electron with an average energy of $\sim$19 eV (Glassgold & Langer 1973). Some of the electrons can then cause secondary ionizations. The energy is transfered to the gas via elastic collisions. The energy transfer timescales for electron-electron and electron-atom collisions are approximately:

$$t_{e,e} \simeq 10^4 \left(\frac{E_e}{1\,\mathrm{eV}}\right)^{3/2} \left(\frac{n_e}{\mathrm{cm}^{-3}}\right)^{-1} \mathrm{s} \tag{1.6}$$

and

$$t_{e,H} \simeq 2 \times 10^7 \left(\frac{E_e}{1\,\mathrm{eV}}\right) \left(\frac{n_H}{\mathrm{cm}^{-3}}\right)^{-1} \mathrm{s} \tag{1.7}$$

(Tielens 2005). In the atomic medium the ionization fraction is significant ($x \sim 0.1$ and $n_e \sim 0.01$–$0.04\,\mathrm{cm}^{-3}$, Kulkarni & Heiles 1987; Jenkins 2013) and the ejected

electron thermalizes via elastic collisions with the electron gas. In the molecular medium, the ionization fraction is low ($x \sim 10^{-8}$ and $n_e \sim 10^{-4}\,\mathrm{cm}^{-3}$, Flower *et al.* 2007) and the energy of the energetic electron is transfered to the gas inelastically, via excitation of rotational levels in H_2, which de-excite collisionally, or dissociation of H_2, with the energy carried by the resulting atoms (Glassgold *et al.* 2012). Cosmic ray heating is the main heating mechanism deep in the molecular clouds. X-rays can heat the gas in a similar manner in the vicinity of massive stars (in the H II regions),

$$\mathrm{H} + h\nu \rightarrow \mathrm{H}^+ + \mathrm{e}^-. \tag{1.8}$$

However, as hydrogen is so abundant, X-ray and UV photons above 13.6 eV are easily absorbed by this process. Away from sources of radiation, heating by ionization proceeds through other species with lower ionization potentials, carbon being the most abundant one. The ionization potential of C I is 11.26 eV, and the interaction

$$\mathrm{C} + h\nu \rightarrow \mathrm{C}^+ + \mathrm{e}^- \tag{1.9}$$

takes place. The maximum available energy is 2.3 eV per ionization, with a typical value of ∼1 eV. Draine (2011) shows that 99.9% of carbon is ionized in this way in the neutral regions. This limits the efficiency of carbon ionization as a heating mechanism. A more important mechanism is the photoelectric (PE) heating where photons eject electrons from the dust grains. For larger grains liberated electrons originate ∼10 nm inside the grain. The majority of such electrons deposit the energy within the grain which is reradiated in the IR (Draine 2003). Only a fraction of electrons reach the grain surface, where they must overcome the work function

and, in the case of charged grains, Coulomb attraction (Stahler & Palla 2005). The result is that approximately one in ten 10 eV photons produce one 1 eV electron, giving an efficiency $\epsilon_{\rm PE} \sim 0.01$. A higher efficiency is possible in planar PAHs, up to $\epsilon_{\rm PE} = 0.15$ (half of 10 eV photons overcoming ∼7 eV work function, Tielens 2005), as the liberated electron is already at the surface. The ionization potential of positively charged PAHs easily exceeds 13.6 eV, but Weingartner & Draine (2001) show that most grains are neutral in the CNM and a large fraction remains neutral in the WNM. The main source of free electrons in the neutral medium is dust, while carbon is the second.

This covers the main sources of gas heating under different conditions. In the vicinity of a star an H II region is primarily heated through X-rays: Stahler & Palla (2005) give an approximate expression for the X-ray heating rate:

$$\Gamma_{\rm X-ray} = 2 \times 10^{-13} \left(\frac{n_{\rm H}}{\rm cm^{-3}}\right)^{1/3} \left(\frac{L_{\rm X}}{10^{30}\,\rm erg\,s^{-1}}\right) \left(\frac{r}{0.1\,\rm pc}\right)^{-8/3} \rm eV\,cm^{-3}\ s^{-1}, \quad (1.10)$$

where $L_{\rm X}$ is the star luminosity in the X-ray band, and r is the distance from the source. The formula is applicable within $r < r_{\rm X}$, where $r_{\rm X}$ is the charactersitic distance, within which most of the energy is deposited, and which is defined as:

$$r_{\rm X} = 2 \left(\frac{n_{\rm H}}{10^3\,\rm cm^{-3}}\right)^{-1} \rm pc, \quad (1.10b)$$

PE heating dominates in CNM clouds. Its efficiency is sensitive to the grain charge distribution which in turn is sensitive to the temperature and radiation field. Weingartner & Draine (2001) provide approximate expressions for typical PE heat-

ing values in CNM and WNM respectively:

$$\Gamma_{\mathrm{PE,CNM}} = 3.2 \times 10^{-13} \left(\frac{n_{\mathrm{H}}}{10\,\mathrm{cm}^{-3}} \right) \mathrm{eV\,cm^{-3}\ s^{-1}} \tag{1.11a}$$

and

$$\Gamma_{\mathrm{PE,WNM}} = 1.8 \times 10^{-15} \left(\frac{n_{\mathrm{H}}}{0.1\,\mathrm{cm}^{-3}} \right) \mathrm{eV\,cm^{-3}\ s^{-1}}. \tag{1.11b}$$

Uncertainties in the temperature, the ionization fraction, the energy of the ISRF and the grain properties can lead to variations up to a factor of a few in Γ_{PE}.

The heating rate due to cosmic rays is the product of the ionization rate and the energy per ionization. Taking into account secondary ionizations and the fraction of energy that goes into the first excited state of hydrogen as explained in Spitzer & Tomasko (1968) the remaining energy per ionization that goes into heating the gas is 6–7 eV. Studies of the ionization rate find values in the region of 10^{-18}–$10^{-16}\,\mathrm{s^{-1}}$ (Dalgarno 2006). Tielens (2005) suggests an even higher value of $3 \times 10^{-16}\,\mathrm{s^{-1}}$. The resulting heating rate is then:

$$\Gamma_{\mathrm{CR}} = 7 \times 10^{-16} n \left(\frac{\zeta_{\mathrm{CR}}}{10^{-16}} \right) \mathrm{eV\,cm^{-3}\ s^{-1}}. \tag{1.12}$$

Cosmic ray heating dominates in molecular clouds.

Other sources of heating include chemical heating from formation of H_2, heating (can also cool) via dust-gas collisions due to different dust-gas temperatures, dissipation of turbulence on the viscous scale, and in the case of dense cores, ambipolar diffusion heating and gravitational heating. The gas can also be heated mechanically by shocks and winds (Sec. 1.3). Mechanical heating keeps the HIM hot.

1.2.2 Cooling

While heating occurs over a continuous range of energies (of absorbed radiation or interacting CRs), cooling occurs mainly via lines. Interstellar gas cools by emitting radiation. A transition is excited in a collision converting kinetic energy into radiation. In view of this Dyson & Williams (1997) pick out five criteria for efficient cooling.

- Frequent collisions; require fairly abudant partners, such as H, He, C, N, O, e^-, their forms and molecules.
- Excitation energy comparable to or less than the thermal kinetic energy, $k_B T$; as it is collisionally excited, e.g. CO (20 K), C^+ (92 K).
- High probability of excitation during the collision.
- That the photon is normally emitted before a second collision occurs on the excited partner; this is not satisfied in H_2.
- That emmited photons are not re-absorbed; this requires optically thin gas, which is usually not satisfied for $^{12}C^{18}O$, so less abundant isotopologues are also important.

Although hydrogen is the most abundant element, it generally is not an effective coolant. H_2 is not an efficient coolant for the same reasons that make it near impossible to observe. Possible quadrupole transitions have low transition rates and energy gaps of 500 K and more. The deuterated molecule, HD, does have a dipole moment and despite its much lower abundance is the more important of the hydrogen molecules as a coolant at 100–200 K.

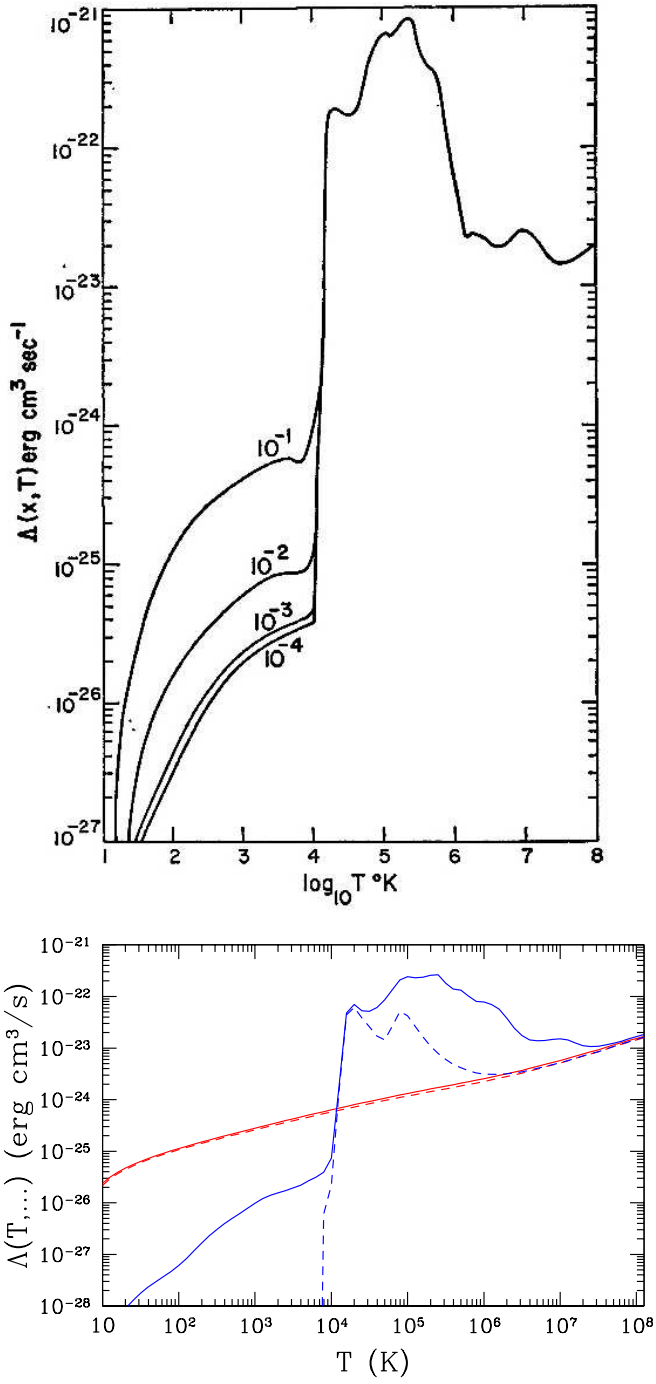

Figure 1.1: The interstellar cooling curve. Top: The Dalgarno & McCray (1972) cooling curve. Different lines correspond to different ionization fractions. Bottom: The Gnedin & Hollon (2012) cooling curve. Solid and dashed lines show solar metallicity and zero metallicity curves, blue and red - collisional ionization equilibrium model and fully ionized gas calculation.

Atomic hydrogen has a hyperfine structure line at 21 cm but it is not important because it has a very low energy and is very long lived. The energy of the first excited state of H I is 10.2 eV $\approx 1.2 k_B \times 10^5$ K. At 10^4 K a small fraction is collisionally excited, but due to its high abudance it is significant. However the ionization potential is 13.6 eV and above $\sim 2 \times 10^5$ K cooling efficiency starts to drop as hydrogen becomes ionized since H II does not have energy levels.

Fully ionized gas cools via bremsstrahlung radiation (also known as free-free emission) as free electrons scatter off ions (Osterbrock 1989). The cooling function is proportional to $T^{1/2}$ in this regime. A classic cooling curve by Dalgarno & McCray (1972) and more recent models by Gnedin & Hollon (2012)[1] are shown in Fig. 1.1. The zero metallicity case in the Gnedin & Hollon cooling curve (dashed blue line) only includes cooling from hydrogen and helium. The curve is exceptionally steep around 10^4 K where Lyman α cooling becomes important. Neutral hydrogen gas is incredibily optically thick to Lyα, but the spontaneous emission of electronic transitions is so fast that collisional deexcitation has virtually no chance of occuring. The radiation is trapped until successive scatterings and velocity dispersion in the gas shift its frequency into the optically thin regime (Hansen & Oh 2006). Helium contributes at higher temperatures, as its energy levels are spaced further apart. Cooling is also possible from He II[2], but otherwise helium cooling is similar to hydrogen cooling. Above 10^5 K cooling begins to decrease as the ionization fraction rises, until bremsstrahlung cooling becomes the dominant mechanism.

Hydrogen is not an efficient coolant at low temperatures, but it is sufficient to cool low metalicity gas (Glover & Clark 2014) and to form the first stars (Bromm

[1] Determined from the plasma emission code Cloudy (Ferland *et al.* 2013)
[2] At $\sim 5 \times 10^5$ K.

Table 1.2: A list of some of the lowest energy transitions of the most abundant atoms and molecules that are potential coolants. Atomic data is from Kramida *et al.* (2013), molecular from Goldsmith & Langer (1978). Square brackets denote fine-structure (forbidden) transitions.

	Excitation energy	
Species	meV	K
H I	10.2 eV	1.2×10^5
He I	19.8 eV	2.3×10^5
He II	40.8 eV	4.7×10^5
[O I]	19.6	228
	28.1	327
[C I][a]	2.03	23.6
	5.38	62.5
[Fe I][a]	51.6	599
	87.3	1010
	110	1280
	122	1410
[Si I]	9.56	111
	27.7	321
[S I]	49.1	570
	71.1	826
[C II]	7.86	91.3
[Fe II]	47.7	554
	82.3	961
	107	1241
	121	1406
H_2	43.5	509
HD	10.9	128
CO[b]	0.47	5.5

[a]: The ionization potential of species is below 13.6 eV, so its likely to be ionized in neutral regions.

[b]: The lowest energy level.

et al. 2002).

At solar metallicity other atoms can contribute to cooling. In order of abundance these are O, C, Ne, Fe, N, Si, Mg and S (Grevesse & Sauval 1998). Nitrogen, neon and magnesium have no suitable levels that could be excited below 10^4 K. The ground states in the remaining atoms have fine structure[1] levels listed in table 1.2. Considering the relative abundances and the temperature needed for collisional excitation it can be seen that [O I] dominates the cooling from 200 K to a few thousand K, [C I] should take over at low temperatures with some contribution from [Si I] around 100 K and [S I] and [Fe I] at temperatures above 500 K. Smith *et al.* (2008) compute the cooling contribution from different species at these temperatures, which reveals that CO rotovibrational lines are the dominant coolant below 40 K.

Photoionizing radiation changes the list of available species. In completely ionized gas there are no atomic energy levels and only bremsstrahlung cooling takes place (red line in Fig. 1.1). A realistic radiation field creates partly ionized species, the most important of which is singly ionized carbon, C II. Away from ionization sources, the ISRF is extinguished of photons above 13.6 eV which are used up in ionizing hydrogen. The ionization potential of C I is 11.26 eV and 99.9% of carbon is in the C II phase (Sec. 1.2.1). The fine structure line of C II is then the dominant coolant at 100 K. Depletion can also change the available coolants. In particular, CO freezes out onto grains in dark cores, reducing cooling and leading to a higher temperature than if all the coolants were in gas phase (Goldsmith 2001).

[1]Fine structure splitting is due to a torque on the electron spin from the magnetic field of the nucleus. In states where the total orbital angular momentum is zero, such as ground states of H, He, N, the electric field does not vary and so there is no magnetic field. The hyperfine structure, as encountered previously in the case of the 21 cm hydrogen line, is due to the interaction of the electron spin and the spin of the nucleus.

The heating and cooling processes in dust are different to those in the gas. Unless the density is high enough that dust and gas are coupled via collisions their temperature might be different. In that case collisions between dust and gas would also heat or cool the gas, depending on which one is hotter.

1.2.3 Pressure equilibrium

The ISM cools via lines which are excited at different temperature ranges for different species. The result of this is a complicated dependance of the cooling function on temperature, which contains steps as new species become excited, decreases with temperature as ionization depletes the coolants, and stays relatively constant where a set of efficient coolant species does not change. The balance between heating and cooling requires:

$$n^2\Lambda - n\Gamma = 0 \tag{1.13}$$

where $n^2\Lambda$ is the cooling rate per unit volume and $n\Gamma$ is the heating rate per unit volume. The cooling rate depends on the rate of collisions in the gas so is proportional to n^2, while the heating rate is proportional to the interactions between gas and photons and so is proportional to n, where n is the number density. For gas to be stable, an increase in temperature must cause a net cooling, while a decrease must lead to a net heating.

Temperature ranges where Λ is flat are unstable, as heating causes expansion and reduces n^2 faster than n so $n^2\Lambda$ falls faster than $n\Gamma$. A simple way to identify the stable regions is to look for steep[1] regions in Λ. The two main regions are from Lyα

[1] It can be shown that if Γ is independent on temperature, the requirement is $\frac{d\Lambda(T)}{dT} > \frac{\Lambda(T)}{T}$ which is true if $\Lambda(T) \propto T^{\alpha}$, with $\alpha > 1$.

cooling at[1] $\sim 10^4\,\mathrm{K}$ and from fine structure lines at $\sim$ 90–500 K . The cooling rate increases by a few orders of magnitude in those ranges and such gas is thermally stable.

A more rigorous argument, evaluating Eq. 1.13, shows that not only can two states be stable, but that the stable states can also be in pressure equilibrium with each other. This is know as the two phase model of the ISM by Field *et al.* (1969). The cold phase coresponds to CNM clouds and the warm phase to diffuse gas of WNM and WIM.

The ideal gas law gives a relationship between number density, temperature and thermal pressure,

$$nT = \frac{P}{k_B}. \tag{1.14}$$

Consider two temperatures that are thermally stable and in pressure equilibrium. At higher pressure these states become unstable as for the given temperatures n increases and so cooling ($\propto n^2$) increases faster than heating ($\propto n$) and so the stable temperatures are lower. Above a certain thermal pressure the temperatures in the Lyα cooling regime would no longer be stable and the warm phase would not be possible. Similarly below a certain pressure the fine-structure-line-regulated temperature would not be able to provide the cool phase. Cox (2005) gives the upper and the lower limits for two-phase equilibrium with heating and cooling functions applicable to the Solar neighborhood of $4400\,\mathrm{K\,cm^{-3}}$ and $1700\,\mathrm{K\,cm^{-3}}$. Redfield & Linsky (2004) measure $2240 \pm 520\,\mathrm{K\,cm^{-3}}$ in the local ISM, but this is only a small fraction of the total pressure. Cox (2005) gives the weight of the ISM

[1] First electronic levels of most relevant species become populated at this temperature. In photoionized regions without neutral hydrogen, other species, such as O II, O III or N II, also become excited at similar temperature.

at midplane as 22000 K cm^{-3}, with the additional support coming from magnetic, cosmic ray and dynamic pressure.

The ISM is not static and many more processes occur than just the thermal instability. In the three phase model of McKee & Ostriker (1977) the cold and neutral phases are embedded in the HIM which is created and constantly replenished by supernova explosions. In general, the picture of two or three phases in pressure equilibrium is a simplistic description. The ISM is violent, and constantly stirred up by feedback from stars (Sec. 1.3), so that at any moment in time ∼50% of gas is in the thermally unstable range (Gazol *et al.* 2001; Heiles 2001).

1.3 Feedback processes in the ISM

1.3.1 Feedback from stars

The role of stars on the galactic ISM manifests in multiple ways. The ISRF (Sec. 1.2.1) consists almost entirely of stellar radiation and light from dust and gas as it is heated by stellar radiation. Of the radiation emitted by stars, UV light above 13.6 eV has been neglected so far as it is absorbed in the vicinity of the star, but as this section shows, the resulting H II regions are important, dynamical structures on their own, driving flows and contributing WIM to the ISM. The stellar winds of massive stars and the supernovae at the end of their lives impart mechanical energy into the ISM, provide coronal gas and regulate the large scale structure of galaxies (Efstathiou 2000).

This feedback is likely to modify how new stars form. The most general effect would be the dispersion of the parental cloud and halting further local star

formation. However, Elmegreen & Lada (1977) propose that the H II region may become gravitationally unstable and form new stars. McCray & Kafatos (1987) propose a similar mechanism for the shells of supernova superbubbles. Dale & Bonnell (2012), even with the ability of numerical simulations to turn feedback on and off, find it is not easy to distinguish triggered (or abandoned, in case of negative feedback) star formation from spontaneous star formation, although Dale *et al.* (2012) find statistical differences in resultant initial mass functions.

This section presents the framework for understanding the stellar feedback processes which are usually considered for the highly idealized conditions of a uniform ISM. The effects of a highly inhomogeneous ISM can be gauged via simulations, such as Rogers & Pittard (2013).

1.3.1.1 Ionizing radiation

As described above, massive (OB) stars ionize an H II region around them. Strömgren (1939) derived the size of the ionized region by assuming an equilibrium state where the number of recombinations inside the region is equal to the number of photoionising photons.

Following the derivation from Osterbrock (1989) the ionization equilibrium condition requires that inside the H II region the rate of ionizations is equal to the rate of recombinations,

$$n_{\mathrm{H}^0} \int_{\nu_0}^{\infty} J_\nu \sigma_\nu \mathrm{d}\nu = n_\mathrm{e} n_\mathrm{p} \alpha(T_\mathrm{e}), \tag{1.15}$$

where n_{H^0}, n_e and n_p are the number densities of neutral hydrogen, electrons and protons respectively, ν_0 is the threshold frequency of ionization, J_ν is the number

of ionizing photons per unit area per unit time per unit frequency interval, σ_ν is the ionization cross-section at frequency ν and α is the recombination coefficient.

The left hand side in Eq. 1.15 is the rate of photoionizations per unit volume and the right hand side is the rate of recombinations per unit volume. As mentioned in Sec. 1.2.1, dust and C^+ are the main sources of free electrons in the neutral medium, but if the medium is ionized, most of the electrons must come from hydrogen. We assume that $n_\mathrm{e} = n_\mathrm{p} = x n_\mathrm{H}$, where x is the ionization fraction and $n_\mathrm{H} = n_\mathrm{p} + n_{\mathrm{H}^0}$. The total recombination coefficient is the sum of the recombination coefficients to all possible levels. Recombinations to the ground state produce an ionizing photon which should enter the left hand side of the equation, but assuming the ionization happens locally these can be excluded[1]. The recombination coefficient to each level depends on the electron velocity and the recombination cross-section (which is related to the ionization cross-section, - see Seaton 1959). Assuming that the electrons follow a Maxwell-Boltzmann distribution function the total recombination coefficient depends only on the electron temperature. Tielens (2005) gives the dependance on temperature as $T_\mathrm{e}^{-4/5}$ and an expression

$$\alpha_2(T_\mathrm{e}) = 4 \times 10^{-10} T_\mathrm{e}^{-4/5}\,\mathrm{cm^3\,s^{-1}} \tag{1.16}$$

matches the tabulated values for the total recombination coefficient to excited ($n \geq 2$) levels in Osterbrock (1989) quite well.

For $T_e \approx 10^4\,\mathrm{K}$ ($k_B T \approx 1\,\mathrm{eV}$) the recombination timescale,

$$t_\mathrm{rec} = \frac{1}{n_\mathrm{e}\alpha_2(T_\mathrm{e})} \approx 126000 \left(\frac{n_\mathrm{e}}{\mathrm{cm^{-3}}}\right)^{-1}\,\mathrm{yr}, \tag{1.17}$$

[1]This is the "on the spot" approximation which allows to only consider primary stellar photons as contributing to J_ν in Eq. 1.15 by replacing $\alpha(T_\mathrm{e})$ with $\alpha_2(T_\mathrm{e})$ from Eq. 1.16.

which is much greater than $t_{\mathrm{e,e}}$ from Eq. 1.6 and so the thermalized assumption is justified.

The total number of recombinations inside an H II region of radius R_S (assuming constant density and electron temperature and $x \approx 1$) is $\frac{4\pi}{3} R_S^3 n_{\mathrm{H}}^2 \alpha_2(T_{\mathrm{e}})$. The total number of primary ionizations, assuming all the ionizing photons are used up in the H II region is equal to the total number of ionizing photons emitted by the star, S_*. The radius of the region (the Strömgren radius) is thus

$$R_S = \left(\frac{3}{4\pi} \frac{S_*}{n_{\mathrm{H}}^2 \alpha_2(T_{\mathrm{e}})} \right)^{1/3} = 69\,\mathrm{pc} \left(\frac{S_*}{10^{49}\,\mathrm{s}^{-1}} \right)^{1/3} \left(\frac{n_{\mathrm{H}}}{\mathrm{cm}^{-3}} \right)^{-2/3}. \tag{1.18}$$

$S_* \approx 10^{49}\,\mathrm{s}^{-1}$ represents an O7 star (Sternberg *et al.* 2003).

By solving Eq. 1.15 it can be shown that x is indeed ≈1 inside the H II region and drops of rapidly at the ionization front as increasing neutral fraction rapidly increases the optical depth. Similar treatment of elements other than hydrogen calculates the ionization structure of the H II region and determines the emission spectra.

The equilibrium solution based on ionization balance does not hold initially while the region is not yet fully ionized. When the ionizing radiation first turns on the ionization front sweeps up to R_S. Following Stahler & Palla (2005), we denote the number of ionizing photons crossing the ionization front per unit time as F_*. These photons are all used up in advancing the ionization front. As gas is initially molecular ($n_{\mathrm{H}_2} = \frac{1}{2} n_{\mathrm{H}}$) one photon is used to dissociate the H_2 and two more to ionize the atoms. If in time $\mathrm{d}t$ the front advances distance $\mathrm{d}R$, then

$$F_* = 4\pi R^2 \frac{3 n_{\mathrm{H}}}{2} \frac{\mathrm{d}R}{\mathrm{d}t}. \tag{1.19}$$

This assumes that the same photons participate in ionizing H I and dissociating H_2. The dissociation threshold for H_2 is 14.7 eV, so it is close, but not exact. F_* is equal to S_* minus the number of recombinations inside the ionized region,

$$F_* = S_* - \frac{4}{3}\pi R^3 n_{\rm H}^2 \alpha_2 = \frac{4}{3}\pi n_{\rm H}^2 \alpha_2 (R_S^3 - R^3), \tag{1.20}$$

and so

$$\frac{{\rm d}R}{{\rm d}t} = \frac{2}{9} n_{\rm H} \alpha_2 (R_S^3 - R^3) R^{-2}. \tag{1.21}$$

Defining $\lambda = R/R_S$ and $\tau = t/t_{\rm rec}$, Eq. 1.21 gives

$$\frac{{\rm d}\lambda}{{\rm d}\tau} = \frac{t_{\rm rec}}{R_S}\frac{{\rm d}R}{{\rm d}t} = \frac{2}{9}(\lambda^{-2} - \lambda), \tag{1.22}$$

which can be solved given the initial condition $\lambda(0) = 0$:

$$\lambda = \left(1 - e^{-2\tau/3}\right)^{1/3}. \tag{1.23}$$

By $t = 2t_{\rm rec}$, R reaches $0.9R_S$. If the parent molecular cloud has $n_{\rm H_2} = 10^3\,{\rm cm}^{-3}$, then $t_{\rm rec} = 62\,{\rm yr}$ and $R_S = 0.4\,{\rm pc}$ (for an O7 star). In 124 years the H II region has expanded to nearly its final size and by Eq. 1.22 the ionization front is still advancing at over $450\,{\rm km\,s}^{-1}$.

As the ionization front approaches R_S its velocity drops, and crucially it drops below the sound speed in the ionized gas. The ionized region is overpressurised compared to the ambient region by a factor of

$$\frac{P_i}{P_0} = \frac{n_i T_i}{n_0 T_0} \tag{1.24}$$

(for $T_i = 10^4\,\mathrm{K}$ and molecular ambient gas with $T_0 = 20\,\mathrm{K}$, $\frac{P_i}{P_0} = 2000$, while for atomic ambient gas of $T_0 = 100\,\mathrm{K}$, $\frac{P_i}{P_0} = 200$). The ionized region then expands (initially at the sound speed in the ionized gas) sweeping up the neutral gas into a shell and driving a shock into the ambient region. The evolution of the ionized region's radius is given by Spitzer (1978),

$$R_i = \left(1 + \frac{7}{4}\frac{c_i t}{R_{i0}}\right)^{4/7} R_{i0}, \tag{1.25}$$

where c_i is the sound speed in the ionized region and R_{i0} is the radius of the ionized region when the shock develops and is approximately equal to R_S.

Dyson & Williams (1997) derive the same relation by considering the hydrodynamic expansion of the ionized region. Three velocities must be recognized: the expansion velocity (v_{exp}), the velocity of the ionization front (v_{IF}) and the shock velocity (v_s). Generally $v_{\mathrm{exp}} < v_{\mathrm{IF}} < v_s$ but the differences in the isothermal, strong shock case are very small and

$$v_{\mathrm{exp}} \approx v_{\mathrm{IF}} \approx v_s \tag{1.26}$$

(Raga *et al.* (2012) derive $v_{\mathrm{exp}} \approx v_{\mathrm{IF}} = v_s - c_0^2 v_s^{-1}$). While $v_{\mathrm{exp}} \approx v_{\mathrm{IF}}$ this does not mean that the total ionized mass is constant. As the region expands its density decreases and new material is ionized to satisfy Eq. 1.18. The newly ionized gas comes from the swept up shell which is dense and so a significant mass can be ionized despite the approximately equal velocities.

Another simplifying assumption is that because the sound speed in the ionized region is high, the entire ionized region including the newly ionized gas is uniform.

The pressure in it can be expressed as

$$P_i = \rho_i c_i^2 \gamma^{-1}. \tag{1.27}$$

The pressure in the shocked neutral gas, P_1, is given by the shock jump conditions (see Sec. 1.3.2),

$$P_1 = \left(\frac{2\gamma M^2}{\gamma+1} - \frac{\gamma-1}{\gamma+1}\right) P_0 = \left(\frac{2\gamma M^2}{\gamma+1} - \frac{\gamma-1}{\gamma+1}\right) \frac{v_s^2 \rho_0}{\gamma M^2}, \tag{1.28}$$

where M is the shock Mach number[1] and the subscript 0 denotes unshocked material. The swept up shell and the ionized region is in pressure equilibrium and so (using isothermal $\gamma = 1$)

$$P_i = P_1 \implies \rho_i c_i^2 = \rho_0 v_s^2. \tag{1.29}$$

Using Eq. 1.18 and the condition that ionizations are matched by recombinations inside the ionized region,

$$\rho_i = \rho_0 \left(\frac{R_S}{R_i}\right)^{3/2}, \tag{1.30}$$

and so

$$v_s = \left(\frac{R_S}{R_i}\right)^{3/4} c_i. \tag{1.31}$$

By using the approximation in Eq. 1.26 to define $v_s = v_{\rm IF} = \frac{{\rm d}R_i}{{\rm d}t}$ and substituting (c_i is constant in the isothermal case):

$$\lambda = R_i/R_S, \qquad \eta = c_i t/R_S, \tag{1.32}$$

[1] In the isothermal case it is customary to use the isothermal sound speed and the isothermal Mach number, completely eliminating factors of γ from the equations.

Eq. 1.31 becomes:

$$\lambda^{3/4}\frac{\mathrm{d}\lambda}{\mathrm{d}\eta} = 1. \tag{1.33}$$

This equation is solved by the Spitzer solution from equation 1.25 for the initial condition $\lambda(0) = 1$ and $R_{i0} = R_S$.

The expansion continues until the pressure in the H II region equalizes with the outside pressure. By Eq. 1.24 the number density inside the ionized region has to drop by a factor of 200–2000 which implies a final radius, using Eq. 1.30, of 34–160R_S. The ionized mass within the region is similarly a factor of 200–2000 higher than without the expansion.

Eq. 1.25 gives the time it takes to reach pressure equilibrium. For $c_i = 15\,\mathrm{km\,s^{-1}}$, $T_i = 10^4\,\mathrm{K}$, $S_* = 10^{49}\,\mathrm{s^{-1}}$ and $n_0 = 20\,\mathrm{cm^{-3}}$ for atomic ambient gas or $n_0 = 10^3\,\mathrm{cm^{-3}}$ for molecular ambient gas, this time is $\sim$150 Myr, significantly longer than the main sequence lifetime of an O star which is $\lesssim$10 Myr (Böhm-Vitense 1992).

The assumption of a perfectly uniform ambient region is unlikely to hold over such temporal and spatial scales. As the star is likely to have formed in the densest part of the cloud, the density is likely to decrease further away from the star or the region may reach the edge of the cloud. The shock will accelerate in the lower density medium leading to a “champagne flow” (Tenorio-Tagle 1979). Density inhomogenieties within the cloud or intercloud medium further complicate the picture. “Pillars” and “globulettes” are identified in observations (e.g. Gahm *et al.* 2007), and are studied numerically (e.g. Gritschneder *et al.* 2010).

1.3.1.2 Supernovae

Stars more massive than $\simeq 8\,\mathrm{M}_\odot$ and accreting white dwarfs in binary systems end their lives in supernova explosions. The power output of a single supernova can outshine the entire host galaxy making them an important component in galactic dynamics.

The evolution of a simplified supernova remnant (SNR) can be divided into three phases. In the initial phase it can be assumed that the entire useful (i.e. not neutrino) energy of the supernova (of the order of $10^{51}\,\mathrm{erg}$) goes into the kinetic energy of the ejecta. The ejecta velocity is then

$$v_{\mathrm{ej}} = \left(\frac{2E_{\mathrm{SN}}}{M_{\mathrm{ej}}}\right)^{1/2} = 10^4 \times \left(\frac{E_{\mathrm{SN}}}{10^{51}\,\mathrm{erg}}\right)^{1/2} \left(\frac{M_{\mathrm{ej}}}{\mathrm{M}_\odot}\right)^{-1/2} \mathrm{km\,s^{-1}}, \tag{1.34}$$

where E_{SN} is the supernova energy and M_{ej} is the ejecta mass. The ejecta sweeps up the ambient gas into a thin shell but does not slow down significantly until the swept up mass (M_{sw}) is comparable to M_{ej}. This happens at a radius

$$R_{\mathrm{I}} = \left(\frac{3M_{\mathrm{ej}}}{4\pi\rho_0}\right)^{1/3} \simeq 2.0 \left(\frac{M_{\mathrm{ej}}}{\mathrm{M}_\odot}\right)^{1/3} \left(\frac{n_0}{\mathrm{cm^{-3}}}\right)^{-1/3} \mathrm{pc}, \tag{1.35}$$

where ρ_0 is the ambient density which is converted to number density n_0 by assuming that the mean particle mass in the atomic gas is $1.3m_{\mathrm{p}}$. A remnant expanding at a constant velocity, v_{ej}, reaches such a radius at a time

$$t_{\mathrm{I}} = 200 \times \left(\frac{M_{\mathrm{ej}}}{\mathrm{M}_\odot}\right)^{5/6} \left(\frac{E_{\mathrm{SN}}}{10^{51}\,\mathrm{erg}}\right)^{-1/2} \left(\frac{n_0}{\mathrm{cm^{-3}}}\right)^{-1/3} \mathrm{yr}. \tag{1.36}$$

Afterwards the swept up gas begins to dominate the dynamics. While the shock

is strong the temperature of the post-shock gas is high ($\gtrsim 10^6$ K) and the cooling is inefficient as most of the gas is ionized. The expansion is adiabatic and it follows the Sedov-Taylor solution (Taylor 1950; Sedov 1959). By neglecting the mass of the ejecta and considering the shock jump conditions for strong adiabatic ($\gamma = 5/3$) shocks (i.e. $\rho_1/\rho_0 = 4$, $P_1/P_0 = 5M^2/4$ and $v_1/v_s = 3/4$, where M is the adiabatic Mach number) the kinetic and internal energies per unit mass in the swept up gas are

$$e_{\rm k} = \frac{1}{2}v_1^2 = \frac{9}{32}v_s^2 \tag{1.37}$$

and

$$e_{\rm i} = \frac{3}{2}\frac{P_1}{\rho_1} = \frac{15}{32}\frac{v_s^2 P_0}{\rho_0 c_0^2} = \frac{9}{32}v_s^2. \tag{1.38}$$

Hence the total conserved energy is (assuming negligible ejecta mass)

$$E_{\rm SN} = \frac{4}{3}\pi\rho_0 R_{\rm SNR}^3 \times (e_{\rm k} + e_{\rm i}) = \frac{3}{4}\pi\rho_0 R_{\rm SNR}^3 v_s^2. \tag{1.39}$$

The differential equation is then

$$R_{\rm SNR}^{3/2}\frac{{\rm d}R_{\rm SNR}}{{\rm d}t} = \left(\frac{4E_{\rm SN}}{3\pi\rho_0}\right)^{1/2}, \tag{1.40}$$

the solution to which for the initial condition $R_{\rm SNR}(0) = 0$ (again following the assumption of negligible ejecta mass) is

$$\begin{aligned} R_{\rm SNR} &= \left(\frac{25}{3\pi}\right)^{1/5}\left(\frac{E_{\rm SN}}{\rho_0}\right)^{1/5} t^{2/5} \\ &\simeq 5.4\left(\frac{E_{\rm SN}}{10^{51}\,{\rm erg}}\right)^{1/5}\left(\frac{n_0}{{\rm cm}^{-3}}\right)^{-1/5}\left(\frac{t}{10^3\,{\rm yr}}\right)^{2/5}{\rm pc} \end{aligned} \tag{1.41}$$

and the expansion velocity,

$$\dot{R}_{\rm SNR} = \frac{2}{5}\left(\frac{25}{3\pi}\right)^{1/5}\left(\frac{E_{\rm SN}}{\rho_0}\right)^{1/5} t^{-3/5}$$
$$\simeq 2100\left(\frac{E_{\rm SN}}{10^{51}\,{\rm erg}}\right)^{1/5}\left(\frac{n_0}{{\rm cm}^{-3}}\right)^{-1/5}\left(\frac{t}{10^3\,{\rm yr}}\right)^{-3/5}{\rm km\,s^{-1}}. \quad (1.42)$$

Using Eqs. 1.38, 1.42, the shock jump conditions and the cooling curve from Sec. 1.2.2 it can be shown that cooling is indeed negligible while the shock is strong, but when the shock weakens and the temperature on the shocked gas falls in the region of efficient cooling the shock becomes nearly isothermal and the swept up material is concentrated into a thin shell behind the shock. Woltjer (1972) calculates that about half the energy is radiated away by the time the shock slows down to[1] $\sim 200\,{\rm km\,s^{-1}}$. At this point, the pressure of the hot gas in the interior of the remnant pushes the shell, in what is termed the "pressure-driven snowplough" phase and $R_{\rm SNR} \propto t^{2/7}$ (McKee & Ostriker 1977). After the interior pressure drops, the shell continues to drift away in the "momentum-driven snowplough" phase and $R_{\rm SNR} \propto t^{1/4}$ (Oort 1951). A simulation by Cioffi *et al.* (1988) shows that the pressure-driven "snowplough" phase is better represented with an "offset" in time, i.e. $R_{\rm SNR} \propto (t - t_{\rm offset})^{3/10}$.

The evolution of actual SNRs is modified by a number of factors. Firstly, the density gradient in the disk means that the supernova expands faster vertically than horizontally. The hot interior gas may escape, supplying the coronal gas with HIM as in the McKee & Ostriker (1977) model. Multiple supernovae in proximity may form superbubbles. Ferrière (1999) estimates that $\sim 60\%$ of supernova occur in

[1] This velocity is very weakly dependent on the parameters used, although other authors use $230\,{\rm km\,s^{-1}}$ (Gent *et al.* 2013) or $250\,{\rm km\,s^{-1}}$ (Tielens 2005).

groups of various sizes. The presence of irregularities, such as high density clouds, can "mass-load" the remnant interior and enhance radiative losses (White & Long 1991; Dyson *et al.* 2002; Pittard *et al.* 2003), converting supernova energy into ISM turbulence and cloud motions.

1.3.1.3 Stellar winds

During their lifetimes stars lose mass via stellar winds, which input mechanical energy and recycle enriched material into the ISM. Lamers & Cassinelli (1999) summarize the theory behind different driving mechanisms, such as the Coronal wind (Parker 1965) which is the mechanism responsible for the Solar wind, of density ∼2–6 protons per cm^3 at the Earth radius and a velocity of ∼400–800 $\mathrm{km\,s^{-1}}$ (Ebert *et al.* 2009, the range is due to the three components identified in the solar wind), resulting in a mass loss of $\sim 2 \times 10^{-14}\,\mathrm{M_\odot\,yr^{-1}}$. Much stronger stellar winds from massive stars are line driven (Castor, Abbott & Klein 1975b), where resonance line scattering imparts net momentum on the ions. As the ions accelerate the radiation emitted by the star is redshifted in the ion frame of reference and continuum photons of shorter wavelength are now able to scatter off the ions. For very luminous stars with many resonance lines, such as Wolf-Rayet stars, the wind velocity and mass loss rate can be as high as $2000\,\mathrm{km\,s^{-1}}$ and $2 \times 10^{-5}\,\mathrm{M_\odot\,yr^{-1}}$ (Nugis & Lamers 2000).

As the wind expands into the ISM it creates a wind blown bubble. The structure of the bubble consists of (from the star outwards) a freely expanding wind, a reverse shock, shocked wind material, shocked swept up material, a forward shock and the ambient medium (the same structure can be seen in other supersonic flows as in Fig. 1.2). The evolution of the bubble is similar to the supernova case in

that it also has three phases: the freely expanding wind phase, the energy conserving phase and the momentum conserving (snowplough) phase. The radius in the energy conserving phase is given by Castor, McCray & Weaver (1975a),

$$R_w = 28\,\mathrm{pc}\left(\frac{L}{10^{36}\,\mathrm{erg\,s^{-1}}}\right)^{1/5}\left(\frac{\mu n_0}{\mathrm{cm^{-3}}}\right)^{-1/5}\left(\frac{t}{10^6\,\mathrm{yr}}\right)^{3/5}, \tag{1.43}$$

where $L = \frac{1}{2}\dot{M}v^2$ is the mechanical luminosity ($\dot{M}$ is the stellar mass loss rate and v is the wind terminal velocity), μ is the mean atomic weight which is 0.6 in ionized gas and n_0 is the number density in the undisturbed ISM. The momentum conserving phase is entered as radiative cooling becomes efficient. The radius is then

$$R_w = 25\,\mathrm{pc}\left(\frac{\dot{M}}{10^{-5}\,\mathrm{M_\odot\,yr^{-1}}}\frac{v}{1000\,\mathrm{km\,s^{-1}}}\right)^{1/4}\left(\frac{\mu n_0}{\mathrm{cm^{-3}}}\right)^{-1/4}\left(\frac{t}{10^6\,\mathrm{yr}}\right)^{1/2} \tag{1.44}$$

(McCray 1983).

Low density channels in the irregular ISM may allow interior gas to leak out of the bubble (Harper-Clark & Murray 2009). The reduced interior pressure slows the expansion of the shell. The hot gas that has leaked out the main bubble may escape the region (Rogers & Pittard 2013) or, if the ambient density is higher, form a temporary bubble itself which is later incorporated back into the main one (Pittard 2013).

1.3.2 Shocks

Shocks are ubiquitous in the ISM. Massive stars drive flows which result in shocks, as shown in Sec. 1.3.1:, expanding H II regions drive shocks, stellar winds create

wind blown bubbles and supernova explosions create supernova remnants. Shocks also arise from active galactic nuclei (Fabian 2012) in processeses qualitatively similar to stellar ones, but on a much larger scale. Large scale shocks also develop as interarm gas infalls onto the spiral arms (Roberts 1969).

1.3.2.1 Hydrodynamic shocks

The theory of shocks and discontinuities is presented in Landau & Lifshitz (1987). A physical discontinuity needs to conserve mass, energy and momentum (all three components), i.e. the flux of these quantities needs to be equal on both sides of the discontinuity (the Rankine-Hugoniot, or RH, conditions). This is easily satisfied if there is no flow across the discontinuity - i.e. the flux is zero. A contact discontinuity is an example of such a case. The pressures must be equal and the velocity perpendicular to the discontinuity must be zero, otherwise the two states would exert forces on each other, but other fluid variables, such as density, temperature or tangental velocity may all vary arbitrarily.

The case with flow across the discontinuity is known as a shock. For an ideal gas (equation of state $P/\rho = k_B T/\mu$ and $\gamma = c_P/c_V$), the RH conditions are satisfied by

$$\frac{\rho_2}{\rho_1} = \frac{v_1}{v_2} = \frac{(\gamma+1)M_1^2}{(\gamma-1)M_1^2+2}, \tag{1.45}$$

$$\frac{P_2}{P_1} = \frac{2\gamma M_1^2}{\gamma+1} - \frac{\gamma-1}{\gamma+1}, \tag{1.46}$$

$$\frac{T_2}{T_1} = \frac{(2\gamma M_1^4 - (\gamma-1))((\gamma-1)M_1^2+2))}{(\gamma+1)^2 M_1^2}, \tag{1.47}$$

where subscripts 1 and 2 denote values downstream and upstream of the shock, v is the velocity perpendicular to the shock in the shock frame of reference and

$M_1 = v_1/c_1$ is the Mach number in region 1. If $M_1 = 1$ there is no discontinuity.

In the adiabatic case, $\gamma = 5/3$, and the equations simplify to:

$$\frac{\rho_2}{\rho_1} = \frac{v_1}{v_2} = \left(\frac{1}{4} + \frac{3}{4M_1^2}\right)^{-1}, \tag{1.48}$$

$$\frac{P_2}{P_1} = \frac{5}{4}M_1^2 - \frac{1}{4}, \tag{1.49}$$

$$\frac{T_2}{T_1} = \frac{5M_1^4 + 14M_1^2 - 3}{16M_1^2}, \tag{1.50}$$

while in the isothermal case ($\gamma = 1$) they become:

$$\frac{\rho_2}{\rho_1} = \frac{v_1}{v_2} = M_1^2, \tag{1.51}$$

$$\frac{P_2}{P_1} = M_1^2, \tag{1.52}$$

$$\frac{T_2}{T_1} = 1 \tag{1.53}$$

(where M_1 is now the isothermal Mach number). In the high Mach number limit the maximum compression[1] in the adiabatic case is 4, while the temperature and pressure increase proportionally to M_1^2. In the isothermal case the compression is not limited and grows as M_1^2, while the temperature is fixed.

An arbitrary discontinuity usually requires two shocks to satisfy the RH conditions, or a shock and a rarefaction wave as shown in Fig. 1.2.

[1]The flow direction across the shock is from the supersonic region to the subsonic region, i.e. from region 1 to region 2, otherwise the entropy would decrease upon crossing the shock.

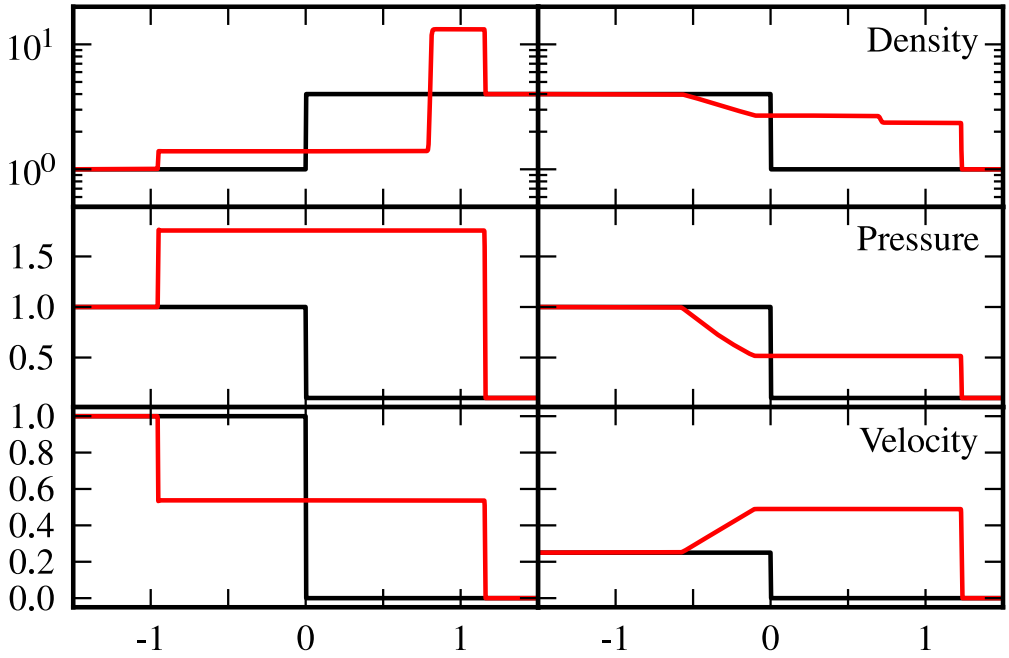

Figure 1.2: Structure of a 1D flow where initially the left and right states (black lines) do not satisfy the RH condition. A flow pattern is set up (red lines) where a forward shock, a contact discontinuity and either a reflected shock (left) or a rarefaction wave (right) establishes connecting the regions.

1.3.2.2 MHD shocks

The presence of a magnetic field adds a sense of direction in the fluid. In the purely hydrodynamical case only longitudinal motions can propagate through the medium, i.e. the sound waves. In MHD a transverse wave can propagate as well, analogous to a wave in a string, with magnetic field lines providing the tension. Such wave is called the Alfvén wave, with the velocity

$$v_i = v_a \cos\theta, \tag{1.54}$$

where v_a is the Alfvén velocity,

$$v_a = \frac{B}{\sqrt{\mu_0 \rho}}, \tag{1.55}$$

where B is the field strength, ρ is the mass density and μ_0 is the magnetic permeability of free space (Alfvén 1942). The possibility of transverse motions modifies the conventional sound waves into magnetosonic waves, the velocity of which is given by

$$v_{s,f}^2 = \frac{v_a^2 + c_s^2}{2} \pm \frac{1}{2}\sqrt{\left(v_a^2 - c_s^2\right)^2 + 4c_s^2 v_a^2 \sin^2\theta} \tag{1.56}$$

(e.g. Kulsrud 2005). Eq. 1.56 permits two wave velocities as its solutions, both of which are physical. The faster of the two is called the fast magnetosonic wave (with velocity v_f) and the slower the slow magnetosonic wave (with velocity v_s). Similarly, the Alfvén wave is also called the intermediate wave as $v_f \geq v_a$ and $v_s \leq v_i$ (and also $v_s \leq c_s \leq v_f$). The different velocities arise because the change in density and the magnetic pressure caused by transverse and longitudinal motion may be of the same sign (fast wave) or opposite sign (slow wave) (Kantrovitch & Petschek 1966). In a frame of reference where the wave propagates in the x direction, and the y and z are chosen such that the field lies in the x–y plane Kantrovitch & Petschek show that the oscilations of the intermediate wave are in the z direction, while fast and slow waves oscillate perpendicularly in the x–y plane. The three waves thus correspond to the three possible, mutually perpendicular, directions of oscillation.

The intermediate wave does not change the density or the total strength of the magnetic field. Thus the velocity of the intermediate wave is constant within the wave and no steepening occurs. An intermediate pulse can rotate the tangential

component of the magnetic field.

Compressive modes of slow and fast waves increase the wave velocity and a shock develops. The addition of magnetic fields modifies the RH conditions. Magnetic pressure modifies the pressure term, while the Lorentz force modifies the momentum of plasma crossing the shock front (Kulsrud 2005). In the fast shock the tangential component of the magnetic field increases across the shock, while in the slow shock it decreases.

By introducing a shock strength parameter, $\delta = \frac{\rho_2}{\rho_1}$, Anderson (1963) rearranged the MHD RH conditions to derive a relationship between upstream and downstream regions (the shock-adiabatic),

$$\left(v_n^2 - \delta v_a^2 \cos^2\theta\right)^2 \left[v_n^2 - \frac{2\delta c_s^2}{\delta + 1 - \gamma(\delta - 1)}\right] - \\ -\delta \sin^2\theta v_n^2 v_a^2 \left[\frac{2\delta - \gamma(\delta - 1)}{\delta + 1 - \gamma(\delta - 1)} v_n^2 - \delta v_a^2 \cos^2\theta\right] = 0 \qquad (1.57)$$

(this form of the equation is taken from Gurnett & Bhattacharjee 2005). All gas variables refer to values in the upstream (unshocked) region, v_n is the normal velocity, v_a is the Alfvénic velocity, θ is the angle between the direction of shock propagation and the magnetic field, and c_s is the adiabatic sound speed. Given the properties in the upstream region δ can be calculated for a given shock velocity (or vice versa) from Eq. 1.57 and the properties in the post-shock region can be calculated from the jump conditions.

In the parallel case, $\theta = 0$, and using $\gamma = 5/3$ and dimensionless velocities (i.e. using $c_s = 1$) Eq. 1.57 becomes

$$\left(v^2 - \delta v_a^2\right)^2 \left[v^2 - \frac{3\delta}{4 - \delta}\right] = 0. \qquad (1.58)$$

This is satisfied if

$$M^2 = v^2 = \frac{3\delta}{4-\delta} \implies \delta = \left(\frac{1}{4} + \frac{3}{4M^2}\right)^{-1} \tag{1.59}$$

or

$$M_a^2 = \delta, \tag{1.60}$$

where $M_a = v/v_a$ is the Alfvénic Mach number. The second solution corresponds to an intermediate shock, but as remarked earlier (see also Kulsrud for a slightly different argument reaching the same conclusion) the intermediate shock does not exist, thus $\delta = 1$, and it is a rotational discontinuity propagating at the intermediate velocity. The first solution gives the same conditions as in the hydrodynamic case in Eq. 1.48. If $v_s < v < v_i$ it corresponds to the slow shock, while if $v_i < v$ and $v_f < v$ the resulting shock is fast. In the remaining case, $v_i < v < v_f$ the hydrodynamic shock is not admissible. In such cases, a perturbation in B_z would reach the shock via the intermediate wave, but be unable to cross it. The solution is to split the shock in two, a fast switch-on shock (which increases B_y above zero) and a slow switch-off shock (which reduces B_y back to zero). The tangential field component modifies the intermediate velocity between the shocks such that the flow is away from the fast shock and towards the slow shock at exactly v_i. The intermediate wave can easily cross the slow shock, but cannot catch up with the fast shock, although the distance between the shocks remains constant.

1.4 Shock-Cloud interactions

The gas in the ISM exists in separate phases, the denser of which form distinct clouds (Sec. 1.1.1). These phases are determined by heating and cooling processes and attempt to reach pressure equilibrium (Sec. 1.2). The stars, particularly the massive ones, are ultimately the source of the heating and of events that throw the ISM out of equilibrium, such as supernovae (Sec. 1.3). The stars form out of the ISM, in the densest parts of molecular clouds.

This circular relationship describes the ecology of galaxies and motivates the study of clouds with flows and in particular shocks. A clumpy medium modifies the expansion of supernova remnants (Rogers & Pittard 2013; Obergaulinger *et al.* 2014). On large scales supernova feedback greatly affects the structure of a galaxy (e.g. Sales *et al.* 2010; Barnes *et al.* 2014). On smaller scales, expanding flows[1] may trigger star formation by compressing and inducing gravitational collapse of pre-existing clumps (Elmegreen 1998), sweeping up a large amount of gas that becomes gravitationally unstable (the Collect and Collapse model, Elmegreen & Lada 1977; Dale, Bonnell & Whitworth 2007a), or by driving an ionization front into the cloud (the Radiation Driven Implosion model, Sandford *et al.* 1982; Dale, Clark & Bonnell 2007b).

An interaction between a shock and a cloud is an ingredient in all of the above processes, but is rarely treated explicitly. To understand the complex dynamics of the ISM, its constituent processes need to be investigated. This section presents a selection of studies relevant to our understanding of the problem. A summary of the parameters used in each of these studies and the main differences from the

[1] Typically expanding H II regions are considered as possible triggers.

standard shock-cloud setup is provided in table 1.3.

1.4.1 Early studies

Observations of supernova remnants Cassiopeia A and the Cygnus Loop (Fig. 1.3) revealed that some optical features in the remnant are moving at a much lower velocity than the expansion speed of the shell (Baade & Minkowski 1954; van den Bergh 1971). These quasi-stationary flocculi were identified as pre-existing circumstellar clouds which had been overrun by a shock and motivated Sgro (1975) and McKee & Cowie (1975) to investigate the interaction between a shock and a cloud. Sgro performed a preliminary low resolution simulation while McKee & Cowie analysed the properties of the flow attempting to derive the quantities such as the velocity of the transmitted shock,

$$v_{\rm cl}/v_b \approx F^{1/2}(\rho_0/\rho_{\rm cl})^{1/2}, \tag{1.61}$$

where $v_{\rm cl}$ is the shock velocity inside the cloud, v_b is the velocity of the blast wave outside the cloud, ρ_0 and $\rho_{\rm cl}$ are the ambient and cloud densities and $F^{1/2}$ is approximately 1 for weaker shocks, up to nearly 2 for strong shocks. The factor F is the ratio of the pressure just behind the transmited shock to the pressure far upstream and depends on flow properties in the bow shock; Sgro derive implicit relations for 1D strong shocks while McKee & Cowie give an empirical expression for 2D strong shocks. Hα emission is explained by radiative cooling of the shocked cloud, while McKee & Cowie also consider the thermal conduction.

Motivated by a Wolf-Rayet wind blown bubble RCW58, Hartquist *et al.* (1986) consider the evolution of a wind as clouds embedded in it evaporate. This mass-

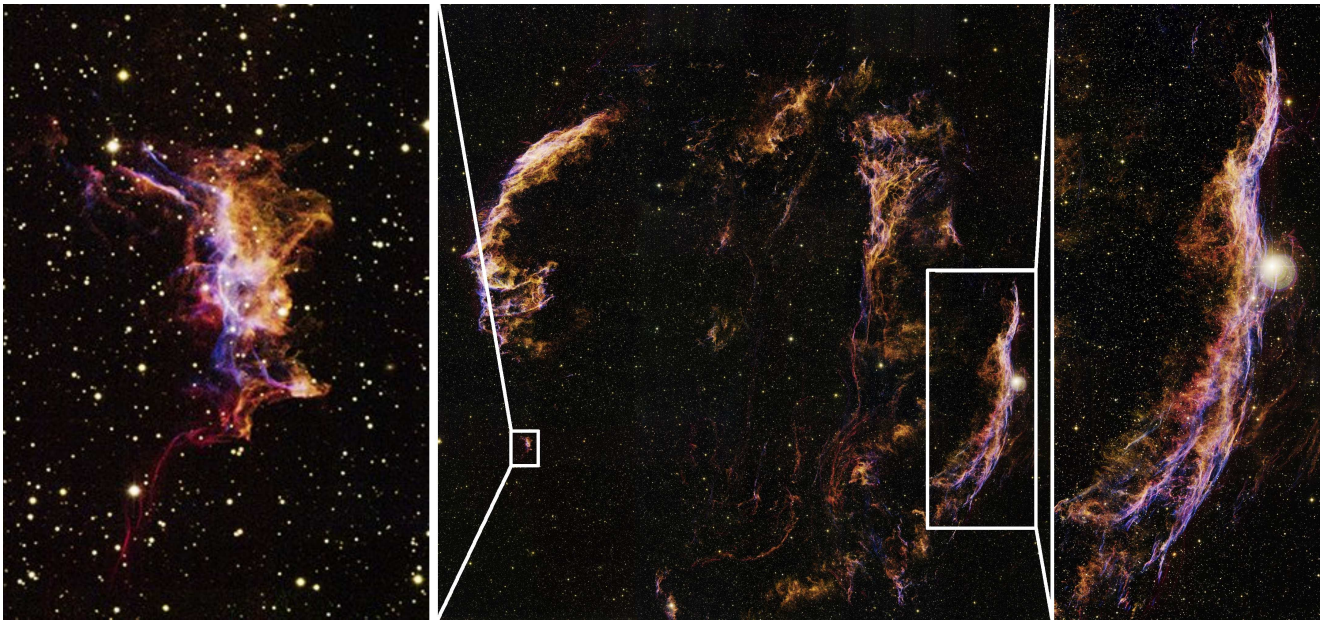

Figure 1.3: The Cygnus Loop SNR. Left: A zoom in on the Southeastern Knot, an isolated shocked clump or perhaps the leading edge of a larger cloud (Graham *et al.* 1994). Right: The Western Veil, an extended shocked structure. Red is H_α, blue is [OIII] and green is [SII]. Original image: T.A. Rector (University of Alaska, Anchorage) and WIYN/NOAO/AURA/NSF.

loading is relevant to interactions between shocks and clouds as the post-shock flow is also mass-loaded in this way. Hartquist *et al.* find that mass-loading pushes the flow Mach number towards unity, weakening the interior shocks of expanding blast waves. Elmegreen (1988) considers moving pressure fronts in a magnetized, cloudy medium. Similar magnetic effects could be relevant in a case where multiple clouds interact with a flow and between themselves. The kinetic energy of the clouds can be dissipated via cloud collisions, but even spatially separated clouds can interact via magnetic field lines.

While these analytical works have provided the basis for understanding shock-cloud interactions, non-linear effects soon dominate and one is forced to resort to

numerical simulations in order to study the problem further. The following sections summarize the existing work in the literature, focussing on adiabatic hydrodynamic simulations, radiative simulations and MHD simulations.

1.4.2 Adiabatic hydrodynamic simulations

Advances in computing power allowed Klein, McKee & Colella (1994) to perform simulations which capture non-linear effects present in the hydrodynamic interaction between a strong shock and a cloud. They performed two-dimensional simulations described by two dimesionless numbers, the Mach number, M, and the density contrast of the cloud to intercloud medium, χ. They show that the dependence on M scales out and the problem can be entirely described by χ. Furthermore they define the cloud crushing timescale,

$$t_{\rm cc} = \chi^{1/2} a_0 / v_b, \tag{1.62}$$

where a_0 is the initial cloud radius and v_b is the shock velocity in the ambient medium, which corresponds to the time it takes the internal shock to cross the cloud. Kelvin-Helmholtz and Rayleigh-Taylor instabilities (Chandrasekhar 1961) destroy the cloud within a few cloud crushing timescales. Klein, McKee & Colella claim that a numerical resolution of 100 zones per cloud radius are required for hydrodynamical instabilities to be resolved and a converged result to be obtained. This important requirement has influenced all future studies.

Stone & Norman (1992) presented the first three-dimensional simulations, which reveal that vortex rings observed in two-dimensional simulations are unstable in three dimensions. Xu & Stone (1995) have noted that an elongated cloud mixes

faster due to a larger surface to volume ratio.

Scaling relations allow to describe the problem in dimensionless units. Klein *et al.* (2003) conducted an experiment in which a laser was used to generate a strong shock (Mach ~ 10) which travelled through a low-density plastic emulating the ISM with an embedded copper microsphere emulating the interstellar cloud ($\chi \sim 10$). They used X-ray radiography to confirm the hydrodynamic simulations.

Poludnenko, Frank & Blackman (2002) consider the presence of multiple (up to 15) clouds. They distinguish between thin and thick cloud distributions determined by the thickness of the distribution and the cloud destruction length, $L_{\rm CD}$. Another important parameter to determine is the critical cloud separation, d_{crit}, which is determined by the lateral cloud expansion before it is destroyed. Distributions thinner than $L_{\rm CD}$ and with an average lateral separation greater than $d_{\rm crit}$ evolve as isolated clouds. When the lateral separation is smaller than $d_{\rm crit}$ clouds will interact and merge before destruction, though the initial compressive phase will proceed as before. For thicker distributions, if the average cloud separation in the direction of the flow is greater than $L_{\rm CD}$ it can be approximated as a series of thin distributions, but if the separation is smaller than $L_{\rm CD}$ (and particularly if the lateral separation is smaller than $d_{\rm crit}$ as well) cloud-cloud interactions dominate.

Patnaude & Fesen (2005) compare observations of the southwest cloud in the Cygnus Loop separated by 11 years allowing them to determine the proper motion of the shocks seen. The velocity of the intercloud shock is[1] $\approx 250\,{\rm km\,s^{-1}}$. The velocity in the cloud varies between 65 and $140\,{\rm km\,s^{-1}}$, suggesting a complex density structure. This allows them to approximate the structure as that of a cloud with

[1]The actual variation is $140 - 260\,{\rm km\,s^{-1}}$, attributed to projection effects and some density variation in the intercloud ISM.

density contrast $\chi \sim 4$ populated with cloudlets of up to $\chi \sim 17$. They then perform simulations of a shock interaction with a low density cloud of similar substructure. A smoothly varying, low density envelope prevents the formation of instabilities, which are not seen in these particular observations. The spacing of cloudlets determines the internal morphology. Denser cloudlets with larger separation evolve as isolated clouds, less dense cloudlets with smaller separation evolve as single clouds. The interaction between cloudlets is most important when their separation is $\sim 4\, r_{\rm cloudlet}$.

1.4.3 Radiative simulations

The effect of radiative cooling on a shocked cloud has been considered in a number of papers. Mellema, Kurk & Röttgering (2002) show that with efficient cooling the cloud fragments into small, long lived fragments. Further 2D models by Fragile *et al.* (2004) confirm these findings within a large parameter space. Large fractions of gas cool below 100 K when $t_{\rm cool} \lesssim 0.05 t_{\rm cc}$, but gas is not able to cool below 1000 K in models where $t_{\rm cool} \gtrsim 0.5 t_{\rm cc}$. They also considered a simulation with 4 clouds and argue that clouds further downstream are destroyed faster and subsequently cool less. Orlando *et al.* (2005) include thermal conduction as well as radiative cooling. While radiative cooling creates cool fragments thermal conduction leads to heating and evaporation of the clouds. They find that thermal conduction efficiently suppresses hydrodynamical instabilities, and in cases where it dominates radiative cooling the cloud evaporates rather than fragmenting. Melioli *et al.* (2005) consider 3D cases with radiative cooling and one to three clouds. They highlight that mass-loading and mixing of the flow is less efficient due to fragmen-

tation of the clouds. The presence of multiple clouds can increase it somewhat, but since fragments condense into compact objects the interaction between the clouds is much weaker than in the adiabatic case.

The above studies use resolutions of between 32 and 200 cells per cloud radius, motivated by adiabatic simulations which have shown that these resolutions are required to meaningfully resolve hydrodynamical instabilities. Yirak, Frank & Cunningham (2010) show that when cooling is concerned the cooling length, $L_{\rm cool}$ needs to be resolved by at least 10 cells. $L_{\rm cool}$ can be approximated from the velocity of the post-shock flow and the cooling timescale, although visual inspection may reveal it to be a few times shorter. Simulations with very efficient cooling would thus need very high resolutions. Underresolved simulations tend to underestimate cooling so the previous results are still valid even though in some cases cooling could have been even more efficient.

1.4.4 MHD simulations

Mac Low *et al.* (1994) include magnetic fields, which prevent the complete destruction of the cloud. The magnetic field is amplified up to equipartition with the post-shock thermal pressure in certain regions: in the parallel field[1] case the flow converges behind the cloud concentrating the parallel component of the field creating a "flux-rope" while in the perpendicular field case the field is compressed upstream of the cloud.

Cloud-wind interactions share dynamical similarities with cloud-shock interactions. Gregori *et al.* (2000) consider a cloud-wind interaction in 3D including mag-

[1]The magnetic field orientation is usually given with respect to the shock front normal i.e. the direction of shock propagation.

netic fields perpendicular to the wind velocity. They find that “flux-ropes” can also form in the perpendicular case and magnetic reconnection is possible in the wake of the cloud.

Magnetic fields together with radiative cooling are considered in the 2D simulations of van Loo *et al.* (2007). Fast mode and slow mode shocks propagate into the cloud (Sec. 1.3.2). Behind the fast shock the gas becomes magnetically dominated and thermally unstable. Such conditions are favourable for MHD waves to produce high density clumps. A dense shell forms behind the slow mode shock at the leading edge of the cloud. This shell subsequently fragments into gravitationally bound clumps which could host sites for massive star formation.

Orlando *et al.* (2008) add anisotropic thermal conduction which is suppressed in the direction transverse to the magnetic field lines. Its effects are reduced compared to unmagnetized cases. The effects of thermal conduction are greatest when the initial magnetic fields are oriented parallel to the direction of shock propagation and they are completely suppressed when the magnetic field is along the cylindrical cloud (in the 3rd direction of their 2.5D simulations). With the chosen parameters, magnetic tension alone is not able to suppress hydrodynamical instabilities, but when the field is orientated perpendicular to the cylindrical cloud thermal conduction can efficiently suppress the instabilities and reduce mass mixing with the surrounding medium.

Shin, Stone & Snyder (2008) present MHD simulations in 3D. At early times the mechanical energy of the shock dominates the evolution, but at late times, even for weak initial fields the density and magnetic field structures depend on the initial field orientation. Fig. 1.4 shows different structures for different field orientations. In the parallel field case a clear “flux-rope” is formed behind the cloud

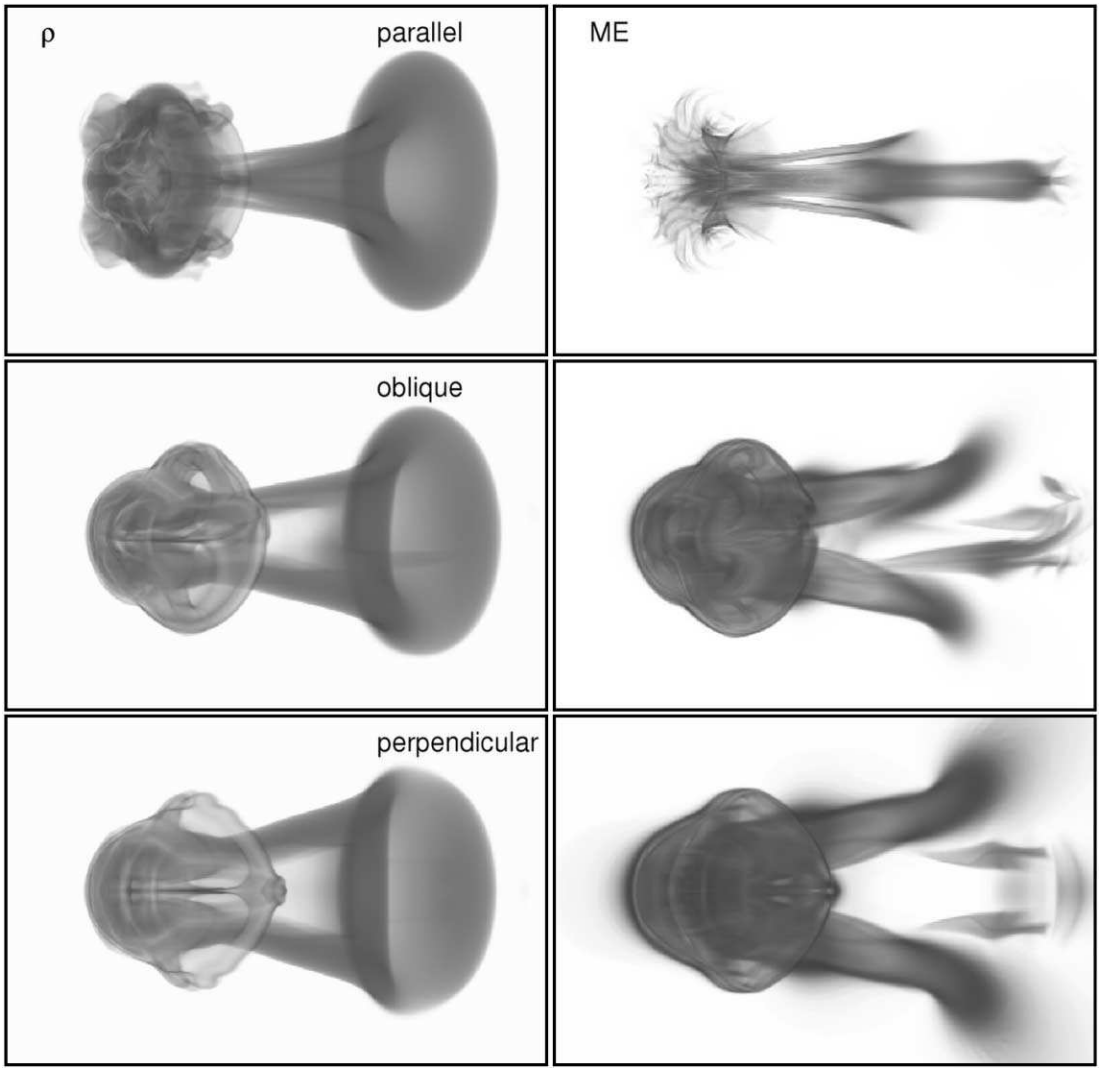

Figure 1.4: Volumetric renderings of cloud density (*left column*) and magnetic energy density (*right column*) for weak-field (pre-shock $\beta = 10$) simulations with parallel, oblique and perpendicular magnetic fields. The time is $7.97 t_{\rm cc}$. Taken from Shin *et al.* (2008).

where the magnetic field is compressed. The upstream side shows the development of instabilities, but instabilities are suppressed in the strong field case and in cases with different field orientations. In the perpendicular and oblique cases the field lines drape around the cloud greatly enhancing the field strength upstream of the cloud but also creating a cone of enhanced magnetic energy behind the cloud. The cloud is accelerated to the velocity of the postshock flow faster than without the magnetic field. The field resists motion that would twist it, but allows motion that causes field lines to slip. This results in a curled up sheet rather than the ring seen in the hydrodynamic case, i.e. vortices form only in the plane perpendicular to the field lines[1].

Further analysis of the effect of field orientation was done by van Loo, Falle & Hartquist (2010), who conducted 3D simulations with radiative cooling. While parallel and perpendicular field orientations are extreme idealizations they find that oblique fields could be classed as quasi-parallel and quasi-perpendicular. In their simulations a pre-shock field angle of 45° matches the evolution of the perpendicular shock interaction very well, while a pre-shock angle of 15° to the shock normal is more similar to the parallel case. Dense clumps are produced only in the quasi-parallel cases.

Li, Frank & Blackman (2013) consider a very different field orientation. Instead of a homogeneous magnetic field pervading both the cloud and the ambient material they consider a magnetic field fully contained within the cloud (either toroidal or poloidal arrangement). Cooling is included so the cloud fragments, the resulting fragments depend strongly on the internal field morphology. The mixing and energy transfer is most efficient when the magnetic field is mostly parallel to the

[1]Note that no such vortices can form in the case of a 2D cylindrical cloud.

direction of shock propagation (i.e. poloidal with the axis along the direction of shock propagation), and least efficient when the magnetic field is perpendicular to the direction of shock propagation (i.e. toroidal with the axis along the direction of propagation).

A recent study by Johansson & Ziegler (2013) includes magnetic fields, radiative heating/cooling and anisotropic heat conduction. They are able to reach very high density enhancements, but no Jeans unstable regions are formed for the parameters chosen. The highest cloud compression is achieved in a perpendicular shock case with the initial $\beta = 10^3$, highlighting that a relatively weak magnetic field can efficiently insulate a cloud without providing significant magnetic pressure which would limit the compression.

1.4.5 Turbulence

A high enough resolution to follow turbulence and vorticity generation in shock - cloud interaction was first used in Klein, McKee & Colella (1994). Nakamura *et al.* (2006) studied further how the turbulence is generated in the interactions. The vortical motions produced by the instabilities is converted into random motion of the cloud fragments when the cloud is shredded. The typical velocity dispersion is of the order of 10% of the shock velocity. A sharper boundary leads to slightly higher dispersions, particularly in the direction of shock propagation. They also find that the onset of instabilities is significantly delayed if the cloud boundaries are smooth. The cloud lifetime may be up to 3 times longer due to the time it takes for a “slip-surface” (a density discontinuity with a velocity shear across it) to form. On the other hand, a fractal substructure of the cloud in the wind-cloud interactions of

Cooper *et al.* (2009) leads to a faster cloud fragmentation as the wind is able to find paths of lesser resistance within the cloud and split off cloudlets. Some individual cloudlets do survive longer, however, as they are shielded by upstream cloudlets.

Pittard *et al.* (2005) considers a case of multiple mass injection regions. When injected mass dominates the mass flux in the wind a global bow-shock forms and the region is largely subsonic, whereas if injection regions are further apart the wind material can flow supersonically between the injection regions. This work uses a $k-\epsilon$ subgrid turbulence model (see Sec. 2.1.1). In Pittard *et al.* (2009) a $k-\epsilon$ treatment of turbulence allows the simulation of a turbulent post-shock flow which is shown to have a particularly strong effect on high density contrast clouds which survive the longest in the post-shock flow and are subject to a longer period of "buffeting". The clouds are accelerated and destroyed faster than in "inviscid" simulations[1]. However, more rapid destruction of clouds generates less total circulation, so that turbulence may be self-limiting. The mass loss rate is found to vary over time. Material stripped off clouds with $\chi = 10^3$ forms a tail which is wider if the environmental turbulence is higher. The $k-\epsilon$ model allows to approximate a high Reynolds number flow at lower resolution. For 2D axisymmetric adiabatic hydrodynamic simulations meaningful convergence can be reached at 32 cells per cloud radius rather than the 100 required in inviscid simulations.

At high Mach numbers Mach scaling holds, and the evolution at different Mach numbers can be related via a scaling factor. In contrast, Pittard *et al.* (2010) show that significant differences in the morphology and evolution occur at low Mach numbers. In particular, when $M < 2.76$, the post-shock flow is subsonic relative to the cloud and a bow-wave instead of a bow-shock develops. The compression of

[1] i.e. those without a $k-\epsilon$ model.

a cloud in such cases is more isotropic. Due to a smaller velocity difference at the slip-surface KH and RT instabilities are limited and the turbulent energy fraction is lower and the vortex ring is weaker. It all adds up to a substantially longer lifetime, of 20–30 t_{cc}.

Other related work

The discussion in the previous subsections is not exhaustive but it aims to show the scope of previous investigations of shock-cloud interactions. Other important insights can be gleaned from related studies of shell-cloud (e.g. Anathpindika & Bhatt 2011; Pittard 2011), wind-cloud (e.g. Vieser & Hensler 2007; Cooper *et al.* 2009), cloud-jet (e.g. Raga *et al.* 2002), cloud-cloud (e.g. Anathpindika 2010; Duarte-Cabral *et al.* 2011), shock-turbulent region (e.g. Inoue *et al.* 2012) interactions and interstellar turbulence (e.g. Seifried *et al.* 2011).

Overview of this Thesis

Chapter 2 describes the numerical code used. Chapter 3 of this Thesis presents hydrodynamic simulations of a large number of clouds in 2D. Chapter 4 presents MHD interactions between a shock and up to 3 nearby clouds. Chapter 5 expands this work to a large number of clouds and also considers weak magnetic fields. Additionally, preliminary 3D simulations are presented. Finally a summary is given in Chapter 6.

Table 1.3: A summary of the investigations discussed in Section 1.4.

Authors	Geometry	Resolution[1]	χ	M	Notes[2]
S75[a]	2D XY	2	500, 2000, 3000	∞	square cloud, (*c*)
MC75[b]	Analytical discussion, (*ck*)				
H86[c]	Analytical discussion of ablation of a cloud embedded in a wind, ()				
E88[d]	Analytical discussion of pressure fronts in magnetized clumpy medium, (*m*)				
SN92[e]	3D XYZ	60	10	10	()
KMC94[f]	2D RZ	120 (240)	3, 10, 30	10, 100, 100	()
M94[g]	2D RZ,XY	50 (240)	10	10, 100	(*m*)
XS95[h]	3D XYZ	25 (53)	10	10	Includes spheroid clouds, ()
G00[i]	3D XYZ	16 (26)	10, 30, 100	1.5, 3	Wind-cloud interaction, (*m*)
MKR02[j]	2D RZ,XY	200	1000	10	(*c*)
PFB02[k]	2D XY	32	500	10	Multiple clouds (up to 15), ()
K03[l]	n/a	n/a	$\sim$10	$\sim$10	Laser experiment
F04[m]	2D XY	200	1000	5, 10, 20, 40	Includes several clouds, (*c*)
M05[n]	2D XY, 3D XYZ	32	500, 5000	7, 17	Includes several clouds, (*c*)
O05[o]	2D RZ, 3D XYZ	32	10	30, 50	(*ck*)
PF05[p]	2D XY	$\sim$450	3, 6, 8, 10	10, 20	Substructure, ()
P05[q]	2D XY	32	∞	20	Several mass injection regions, ()
N06[r]	2D RZ, 3D XYZ	120 (960)	10, 100	1.5, 10, 100, 1000	()
V07[s]	2D RZ	640	45	1.5, 2.5, 5	(*cm*)
O08[t]	2.5D XYZ	132 (528)	10	50	(*ckm*)
SSS08[u]	3D XYZ	68	10	10	(*m*)
C09[v]	3D XYZ	384 (512)	630, 910, 1260	4.6	Wind-cloud, incl. fractal cloud, (*c*)
P09[w]	2D RZ	128 (256)	10, 100, 1000	10	Includes subgrid turbulence model, ()
P10[x]	2D RZ	128	10, 100, 1000	1.5–40	Includes subgrid turbulence model, ()
VFH10[y]	3D XYZ	480	45	2.5	(*cm*)
YFC10[z]	2D RZ, 3D XYZ	192 (1536)	100	50	(*c*)
JZ13[α]	3D XYZ	100	100	30	(*ckm*)
LFB13[β]	3D XYZ	80	100	10	Cloud with internal magnetic fields (*cm*)

[1]: Where different resolutions were used a typical resolution is given with the maximum resolution in parentheses.

[2]: Deviations from the standard shock cloud interaction noted, in the parentheses *c* denotes that radiative cooling (using a cooling curve) was included, *k* - thermal conduction and *m* - magnetic fields.

The references are: [a]Sgro (1975),[b]McKee & Cowie (1975), [c]Hartquist *et al.* (1986), [d]Elmegreen (1988), [e]Stone & Norman (1992), [f]Klein, McKee & Colella (1994), [g]Mac Low *et al.* (1994), [h]Xu & Stone (1995), [i]Gregori *et al.* (2000), [j]Mellema, Kurk & Röttgering (2002), [k]Poludnenko, Frank & Blackman (2002), [l]Klein *et al.* (2003), [m]Fragile *et al.* (2004), [n]Melioli *et al.* (2005), [o]Orlando *et al.* (2005), [p]Patnaude & Fesen (2005), [q]Pittard *et al.* (2005), [r]Nakamura *et al.* (2006), [s]van Loo *et al.* (2007), [t]Orlando *et al.* (2008), [u]Shin *et al.* (2008), [v]Cooper *et al.* (2009), [w]Pittard *et al.* (2009), [x]Pittard *et al.* (2010), [y]van Loo, Falle & Hartquist (2010), [z]Yirak, Frank & Cunningham (2010), [α]Johansson & Ziegler (2013), [β]Li, Frank & Blackman (2013).

Chapter 2

Numerical Methods

The calculations presented in this Thesis were performed using the numerical code *mg*. This chapter presents the basic structure of hydrodynamic and ideal MHD codes with particular emphasis on the implementation in *mg*.

2.1 Basic equations

A numerical method provides approximate solutions to equations which would be exceptionally hard to solve otherwise. In the hydrodynamic case the equations describing the flow are the Euler equations for inviscid flow or the Navier-Stokes equations for viscous flow.

In *mg* the Euler equations are supplemented by a k-ϵ subgrid turbulence model which models the mean properties of the flow with fully developed, high Reynolds number turbulence.

The full set of equations (in Cartesian coordinates, see also Pittard *et al.* 2009, for a description including cylindrical coordinates) consists of: the continuity equa-

tion,

$$\frac{\partial \rho}{\partial t} + \nabla \cdot (\rho \mathbf{u}) = 0, \tag{2.1}$$

momentum equations for the three components of momentum,

$$\frac{\partial \rho u}{\partial t} + \nabla \cdot (\rho u \mathbf{u}) = -\frac{\partial P}{\partial x} + \nabla \cdot \boldsymbol{\tau}_x, \tag{2.2}$$

$$\frac{\partial \rho v}{\partial t} + \nabla \cdot (\rho v \mathbf{u}) = -\frac{\partial P}{\partial y} + \nabla \cdot \boldsymbol{\tau}_y, \tag{2.3}$$

$$\frac{\partial \rho w}{\partial t} + \nabla \cdot (\rho w \mathbf{u}) = -\frac{\partial P}{\partial z} + \nabla \cdot \boldsymbol{\tau}_z, \tag{2.4}$$

the energy equation,

$$\frac{\partial e}{\partial t} + \nabla \cdot [(e+p)\mathbf{u} - \mathbf{u} \cdot \boldsymbol{\tau}] - \frac{\gamma}{\gamma - 1} \nabla \cdot (\mu_{\mathrm{T}} \nabla T) = S_E, \tag{2.5}$$

an advection equation for the advected scalar (used to distinguish different regions),

$$\frac{\partial \rho \kappa}{\partial t} + \nabla \cdot (\rho \kappa \mathbf{u}) - \nabla \cdot (\mu_{\mathrm{T}} \nabla \kappa) = 0, \tag{2.6}$$

and the equations for the turbulent energy,

$$\frac{\partial \rho k}{\partial t} + \nabla \cdot (\rho k \mathbf{u}) - \nabla \cdot (\mu_{\mathrm{T}} \nabla k) = S_k, \tag{2.7}$$

and the turbulent energy dissipation rate,

$$\frac{\partial \rho \epsilon}{\partial t} + \nabla \cdot (\rho \epsilon \mathbf{u}) - \nabla \cdot (\mu_\epsilon \nabla \epsilon) = S_\epsilon. \tag{2.8}$$

Here ρ is the mass density, $\mathbf{u}$ is the velocity with u, v, w its components in the x, y and z directions respectively, p is the thermal pressure, e is the total (thermal plus

kinetic) energy density given by

$$e = \frac{p}{\gamma - 1} + \frac{1}{2}\rho \mathbf{u}^2, \tag{2.9}$$

T is the temperature, κ is an advected scalar, k is the turbulent energy per unit mass, ϵ is the turbulent energy dissipation rate per unit mass and the diffusion coefficients are

$$\mu_{\mathrm{T}} = \rho C_\mu \frac{k^2}{\epsilon}, \quad \mu_\epsilon = \frac{\mu_{\mathrm{T}}}{\sigma_\epsilon}, \tag{2.10}$$

with $C_\mu = 0.09$ and $\sigma_\epsilon = 1.3$. The source terms are,

$$S_k = P_{\mathrm{t}} - \rho\epsilon, \quad S_\epsilon = \frac{\epsilon}{k}(C_1 P_{\mathrm{t}} - C_2 \rho\epsilon), \tag{2.11}$$

where $C_1 = 1.4$, $C_2 = 1.94$ and the turbulent production term is

$$P_{\mathrm{t}} = \mu_{\mathrm{T}} \sum_{i=1}^{3}\sum_{j=1}^{3} \frac{\partial u_i}{\partial x_j}\left(\frac{\partial u_i}{\partial x_j} + \frac{\partial u_j}{\partial x_i}\right) - \frac{2}{3}\nabla\cdot\mathbf{u}(\rho k + \mu_{\mathrm{T}}\nabla\cdot\mathbf{u}). \tag{2.12}$$

The energy source term is,

$$S_E = -S_k - n^2\Lambda + n\Gamma, \tag{2.13}$$

where $n^2\Lambda$ and $n\Gamma$ are cooling and heating terms if cooling and heating are included. $\boldsymbol{\tau}$ is the turbulent stress tensor,

$$\tau_{ij} = \mu_{\mathrm{T}}\left(\frac{\partial u_i}{\partial x_j} + \frac{\partial u_j}{\partial x_i}\right) - \frac{2}{3}\delta_{ij}(\rho k + \mu_{\mathrm{T}}\nabla\cdot\mathbf{u}) \tag{2.14}$$

and $\boldsymbol{\tau}_l$ is used to denote $(\tau_{li}, \tau_{lj}, \tau_{lk})^{\mathrm{T}}$.

2.1.1 Sub-grid turbulence model

The evolution of the velocity field in the presence of turbulence is chaotic in nature and cannot be followed accurately. However, the average quantities, either in time or in space, show a more consistent behaviour and a statistical model could potentially predict it. Unfortunately, the resulting equations have more unknowns than equations and adding additional relationships only adds more unknowns (in the form of velocity correlations). This is called the *closure problem of turbulence* (see e.g. Davidson 2004).

A most widely used model is the k-ϵ model of Jones & Launder (1972). It is a one point closure (where the turbulent terms are completely determined by the properties at that point), two equation, eddy-viscosity model. The energy is concentrated on the largest eddies and is dissipated in the smallest, which act to increase the effective viscosity. Eq. 2.7 specifies that the change in turbulent (kinetic) energy is governed by the flux of, generation of and dissipation of turbulent energy, with experimentally determined constants. Eq. 2.8 is completely empirical, but is calibrated against a few well know problems. The model uses five free, experimentally calibrated, parameters, C_μ, σ_ϵ, C_1 and C_2 (the fifth one $\sigma_k = 1$ is dropped from eq. 2.7). It works surprisingly well for shear flows, but can fail spectacularly for non-anisotropic flows or when strong pressure gradients are present in the boundary layers (Hanjalić 1994). The main advantage of k-ϵ is that it is relatively easy to implement, and the cases where it fails are well documented.

The implementation of the k-ϵ model is described in Falle (1994). In the following sections the turbulent terms are neglected and only the implementation of the underlying Euler's equations is presented.

2.2 Finite volume methods

In a finite volume approximation the domain is subdivided into finite volumes and the differential equations in Sec. 2.1 are integrated over that volume, e.g.

$$\iiint_V \frac{\partial \rho}{\partial t}\,\mathrm{d}V + \iiint_V \nabla\cdot(\rho\mathbf{u})\,\mathrm{d}V = 0, \tag{2.15}$$

which, by the divergence theorem is

$$\frac{\partial m}{\partial t} + \oint_A \rho(\mathbf{u}\cdot\mathbf{n})\,\mathrm{d}A = 0. \tag{2.16}$$

Eq. 2.16 states that the change of mass contained in a volume, V, during a time interval $\mathrm{d}t$, is equal to the flux of mass through the surface of this volume. The flux through a boundary between two volumes moves the mass but the total amount remains constant. Such a form is conservative, which is desirable as the underlying property is physically conserved as well.

In order to numerically solve the equations they have to be discretised. The finite volumes divide the domain into cells (we will assume that the cells are cubes of side length h, although such an assumption is not necessary in general) and the time is divided into snapshots. The objective of a numerical method is to advance the solution from the state at the current snapshot to the next snapshot in time.

The change over one time step is given by integrating the flux over the time step,

$$\rho_{ijk}^{n+1} - \rho_{ijk}^{n} + \int_{t_n}^{t_{n+1}} F_{ijk}(\rho)\,\mathrm{d}t = 0, \tag{2.17}$$

where F_{ijk} is the sum of fluxes across the six surfaces bounding the cell ijk. For

simplicity we limit the flow to one direction, so that for a conserved variable, q,

$$F_i(q) = F_{i+1/2}(q) - F_{i-1/2}(q), \tag{2.18}$$

and

$$F_{i+1/2}(q) = h^{-2} \int_{A_{i+1/2}} q\mathbf{u}\cdot\mathbf{n}\,\mathrm{d}A_{i+1/2}, \tag{2.19}$$

where $A_{i+1/2}$ is the boundary between cells i and $i+1$.

Eq. 2.17 is an exact version of Eq. 2.1, but in order to solve it F needs to be approximated by $\bar{F}$, so that

$$\int_{t_n}^{t_{n+1}} F_{i+1/2}(q) = \Delta t \bar{F}^n_{i+1/2}(q). \tag{2.20}$$

The prescription for the update (with the flow restricted to one direction, and with turbulent and source terms to be added separately) is then

$$\rho_i^{n+1} = \rho_i^n - \Delta t \bar{F}^n_{i+1/2}(\rho) + \Delta t \bar{F}^n_{i-1/2}(\rho), \tag{2.21}$$

$$(\rho u)_i^{n+1} = (\rho u)_i^n - \Delta t \bar{F}^n_{i+1/2}(\rho u) + \Delta t \bar{F}^n_{i-1/2}(\rho u) - \Delta t \bar{p}_i^n, \tag{2.22}$$

$$e_i^{n+1} = e_i^n - \Delta t \bar{F}^n_{i+1/2}(e+p) + \Delta t \bar{F}^n_{i-1/2}(e+p). \tag{2.23}$$

2.3 The Riemann problem

The fluxes, $\bar{F}$, are approximated by solving the Riemann problem. In it the boundary between two states keeping them separated is removed and the flow is allowed to evolve. Such a flow may include two shocks and/or rarefaction waves and a contact discontinuity in the region between them as in Fig. 1.2. These three boundaries

separate the flow into four regions. The solution is self-similar (e.g. Leveque 1998), i.e. $f(x,t) = f(x/t)$ which means that the flow through the interface (at $x = 0$) is constant in time[1].

There are six possible cases for the conditions on the boundary: four cases where one of the constant regions falls on the boundary and two cases where a rarefaction wave spans the boundary. The two inner regions, which are separated by the contact discontinuity are at the same pressure, and velocity. This pressure, p_*, is determined by solving the equation

$$f(p_*, \mathbf{P}_\mathrm{L}) + f(p_*, \mathbf{P}_\mathrm{R}) + u_\mathrm{R} - u_\mathrm{L} = 0 \tag{2.24}$$

(Toro 2009), where

$$f(p_*, \mathbf{P}) = \begin{cases} (p_* - p)\left[\dfrac{2}{((\gamma+1)p_* + (\gamma-1)p)\rho}\right]^{1/2} & \text{if } p_* > p \text{ (shock)}, \\ \dfrac{2a}{\gamma-1}\left[\left(\dfrac{p_*}{p}\right)^{\frac{\gamma-1}{2\gamma}} - 1\right] & \text{if } p_* \leq p \text{ (rarefaction)}. \end{cases} \tag{2.25}$$

$\mathbf{P}$ contains the primitive variables (ρ, u, p) either for the left state ($\mathbf{P}_\mathrm{L}$) or the right state ($\mathbf{P}_\mathrm{R}$). $a = \sqrt{\frac{\gamma p}{\rho}}$ is the adiabatic sound speed. The case with two rarefactions is linear in $p_*^{(\gamma-1)/(2\gamma)}$ and solvable directly. Otherwise an iterative method is used

$$p_{*,i+1} = \frac{w_\mathrm{R} p_\mathrm{L} + w_\mathrm{L} p_\mathrm{R} - w_\mathrm{R} w_\mathrm{L}(u_\mathrm{R} - u_\mathrm{L})}{w_\mathrm{R} + w_\mathrm{L}}, \tag{2.26}$$

[1] In order for flow to be constant across the interface it must not be affected by waves emanating from other boundaries. This imposes the limit on the timestep (the *Courant-Friedrichs-Lewy* condition), $\Delta t_{\max} = C\frac{h}{u_{\max}}$, where $u_{\max}$ is the maximum propagation speed across the grid. If wave interactions do not modify their propagation speed $C \sim 0.9$ is sufficient to ensure that the conditions at the interface do not change. A more conservative $C = 0.4$ is used in *mg* which avoids wave interactions completely and provides stability at higher dimensions.

where

$$w_{\mathrm{K}} = \rho_{\mathrm{K}} a_{\mathrm{K}} w(p_{*,i}/p_{\mathrm{K}}) \tag{2.27}$$

and

$$w(x) = \begin{cases} \left[1 + \dfrac{\gamma+1}{2\gamma}(x-1)\right]^{1/2} & \text{if } x \geq 1, \\ \dfrac{(\gamma-1)(1-x)}{2\gamma(1-x^{\frac{\gamma-1}{2\gamma}})} & \text{if } x < 1, \end{cases} \tag{2.28}$$

The initial guess is provided by a linear solver. The linear solver is similar to the two shock approximation in Toro:

$$\begin{cases} p_0 = \max(p_{\mathrm{floor}}, p_{\mathrm{TS}}), \\ p_{\mathrm{TS}} = \dfrac{g_{\mathrm{L}}(\hat{p})p_{\mathrm{L}} + g_{\mathrm{R}}(\hat{p})p_{\mathrm{R}} - (u_{\mathrm{R}} - u_{\mathrm{L}})}{g_{\mathrm{L}}(\hat{p}) + g_{\mathrm{R}}(\hat{p})}, \\ g_{\mathrm{K}}(p) = \left(\dfrac{2}{[(\gamma+1)p + (\gamma-1)p_{\mathrm{K}}]\rho_{\mathrm{K}}}\right)^{1/2}, \end{cases} \tag{2.29}$$

where p_{floor} is a small positive value required to ensure that pressure stays positive and $\hat{p}$ is some initial guess. In *mg* p_{L} is used as a guess in g_{L} and p_{R} in g_{R} which after some algebraic manipulation reduces to

$$p_0 = \frac{\rho_{\mathrm{R}} a_{\mathrm{R}} p_{\mathrm{L}} + \rho_{\mathrm{L}} a_{\mathrm{L}} p_{\mathrm{R}} - \rho_{\mathrm{R}} \rho_{\mathrm{L}} a_{\mathrm{R}} a_{\mathrm{L}} (u_{\mathrm{R}} - u_{\mathrm{L}})}{\rho_{\mathrm{R}} a_{\mathrm{R}} + \rho_{\mathrm{L}} a_{\mathrm{L}}}. \tag{2.30}$$

This method to determine p_* can give a result that is as accurate as required, but requires several iterations and can be slow. So unless p_* given by the linear solver differs by more than 10% from either p_{L} or p_{R} the exact solver is not called and the linear result is used.

Once the pressure in the intermediate region is know, the velocity of the waves (shocks or rarefactions) can be calculated and the conditions at the boundary de-

termined. The velocity, u_*, is given by, e.g.,

$$u_* = u_{\mathrm{R}} + f(p_*, \mathbf{W}_{\mathrm{R}}), \tag{2.31}$$

although in *mg* an equivalent form is used:

$$u_* = \frac{\rho_{\mathrm{R}} a_{\mathrm{R}} u_{\mathrm{R}} w(p_*/p_{\mathrm{R}}) + \rho_{\mathrm{L}} a_{\mathrm{L}} u_{\mathrm{L}} w(p_*/p_{\mathrm{L}}) - p_{\mathrm{R}} + p_{\mathrm{L}}}{\rho_{\mathrm{R}} a_{\mathrm{R}} w(p_*/p_{\mathrm{R}}) + \rho_{\mathrm{L}} a_{\mathrm{L}} w(p_*/p_{\mathrm{L}})}. \tag{2.32}$$

The density either side of the contact discontinuity depends on the type of the wave. If it is a shock the density jump can be calculated from the pressure jump and

$$\rho_{*,\mathrm{K}} = \rho_{\mathrm{K}} \left[\frac{\frac{p_*}{p_{\mathrm{K}}} + \frac{\gamma-1}{\gamma+1}}{\frac{\gamma-1}{\gamma+1}\frac{p_*}{p_{\mathrm{K}}} + 1} \right], \tag{2.33}$$

while behind a rarefaction wave we assume an isoentropic expansion and

$$\rho_{*,\mathrm{K}} = \rho_{\mathrm{K}} \left(\frac{p_*}{p_{\mathrm{K}}} \right)^{1/\gamma}. \tag{2.34}$$

In *mg* a single expression is used,

$$\rho_{*,\mathrm{K}} = \rho_{\mathrm{K}} \left[\frac{a_{\mathrm{K}} w(p_*/p_{\mathrm{K}})}{a_{\mathrm{K}} w(p_*/p_{\mathrm{K}}) \pm (u - u_{\mathrm{K}})} \right] \tag{2.35}$$

(the sign in the denominator is positive for $\rho_{*,\mathrm{R}}$ and negative for $\rho_{*,\mathrm{L}}$).

If $u_* > 0$ then the boundary lies on the left of the contact discontinuity. The left wave is a shock if $p_* > p_L$. Its velocity is $S_{\mathrm{L}} = u_{\mathrm{L}} - a_{\mathrm{L}} w(p_*/p_{\mathrm{L}})$. If $S_{\mathrm{L}} > 0$ the left shock is to the right of the interface and values on the left, $\boldsymbol{P}_{\mathrm{L}}$, are used. If $S_{\mathrm{L}} < 0$ then the interface is between the left shock and the contact discontinuity and values

$\boldsymbol{P}_{*,\mathrm{L}}$ are used. If $p_* < p_\mathrm{L}$ the left wave is a rarefaction wave, its *head* travels at speed $S_\mathrm{LH} = u_\mathrm{L} - a_\mathrm{L}$ and its *tail* speed at $S_\mathrm{LT} = u_* - a_{*,\mathrm{L}}$. If $S_\mathrm{LT} < 0$ the *tail* is to the left and $\boldsymbol{P}_{*,\mathrm{L}}$are used. If $S_\mathrm{LH} > 0$ the *head* is to the right and $\boldsymbol{P}_\mathrm{L}$ are used. Finally, if $S_\mathrm{LH} < 0$ and $S_\mathrm{LT} > 0$ the interface falls within the rarefaction. The values in the rarefaction fan are constant along characteristics x/t and are given by

$$\begin{cases} \rho_{\mathrm{K,fan}}(x,t) = \rho_\mathrm{K}\left[\dfrac{2}{\gamma+1} \pm \dfrac{\gamma-1}{(\gamma+1)a_\mathrm{K}}\left(u_\mathrm{K} - \dfrac{x}{t}\right)\right]^{\frac{2}{\gamma-1}}, \\ u_{\mathrm{K,fan}}(x,t) = \dfrac{2}{\gamma+1}\left[\dfrac{\gamma-1}{2}u_\mathrm{K} \pm a_\mathrm{K} + \dfrac{x}{t}\right], \\ p_{\mathrm{K,fan}}(x,t) = p_\mathrm{K}\left[\dfrac{2}{\gamma+1} \pm \dfrac{\gamma-1}{(\gamma+1)a_\mathrm{K}}\left(u_\mathrm{K} - \dfrac{x}{t}\right)\right]^{\frac{2\gamma}{\gamma-1}} \end{cases} \tag{2.36}$$

(Toro 2009)(the sign next to factors involving a_L is positive and it is negative next to a_R). The interface value lies on the characteristic $x/t = 0$ and after some manipulation:

$$\begin{cases} u_{\mathrm{K,fan}} = \dfrac{\gamma-1}{\gamma+1}\left(u_\mathrm{K} \pm \dfrac{2}{\gamma-1}a_\mathrm{K}\right), \\ p_{\mathrm{K,fan}} = p_\mathrm{K}\left[\dfrac{\pm u_{\mathrm{K,fan}}}{a_\mathrm{K}}\right]^{\frac{2\gamma}{\gamma-1}}, \\ \rho_{\mathrm{K,fan}} = \gamma p_{\mathrm{K,fan}} u_{\mathrm{K,fan}}^{-2} \end{cases} \tag{2.37}$$

(again, the variable sign is positive for left states and negative for right states).

If $u_* < 0$ then the boundary lies on the right of contact discontinuity. In this case there is a change in signs (e.g. $S_\mathrm{RT} = u_* + a_{*,\mathrm{R}}$, $S_\mathrm{RH} = u_\mathrm{R} + a_\mathrm{R}$, $S_\mathrm{RT} = u_* + a_{*,\mathrm{R}}$) and all the checks are inverted, i.e. if $S_\mathrm{R} < 0$ then right values, $\boldsymbol{P}_\mathrm{R}$, are used.

The method is generalised to two and three dimensions via operator splitting. The total flux is the sum of each 1-dimensional flux. Some artificial dissipation is added to the momentum and energy fluxes to improve the stability, particularly

near grid aligned shocks (Quirk 1994). Viscous fluxes and source terms are also operator split and are calculated separately. Cell values are then updated with all the contributions.

2.3.1 Second order accuracy

The original Godunov method described here is first order accurate in space and time and turns out to be very diffusive. In *mg* second order accuracy is used balancing the accuracy and computational cost.

First order spatial reconstruction assumes that values are constant within the cells (piecewise constant method). Second order accuracy is achieved by assuming the values vary linearly within the cell, and the stored value is the average over the entire cell. There are several ways to determine the slope although in order to avoid introducing non-physical features certain criteria have to be met. The reconstruction cannot change the direction of change across the interface and it cannot introduce spurious maxima (i.e. the edge value cannot be greater than average values of both cells). To avoid spurious maxima the gradient within the cell is limited (this is know as a slope limiter).

In *mg* the gradient in cell i is given by

$$\frac{\partial q_i}{\partial x} = \frac{1}{h}\,\mathrm{av}(q_i - q_{i-1}, q_{i+1} - q_i), \tag{2.38}$$

where the averaging function satisfying the conditions noted is

$$\mathrm{av}(a,b) = \begin{cases} \dfrac{a^2 b + a b^2}{a^2 + b^2} & \text{if } ab > 0 \text{ and } a^2 + b^2 \neq 0, \\ 0 & \text{otherwise.} \end{cases} \tag{2.39}$$

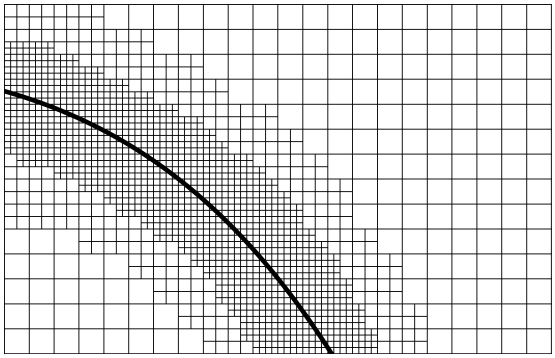

Figure 2.1: An example of an AMR grid.

To achieve second order accuracy in time a second order Runge-Kutta method is used. The solution is first advanced half a timestep (using a piecewise constant spatial reconstruction). The resulting state is then used to compute fluxes (using a piecewise linear spatial reconstruction) and sources which are used to advance the initial state by a full timestep.

2.4 Adaptive Mesh Refinement

When the flow is smooth over a large fraction of the domain but fine details emerge in small regions a great speed up can be achieved if a coarse grid is used in smooth flow regions and a fine grid only where it is required. This can be done without sacrificing the accuracy, or alternatively can increase the accuracy at the same computational cost. If locations where the fine mesh is required are known in advance a static non-uniform grid could be used, but more generally the requirements change as the solution evolves. In that case an Adaptive Mesh Refinement (AMR) method dynamically creates finer grid levels where the solution requires it and removes (derefines) these levels once they are no longer needed.

In *mg* each grid level increases the resolution by a factor of 2 in each direction. In a refined level n the time step is

$$\Delta t_n = \frac{\Delta t_{n-1}}{2^i} \tag{2.40}$$

for the smallest integer $i \geq 0$ that satisfies the time step limit. Two grids (G^0 and G^1) cover the entire domain. Finer grids were added where they were needed and removed where they were not, based on the refinement criteria controlled by differences in the solutions on the coarser grids. If the difference between a conserved variable in the finest grid, and its projection from a grid one level down is greater than 1% the cell is marked for refinement. If the difference in the two preceding levels drops below 1% the cell is marked for derefinement. The refinement criteria is then somewhat diffused to ensure a smooth transition between multiple levels as shown in Fig. 2.1.

2.5 MHD

The MHD problem solves the equations of ideal MHD.

$$\frac{\partial \rho}{\partial t} + \nabla \cdot (\rho \mathbf{u}) = 0, \tag{2.41}$$

$$\frac{\partial \rho u}{\partial t} + \nabla \cdot (\rho u \mathbf{u}) + \frac{\partial P}{\partial x} = \nabla \cdot (B_x \boldsymbol{B}), \tag{2.42}$$

$$\frac{\partial \rho v}{\partial t} + \nabla \cdot (\rho v \mathbf{u}) + \frac{\partial P}{\partial y} = \nabla \cdot (B_y \boldsymbol{B}), \tag{2.43}$$

$$\frac{\partial \rho w}{\partial t} + \nabla \cdot (\rho w \mathbf{u}) + \frac{\partial P}{\partial z} = \nabla \cdot (B_z \boldsymbol{B}), \tag{2.44}$$

$$\frac{\partial E}{\partial t} + \nabla \cdot [(E + P)\mathbf{u}] = \nabla \cdot ([\boldsymbol{B} \cdot \boldsymbol{u}]\boldsymbol{B}), \tag{2.45}$$

$$\frac{\partial \boldsymbol{B}}{\partial t} = \nabla \times (\boldsymbol{u} \times \boldsymbol{B}), \tag{2.46}$$

where P is the total pressure (gas pressure, $p_{\rm g}$, plus magnetic pressure, $p_{\rm m} = \frac{1}{2}B^2$) and $E = \frac{p_g}{\gamma - 1} + p_m + \frac{1}{2}\rho u^2$ is the total energy per unit volume. The units are chosen such that factors of 4π and the speed of light do not appear. Note that the k-ϵ subgrid model is not used.

The problem is significantly more complicated as the MHD equations give rise to three waves (see Sec. 1.3.2.2) which result in seven regions that need to be computed (instead of four in the hydrodynamic case). The problem is expressed in primitive variables,

$$\frac{\partial \boldsymbol{P}}{\partial t} + \bar{\mathbf{A}} \frac{\partial \boldsymbol{P}}{\partial x} = 0, \tag{2.47}$$

where

$$\boldsymbol{P} = \left[\rho, v_x, v_y, v_z, p_{\rm g}, B_y, B_z\right]^T \tag{2.48}$$

is the vector of primitive variables, and

$$\mathbf{A}(\boldsymbol{P}) = \begin{bmatrix} v_x & \rho & 0 & 0 & 0 & 0 & 0 \\ 0 & v_x & 0 & 0 & \frac{1}{\rho} & \frac{B_y}{\rho} & \frac{B_z}{\rho} \\ 0 & 0 & v_x & 0 & 0 & -\frac{B_x}{\rho} & 0 \\ 0 & 0 & 0 & v_x & 0 & 0 & -\frac{B_x}{\rho} \\ 0 & \rho a^2 & 0 & 0 & v_x & 0 & 0 \\ 0 & B_y & -B_x & 0 & 0 & v_x & 0 \\ 0 & B_z & 0 & -B_x & 0 & 0 & v_x \end{bmatrix} \tag{2.49}$$

is the Jacobian matrix of fluxes with respect to primitive variables. The problem is linearized by using a mean matrix,

$$\bar{\mathbf{A}}(\boldsymbol{P}_{\mathrm{L}}, \boldsymbol{P}_{\mathrm{R}}) = \mathbf{A}(\frac{1}{2}[\boldsymbol{P}_{\mathrm{L}} + \boldsymbol{P}_{\mathrm{R}}]), \tag{2.50}$$

determined from the left and right states. The fluxes are then computed using a linear Riemann solver from the eigenvectors of $\bar{\mathbf{A}}$ as described in Falle, Komissarov & Joarder (1998) and Ager (2009).

An additional complication in the MHD problem is the condition

$$\nabla \cdot \boldsymbol{B} = 0, \tag{2.51}$$

which, unless it is enforced explicitly, can be violated by numerical errors introducing magnetic monopoles. This can break the solution, in particular near discontinuities (Brackbill & Barnes 1980).

In *mg* the divergence cleaning algorithm of Dedner *et al.* (2002) is used to transport the errors towards the boundaries and dampen them.

Chapter 3

Hydrodynamic Simulations

3.1 Introduction

The energy input from massive stars (discussed in Section 1.3) is responsible for many dynamic features of the ISM. For example, the energy input in regions of vigorous star formation creates bubbles of hot plasma which may overlap to create superbubbles. Such structures are large enough that they can burst out of their host galaxies, and vent mass and energy into the intergalactic medium. The evolution of such flows depends on the properties of the surrounding ISM. As a large mass fraction may reside in dense clouds of small volume fraction (Section 1.1.1), these clouds can dominate the evolution as they 'mass-load' the flow. An understanding of gas dynamics in such regions, therefore, requires knowledge of how hot plasma interacts with the cold, dense material present in the interstellar medium.

The response of a cloud to a given set of conditions remains to be fully elucidated. Although a large literature on interactions involving single clouds exists (see Section 1.4), there are only a handful of studies on the interaction of a flow

overrunning multiple clouds (Jun *et al.* 1996; Steffen *et al.* 1997; Poludnenko *et al.* 2002; Pittard *et al.* 2005). For instance, turbulence is generated by the instabilities in the 'slip-surface' of an isolated cloud (Nakamura *et al.* 2006), but turbulence from upstream clouds and from the flow deflected around the clouds could result in ever more violent interactions. On the other hand, 'mass-loaded' flows tend towards Mach number of 1 (Hartquist *et al.* 1986), which as shown by Pittard *et al.* (2010) can result in a gentler interaction, where a cloud is compressed more uniformly. There remains a clear need for further studies to examine the collective effects of clouds on a flow, and to determine whether there are differences between the behaviours of upstream and downstream clouds.

This is a first step in a long term study of the global effects of clouds on an overrunning flow. To simplify the problem and reduce the number of free parameters we have assumed adiabatic behaviour, with a ratio of specific heats $\gamma = 5/3$. It allows us to follow the generic behaviour of a flow interacting with clouds. In future we will perform calculations which include heating and radiative losses. We investigate how cloud destruction affects the density, speed and Mach number of the flow. We also determine whether the position of a cloud within the clumpy region significantly affects its evolution. In Section 3.2 we describe the initial conditions and a convergence study which informs the subsequent work in this chapter. Our results are presented in Section 3.3, and conclusions and motivation for further work are addressed in Section 3.5.

3.2 Method

3.2.1 Numerical setup

The computations were performed with the *mg* hydrodynamic code (see Chapter 2).

The initial conditions prescribe clouds and an ambient medium at uniform pressure. The clouds have a density profile

$$\rho(r) = \rho_{\rm amb}[\psi + (1-\psi)\eta] \tag{3.1}$$

(see Pittard *et al.* 2009), where

$$\eta = \frac{1}{2}\left(1 + \frac{\alpha - 1}{\alpha + 1}\right), \tag{3.2}$$

$$\alpha = \exp\{\min[20.0, p_1((r/r_{\rm cl})^2 - 1)]\}. \tag{3.3}$$

r is the distance from the centre of the cloud, $r_{\rm cl}$ is the cloud radius, p_1 is the parameter controlling the steepness of the edge (throughout this work a value of $p_1 = 10$ is used giving a fairly sharp edge) and $\psi \simeq \chi = \rho_{\rm max}/\rho_{\rm amb}$.

Behind the shock front the flow properties are determined by the Rankine-Hugoniot jump conditions (Section 1.3.2.1). Zero derivative boundary conditions (allowing free inflow/outflow, but care must be taken if disturbances reach the boundary) were imposed in the x direction. In single cloud simulations the same boundary conditions were used in the y direction, while multiple cloud simulations used periodic boundary conditions in y.

In the single cloud simulations the cloud was centred on the grid origin, and a planar shock front was imposed at $x = -3$. Time zero is defined to be the time

when the shock first encounters the upstream edge of the cloud. Each simulation is described by the Mach number of the shock, M, and the cloud density contrast, χ. The adiabatic non-conducting simulations are scale free and can be expressed in dimensionless units. The time is measured in units of the cloud crushing time-scale, $t_{\rm cc} = \chi^{1/2} r_{\rm cl}/v_{\rm b}$, where $r_{\rm cl}$ is the initial cloud radius and $v_{\rm b}$ is the shock velocity in the ambient medium (Klein *et al.* 1994), the cloud radius is taken to be the unit of length, so that $r_{\rm cl} = 1$ and the unit of density is taken to be the density of the ambient, unshocked gas. Kelvin-Helmholtz (KH) and Rayleigh-Taylor (RT) instabilities destroy the cloud in $\approx 10\, t_{\rm cc}$ for strong-shock interactions, with weaker shocks taking longer (see Pittard *et al.* 2010).

In the multiple cloud simulations the clouds are initially randomly distributed within a rectangular region which we refer to as the 'clumpy region'. Each cloud has an identical radius and density contrast, and because of the 2D geometry each cloud represents an infinite cylinder. The size of this region is $400\, r_{\rm cl} \times 400\, r_{\rm cl}$, unless otherwise noted. A key parameter in the multi-cloud simulations is the ratio of total cloud mass to inter-cloud mass in the clumpy region, MR. In this work, mass ratios of $MR = 0.25$–4 are investigated. Time zero occurs when the shock is just outside the clumpy region, but is often shifted in the subsequent analysis to coincide with the shock entering the region of interest. The clumpy region is divided into 4 equally sized blocks (shown in Fig. 3.7) with block 1 being furthest upstream and the first to be hit by the shock. Various properties of the total cloud material within a given block and select individual clouds within each block were monitored through the use of advected scalars which 'colour' the flow. In particular, the velocity and mass of cloud material in individual blocks and clouds are studied. An algorithm which searches for the cells which are furthest downstream and contain a pressure

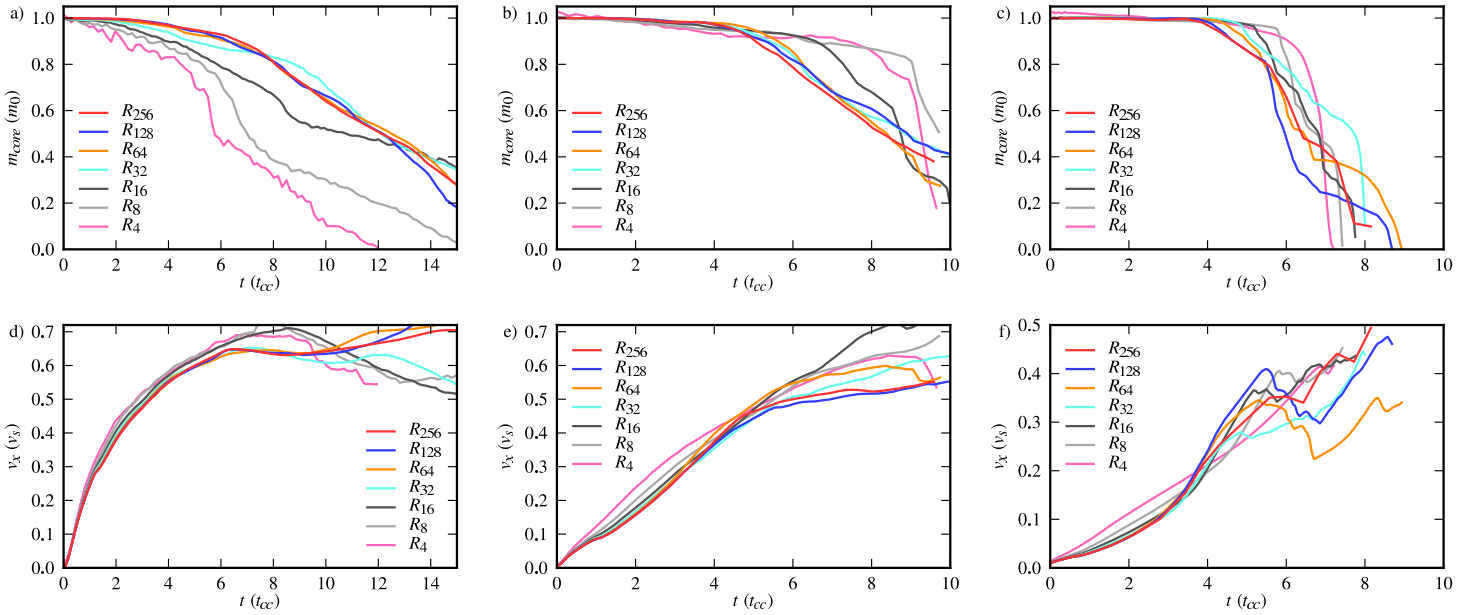

Figure 3.1: Convergence tests for 2D simulations of a Mach 5 shock hitting a cylindrical cloud with density contrast $\chi = 10$ (left column), $\chi = 10^2$ (centre column), and $\chi = 10^3$ (right column). The time evolution of the core mass ($m_{\rm core}$, top row) and the mean cloud velocity ($v_{\rm x}$, bottom row) are shown.

higher than the ambient pressure is used to track the position of the shock as a function of time.

3.2.2 Convergence studies

Previous resolution tests of numerical shock-cloud interactions (e.g., Nakamura *et al.* 2006)) have revealed that adiabatic, hydrodynamic simulations need ∼100 cells per cloud radius (R_{100}) for a converged result. Simulations including more complex physics, especially ones with strong cooling, have been found to need higher resolutions (Yirak *et al.* 2010). In contrast, Pittard *et al.* (2009) found that adiabatic simulations with a k-ϵ subgrid turbulence model show better con-

vergence, and (most importantly for this work) converge at lower resolutions.

Currently, multiple cloud simulations cannot be performed at a resolution as high as R_{100} and 3D simulations are also much more expensive computationally. The first (and to our knowledge, only) resolution tests of a multiple cloud interaction were performed by Poludnenko *et al.* (2004), who showed how resolutions of R_{16}, R_{32} and R_{64} affect the shock position at a given time. They concluded that the differences between their results were smaller than the sensitivity of their proposed experimental design so no further analysis was done. All the more extensive resolution tests in the current astrophysical literature concern 2D simulations of an individual cloud.

We have therefore performed various resolution tests including 2D single cloud simulations for different values of χ and M. Compared convergence in 2D with different Riemann solvers and with and without k-ϵ model. A 3D single cloud simulation with $M = 5$ and $\chi = 10^2$ was investigated with different resolutions up to R_{64}. Multiple (13 and 48) cloud simulations with $M = 3$, $\chi = 10^2$ and $MR = 1$ and 4 were also performed at resolutions R_4, R_8, R_{16} and R_{32}.

We focus on two measures which are affected by the mixing of cloud material into the flow. These are the mean cloud velocity ($\langle v_x \rangle$) and the core[1] mass of the cloud ($m_{\rm core}$). The latter is defined as the sum total of cloud mass in grid cells where more than half the cell's mass is cloud material.

[1] In this Chapter, core refers to a collection of cells where the advected scalar indicates that more than half of the material in cell originates from the initial cloud. These cells need not be contiguous. A conserved quantity in the core is calculated by adding up cloud contributions in all of the cells classed as core.

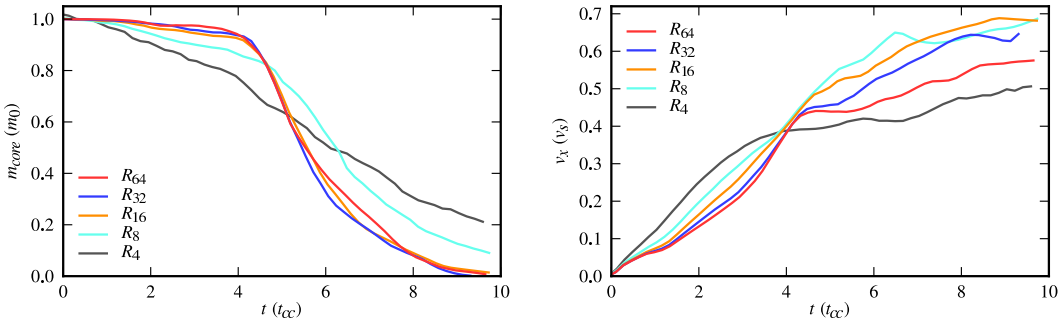

Figure 3.2: Convergence tests for 3D simulations of a Mach 5 shock hitting a spherical cloud with density contrast $\chi = 10^2$. The time evolution of the core mass ($m_{\rm core}$, left) and the mean cloud velocity ($v_{\rm x}$, right) are shown.

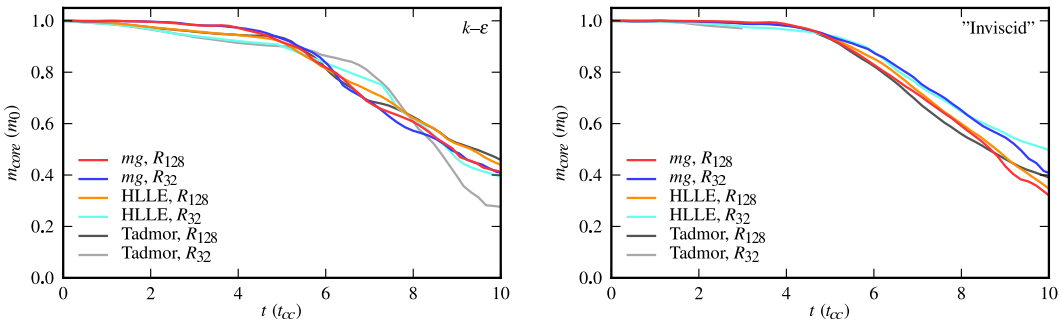

Figure 3.3: Comparison of the core mass ($m_{\rm core}$) evolution when using the linear/exact Riemann solver in mg and other Riemann solvers. The k-ϵ subgrid model is enabled in the left panel and disabled in the right panel. We experienced difficulties with one of the Tadmor calculations which stops at $t = 3\,t_{\rm cc}$.

3.2.2.1 Single cloud resolution tests

Fig. 3.1 shows the evolution of $m_{\rm core}$ and $\langle v_x \rangle$ for 2D simulations of cylindrical clouds hit by an $M = 5$ shock for a range of values of χ.

In all cases the interaction leads to most of the core mass being mixed with ambient material by $t \approx 10\,t_{\rm cc}$. The simulations at lower density contrasts are most resolution dependent. When $\chi = 10$ the cloud mixes faster at lower resolutions.

The opposite is true when $\chi = 10^2$. For $\chi \lesssim 10^2$, simulations with at least 32 cells per cloud radius are much better converged than simulations at lower resolution. For the highest density contrast studied ($\chi = 10^3$) convergence is obtained at lower resolution.

We now examine the resolution dependence of a spherical cloud in a 3D simulation. Fig. 3.2 shows the evolution of the core mass and mean cloud velocity as a function of resolution for a cloud with $\chi = 10^2$ hit by a Mach 5 shock. While the velocity diverges a bit after $5\,t_{cc}$, the core mass evolution at R_{16} exhibits the same features as at R_{32} and R_{64}, whereas in 2D a resolution of R_{32} is required for a similar level of convergence. Thus, it appears that the extra degrees of freedom for instabilities in 3D versus 2D has the effect that convergence is achieved at lower resolutions.

The geometry makes a significant difference to the cloud evolution. Panel b of Fig. 3.1 shows that a cylindrical cloud has lost about half of its core mass by $t \approx 8\,t_{cc}$, whereas Fig. 3.2 shows that for a spherical cloud this occurs by $t \approx 6\,t_{cc}$.

The Riemann solver in *mg* is such that if the time-averaged pressure returned by the linear solver differs by less than 10% from the pressures in the left and right states, the solution from the linear solver is used. Otherwise an exact solver with the standard Secant method is used. We have compared the effects of different Riemann solvers on single cloud simulations. In particular we have used HLLE (Einfeldt 1988) and Tadmor (Nessyahu & Tadmor 1990) solvers. With a first order (spatial and temporal) update the scheme is very diffusive irrespective of which Riemann solver is used (although the *mg* solver is the least diffusive). Fig. 3.3 shows results with the standard second order scheme. It reveals that the different solvers produce similar results at high resolutions, while the k-ϵ model reduces the

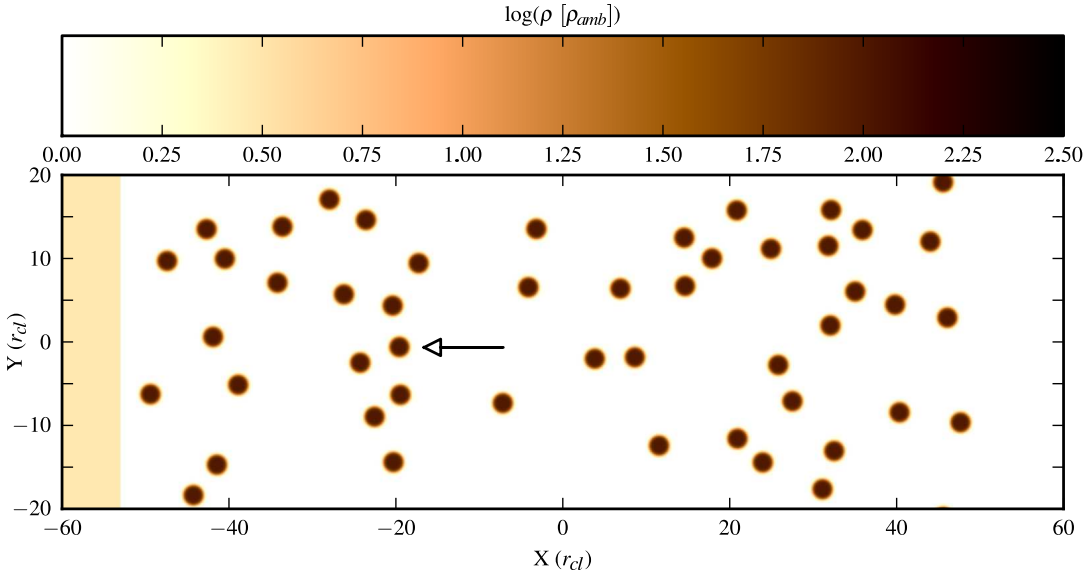

Figure 3.4: The initial ($t = 0$) cloud distribution for a simulation of a shock overrunning multiple cylindrical clouds. The shock Mach number $M = 3$, the cloud density contrast $\chi = 10^2$, and the ratio of cloud mass to intercloud mass in the clumpy region is $MR = 4$. The arrow marks an individual cloud for which the properties were monitored in time - see Fig. 3.6.

resolution dependence, especially at late times (cf. Pittard *et al.* 2009).

3.2.2.2 Multiple clouds resolution test

We have also performed a convergence study for 2D multi-cloud simulations. In this study a Mach 3 shock overruns 48 identical cylindrical clouds, each with a density contrast to the intercloud medium of $\chi = 10^2$. The ratio of cloud mass to intercloud mass within the clumpy region is $MR = 4$. Fig. 3.4 shows the initial setup and distribution of clouds. The clouds fill a region which is $100\,r_{\rm cl}$ deep and $40\,r_{\rm cl}$ wide, with periodic boundaries in y. Resolutions of R_4, R_8, R_{16} and R_{32} were used. The latter required a grid with an effective size of 12800×1280.

The shock exits the clumpy region at around $t = 12.5\,t_{\rm cc}$ in all of the simu-

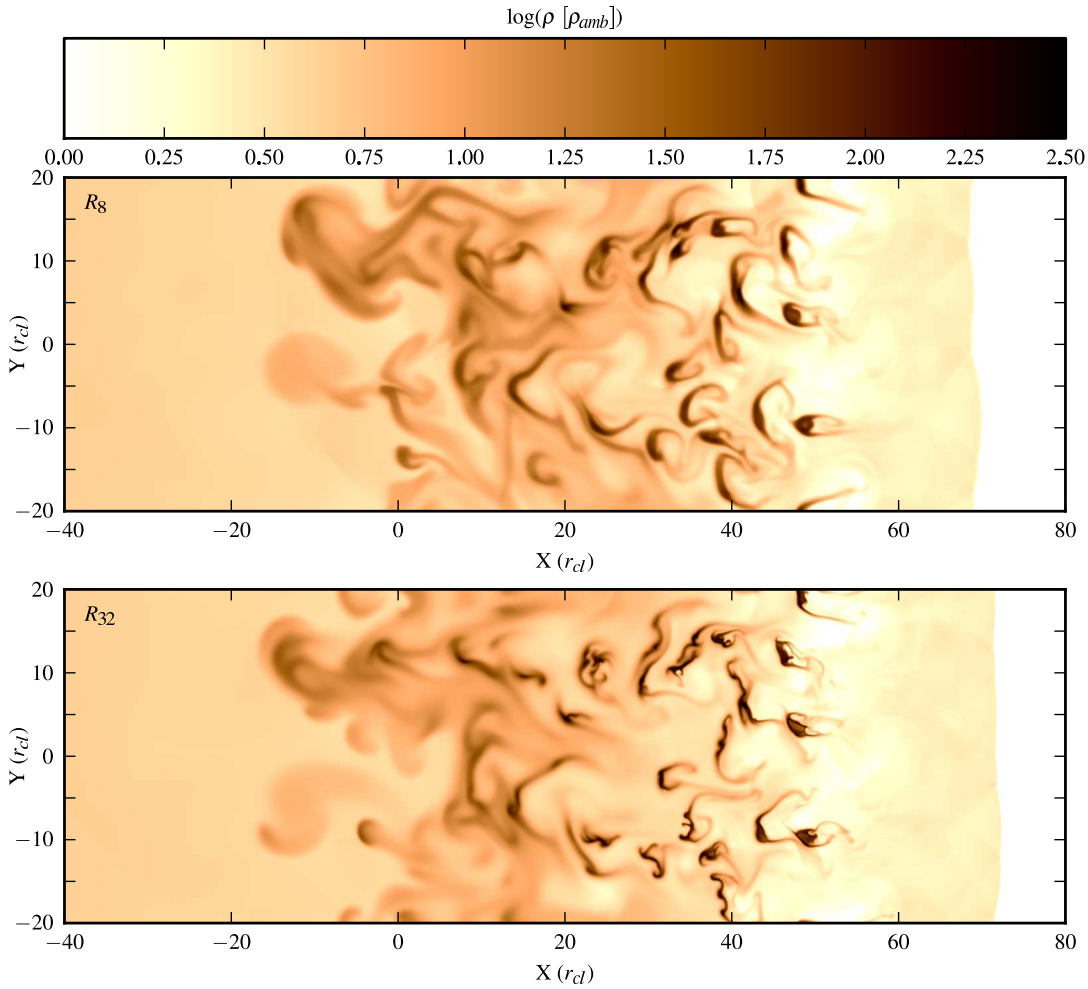

Figure 3.5: Resolution test for a Mach 3 shock overrunning multiple cylindrical clouds with the initial setup shown in Fig. 3.4. A logarithmic density plot is shown at $t = 14.2\,t_{cc}$ for resolutions of R_8 (top) and R_{32} (bottom).

lations. Density plots for times just after this moment are shown in Fig. 3.5 for the R_8 and R_{32} simulations. Higher compressions and greater fragmentation are seen in the higher resolution simulation. However, while significant differences in the behaviour of any individual cloud in the simulation can be identified, Fig. 3.6 shows that important *global* parameters in the multiple cloud simulation, such as

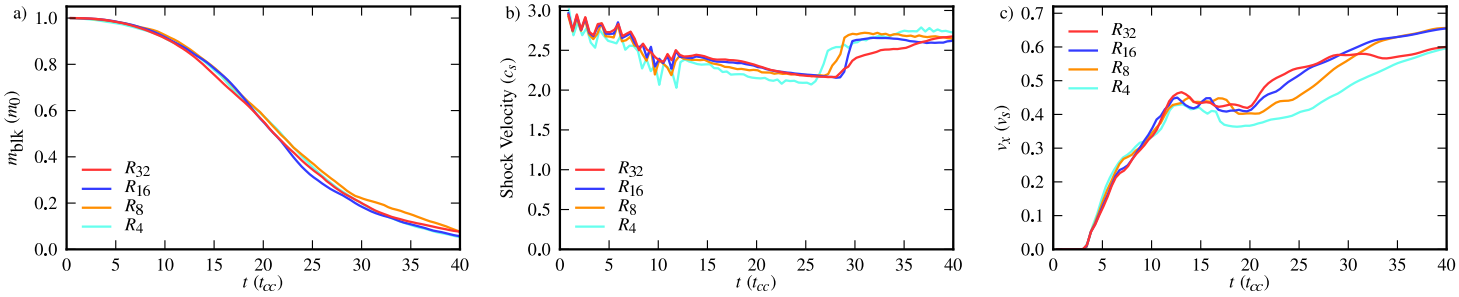

Figure 3.6: Resolution test for a Mach 3 shock overrunning multiple cylindrical clouds with $\chi = 10^2$ and $MR = 4$ (see Fig. 3.5). The time evolution of a) the total mass of all of the cloud cores ($m_{\rm blk}$), b) the mean shock velocity (normalized to the ambient intercloud sound speed) and c) the average core velocity of a single cloud ($v_{\rm x}$), are shown.

the rate at which cloud mass is mixed into the flow (shown as the time evolution of the total mass of all of the cloud cores in Fig. 3.6a), the rate at which momentum is transferred from the flow to the clouds (shown as the velocity of a single cloud, Fig. 3.6c), and shock velocity (Fig. 3.6b) are *not* very sensitive to the resolution used.

Indeed, it is clear from Fig. 3.6 that a resolution of R_8 is sufficient in order to obtain an accurate representation of the global effect of multiple clouds on a flow. In previous multi-cloud simulations resolutions of R_{32} and R_{16} have been adopted (Poludnenko *et al.* (2002) and Poludnenko *et al.* (2004), respectively), but we show here that a somewhat lower resolution can be safely used, at least when a sub-grid turbulence model is employed. Therefore, we perform all other simulations in this work at a resolution of R_8.

Table 3.1: Summary of the multi-cloud simulations performed.

Simulation	χ	MR	ncc[a]	Shock Mach number
chi2MR0.25	10^2	0.25	128	3
chi2MR1	10^2	1	505	1.5, 3, 10
chi2MR1_double[b]	10^2	1	1110	3
chi2MR4	10^2	4	1959	1.5, 2, 3, 10
chi3MR0.25	10^3	0.25	13	3
chi3MR1	10^3	1	51	3
chi3MR4	10^3	4	203	3

[a]: Number of clouds in the clumpy region

[b]: Simulation *chi2MR1_double* has the same cloud distribution as *chi2MR1* but it is repeated in the x-direction to obtain a distribution with twice the depth along the direction of shock propagation.

3.3 Results

In this section we show the results of a number of simulations with different values of M, χ, and MR. Table 3.1 summarizes the simulations that were performed. We adopt a naming convention such that *m3chi2MR1* refers to a simulation with $M = 3$, $\chi = 10^2$ and $MR = 1$.

3.3.1 Mach 3 shock interactions

We first focus on simulations for a Mach 3 shock. Figs. 3.7 and 3.8 show the time evolution of the density distribution in simulation *m3chi2MR4*, which contains 1959 clouds. The shock sweeps through the clumpy region, propagating fastest through the channels between clouds. Behind the shock, the overrun clouds are in various stages of destruction, with the clouds closest to the shock being those which are in

the earliest stage of interaction and which, therefore, are the most intact. Further behind the shock the clouds gradually lose their identities as they are mixed into the

flow. Fig. 3.7 shows that a global bowshock moves upstream into the post-shock flow. Although the bowshock disappears out of view in Fig. 3.8, it remains on the grid which extends to $x = -450$. Low density (and pressure) regions in the post-shock flow are visible behind clouds as the flow rushes pass. The global shock front is momentarily deformed by each cloud that it encounters as it sweeps through the clumpy region. These local deformities in the shock front gradually accumulate into a distortion of the shock front on larger length scales. The shock is most deformed as it reaches the end of the clumpy region (see the middle panel of Fig. 3.8). The other striking feature of the interaction is the formation of a dense shell in the post-shock flow due to the addition of mass from the destruction of the clouds. This is clearly seen in the panels in Fig. 3.8 and is the most important large-scale structure formed in the global flow as a result of the interaction.

The shock slows as it sweeps through the clumpy region and transfers momentum to cloud material. When the clumpy region is highly porous, the deceleration of the shock front is minimal and the clouds gradually reach the velocity of the post-shock flow. This occurs if the global cloud cross section is small (for instance, when the mass ratio is low (e.g., $MR = 0.25$) and/or when the cloud density contrast, χ, is high (e.g., $\chi = 10^3$, $MR = 1$ as in simulation *m3chi3MR1*).

Fig. 3.9 shows snapshots of the density distribution at the time that the shock exits the clumpy region in models *m3chi2MR1* (top), *m3chi2MR1_double* (middle), and *m3chi3MR4* (bottom). All of these models have lower number densities of clouds than model *m3chi2MR4*: in the first two models it is because the value of

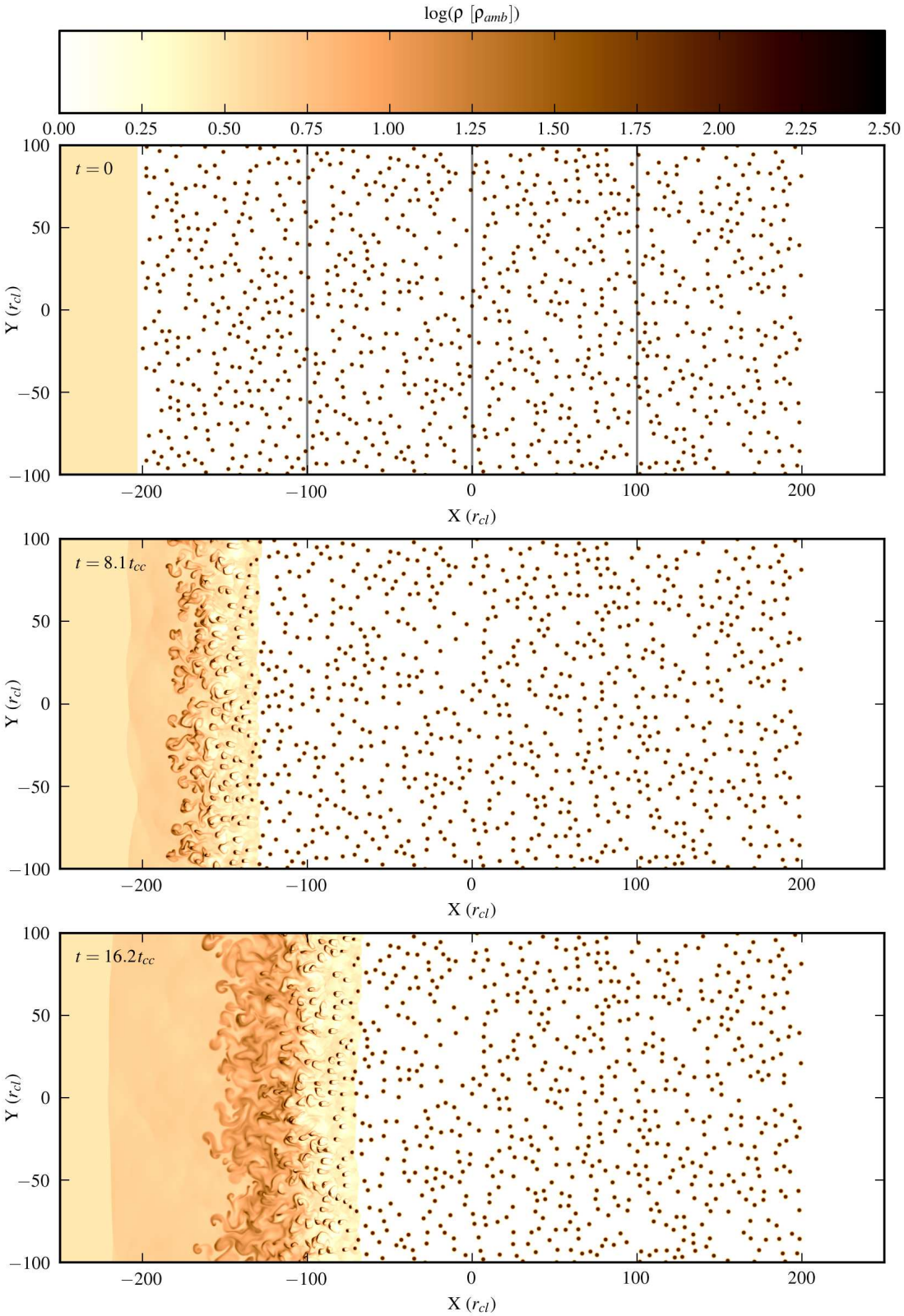

Figure 3.7: The time evolution of the logarithmic density for model *m3chi2MR4*, shown at $t = 0$ (top), $t = 8.1\,t_{\rm cc}$ (middle) and $t = 16.2\,t_{\rm cc}$ (bottom). The top panel also shows how the different cloud regions are defined.

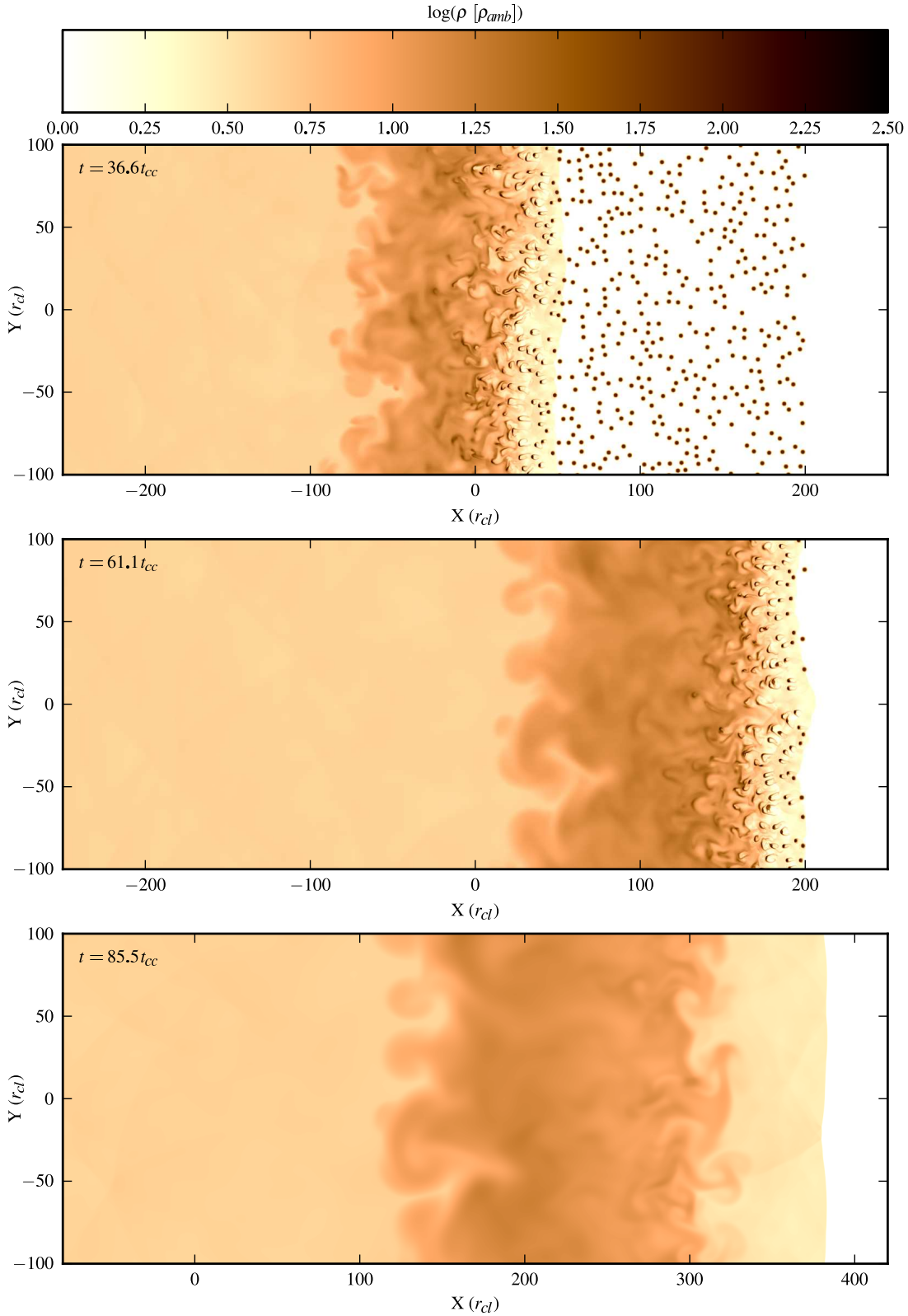

Figure 3.8: As Fig. 3.7 but at $t = 36.6\,t_{\rm cc}$ (top), $t = 61.0\,t$cc (middle) and $t = 85.5\,t_{\rm cc}$ (bottom).

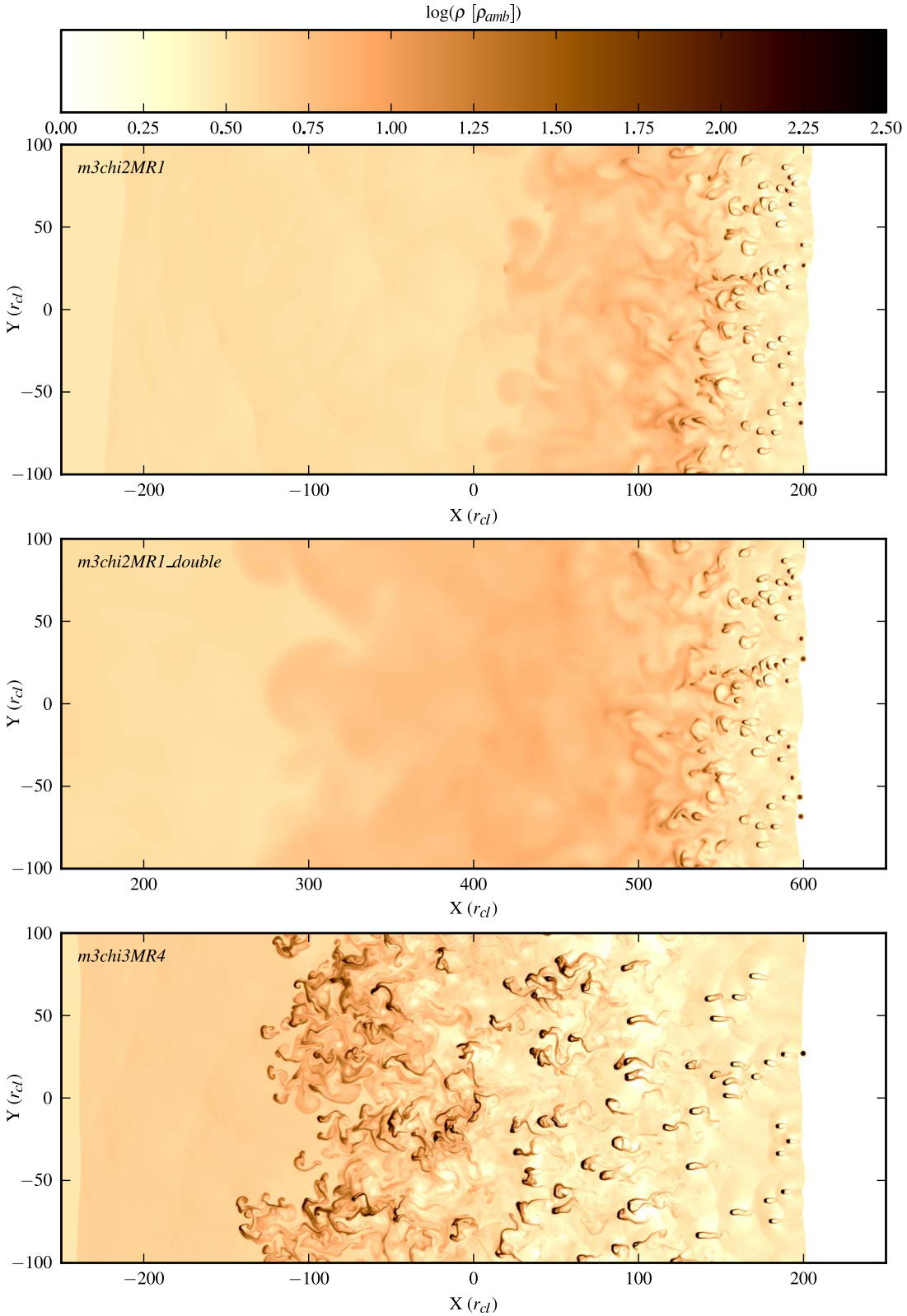

Figure 3.9: Snapshots of logarithmic density for models *m3chi2MR1* (top), *m3chi2MR1_double* (middle), and *m3chi3MR4* (bottom). The snapshots are taken as the shock front is exiting the cloudy region which occurs at $t = 46\,t_{\rm cc}$, $t = 95\,t_{\rm cc}$ and $t = 13.5\,t_{\rm cc}$ respectively.

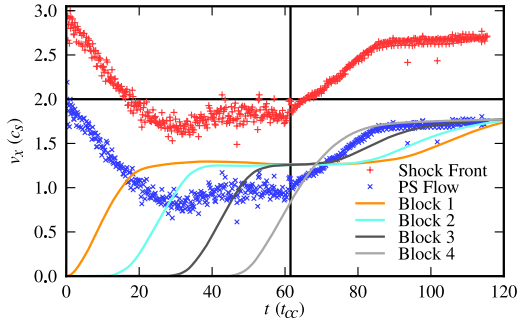

Figure 3.10: The time evolution of the mean x-velocity (v_x) for cloud material for each different block in simulation *m3chi2MR4*. Also shown are the average velocity of the shock front and the velocity immediately behind the shock front. The vertical line indicates the time when the shock leaves the clumpy region, while the horizontal line indicates the initial speed of the post-shock flow.

MR is reduced, while in model *m3chi3MR4* it is because the density contrast of the clouds has increased while the value of *MR* is unchanged. As such, the clumpy region in each of these models is more porous than in model *m3chi2MR4*, and the shock is able to sweep through without such a significant reduction in its velocity. Comparison of Figs. 3.7, 3.8 and 3.9 also reveals significant differences between these models in the structures of the flow through the clumpy region.

3.3.1.1 Velocity behaviour

As the shock sweeps through a clumpy region, it causes clouds in block 1 to accelerate first; then clouds in blocks 2, 3 and 4 accelerate. This transfer of momentum to the clouds inevitably causes the shock and the post-shock flow to slow. Figs. 3.10 and 3.11 show the time evolution of the average velocity of cloud material within particular blocks of clouds (e.g., as delineated in the top panel of Fig. 3.7) normalized to the intercloud sound speed. Fig. 3.10 shows that the shock front slows down to about 50% of its initial velocity (though it remains supersonic). In this

simulation we find that the first 3 blocks of clouds accelerate up to $1.25\,c_1$ (where c_1 is the sound speed in the intercloud ambient medium). However, by this point the post-shock flow immediately after the shock has decelerated to marginally below $1\,c_1$. Hence, material stripped from the upstream clouds pushes against the downstream clouds, compressing the clumpy region.

The shock front advances at roughly constant velocity after having reached a minimum while in the clumpy region. However, as the shock front leaves the clumpy region it reaccelerates at a roughly constant rate until it reaches a velocity somewhat smaller than the initial shock velocity. After that it accelerates very slowly, and asymptotically reaches its initial velocity (corresponding to Mach 3).

The final block of clouds is not held back by further clouds downstream and therefore does not stop accelerating at the same velocity as the other blocks. Instead it accelerates until it reaches the velocity of the post-shock flow after the shock stops reaccelerating. Blocks 3, 2 and 1 repeat this behaviour in that order.

Figs. 3.11a) and b) show the velocities obtained in simulations *m3chi2MR1* and *m3chi2MR1_double*, for which the mass ratio of cloud to intercloud material in the clumpy region is unity (the number density of clouds is therefore 4× lower than in model *m3chi2MR4*). Model *m3chi2MR1_double* has a cloud distribution that is identical to that of model *m3chi2MR1*, but the distribution is repeated once to create a clumpy region that is twice as deep. In both cases the clumpy region is more porous and therefore, the reductions in the shock and post-shock velocities are not as severe as those seen in model *m3chi2MR4*. For this reason, the clouds are also accelerated initially to a higher velocity ($\approx 1.7 c_1$) than in model *m3chi2MR4*.

As previously stated, the clumpy region can also be made more porous by increasing χ for a fixed *MR*. Fig. 3.11c) shows the velocity profiles obtained from

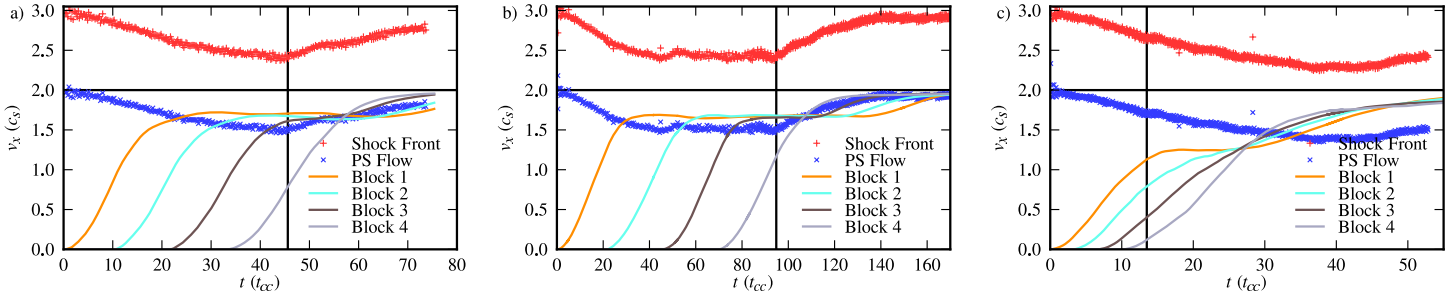

Figure 3.11: As Fig. 3.10 but for simulations a) *m3chi2MR1*, b) *m3chi2MR1_double* and c) *m3chi3MR4*.

model *m3chi3MR4*. As expected, the shock does not decelerate as much as in model *m3chi2MR4*. However, model *m3chi3MR4* behaves differently in another way: because each cloud is more resistant to the flow, the clouds are not completely destroyed by the time the shock leaves the clumpy region (at $t \approx 13\,t_{\rm cc}$) when the collective cloud material from each block is still accelerating. In turn, due to continuing mass-loading of the flow, the shock continues to decelerate *after* it has left the clumpy region. In fact, the shock front decelerates until $t \approx 36\,t_{\rm cc}$, remains at constant velocity until $t \approx 44\,t_{\rm cc}$ and reaccelerates thereafter.

3.3.1.2 Stages of interaction

The behaviour of the simulations noted in the previous section allows the identification of 4 distinct phases in the evolution of the shock front. Firstly, there is a shock *deceleration* phase as the shock enters the clumpy region. This may be followed by a *steady* phase, when the shock front moves at constant velocity. The third stage is a *reacceleration* phase during which the shock front accelerates (at a fairly steady rate) into the homogeneous ambient medium. This stage always starts after the shock has traversed through the whole of the cloudy region, but not necessarily

immediately after. The *final* stage begins once the shock's acceleration slows. At this point the shock propagates with a velocity slightly slower than its initial velocity, but is continuing to accelerate very slowly, due to the constant velocity inflow trying to return the shock to its initial velocity.

The number and timings of the stages is model specific. In models for which the lifetime of the clouds is less than the crossing time of the shock through the clumpy region, the steady phase ends when the shock leaves the clumpy region (see, e.g., simulation *m3chi2MR4* in Fig. 3.10). In models for which significant mass loading of the flow continues after the shock leaves the clumpy region the end of the steady phase is delayed (see, e.g., *m3chi3MR4* in Fig. 3.11c).

The steady stage is best seen in models *m3chi2MR4* and *m3chi2MR1_double*, and to some extent it is also visible in model *m3chi3MR4*. These are the simulations with the most mass in the clouds. Models *chi2MR4* and *chi3MR4* have the highest cloud to intercloud mass ratios of 4. In fact, the onset of a steady stage seems to intimately depend on the formation of a dense shell (see Sec. 3.3.1.3).

In contrast, model *m3chi2MR1* (Fig. 3.11a) does not achieve a steady state. Instead the shock velocity evolves from the deceleration phase immediately into the reacceleration phase. One might expect that there is a better chance for a steady stage to occur if the clumpy region is deep. Fig. 3.11b indeed shows that a steady state occurs in model *m3chi2MR1_double* where the clumpy region is twice as deep as in model *m3chi2MR1*. The onset of the steady stage occurs when the shock is approximately halfway through the clumpy region, and all 4 stages can now be distinguished as in model *m3chi2MR4*.

For all of the $\chi = 10^2$ models, the reacceleration stage begins the moment the shock leaves the clumpy region, but for the $\chi = 10^3$ runs the onset of this stage

shows more complicated behaviour. Because clouds with a higher density contrast evolve more slowly, significant evolution of the global flow can occur after the shock front leaves the clumpy region. Fig. 3.11c shows that this occurs in model *m3chi3MR4*, as the continued deceleration of the shock is evident. At some later time, presumably when the clouds are finally fully entrained into the flow, the shock starts to accelerate. There is also a hint of a steady stage in model *m3chi3MR4*, but examination of the velocity graphs reveals that it occurs at a much later evolutionary stage than in model *m3chi2MR4* (as seen, e.g., when compared to the velocity evolution of material mixed in from the various blocks). Given that there are about 10× fewer clouds in model *m3chi3MR4* than in *m3chi2MR4* this can be explained by the relative time-scales involved in the shell formation which is discussed next.

3.3.1.3 Shell formation and evolution

Figs. 3.7 and 3.8 show that in model *m3chi2MR4*, a shell forms in the post-shock flow at $t = 16.2\,t_{\rm cc}$. It is fully developed by $36.6\,t_{\rm cc}$. At $t = 36.6\,t_{\rm cc}$ 7 distinct regions can be distinguished. A uniform ambient medium (without any clouds) lies at the right edge of the figure, while at the far left of the grid (off the figure in this case) lies the original post-shock flow specified by inflow boundary conditions at the upstream edge. A further 5 regions (from right to left) exist in between these other two. A region of unshocked clouds lies in the range $50 \lesssim x < 200$. Shocked clouds embedded in a relatively low density postshock flow lie in the region $30 \lesssim x \lesssim 50$. Shocked clouds are being overrun by a denser shell in the region $-20 \lesssim x \lesssim 30$, though individual cores are still visible. This shell becomes gradually more uniform towards $x \approx -70$. The upstream edge of this dense shell is fairly distinct from the less dense gas that it abuts (at $x \approx -70$). The latter is gas in the original supersonic

post-shock flow which has shocked against the clumpy region. This final region is bounded by a bow shock which lies off the left edge of the figure.

Fig. 3.12 shows the evolution of the density in the shell. Initially the average postshock density in the clumpy region is only about twice that of the shocked intercloud gas. However, as the clouds are destroyed and their mass mixes into the global flow, the density in this region increases. In model *m3chi2MR4*, a dense region, downstream of the region where distinct clouds are still visible, has formed by about the time that the shock reaches its minimum velocity. This is the 'shell'. The compression of the shell progresses a little further, until a state in which the maximum density is steady in time is reached. This is reinforced by the simulation (model *m3chi2MR1_double*) for a wide clumpy region, which shows that the shell only becomes wider with time after this point. Once there are no more clouds blocking the path of the shell, it starts to expand from its leading edge, and the maximum density within it drops. This is seen clearly from Fig. 3.12, and is preceded by the shock reaching the edge of the clumpy region. Simulations with $\chi = 10^3$ behave slightly differently - in these the density of the shell continues to increase after the shock has left the clumpy region due to the continued ablation of material from the longer-lived clouds.

3.3.1.4 Mach number profile

Fig. 3.13 shows the y-averaged Mach number profile of the flow in simulation *M3chi2MR4* at $t = 44.8\, t_{cc}$. The undisturbed post-shock flow is mildly supersonic[1]

[1] In this section the velocity relative to the undisturbed ambient medium is compared to the local sound speed. A notion of 'supersonic' flow refers to the potential of the flow to impact against an immovable obstacle, or a very high density cloud in the ambient medium, rather than any actual structure of the present flow.

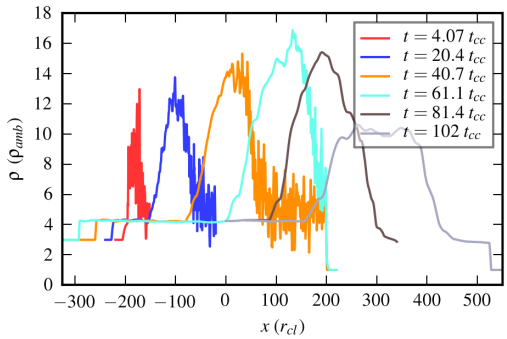

Figure 3.12: The density (ρ), volume averaged over y, as a function of x in simulation *M3chi2MR4*, at different times. The shock exits the clumpy region at $t \approx 60\, t_{cc}$.

($M \approx 1.04$), as seen at the far left of the panel. The shock at this time is just downstream of $x = 100$.

In the region between $70 \lesssim x \lesssim 108$ clouds are overrun by the flow and accelerated by the gas streaming past, so that the Mach number of the flow increases as x decreases. While the clouds remain identifiable as distinct entities, their interiors remain colder than the shocked intercloud flow, as initially the dense clouds are in pressure equilibrium with their less dense surroundings, so that their temperatures are lower than that of the intercloud medium by a factor of χ. Together these effects ensure that the Mach number of the flow eventually exceeds the Mach number in the undisturbed post-shock flow. The local Mach number reaches a peak of about 1.4, at a location corresponding to the downstream edge of the shell (which occupies a region between $-50 \lesssim x \lesssim 70$).

As the clouds begin to lose their individual identities their material is heated as it is mixed into the surrounding flow. This increases the sound speed of this material, and reduces the overall Mach number of the flow. The Mach number continues to decline with decreasing x until the cloud material is fully mixed (which occurs at

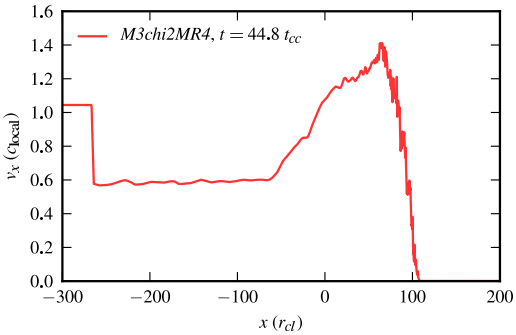

Figure 3.13: The local Mach number (x-velocity, $v_{\rm x}$, in the units of the local sound speed, $c_{\rm local}$), volume averaged for all values of y, as a function of x in simulation *M3chi2MR4*, at $t = 44.8\,t_{\rm cc}$. The shock is at $x \approx 108$ and the bow shock is at $x \approx -265$.

the upstream edge of the shell in this simulation). The region of constant Mach number ($M \approx 0.6$) between the upstream edge of the shell (at $x \approx -50$) and the bow shock at the head of the clumpy region (at $x \approx -265$) is the gas in the original post-shock flow which has shocked against the clumpy region.

3.3.2 Dependence on shock Mach number

Fig. 3.14 shows density snapshots when the shock front is exiting the clumpy region for models *m1.5chi2MR4*, *m2chi2MR4* and *m10chi2MR4*. It is clear that a slower shock produces less compression, and that the shell which then forms is wider. In addition, weak shocks take longer to destroy clouds, so the shell forms further from the shock front. Perhaps most significantly, as the shock decelerates during its passage through the clumpy region it can slow so much that it decays into a wave which advances at the intercloud sound speed. This is seen in both the $M = 1.5$ and $M = 2$ simulations for which Fig. 3.14 reveals very weak density jumps at the edges of the clumpy regions.

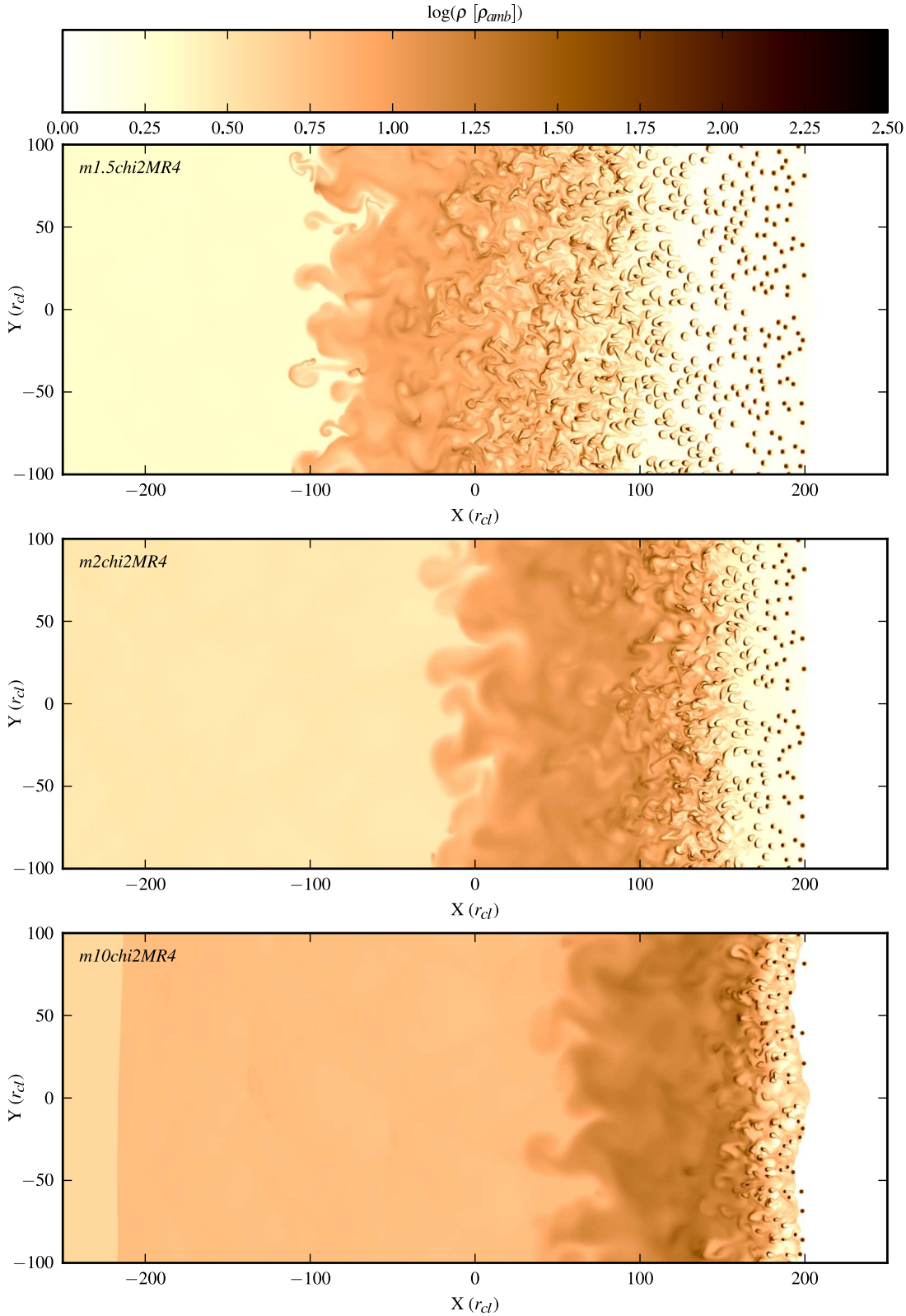

Figure 3.14: Snapshot of logarithmic density for models *m1.5chi2MR4* (top), *m2chi2MR4* (middle) and *m10chi2MR4* (bottom). The snapshots are taken as the shock front is exiting the cloudy region which occurs at $t = 52.9\,t_{\rm cc}$, $t = 61.1\,t_{\rm cc}$ and $t = 58.3\,t_{\rm cc}$ respectively. Relative to its initial speed, the $M = 2$ shock is slowed the most.

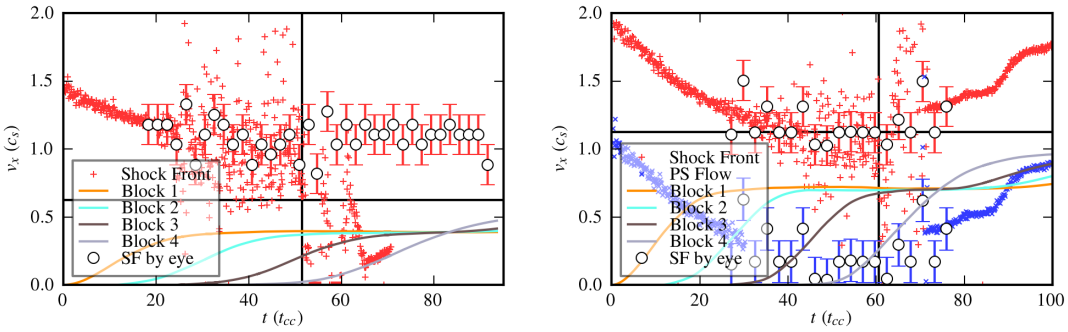

Figure 3.15: The time evolution of the x component of the velocity (v_x) averaged over all values of y, for different regions in simulations *m1.5chi2MR4* (left) and *m2chi2MR4* (right). Also shown are the average shock front velocities. The shock velocity varies when parts of the shock front become subsonic. Vertical lines indicate the time when the shock leaves the clumpy region.

Fig. 3.15 displays the x component of the velocity averaged over all y for the *m1.5chi2MR4* and *m2chi2MR4* simulations normalized to the ambient intercloud sound speed. The points show the velocity of the shock calculated by an algorithm which searches for a pressure jump. However, when the shock decays into a wave the pressure jump largely disappears and this calculation fails. The points with error bars then show the velocity of the disturbance determined by measuring, by eye, the position of the leading edge of the disturbance. In the $M = 2$ simulation the average velocity of the shock/wave disturbance is close to transonic. Close examination reveals that the shock appears fragmented and local regions of sonic waves can be seen. The shock completely decays into a sonic wave in the $M = 1.5$ simulation. These results are in harmony with theoretical predictions based on a uniform density region suggesting that a supersonic to subsonic transition occurs at this mass ratio if the initial shock Mach number is $M \sim 2$ (see Sec. 3.3.3 for further details).

3.3.3 The reduction in the shock speed

Fig. 3.16 shows the minimum shock speed (normalized to the initial shock speed) as a function of shock Mach number obtained in simulations with $MR = 4$ and $\chi = 10^2$ (plotted as red crosses). The minimum shock speed in each case occurs during a 'steady' stage when the shock is moving through the clumpy region. The error bars correspond to the 1σ spread in measured speeds. We have already noted that in the $M = 1.5$ simulation the shock slows to the point that the disturbance becomes a wave. In this case the minimum speed is limited by the sound speed in the intercloud medium, as seen in Fig. 3.16. The situation in the $M = 2$ simulation is not so straightforward - a global shock front is visible but there are local regions where a wave is seen instead.

We can compare the measured shock speed to the expected speed of a shock transmitted into a region of enhanced density. For this we make use of eq. 5.4 in Klein *et al.* (1994), for a shock interacting with a single cloud:

$$v_s = (F_{st}F_{c1})^{1/2}\chi^{-1/2}v_0. \tag{3.4}$$

Here $F_{st} \equiv P_3/P_1$, where P_1 is the pressure far upstream and P_3 is the stagnation pressure (just upstream of the cloud), and $F_{c1} \equiv P_4/P_3$ is the ratio of the pressure just behind the transmitted shock and the stagnation pressure. In the limit of high Mach number and high density contrast,

$$F_{st} \simeq 1 + \frac{2.16}{1 + 6.55\chi^{-1/2}}. \tag{3.5}$$

To apply this expression to our multi-clump simulations we need an 'effective' value

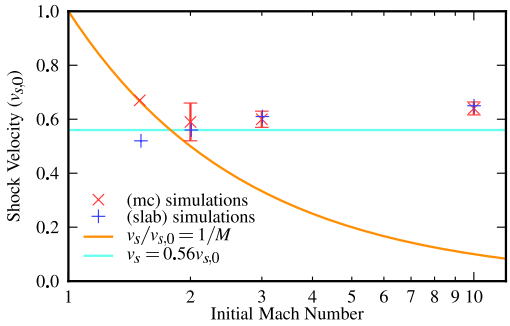

Figure 3.16: The reduction in shock speed (red crosses, as measured during the 'steady' phase as the shock propagates through the clumpy region) normalized to the initial shock speed. The reduction is plotted as a function of the initial shock Mach number, M, for simulations with $\chi = 10^2$ and $MR = 4$. Also shown is the equivalent reduction in speed of a shock propagating through a uniform density enhancement (blue crosses - see Sec. 3.3.4).

for χ which accounts for the inhomogeneity of the clumpy region. We choose this value to be $\chi_{\rm eff} = MR+1$, which is the average density contrast of the region (total mass of the region divided by the mass a same size region of ambient density would have). Furthermore, in simulations where the clumpy region is replaced with a region of uniform density (see Sec. 3.3.4), it is clear that $P_4 = P_3 = P_2$, where P_2 is the pressure just after the bow shock. We shall assume that this is also the case for our multiple cloud simulations, and therefore adopt $F_{\rm c1} = 1$. For our clumpy simulations with $MR = 4$ and $\chi = 10^2$ we therefore obtain $\chi_{\rm eff} = 5$ and $F_{\rm st} = 1.55$, so that eq. 3.4 gives $v_{\rm s} = 0.56 v_0$. As can be seen, this is comparable to the values shown in Fig. 3.16, in which the $v_s = 0.56 v_0$ line is plotted.

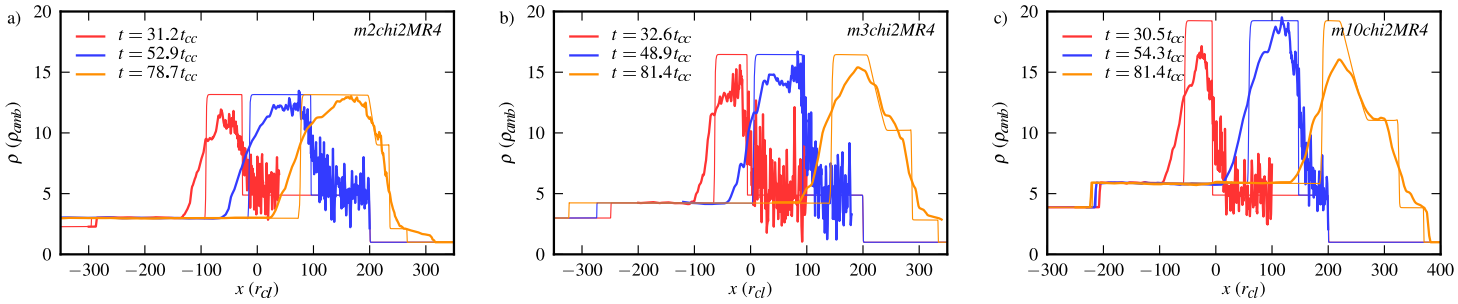

Figure 3.17: Snapshots of the x-dependence of the density (ρ) averaged over all values of y (thick lines) from simulations a) *m2chi2MR4*, b) *m3chi2MR4* and c) *m10chi2MR4*. Also shown are density profiles from simulations with uniform but corresponding density. In all cases the shock exits the region of enhanced density (smooth or clumpy) at $t \approx 60\, t_{cc}$.

3.3.4 Comparisons to a shock encountering a region of uniform density

In the limit of an infinitely deep/thick cloud distribution we expect the global behaviour of the shock to approach that of a shock encountering a uniform medium of the same average density. This could be similar to the steady state reached in some of our simulations. Therefore, we have performed a number of additional calculations of a shock encountering a uniform region of enhanced density equal to the average density of a clumpy region with $MR = 4$. The minimum shock speed through this region is shown in Fig. 3.16 with blue crosses. As can be seen, the agreement with the multi-cloud simulations is very good, with significant deviation only at $M = 1.5$. Clearly the minimum shock speed obtained in our multi-cloud simulations is close to the shock speed occurring in a comparable region of uniform density.

Fig. 3.17 compares the x-dependence of the density, averaged over all values of

y, given by simulations of a shock interacting with a uniform region of enhanced density to analogous profiles obtained from our multiple cloud simulations. One notices the similarity between the profiles: the maximum density of the shell and the reduction in density after the shock exits the higher density/clumpy region are similar. Obviously, the uniform region simulations yield distinct edges and slopes corresponding to the shocks and rarefaction waves, whereas the multiple cloud simulations give smoother profiles. The smoothing length is of the order of $L_{\rm CD}$, which is the distance that a cloud is displaced by the flow prior to its destruction (Poludnenko *et al.* 2002). For the same reason the width of the densest part of the shell is narrower in the multiple cloud simulations.

Consider a shock transmitted into a uniform density region. The velocity jumps according to the Rankine-Hugoniot conditions. As the shock front is moving faster than the postshock flow, the width, w of the compressed region increases at a rate given by:

$$\frac{\mathrm{d}w}{\mathrm{d}t} = v_{\rm s} - v_{\rm ps} = \left(\frac{3}{4M_{\rm u}} + \frac{M_{\rm u}}{4}\right) c_{\rm u}. \tag{3.6}$$

where $M_{\rm u}$ is the Mach number of a shock transmitted into a uniform medium and $c_{\rm u}$ is the sound speed in that medium. Eqs. 3.4 and 3.5 can be used to determine $M_{\rm u}$, but the approximation in eq. 3.5 is only valid at high Mach numbers and high density contrasts. However, we can obtain an estimate based on eq. 3.4. As $F_{\rm st} \geq 1$ and, because the shock is steady, $F_{\rm c} = 1$ (Klein *et al.* 1994), $M_{\rm u} \geq M_0$ and so $\frac{\mathrm{d}w}{\mathrm{d}t} \geq \frac{M_0 c_1}{4}$. Furthermore, two limiting cases can be found. In the limit of a weak shock $\frac{\mathrm{d}w}{\mathrm{d}t} \approx c_{\rm u}$; this is the minimum value, and it would be higher in all other cases. In the limit of a strong shock and high χ, $\frac{\mathrm{d}w}{\mathrm{d}t} \approx 0.44 M_0 c_{\rm u}$.

Fig. 3.17 shows that the widths of shells in clumpy regions correspond well to those in regions of equivalent uniform density. As such eq. 3.6 can be used, with $M_{\rm u}$ either determined from a corresponding uniform density case, or by replacing it with $v_{\rm s}/c_{\rm u}$, with $c_{\rm u}$ determined for the medium of corresponding uniform density. The limiting cases would be different though. In the weak shock limit, the shock may decay into a sound wave. In such a case $\frac{{\rm d}w}{{\rm d}t} \approx c_1$, but it could be significantly less depending on how this affects individual cloud lifetimes. In the limit of very high χ the upstream edge of the shell takes a long time to reach $v_{\rm ps}$ and is effectively stationary, so $\frac{{\rm d}w}{{\rm d}t} = v_{\rm s}$.

3.3.5 Individual cloud evolution

We expect individual clouds to evolve differently when overrun by a mass-loaded evolved shock which has been altered by the presence of clouds further upstream than when they are overrun by a steady planar shock. Section 3.3.1.1 shows that the shock Mach number and in turn the velocity of the post shock flow decreases as the shock sweeps up cloud material. The lower velocity of the shock should prolong the lifetime of a cloud, but this may be offset by the increased density of the flow. Furthermore, the postshock flow is much more turbulent. This aids the development of cloud-destroying instabilities (see Pittard *et al.* 2009). Finally, a region of higher density follows some distance behind the shock. In the extreme case it is a dense shell, but even if a shell does not fully form, remnants of upstream clouds may well interact with clouds further downstream. Therefore, it is difficult to predict whether downstream clouds are destroyed more readily than their upstream counterparts. However, we can use our simulation results to investigate this.

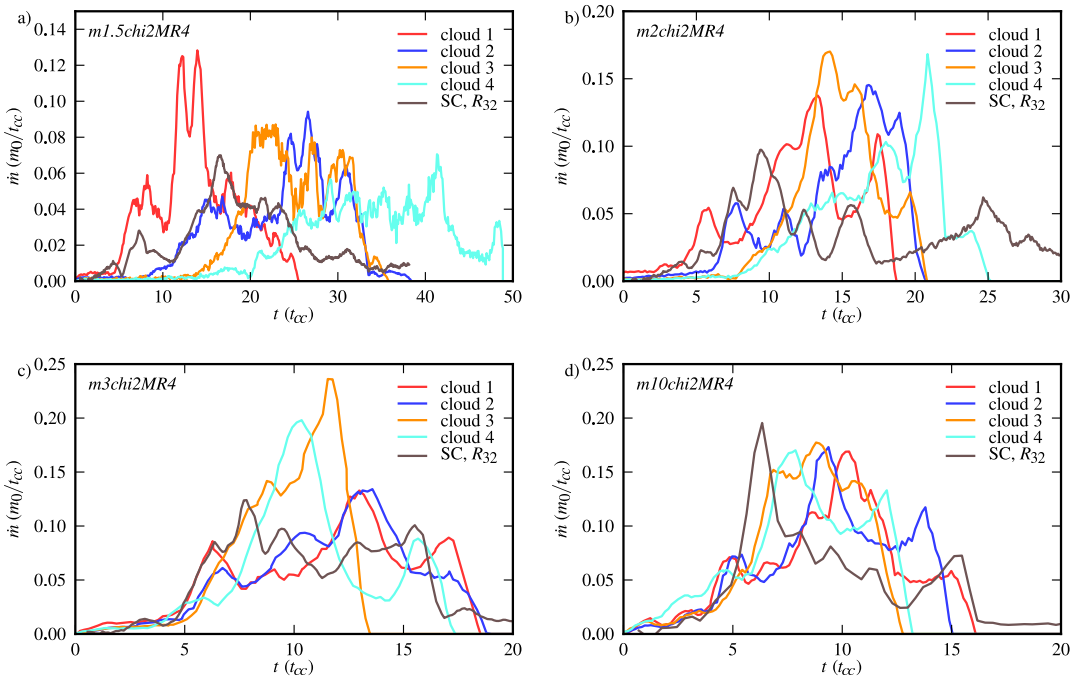

Figure 3.18: Normalized mass loss rates ($\dot{m}$) for select individual clouds in simulations *chi2MR4* for different Mach numbers: a) $M = 1.5$, b) $M = 2$, c) $M = 3$ and d) $M = 10$.

Mass loss rates from different clouds in the simulations are shown in Fig. 3.18. Each cloud is from a particular block (see, e.g., Fig. 3.7), and the time in each plot has been shifted so that $t = 0$ corresponds to the time when the shock first encounters the cloud under consideration. The greatest differences between the evolution of different clouds in a given simulation occur in model *m1.5chi2MR4*, as shown in Fig. 3.18a. Here the cloud in the block which is the first to be hit by the shock (labelled 'cloud 1') encounters a flow which is relatively unmodified by the small number of clouds which lie further upstream. Although the interaction is relatively weak because of the modest shock Mach number, significant mass-loss from the cloud occurs after $t = 5\,t_{cc}$, and the core of the cloud is completely

destroyed by $t \approx 27\,t_{cc}$ (a similar lifetime occurs for spherical clouds - see Pittard *et al.* 2010). In contrast, significant mass-loss does not occur until $t \approx 10\,t_{cc}$ for the cloud in the second block (labelled 'cloud 2'), and until $t \approx 12\,t_{cc}$ and $13\,t_{cc}$ for clouds in the third and fourth blocks (labelled 'cloud 3' and 'cloud 4', respectively). The low initial mass-loss rates from clouds further downstream is due to the decay of the shock into a wave as it moves through the clumpy medium. While the flow past the cloud is subsonic the mass-loss rate remains very low.

The same initial behaviour is also seen in simulation *m2chi2MR4*, as shown in Fig. 3.18b. In contrast, at higher shock Mach numbers (models *m3chi2MR4* and *m10chi2MR4* in Fig. 3.18) the shock remains supersonic as it transits through the clumpy region, and differences between the clouds in the evolution of their mass-loss rates are not so readily apparent (see Fig. 3.18c and d).

It is clear that the cloud lifetimes must be compared in a statistical way. Fig. 3.19 shows the ratio of the lifetimes of individual clouds to the lifetime of the equivalent cloud hit by a 'clean' shock (i.e. initially with no post-shock structure due to interactions with upstream clouds), $R_{\rm life}$. Table 3.2 give lifetimes of clouds from a single cloud resolution test and from a multiple cloud distribution at two different resolutions. Note that the resolution test shows longer lifetimes in low resolution simulations, and the lifetime also depends on the threshold criteria chosen[1]. Different conclusions could then be erroneously drawn depending on which lifetimes are compared. The panel on the left in Fig. 3.19 uses the same resolution single cloud simulation as reference (one simulation uses R_{16} the rest use R_8). It seems to suggest that clouds in the clumpy region are destroyed quicker than an isolated

[1]A cloud is considered destroyed once the mass in the cells dominated by cloud material drops below a threshold fraction of the initial cloud mass. Three such thresholds were used, $1/e$, 0.25 and 0.1.

cloud, and to show a trend that in higher mass ratio distributions the destruction is even quicker. However, note that the single higher resolution simulation (MR4, R_{16}) bucks this trend. We know from Sec. 3.2.2.2 that multiple cloud simulations are less dependent on resolution than simulations of isolated clouds. By comparing a multiple cloud simulation to a single cloud simulation at the same resolution, differences arise at resolution where the single cloud case is under-resolved (e.g. compare Figs. 3.1b and 3.6a). In the case of cloud lifetimes the difference arises because in simulations of isolated clouds KH and RT instabilities need to develop for the cloud to be destroyed, and these instabilities are suppressed if the resolution is too low. In contrast, in the multiple cloud case the flow is already turbulent and mass-loaded due to the presence of upstream clouds. Cloud destruction in such an environment is less sensitive to resolution, and thus it appears the clouds are destroyed faster. However, when comparing cloud lifetimes to a high resolution isolated case at R_{128} (right panel of Fig. 3.19) we find that the trend is reversed and the lifetimes appear enhanced (again, R_{16} remains almost unchanged). It is clear, therefore, that our current simulations do not provide a definite answer and that to obtain one, the lifetimes must be compared from simulations at as high a resolution as possible - ideally both the isolated single cloud simulations and the multiple cloud simulations would be at a resolution of R_{128}. This is beyond our current computational resources.

Two further simulations were performed with clouds of identical radii, but different density contrasts. As before $M = 3$ and $MR = 4$. The size of the clumpy region is reduced to $300\,r_{\rm cl} \times 120\,r_{\rm cl}$ and the resolution increased to R_{16}.

The first distribution, called *M3MR4_uniform*, consists of 420 clouds, 6 of which have $\chi = 10^3$ and the rest have $\chi = 10^2$. The random distribution is repeated along

Table 3.2: Cloud lifetimes (with respect to different thresholds, see text) for an isolated cloud at different resolutions and clouds in the *m3chi2MR4* distribution at R_8 and R_{16}. The four clouds which are monitored in the multiple cloud simulations are identified by their initial x-coordinate.

Cloud		Lifetime (t_{cc}) 1/e	0.25	0.1
SC,	R_{128}	11.0	12.1	14.7
	R_{64}	12.0	13.4	15.2
	R_{32}	12.5	14.0	15.6
	R_{16}	11.3	12.4	16.9
	R_8	14.2	18.0	20.3
	R_4	17.7	19.4	26.4
m3chi2MR4,	$x = -151$	12.5	13.6	15.9
	$x = -52$	12.5	13.4	15.5
	$x = 51$	10.4	10.9	11.6
	$x = 151$	10.4	11.6	15.1
m3chi2MR4_R$_{16}$,	$x = -151$	12.3	12.9	15.2
	$x = -52$	12.2	12.8	15.5
	$x = 51$	12.6	13.6	14.4
	$x = 151$	11.3	12.4	13.7

x three times, with an offset in y to remove alignment effects while keeping the local distribution around the respective clouds identical. Fig. 3.20 shows the initial distribution around one of the higher density clouds and snapshots focusing on the later evolution of some of the $\chi = 10^3$ clouds, one towards the upstream edge of the distribution, and another towards the downstream edge. The shell is not yet formed when the high density upstream cloud is shocked. The surrounding lower density clouds are advected downstream relative to the higher density cloud, which ends up protruding into relatively smooth flow behind the global bow shock. In contrast, the shell is fully formed at the time the high density downstream cloud

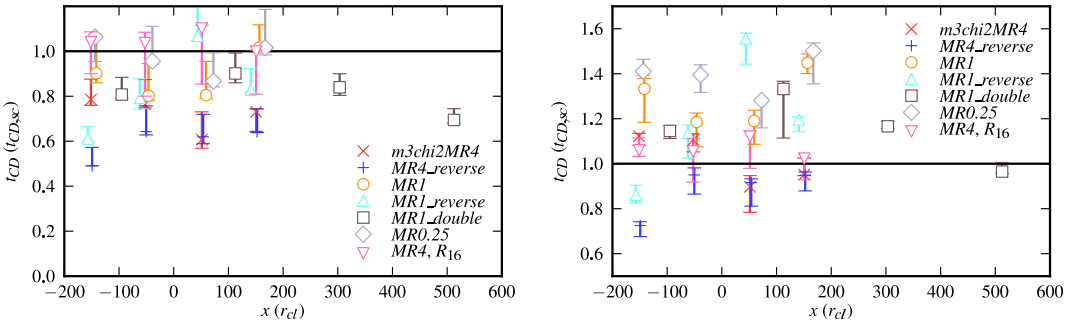

Figure 3.19: Ratio of the lifetime of a downstream cloud ($t_{\rm CD}$) to the equivalent lifetime obtained when the cloud is hit by a 'clean' shock with a uniform post-shock flow. The left panel shows the ratio to a simulation at the same resolution (R_8 or R_{16}) and the right panel shows the ratio to a high resolution (R_{128}) single cloud simulation.

is shocked and this cloud is engulfed in a high density flow. The forward shock is visibly much weaker at this point.

The second distribution, called *M3MR4_variable*, consists of 207 clouds. The density contrast varies from 11 to 947, uniformly distributed in log space. This distribution is much more dominated by high density clouds. The median χ is 112, the average is 218, the mass weighted average is 532 and half the total cloud mass is contained in just 28 clouds with $\chi > 630$. As such, no shell is formed in Fig. 3.21. The evolution of six clouds is followed, three upstream and three downstream. Clouds with $\chi = 83$ and $\chi = 320$ are marked by arrows in Fig. 3.21 (lower and upper arrows respectively), additionally a cloud with $\chi = 32$ is also followed.

The lifetimes normalized to the lifetime of the same isolated cloud versus position within the clumpy region are plotted in Fig 3.22. As previously noted the definition of the cloud destruction time and the resolution of the reference isolated cloud simulation can have a significant effect. Here the cloud destruction time is defined as the time when $1/e$ of the initial cloud mass remains in cells dominated

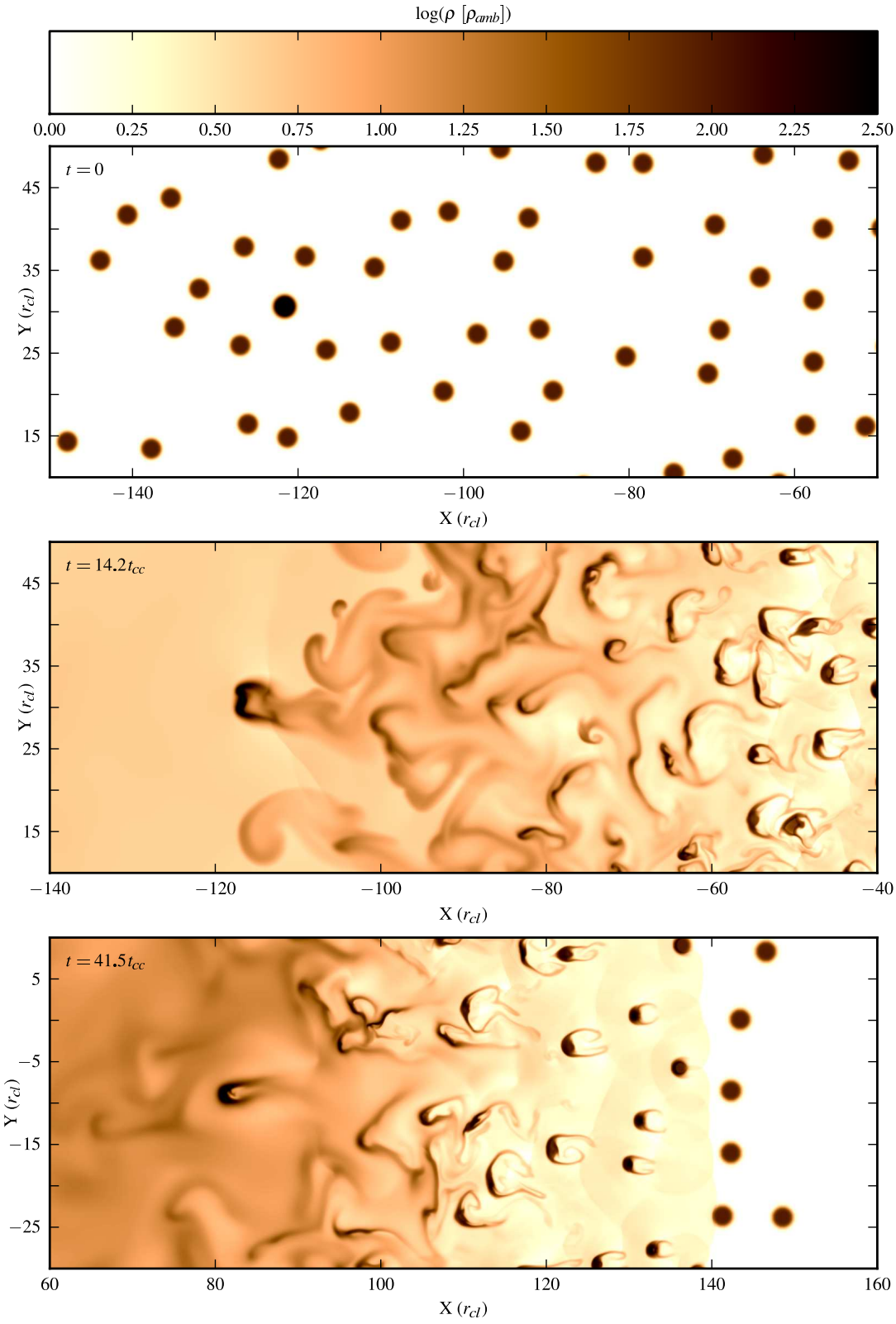

Figure 3.20: Snapshots of regions in the *M3MR4_uniform* distribution. The top panel shows the initial distribution around one of the higher density clouds (which have $\chi = 10^3$ instead of $\chi = 10^2$). The other two panels show snapshots $\sim 10\, t_{\rm cc}$ (here $t_{\rm cc}$ refers to the cloud crushing time-scale of a $\chi = 10^2$ cloud) after the shock hits the higher density clouds towards the upstream end of the distribution (middle) and the downstream end (bottom).

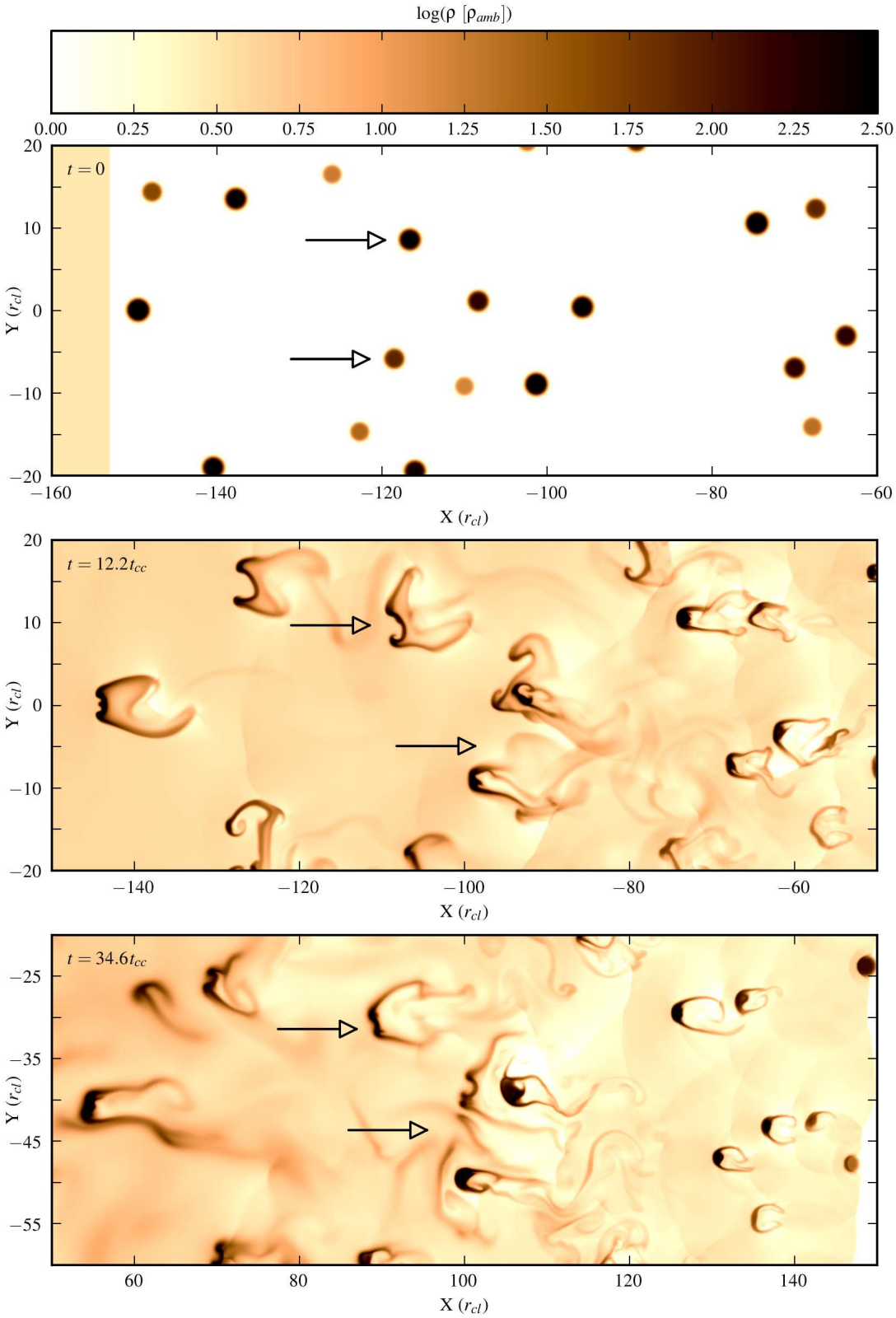

Figure 3.21: Snapshots of regions in the *M3MR4_variable* distribution. The top panel shows the initial distribution around two traced clouds of $\chi = 320$ and $\chi = 83$ (clouds and the location of their remnants are identified by arrows). The other two panels show snapshots $\sim 10\, t_{cc}$ (of $\chi = 10^2$ cloud) after the shock hits the two clouds towards the upstream end of the distribution (middle) and the downstream end (bottom). The $\chi = 320$ cloud remains visible at the same relative position at these later times, but the $\chi = 83$ cloud is already well mixed.

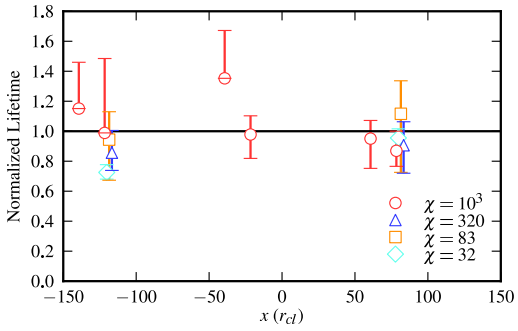

Figure 3.22: Cloud lifetime normalized to reference single cloud simulation as a function of position within the region. The cloud destruction threshold of $m_{\rm cl}/e$ and a reference simulation at R_{32} are taken as representative and the values are shown as symbols. The range possible by choosing a different threshold ($0.25\,m_{\rm cl}$ or $0.1\,m_{\rm cl}$) and/or a different resolution of the reference simulation (R_{16} or R_{128}) is shown by error bars.

by cloud material and a resolution R_{32} for the reference simulations is adopted. The results are plotted as symbols. Alternatively, cloud lifetimes were sampled at a cloud destruction threshold of 0.25 and 0.1 of the initial cloud mass, and single cloud reference simulations at resolutions of R_{16} and R_{128} were also used. In total this gives 9 possible combinations, and the range spanned by them is shown by the error bars.

The $\chi = 10^3$ clouds from the *M3MR4_uniform* simulation show a very weak trend towards reduced lifetimes as shown by the red circles in Fig. 3.22. The two most downstream clouds are destroyed 5–15% faster than an isolated cloud (although some criteria show unchanged lifetimes). In contrast, the two most upstream clouds are longer lived and it remains unclear why this is the case. Perhaps unlike the clouds further downstream these two upstream clouds are still affected by the rather low resolution used for the multiple cloud simulations (R_8). The longest lived $\chi = 10^3$ cloud from the *M3MR4_uniform* simulation is initially lo-

cated at $x = -40\,r_{\rm cl}$. It is the only cloud that is overrun by the shell, but the shell is thin enough at this point that it breaks through. It is again unclear why it remains intact the longest.

The variation of lifetime due to position within the distribution is quite small: the difference between the two most upstream clouds and the two most downstream clouds is 18%. This is comparable to the effect of local conditions. As the distribution is repeated three times, the local distributions are the same between the three regions, but the two clouds within a region have slightly different locations of neighbours. For the two most upstream and the two most downstream clouds this effect is 13%.

For the *M3MR4_variable* simulation the lifetimes are roughly unchanged as well. In fact, lower density clouds are destroyed faster upstream than downstream. In the case of the $\chi = 32$ cloud the reason is that upstream the shock is stronger and the cloud is accelerated faster. As higher density clouds accelerate slowly, the $\chi = 32$ cloud collides into a downstream cloud and is destroyed faster than in the isolated case. In the downstream region, the shock is slower and it takes longer for the same collision to occur.

3.4 Discussion

Our work is relevant to objects where hot, diffuse gas interacts with a colder dense phase. In many of these objects the cold phase, despite its low volume filling fraction, may dominate the dynamics of the hot phase, and thus significantly change the morphology and evolution of the object, and its emission. On the smallest scales these objects include wind-blown bubbles and supernova remnants. Cowie *et al.*

(1981) were the first to study the behaviour of supernova remnants expanding into a clumpy medium. They found that the destruction of the clouds leads to the highest densities in the remnant occurring over the outer half radius (in contrast, when there is no mass loading, a thin dense shell forms at the forward shock). These findings have since been supported by Dyson & Hartquist (1987), who reported a similar 'thick shell' morphology in their similarity solutions, and by the additional numerical simulations presented by Dyson *et al.* (2002) and Pittard *et al.* (2003). The X-ray emission in these cases becomes softer and more extended. In other work, Arthur & Henney (1996) studied the effects of mass loading by hydrodynamic ablation on supernova remnants evolving inside cavities evacuated by the stellar winds of the progenitor stars. They showed that the extra mass injected by embedded clumps was capable of producing the excess soft X-ray emission seen in some bubbles in the Large Magellanic Cloud. We conclude, therefore, that cloud destruction by ablation, as in the simulations presented in our paper, can be looked for by searching for its affect on the X-ray emission of supernova remnants.

The interaction between a wind and individual clouds is also seen in observations of planetary nebula. For instance, in NGC 7293 (the Helix nebula) long molecular tails and bright crescent-rimmed clouds are spectacularly resolved (O'Dell *et al.* 2005; Hora *et al.* 2006; Matsuura *et al.* 2007). The tails in the outer part of the nebula are less clear due to projection effects, but appear to be a separate population displaying wider opening angles. This may reflect changes in the diffuse flow past the clouds, possibly due to the material stripped off the clouds further upstream. Observations indicate that the flow past the clouds is mildly supersonic. Although numerical simulations are able to match the basic morphology of the tails (Dyson *et al.* 2006), dedicated 3D simulations of clouds with very high density contrasts to

the ambient flow are required in order for further insight to be gained.

On larger scales, we note that there is substantial support for mass-loading in starburst regions. Broad emission-line wings are seen in many young star forming regions including 30 Doradus (Chu & Kennicutt 1994; Melnick *et al.* 1999), NGC 604 (Yang *et al.* 1996), and NGC 2363 (Roy *et al.* 1992; Gonzalez-Delgado *et al.* 1994), and more distant dwarf galaxies (e.g. Marlowe *et al.* 1995; Izotov *et al.* 1996; Homeier & Gallagher 1999; Sidoli *et al.* 2006). More recently, Westmoquette *et al.* (2007a,b) reported on the broad emission-line component in the dwarf irregular starburst galaxy NGC 1569. Although the nature of the broad lines has yet to be fully determined, evidence is mounting that it is associated with the impact of cluster winds on cool gas knots. It therefore traces both mass-loading of wind material and mass entrainment. Further support for mass-loading comes from the analysis of hard X-ray line emission within starburst regions. Strickland & Heckman (2009) determine that as much material is mass-loaded into the central starburst region of M82 as is expelled by the winds and supernovae which pressurize the region. A key future goal is the development of numerical simulations of the multi-phase gas within starburst regions, and predictions for broad emission-line wings and X-ray emission.

Starbursts are often associated with galactic outflows. These flows are observed to be filamentary. The consensus view is that the clumps at the heads of the filaments are material which is ripped out of the galactic disk as the galactic wind develops (i.e. representing additional, distributed, mass-loading). In some cases the filaments appear to be confined to the edges of the outflow (Shopbell & Bland-Hawthorn 1998), while in other objects they appear to fill the interior of the wind (Veilleux & Bland-Hawthorn 1997). It is clear that material stripped from the Hα

emitting clouds is entrained into the outflow (see, e.g. Cooper *et al.* 2008), but the exact amount is notoriously difficult to measure (Veilleux *et al.* 2005). Again, future dedicated simulations are needed to help address this issue.

A key question concerns the ultimate fate of gas within galactic outflows. Observations and simulations indicate that the majority of the energy in galactic winds is in the kinetic energy of the hot gas, while the mass in the outflow is dominated by the warm photoionized gas. The former has a good chance of escaping the gravitational potential of the host galaxy, while the latter in many cases is unlikely to do so. Even when simple energetic arguments suggest that the ISM can be completely expelled from a starbursting galaxy, whether it will actually occur depends strongly on the geometry and multiphase nature of the ISM (see, e.g., Heckman *et al.* 1995). For instance, if a centrally concentrated starburst occurs in a galaxy with a disk-like ISM, blowout of the superbubble along the minor axis can allow the bulk of the ISM in the disk to be retained by the galaxy. With a multiphase ISM the diffuse intercloud medium may be ejected while large dense clouds remain in the disk.

Recent work by Oppenheimer & Davé (2008) indicates that the range of galactic winds is primarily determined by the interaction of the wind with the ambient environment, with the gravity of the parent galaxy playing a less significant role. Their simulations also show that across cosmic time the average wind particle has participated in a wind several times. However, further investigations are needed, since their simulations currently lack the resolution required to make accurate quantitative predictions of the slowing of the winds and wind recycling. Furthermore, the wind's multiphase nature must be addressed. Studies like ours are relevant to this work since the destruction and acceleration time-scales which we find for our clumpy region have some bearing on the mixing and stalling time-scales of a

galactic wind. Such simulations could be tested against observations of the extent of galactic winds (e.g. Tumlinson *et al.* 2011; Tripp *et al.* 2011).

3.5 Conclusions

We have performed a detailed hydrodynamic investigation of a shock running through a clumpy region. We find the following key behaviour:

- The stripping of material from the clouds 'mass-loads' the post-shock flow and leads to the formation of a dense shell. Fully-mixed material within the shell reaches a maximum density, after which the shell grows in width. The shell expands and its density drops once there are no more clouds to mix in.

- The evolution of the shock can be split into several distinct stages. During the first stage, the shock decelerates. Then in some cases its velocity becomes nearly constant. After deceleration and the constant speed phase, if it occurs, the shock accelerates and finally approaches the speed it had in the uniform medium before it encountered the clumpy region. A steady stage does not always occur (e.g., if the clumpy region is not very deep).

- When the mass-loading is sufficient, the flow can be slowed to the point that the shock degenerates into a wave.

- The clumpy region becomes more porous as the number density of clouds is reduced, which occurs for lower values of MR, and/or increased values of χ.

- Downstream clouds experience a modified shock. The slower shock leads to a gentler initial interaction, but this is offset by the high level of turbulence

in the post-shock flow and the dense shell if it is formed.

- Clouds of higher density than the typical cloud are engulfed by the shell. The morphology of clouds that are engulfed by the shell and ones that escape it is very different.

- Downstream clouds can be destroyed up to 50% faster than a similar cloud in an 'isolated' environment, though 15% is more typical. However, great care must be taken when comparing cloud lifetimes from single cloud and multiple cloud simulations. When taking account of the effects of resolution we find that cloud lifetimes are largely comparable across a wide range of cloud densities and the properties of the clumpy region (e.g. the mass ratio, MR). Thus turbulence effects appear to be self-limiting.

We have determined the necessary conditions (in terms of the cloud density contrast and the ratio of cloud mass to intercloud mass) for a clumpy region to have a significant effect on a diffuse flow. The lifetime of clouds is a key factor in this respect. Pittard *et al.* (2009) first showed that clouds can be destroyed more quickly when overrun by a highly turbulent environment, although the strength of this turbulence was treated as a free parameter. In contrast, in this Chapter we have presented the first self-consistent simulations of a highly turbulent flow overrunning clouds, where the enhanced turbulence is a natural consequence of the flow overrunning clouds further upstream. We note that one must be mindful of resolution effects when interpreting the results. A resolution of R_8 is good enough for convergence of global statistics. Resolutions of at least R_{16} are necessary to study individual clouds, but care must still be taken. Future simulations should be conducted at a resolution of R_{32} (though R_{128} would be preferable), which would

remove most of the remaining resolution effects. 3D simulations are also required for a physically realistic description of the turbulent energy cascade (Boffetta *et al.* 2000).

The results of this investigation reveal that in some cases the detail of the interaction need not be modelled. If the shock crossing time of the clumpy region is significantly greater than the lifetime of an individual cloud a steady state is reached. Ignoring the edge effects this steady state can be modelled by a 1D calculation of a uniform region with appropriately chosen density. This allows to quickly estimate the minimum velocity that the shock will slow down to. However, as the in the clumpy region the sound speed is higher in the intercloud medium than in the equivalent uniform density region, the minimum velocity is cannot decrease below the sound speed in the intercloud medium. A shock decays into a sound wave if the minimum velocity in 1D calculation is below the sound speed of intercloud medium.

The simulations presented in this Chapter are purely hydrodynamic. The next chapter will investigate the effects of magnetic fields on the flow dynamics. In the future we will also investigate the ability of a flow to force its way through a finite-sized clumpy medium, and determine how this depends on the ratio of the mass injection rate from the clouds to the mass flux in the wind.

Chapter 4

MHD Simulations with two and three clouds

4.1 Introduction

An important process relevant to the structure of the interstellar medium (ISM), is the interaction between a shock and clouds. This interaction is predominantly studied numerically and is usually focussed on an isolated idealized cloud for simplicity (see Sec. 1.4).

Simulations in which the interaction of a flow over numerous obstacles is studied in detail are only just becoming feasible. However, it is clear that the flow responds differently to the presence of a group of clouds, with a global bow shock forming when the clouds are relatively close (see Chapter 3 and also Poludnenko *et al.* 2002, Pittard *et al.* 2005). The degree to which the nature of the flow changes depends on the relative amount of mass added to the flow by the destruction of the clouds, i.e. the mass-loading factor. Simulations extending Poludnenko *et al.* work

to higher mass-loading factors were presented in Chapter 3. This work found that while the global flow is strongly affected by the presence of clouds with density contrasts of $\chi = 10^2$, it nevertheless evolves similarly to a region of equivalent, uniform density (see Fig. 3.17. However, further significant changes arise when the cloud density contrast increases to $\chi = 10^3$. In this case the total mass in the clouds becomes dominant at a much lower volume fraction (equivalently a lower total cross-section of the clouds). The resulting interaction does not affect the structure of the shock much, but significantly mass-loads the post-shock flow. This ongoing mass-loading of the flow as the clouds are destroyed can cause the shock to decelerate even after it has left the clumpy region (see Fig 3.11c).

The evolution of a cloud also changes when additional clouds are nearby. In isolation, clouds lose most of their mass through KH instabilities, with the largest scale instabilities taking some time to grow. Turbulence in mass-loaded flows accelerates the development of large scale instabilities, while high density of the mass-loaded post-shock flow leads to larger mass fraction lost via ablation. .

The presence of magnetic fields can strongly affect the interaction. In 2D axisymmetry, magnetic fields parallel to the shock normal suppress Richtmyer-Meshkov (RM) and KH instabilities, and reduce mixing. The magnetic field is amplified behind the cloud due to shock focusing and forms a 'flux rope' (Mac Low *et al.* 1994). In contrast, in 3D simulations with strong fields perpendicular or oblique to the shock normal the shocked cloud becomes sheet-like at late times, and oriented parallel to the postshock field. The cloud then fragments into vertical or near-vertical columns (Shin *et al.* 2008). More recent work including magnetic fields, anisotropic thermal conduction and radiative cooling of 3D shock-cloud interactions finds that intermediate strength fields are most effective at producing long-lasting density

fragments - stronger fields prevent compression while weak fields do not sufficiently insulate the cloud to allow efficient cooling (e.g., Johansson & Ziegler 2013).

Relatively few investigations of the interaction of a flow with multiple magnetized clouds exist. The response of a clumpy and magnetized medium to a source of high pressure was considered by Elmegreen (1988), who derived jump conditions for cloud collision fronts under a continuum approximation. This work was extended using a multi fluid formalism by Williams & Dyson (2002), who showed that shocks can rapidly broaden and thus create a more benign environment which aids the survival of multiphase structure passing through the shock.

MHD studies of the interaction of a shock with a single-cloud show that the field is amplified not so much in the shear layers and vortices but rather in regions of compression: ahead of the cloud for perpendicular shocks where field lines bunch up, and in a 'flux rope' behind the cloud where the flow converges for the parallel-shock case (Mac Low *et al.* 1994). These simulations show that magnetic fields limit mixing and fragmentation, but do not stop it completely, and provide support to the cloud perpendicular to the field lines. Our goal in this Chapter is to determine the degree to which neighbouring clouds change this picture. In particular, we are interested in the amplification of the magnetic field and the presence of magnetically dominated regions with $\beta < 1$. Can clouds present in regions of enhanced magnetic field enhance the field further or does it saturate? Because of the complex nature of the interaction and the many free parameters which now also include the positions and separations of clouds, we limit this current study to interactions involving two or three clouds. For computational reasons we also limit our study to 2D (i.e. our clouds are infinite cylinders). This work will serve as a basis for future work exploring the interaction of a shock with many 10s and 100s

of clouds in 2D and 3D.

4.2 Method

The computations were performed using the ideal MHD code *mg* (see Sec. 2.5). We assume that the ionization fraction is high enough that ions and neutrals are fully coupled and can be treated as a single fluid. Explicitly, we choose the average particle mass, $\mu = 0.61 m_{\rm H}$, corresponding to a fully ionized ISM.

The simulations utilized 2D XY-Cartesian grids, so that the clouds are actually infinite cylinders. A typical grid extended $X \in [-50 : 190]\, r_{\rm cl}$ and $Y \in [-50 : 50]\, r_{\rm cl}$, where $r_{\rm cl}$ is the cloud radius (identical clouds are assumed). Inflow boundary conditions were used at the negative X boundary, being set by the shock jump conditions. Free inflow/outflow conditions were used at the other three boundaries. Simulations were performed with two sets of resolutions: 32 cells per cloud radius (R_{32}), and 128 cells per cloud radius (R_{128}). The lower resolution runs used seven grid levels, with $\Delta x = 2\, r_{\rm cl}$ on the G^0 grid, while the higher resolution simulations used eight grid levels, with $\Delta x = 1\, r_{\rm cl}$ on the G^0 grid.

The simulations set up two or three clouds with a cloud density contrast of $\chi = 100$ and with soft edges following the same density profile as in Chapter 3 with $p_1 = 10$ (again). In all simulations the sonic Mach number of the shock was 3. The strength of the magnetic field and its orientation to the shock was varied. Values for the Alfvénic Mach number, the pre-shock field angle and the plasma β in different regions are given in Table 4.1. A different advected scalar is used for each cloud to track the cloud material. The time is measured in units of the cloud crushing time-scale, $t_{cc} = \chi^{1/2} r_{\rm cl}/v_b$, where v_b is the shock velocity in the

Table 4.1: Summary of the magnetic field strength and orientation in the single- and multi-cloud simulations performed. The value of the plasma β in the pre-shock (i.e. β_0) and post-shock regions is also provided, as well as its approximate value in the bow-shock region.

			Value of β in each region		
Case name	B angle	M_a	Pre-shock	Post-shock	Bow-shock
b15b1	15°	2.91	1.13	6.06	7.1
byb1	89.°9	2.91	1.13	1.25	1.2
byb5	89.°9	6.16	5.06	6.05	5.5
bxb1	0°	2.91	1.13	12.4	21
bxb0.5	0°	2.03	0.55	6.05	10.5

ambient medium. The bow-shock reaches the Y boundaries at around $7.5\,t_{cc}$ and the simulations are terminated shortly afterwards. Adiabatic behaviour is assumed with $\gamma = 5/3$.

4.3 Results

The collective interactions between a large number of clouds can be incredibly complex. To better understand them we begin by reviewing the basic behaviour of a shock striking an isolated, magnetized, cylindrical cloud. We then investigate the simplest of multiple cloud cases, that of two clouds, before applying the insight from the two-cloud simulations to simulations with three clouds. Single-cloud simulations are named using the format *sc bAbB*, where the '*sc*' indicates that it is of a single-cloud, the '*A*' indicates the orientation of the field ('*x*', '*15*' and '*y*' indicate parallel, oblique and perpendicular shocks) and '*B*' indicates the value of the pre-shock plasma β. Two-cloud simulations are named using the format *s2wYoX bAbB* (or often using the shortened forms *wYoX* or *wYoX bAbB*). Similarly, three-cloud

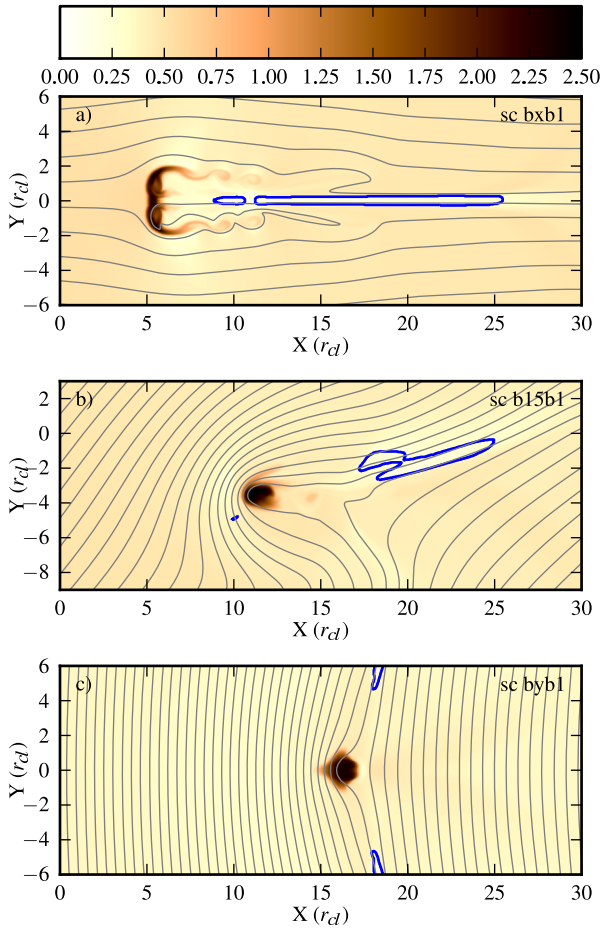

Figure 4.1: The morphology of interactions of a shock with a single cylindrical cloud. The calculations are in 2D, the sonic Mach number is 3 and the Alfvénic Mach number is 2.91 ($\beta_0 = 1.13$). The shock is a) parallel, b) oblique, and c) perpendicular . The cloud is initially positioned at the origin. The colour-scale shows the logarithmic density in units of ambient density and magnetic field lines are also shown. The contour indicates regions with low plasma β and low momentum ($\beta < 1$ and $\rho|\mathbf{u}| < 0.5 \times \rho_{ps}|\mathbf{u}_{ps}|$). The time of the interaction is $t = 4\,t_{cc}$.

simulations are named using the format *s3wRaθ bAbB* (again also with shortened versions). *wYoX* and *wRaθ* identify the relative positions of clouds, see Secs 4.3.2 and 4.3.3 respectively for further details.

4.3.1 Single-cloud interactions

4.3.1.1 Parallel shocks

We begin by reviewing the morphology of the 2D interaction of a shock with a single magnetized, cylindrical cloud. In the parallel field case a 'flux rope' forms directly behind the cloud: the flow converging behind the cloud compresses the field lines, thus increasing the magnetic pressure which prevents the post-shock flow from entering it (see Fig. 4.1a). As a result the 'flux rope' not only has a low plasma β, but it also has very low momentum. These two conditions ($\beta < 1$ and $\rho|\mathbf{u}| < 0.5 \times \rho_{ps}|\mathbf{u}_{ps}|$) specify the 'flux rope' region in the parallel field case, but can also be met in other field arrangements.

Another important feature in the flow are the 'wings'. This is a region or regions alongside the flux rope which delineates where the flow is stripping material away from the cloud. This region shows up in the magnetic field structure of simulations with parallel shocks as the reversal of the magnetic field. In general the 'wings' are shielded from the momentum of the flow, although occasionally they may contain higher density fragments stripped off the upstream cloud.

4.3.1.2 Oblique shocks

In our oblique shock simulations a preshock field orientation of $\theta_0 = 15°$ was chosen to be a representative oblique field case. This gives $\theta_{ps} = 45°$ in the post-shock medium. When an oblique shock interacts with an isolated cylindrical cloud we find that the field lines wrap around the cloud keeping its cross-section roughly circular in shape (see Fig. 4.1b). Field lines above the cloud become nearly parallel to the

direction of shock propagation[1] and some material is stripped off along them. Field lines below the cloud span a range of angles, with the region immediately upstream of the cloud having field lines nearly parallel to the shock front. Field amplification and 'shielding' (i.e. where gas has minimal exposure to the ambient flow - e.g. gas in the lee of a cloud) now occur in distinct, but overlapping regions. The cloud is accelerated downstream and also laterally (in Fig. 4.1b the cloud is seen to move to lower Y). The asymmetry of the cloud's motion reflects the asymmetric bunching and tensioning of the field lines and the direction of the postshock flow. Note that because the cloud in this simulation is actually an infinite cylinder field lines cannot easily slip past it. If the cloud were spherical we would expect some splitting and rearranging of the field, which could significantly change the forces acting on the cloud.

4.3.1.3 Perpendicular shocks

In the perpendicular field case, the magnetic field is initially amplified directly upstream of the cloud where the flow stagnates against it (see Fig. 4.1c). Because field lines cannot slip around the surface of the cloud (again due to its nature as an infinite cylinder), magnetic pressure and field tension continue to build with the result that the cloud accelerates rapidly downstream (compare the positions of the clouds in Fig. 4.1). This rapid acceleration acts to reduce the magnetic pressure and tension. Again we expect the evolution of a spherical cloud to be quite different.

[1] The postshock flow is about $-7°$ to the shock normal.

4.3.2 Two-cloud interactions

We now investigate the interaction of magnetized shocks with two closely positioned clouds. We first examine the morphology of the interaction, and then discuss the acceleration of the clouds and the evolution of the plasma β. The two-cloud arrangements are specified by their 'width', which is the lateral distance between the cloud centres in units of the cloud radius (i.e. the separation of the clouds in the 'y' direction), and by their 'offset', which is the longitudinal distance between the clouds (i.e. their separation in the 'x' direction). $t = 0$ is defined as the time that the shock reaches the leading edge of the more upstream of the two clouds.

4.3.2.1 Parallel shocks

In interactions with a parallel shock, the presence of a second cloud alongside the first cloud has the effect of suppressing the lateral re-expansion of the cloud. This is easily seen when comparing the single-cloud simulation *sc* and the two-cloud simulation *w4o0* (in panels a) and b) of Fig. 4.2, respectively). The flow between the clouds is slowed and squeezed, but accelerates once past the clouds. The initial high pressure between the clouds drops due to the Bernoulli effect, causing the initial outwardly directed orientation of the flux ropes to change towards an inwardly directed orientation[1].

As the initial position of one of the clouds is moved downstream the lateral suppression of the upstream cloud is reduced and it evolves more like the single cloud case. However, the downstream cloud is still much more affected by lateral confinement (see the results for *w4o8* shown in Fig. 4.2c).

[1]This behaviour is also seen in purely hydrodynamic simulations (Pittard *et al.* 2005).

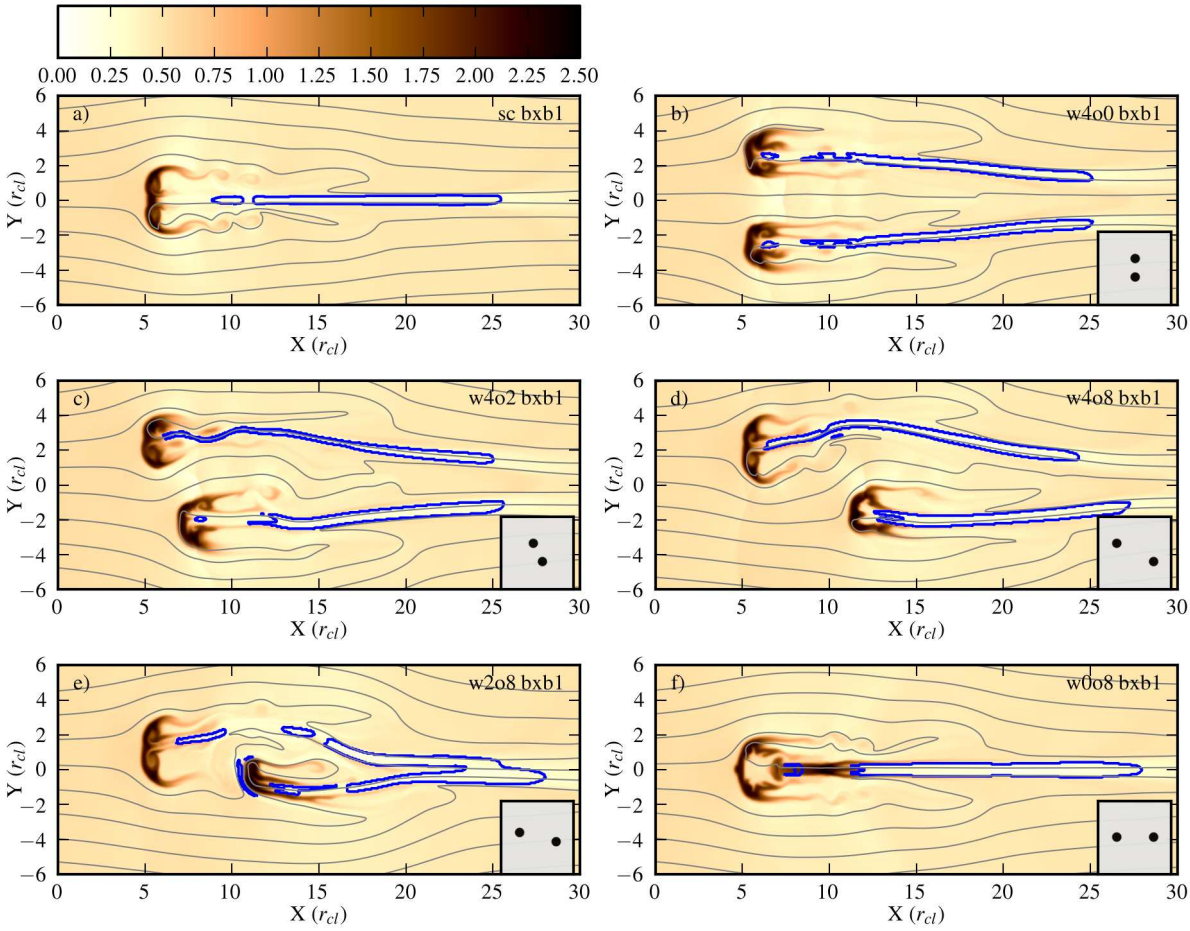

Figure 4.2: Snapshots of the morphology of (a) an individual cloud and (b)–(f) two-clouds with varying separation and offset at $t = 4\,t_{\rm cc}$. In all cases the magnetic field is parallel to the shock normal and $\beta_0 = 1.13$. The contour again shows the 'flux rope' ($\beta < 1$ and $\rho|\mathbf{u}| < 0.5 \times \rho_{\rm ps}|\mathbf{u}_{\rm ps}|$), while the colour-scale shows the logarithmic density. The two-cloud simulations are identified by the initial 'width' and 'offset' of the clouds - the relative positions of the cloud at $t = 0$ are shown in the inset of each panel (shown at reduced scale). The resolution is R_{32}. At higher resolution the fine scale structure changes somewhat, but the general features of the flow and their dependence on the initial arrangement of the clouds remain unchanged.

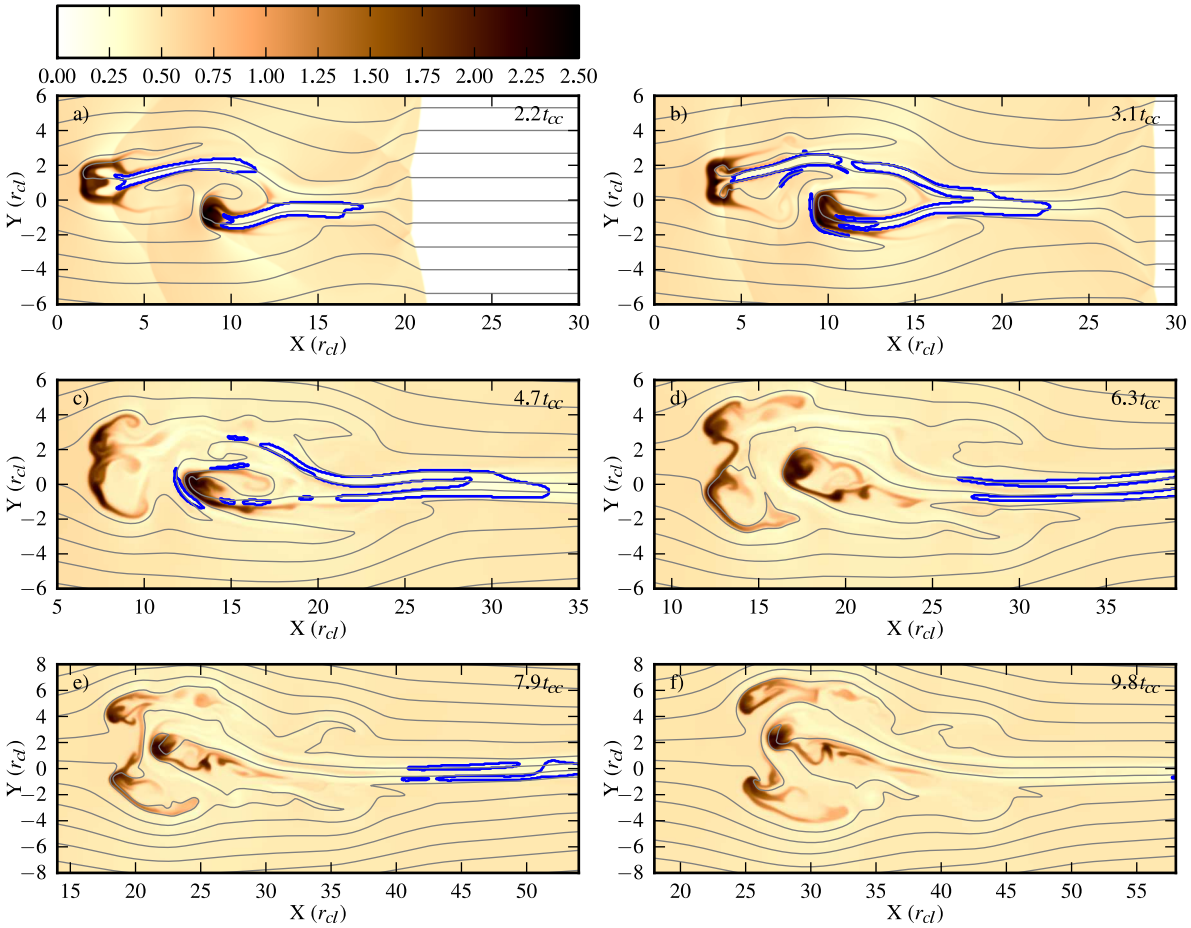

Figure 4.3: The time evolution of the two-cloud simulation *s2w2o8* (the clouds are positioned with an initial 'width' $= 2\,r_{\rm cl}$ and 'offset' $= 8\,r_{\rm cl}$). The magnetic field is parallel to the shock normal and $\beta_0 = 1.13$. The logarithmic density and magnetic field evolution are shown at times $t = 2.2$, 3.1, 4.7, 6.3, 7.9 and $9.8\,t_{\rm cc}$. The contour shows the 'flux rope' ($\beta < 1$ and $\rho|\mathbf{u}| < 0.5 \times \rho|\mathbf{u}|_{\rm ps}$). In this simulation the downstream cloud is confined by the presence of the upstream cloud. Note the changes in the x- and y-coordinates in each panel.

The morphology of the downstream cloud is dependent on the 'width' as well as the 'offset', though the 'width' is the dominant parameter. The simulations *w4o8*, *w2o8* and *w0o8* shown in panels c)-e) of Fig. 4.2 illustrate the diversity of the downstream cloud morphology, which we find can be categorized into three main types. When there is a sufficient gap between the clouds for the flow to weave through (e.g., as in simulation *w4o8* - see Fig. 4.2d), the downstream cloud is confined in a similar manner as if there was a cloud alongside it. In contrast, when a cloud is directly behind an upstream cloud (e.g., as in simulation *w0o8* - see Fig. 4.2f), it falls in its 'flux rope'. The cloud is shielded from the flow and does not accelerate. The flow that tries to converge behind the upstream cloud (which forms the 'flux rope') instead now converges on the downstream cloud, compressing it into an elongated shape. The upstream cloud is also affected by the presence of the downstream cloud. As it accelerates towards the downstream cloud the tenuous gas between them is compressed, modifying the morphology of the upstream cloud in advance of their collision.

The third type of behaviour occurs when the downstream cloud is positioned such that it lies in the 'wings' of the flow around the upstream cloud (e.g., see simulation *w2o8* - shown in panel e of Fig. 4.2). To better understand the nature of this interaction we also show the time evolution of this simulation in Fig. 4.3. We find that the 'flux ropes' of the two clouds merge downstream, while the magnetic field near the clouds becomes highly irregular. The latter is affected by the fact that the background flow becomes quite turbulent as it tries to force its way between the clouds at the same time as the clouds are distorted and influenced by the flow. The turbulent nature of the flow appears to be quite efficient at stripping material away from the downstream cloud. In spite of this, the cloud is mostly confined

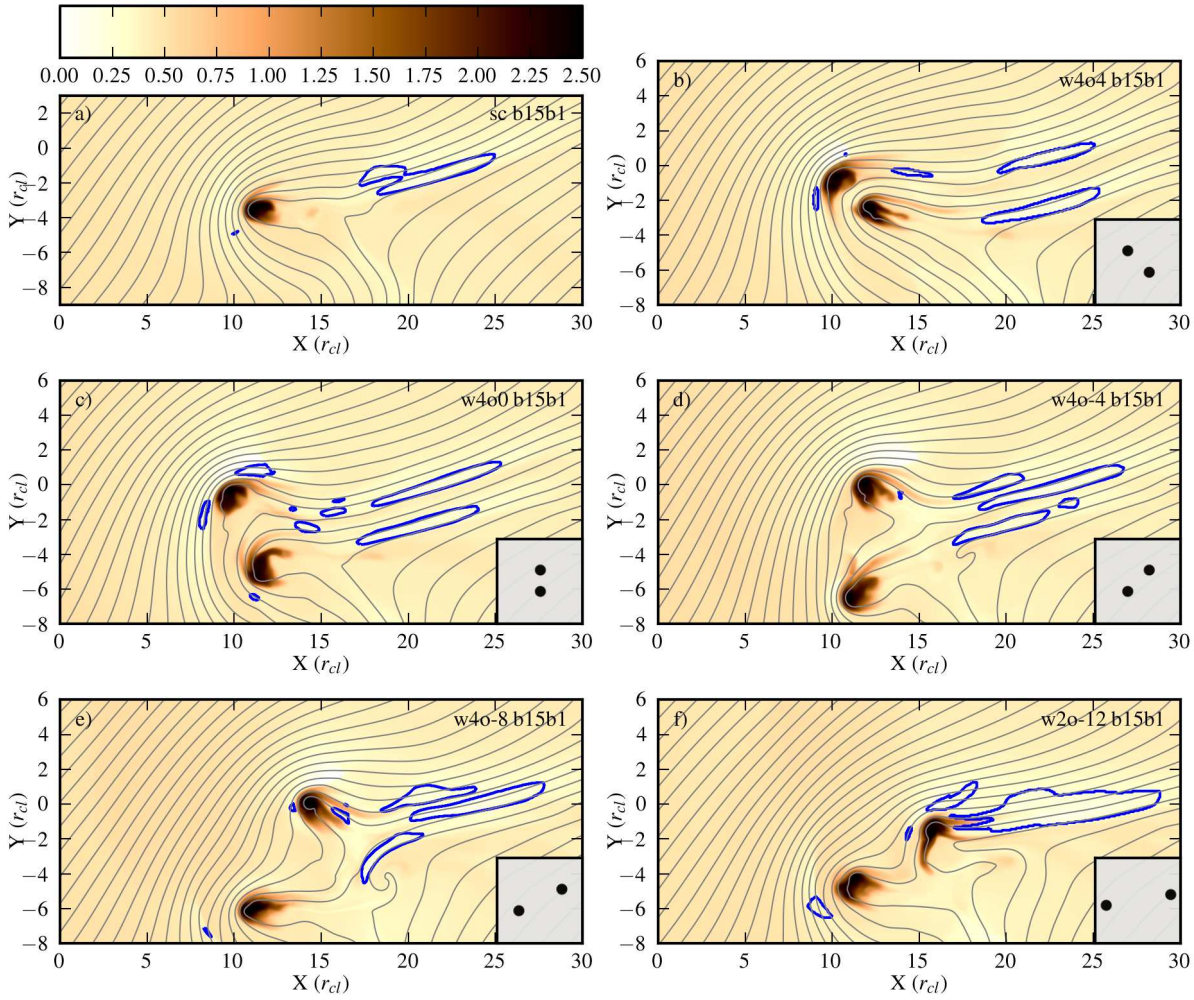

Figure 4.4: Snapshots at $t = 4\,t_{cc}$ of the morphology and field structure of shock-cloud simulations with an oblique magnetic field ($\theta_0 = 15°$ and $\beta_0 = 1.13$). Panel a shows the interaction with a single cylindrical cloud (*sc b15b1*), while the remaining panels show the interaction with two cylindrical clouds. The colour-scale shows the logarithmic density while the contour shows the 'flux rope'.

into an r_{cl}-sized clump and does not spread very far along its field lines. Similar behaviour for the downstream cloud is also seen in simulation *w4o8* at late times as the upstream cloud expands and the downstream cloud is pushed into the shielded region.

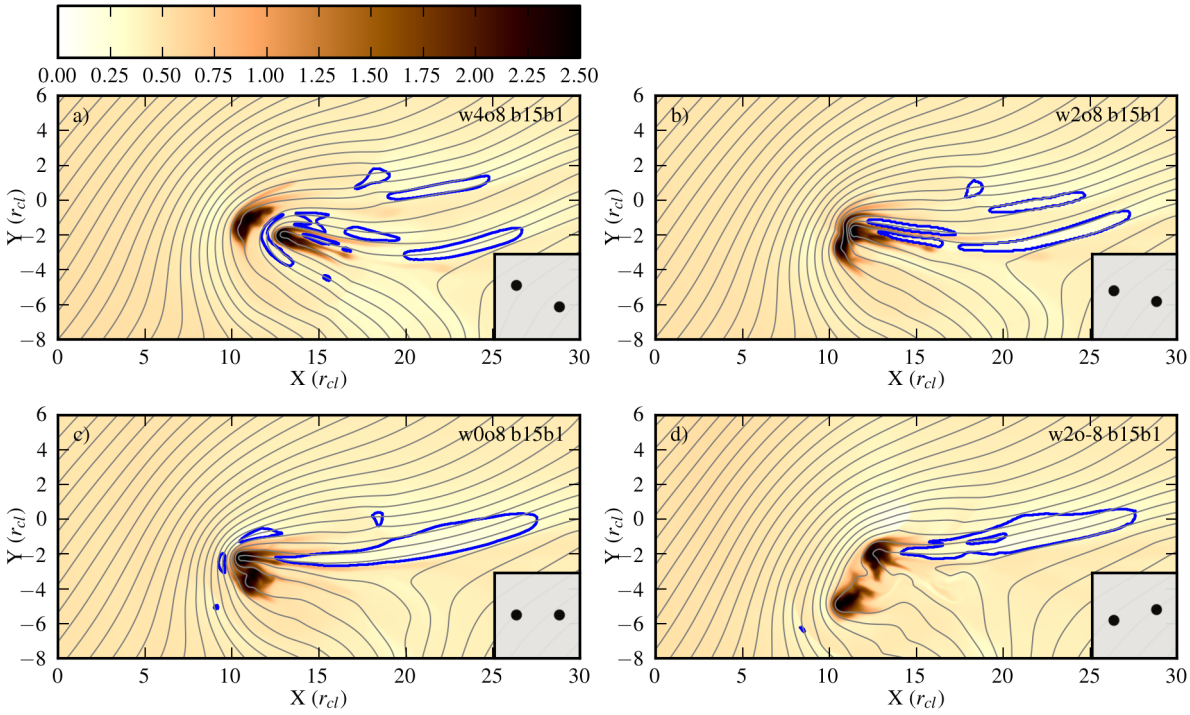

Figure 4.5: Two-cloud oblique-field snapshots like those in Fig. 4.4 but for a fixed cloud 'offset' of $8\,r_{\rm cl}$ and varied 'width'.

4.3.2.2 Oblique shocks

We now study the interaction of an oblique shock with two cylindrical clouds. As the oblique magnetic field is not symmetric about the x-axis it provides another direction to supplement the 'upstream' and the 'downstream' designations. We define the 'upfield' cloud as the one whose field lines encounter the shock front first. In the cases considered the upfield cloud is almost always the 'top' cloud (i.e. has an initial positive 'y' position). The exceptions are simulations *w2o-8* where the two clouds lie on roughly the same field lines, and *w2o-12* which was chosen specifically to have the 'bottom' cloud as the 'upfield' one.

Figs 4.4 and 4.5 compare snapshots of the density and magnetic field structure of a single cloud case and a range of two cloud arrangements at $t = 4\,t_{\rm cc}$. *Note*

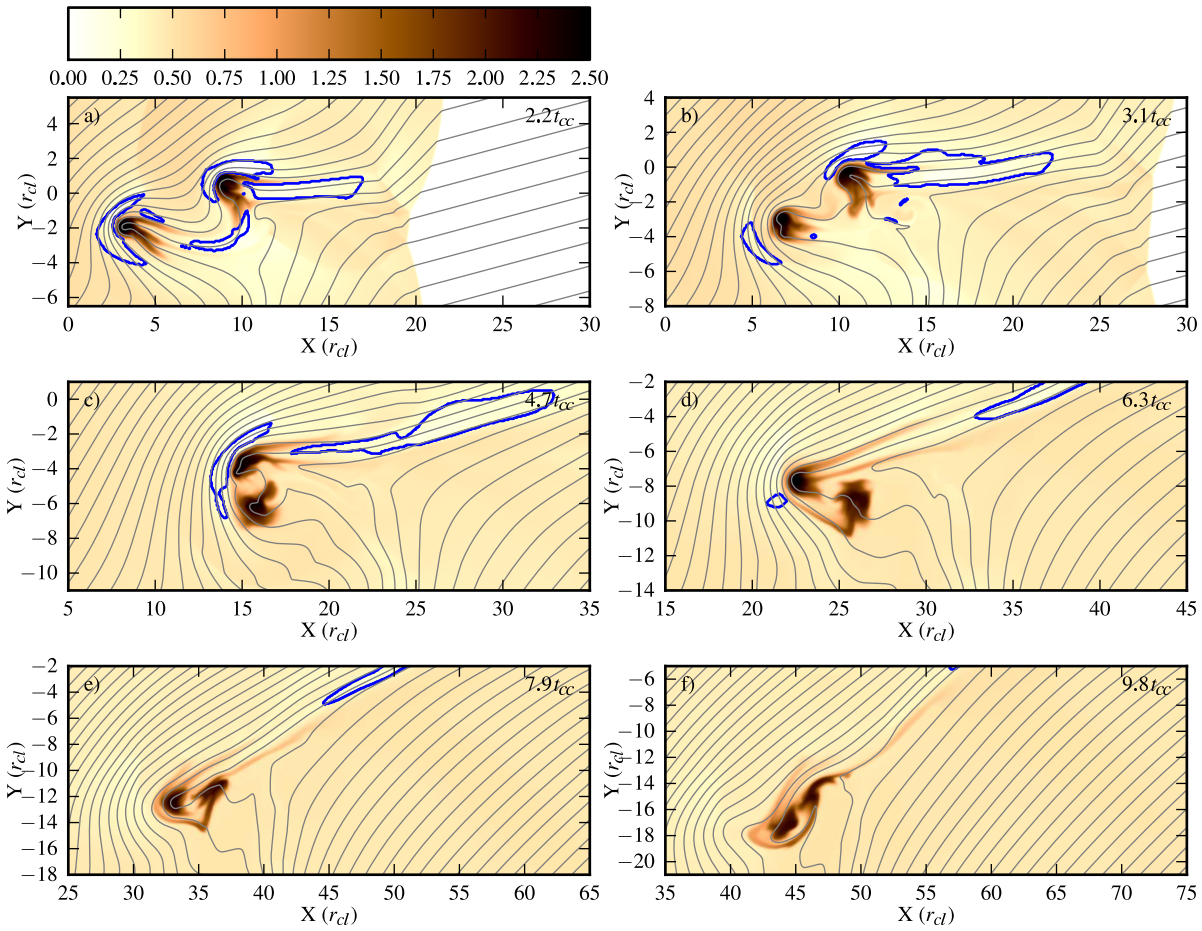

Figure 4.6: The evolution of the two-cloud simulation *s2w2o-8* (the clouds are positioned with an initial 'width' $= 2\,r_{\rm cl}$ and 'offset' $= -8\,r_{\rm cl}$). The magnetic field is oblique to the shock normal ($\theta = 15°$ and $\beta_0 = 1.13$). The logarithmic density and magnetic field evolution are shown at times $t = 2.2$, 3.1, 4.7, 6.3, 7.9 and $9.8\,t_{\rm cc}$. The contour shows the 'flux rope' ($\beta < 1$ and $\rho|\mathbf{u}| < 0.5 \times \rho|\mathbf{u}|_{\rm ps}$). In this simulation the cloud which is initially upstream (i.e. the bottom cloud) is accelerated past the top cloud such that it becomes the most downstream cloud for $t \gtrsim 4.7\,t_{\rm cc}$.

that a negative 'offset' signifies that the 'top' cloud is the downstream one. In all cases the field geometry causes the clouds to accelerate downwards (to more negative y positions) at the same time that they are accelerated downstream (to more positive x-positions). We see that the nature of the interaction is significantly modified by the presence of the second cloud, and that it depends on the relative initial positions of the clouds. In some cases the downstream cloud is protected from the oncoming flow by its position in the lee of the upstream cloud (e.g. as seen in simulation *w4o4* in Fig. 4.4b, and in simulations *w4o8* and *w2o8* in Fig. 4.5a and b). In other cases the downstream cloud feels the full fury of the oncoming flow (e.g., as seen for the top clouds in simulations *w4o-4* and *w4o-8* in panels d and e in Fig. 4.4). Whether the top or bottom cloud accelerates fastest downstream depends on their relative orientation to the shock and the field (e.g., in simulation *w4o4* in Fig. 4.4 and in simulations *w4o8* and *w2o8* in Fig. 4.5 the top cloud accelerates fastest downstream, while in simulations *w4o-4*, *w4o-8* and *w2o-12* in Fig. 4.4 and *w2o-8* Fig. 4.5 the bottom cloud does so). Note that the bottom cloud in simulation *w0o8* shown in Fig. 4.5 is initially the upstream cloud.

Because the field lines are now forced to bend around two clouds, in many cases the region where the magnetic field is parallel to the direction of the shock propagation becomes larger and another region where the field is perpendicular extends between the two clouds (see e.g., simulations *w4o4*, *w4o0* and *w4o-4* in Fig. 4.4). The clouds are also a lot less circular than compared to the case of a single cloud with an oblique field (compare any panel in Figs 4.4 and 4.5 with panel a in Fig. 4.4). Stripping now frequently occurs along multiple directions.

In many cases the wrapping of the field lines causes the top cloud to be accelerated downwards (i.e. to more negative y positions) faster than the bottom cloud

is accelerated in this direction. This can cause the clouds to either collide or come as close together as allowed by the magnetic pressure which builds between them (see simulations *w4o8* and *w2o8* in Fig. 4.5). In other cases we find that the upstream cloud can become the most downstream cloud as the interaction evolves. Fig. 4.6 shows a time sequence from simulation *w2o-8b15b1* which shows how the upstream cloud (in this case the bottom cloud) overtakes the downstream (top) cloud. Once the bottom cloud moves into the 'lee' of the top cloud it experiences reduced confinement forces and begins to diffuse. Simultaneously the top cloud becomes more exposed to the oncoming flow and experiences another episode of compression. This type of behaviour is seen in a large range of oblique simulations.

4.3.2.3 Perpendicular shocks

Finally, we study the interaction of a perpendicular shock with two cylindrical clouds. Figs. 4.7 and 4.8 compare snapshots of the density and magnetic field structure of interactions of a single cloud and two clouds with a perpendicular shock at $t = 4\,t_{cc}$. In Fig. 4.7 the plasma β of the pre-shock medium is $\beta_0 = 5.06$, whereas the field is significantly stronger in Fig. 4.8 ($\beta_0 = 1.13$). As the field strength increases the magnetic field increasingly controls the dynamics of the interaction. This is evident from the suppressed instabilities and cloud mixing, enhanced diffusion of the cloud along the field lines, greater acceleration of the clouds downstream, and straighter field lines in Fig. 4.8 versus Fig. 4.7.

We again find that the presence of a second cloud has a major influence on the nature of the interaction. As the field lines wrap around the two clouds they are driven towards each other very rapidly. If clouds lie on the same field line they merge into a single clump (see the time evolution of simulations *w4o0* in Figs. 4.9

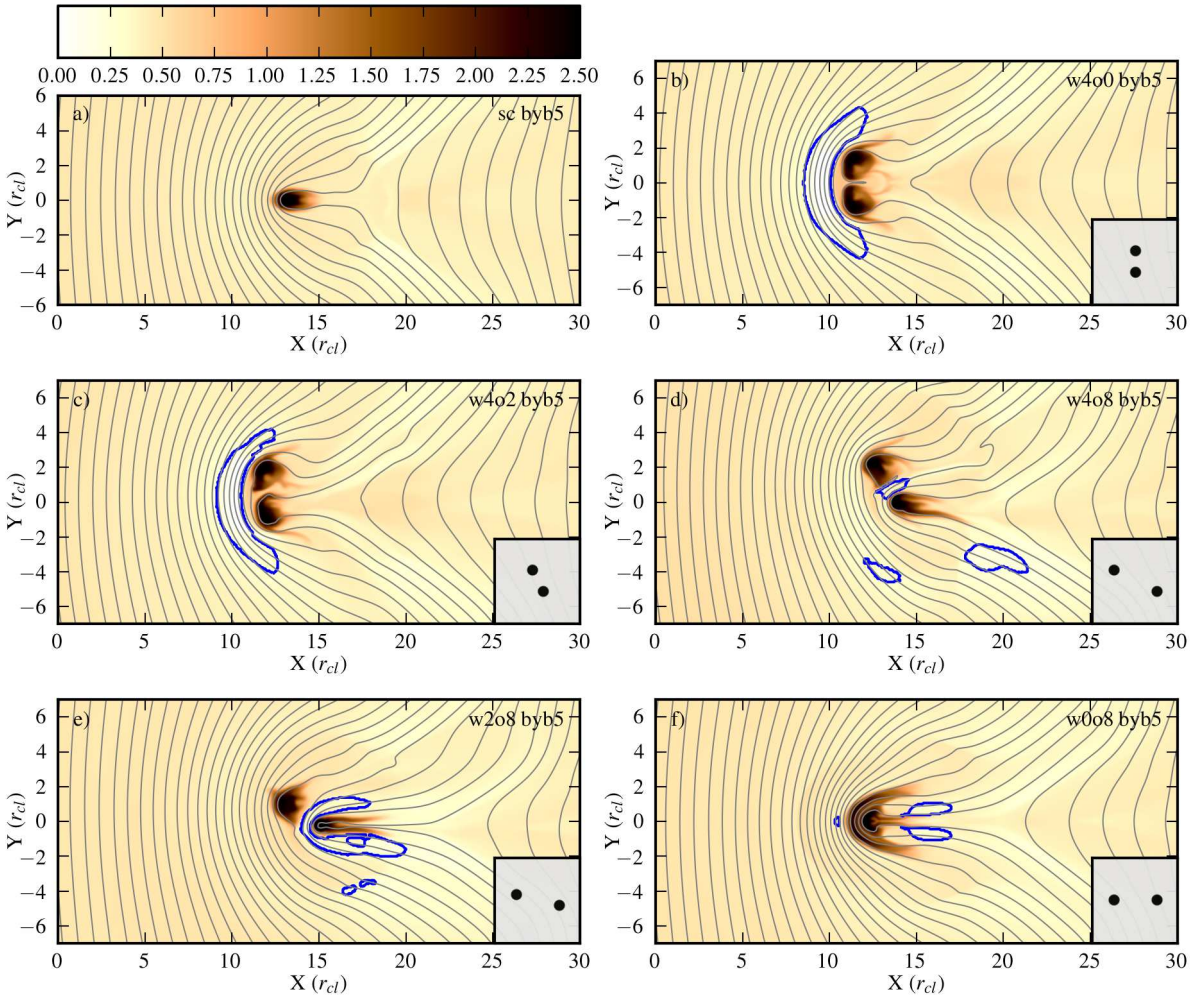

Figure 4.7: As Fig. 4.4 but with perpendicular magnetic fields and $\beta_0 = 5.06$. The time of each snapshot is again $t = 4\,t_{cc}$.

and 4.10). During this process a large continuous region of high magnetic pressure forms upstream of the clouds. Comparison of Figs. 4.9 and 4.10 reveals that there is some numerical diffusion present in the R_{32} simulations but that the same general behaviour occurs[1]. If the clouds do not lie on the same field line then a build up

[1]Because of this difference in numerical diffusion we find that the degree to which clouds merge when they do not lie on the same field lines is dependent on the resolution, with higher resolution simulations better able to prevent mixing and maintain distinct clouds in such cases (stronger fields also tend to keep clouds separate). R_{128} resolution is also necessary for accurate calculation of the plasma β in some circumstances - see Sec. 4.3.2.5.

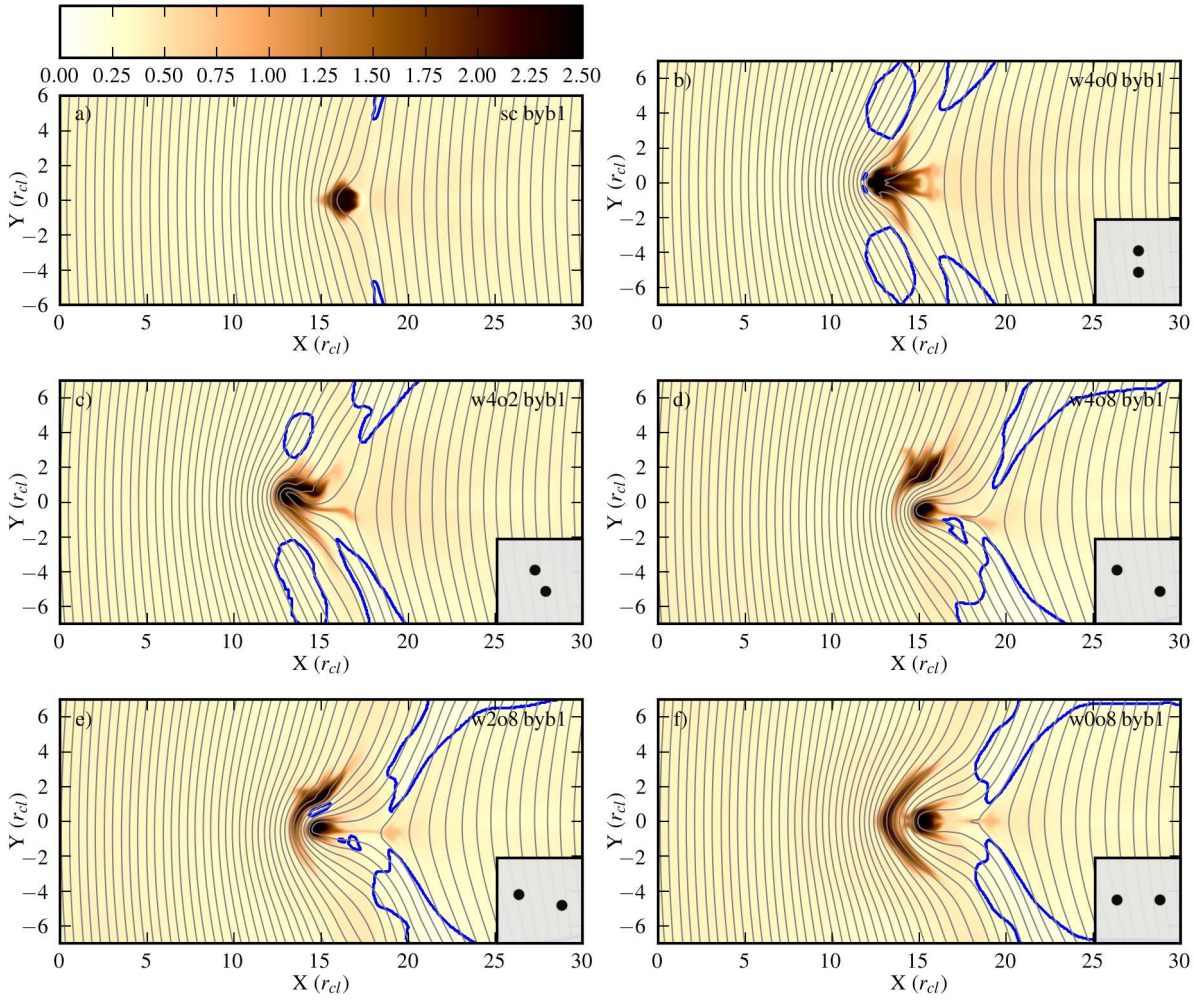

Figure 4.8: As Fig. 4.7 but with $\beta_0 = 1.13$. The time of each snapshot is again $t = 4\,t_{\rm cc}$. The stronger magnetic field now controls the dynamics more compared to the simulations shown in Fig. 4.7.

in the magnetic pressure between the clouds prevents their merger (see simulation *w4o8* in Fig. 4.7 where the contour between the clouds highlights the region of high magnetic pressure). Lazarian (2013) argues that the actual reconnection diffusion in turbulent plasmas might be quite fast and there might be a resemblance between numerical diffusion and magnetic reconnection in turbulent flows.

If the clouds are aligned or nearly-aligned with the direction of shock propa-

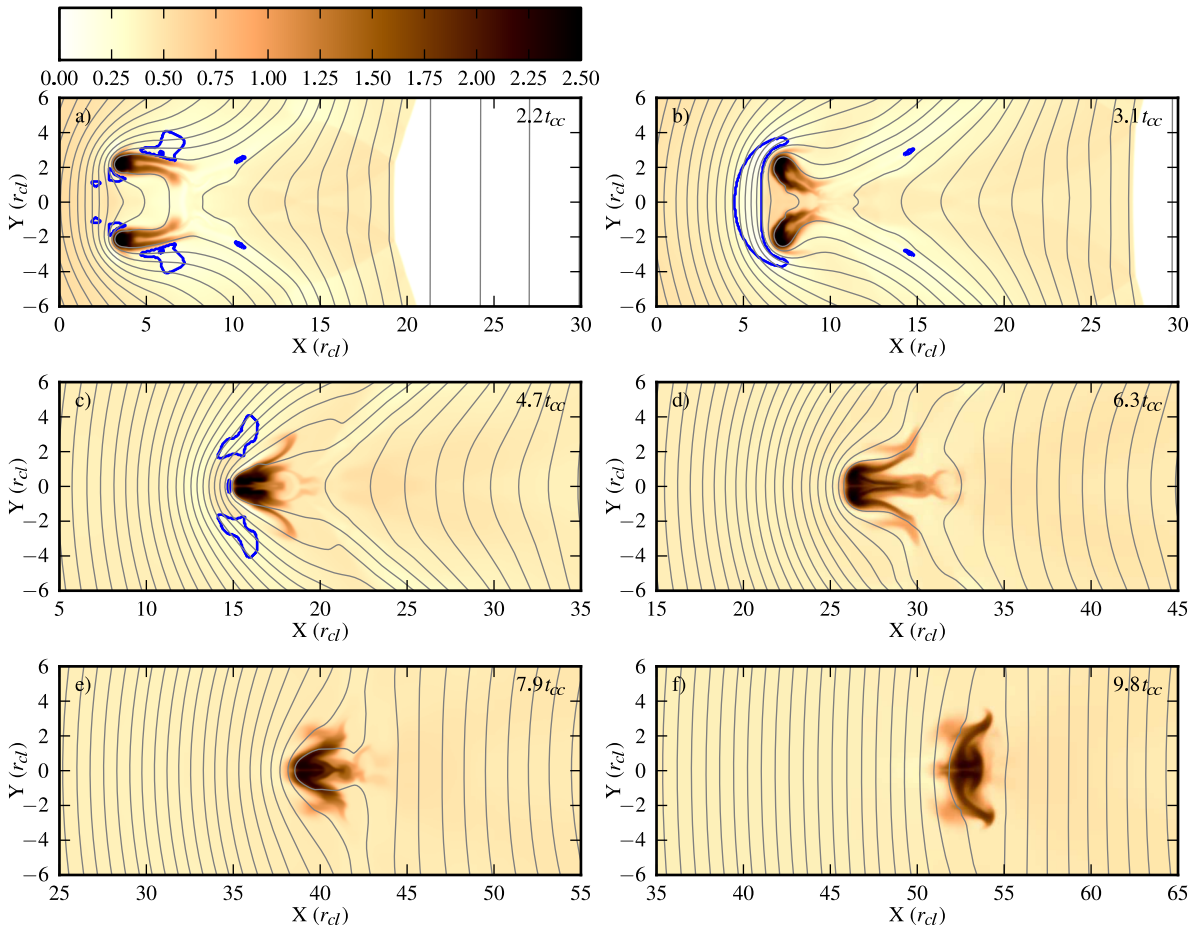

Figure 4.9: The time evolution of the two-cloud simulation *w4o0_byb5* (the clouds are positioned with an initial 'width' $= 4\,r_{\rm cl}$ and 'offset' $= 0\,r_{\rm cl}$). The magnetic field is perpendicular to the shock normal ($\beta_0 = 5.06$). The logarithmic density and magnetic field evolution are shown at times 2.2, 3.1, 4.7, 6.3 and 7.9 $t_{\rm cc}$ (top to bottom). The contour shows the 'flux rope' ($\beta < 1$ and $\rho|\mathbf{u}| < 0.5 \times \rho|\mathbf{u}|_{\rm ps}$). See also the second panel in Fig. 4.7.

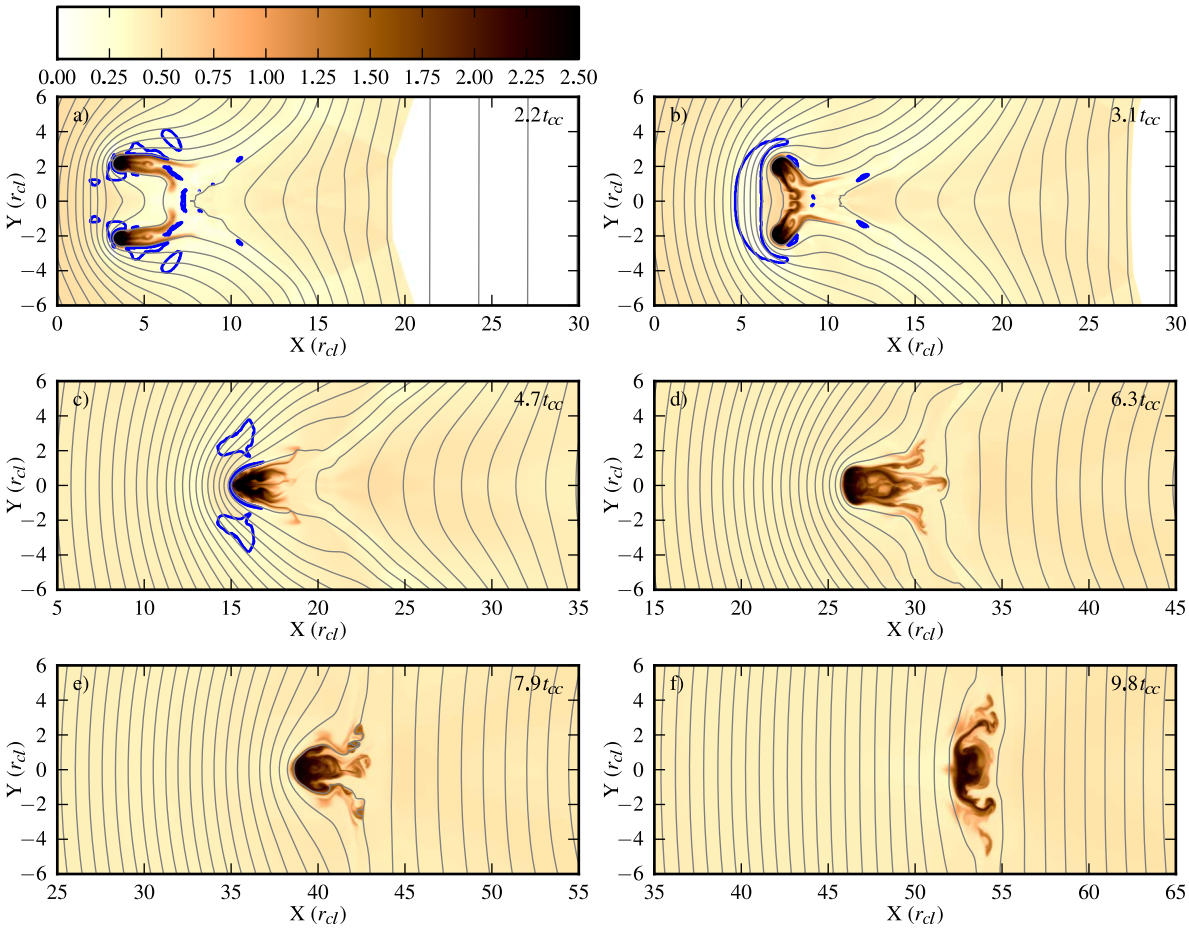

Figure 4.10: As Fig. 4.9 but with a resolution of 128 cells per cloud radius (instead of 32).

gation the downstream cloud is shielded from the oncoming flow by the upstream cloud which moves very close towards it (see simulations *w2o8* and *w0o8* in Fig. 4.7). In such cases, the magnetic field lines between the clouds prevent the clouds from merging. The downstream cloud is compressed laterally by the upstream cloud which wraps around it.

In some cases, clouds which are initially separated quite widely can be driven towards each other to end up in a very compact arrangement. This behaviour is shown in Fig. 4.11, which shows the evolution of the interaction in simulation *w4o4*.

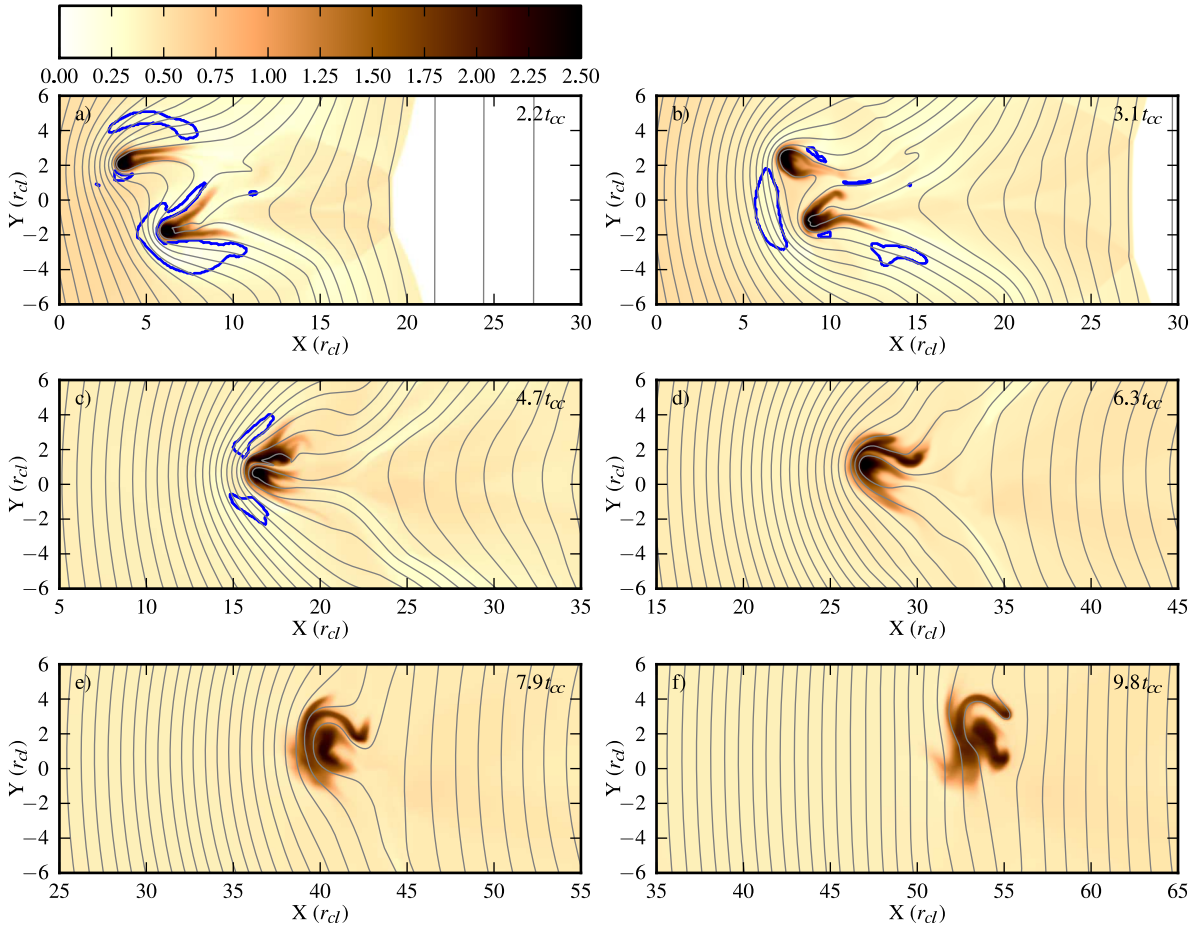

Figure 4.11: The time evolution of the two-cloud simulation *w4o4_byb5* (the clouds are positioned with an initial 'width' $= 4\,r_{\rm cl}$ and 'offset' $= 4\,r_{\rm cl}$). The magnetic field is perpendicular to the shock normal ($\beta_0 = 5.06$). The logarithmic density and magnetic field evolution are shown at times $t = 2.2$, 3.1, 4.7, 6.3 and $7.9\,t_{\rm cc}$ (top to bottom). The contour shows the 'flux rope' ($\beta < 1$ and $\rho|\mathbf{u}| < 0.5 \times \rho|\mathbf{u}|_{\rm ps}$). In this simulation the clouds accelerate towards each other with the upstream cloud eventually wrapping around the downstream cloud.

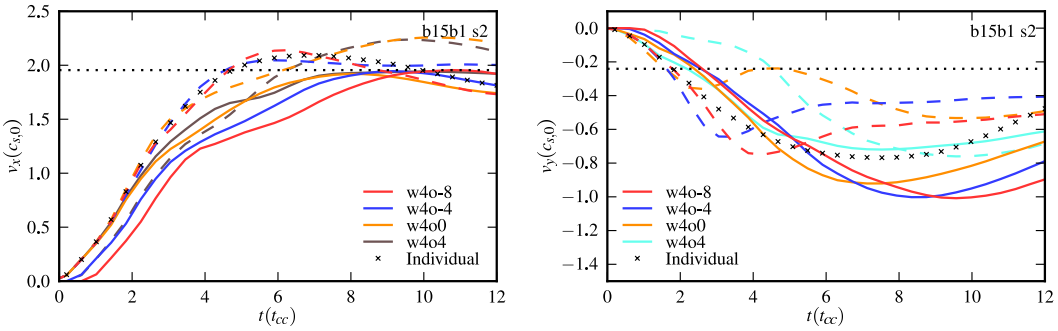

Figure 4.12: Evolution of the x (v_x, left panel) and y (v_y, right panel) cloud velocity components in simulations with two clouds and oblique magnetic fields. The velocity is normalized by the sound speed of the intercloud ambient medium. The initial 'width' of the cloud distribution is identical in each simulation (being $4\,r_{\rm cl}$), while the 'offset' is varied. In each panel the 'top' cloud in the distribution is shown using solid lines while dashed lines correspond to the 'bottom' cloud. The dotted black line shows the intercloud velocity of the post-shock flow. Also shown is the velocity evolution of a single cloud simulation (indicated by the black crosses).

In such cases, shock compression of the field lines naturally reduces the 'offset' between the clouds, while their 'width' is easily reduced by their motion along the field lines. In this example the downstream cloud moves towards the low pressure region behind the upstream cloud and away from the high (magnetic) pressure region around the outside edge of the combined clouds. The field lines between the clouds prevent complete merging in this instance.

4.3.2.4 Cloud velocities

In simulations with a parallel or perpendicular magnetic field the clouds generally develop a small y component to their velocity which often draws the clouds towards each other (see, e.g., simulation *w2o8* in Fig. 4.3 and simulation *w4o4_byb5* in Fig. 4.11).

However, the velocity evolution of a cloud is generally far more significant when

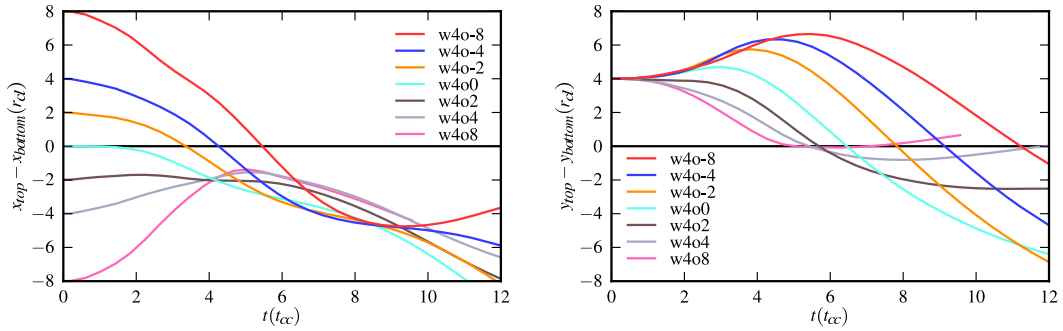

Figure 4.13: The evolution of the x and y separations of the clouds in two-cloud simulations with oblique magnetic fields. A sign change (i.e. movement across the horizontal black line) represents a switch in relative position.

the magnetic field is oblique. A clear and systematic distinction between the x velocity component of the 'top' and 'bottom' clouds can be seen in Fig. 4.12. The 'upstream' cloud accelerates first which is the 'top' cloud for positive 'offset' and the 'bottom' cloud if the 'offset' is negative. Initially, the x velocity in the 'bottom' cloud grows at a rate similar to the isolated cloud case (compare the dashed lines for simulations *w4o-8*, *w4o-4* and *w4o0* with the black crosses). The v_x velocity of each of these clouds overshoots slightly the post-shock flow value, as does the isolated cloud. In contrast, the acceleration of the 'top' cloud is notably slower after about 2.5 t_{cc} and in all simulations it reaches the post-shock flow value without any overshoot.

The right panel of Fig. 4.12 shows the evolution of the y velocity component of the clouds. In the single cloud case the cloud significantly overshoots the velocity of the postshock flow which has a normalized value $v_y \approx -0.25\,c_{s,0}$. The single cloud reaches its peak y velocity of $\approx -0.8\,c_{s,0}$ at $t \approx 7.5\,t_{cc}$, before decelerating. At late times we would expect the cloud v_y to asymptote towards that of the postshock flow but this clearly takes place on time-scales in excess of $12\,t_{cc}$. The y velocity

component of the clouds in the two-cloud simulations follows the same broad behaviour of initial acceleration, overshoot of the equilibrium value, and deceleration towards the postshock speed, but there are significant differences in the details. The 'top' cloud accelerates downward slowly initially, but significantly overshoots the isolated cloud case later on (unless the 'top' cloud is also the 'upstream' one (e.g., *w4o4*), in which case its behaviour is closer to the isolated cloud). In contrast the 'bottom' cloud initially accelerates faster than the isolated cloud, but starts slowing down much sooner (reaching a peak velocity of $\approx -0.65\, c_{s,0}$ at $t \approx 3\, t_{cc}$ for *w4o-4*). Simulation *w4o4* is again the exception - as the 'bottom' cloud is initially 'downstream' it is shielded from the flow and accelerates very slowly initially. Finally we note that some clouds (e.g., the 'bottom' cloud in simulation *w4o0*) undergo a second period of acceleration.

Overall, we find that the 'bottom' cloud moves faster in the 'x' direction and the 'top' cloud moves faster in the 'y' direction. Thus if initially the 'upstream' cloud is the 'bottom' one then the upstream cloud will overtake the downstream cloud. This is highlighted in the left panel of Fig. 4.13 where we see that the clouds swap relative positions (i.e. cross the horizontal black line) in simulations *w4o-8*, *w4o-4*, *w4o-2* and *w4o-1*. It is also observed in simulation *w2o-8* as shown in Fig. 4.6.

However, we also find that the 'top' and 'bottom' clouds swap their relative y positions in all of the simulations with 'width' $= 4\, r_{cl}$ that we have investigated. This is shown in the right panel of Fig. 4.13 where all the simulations cross the horizontal black line, irrespective of the initial 'offset'. We observe that a swap-over even occurs in simulations like *w4o-8*, where the 'bottom' cloud is the first to accelerate and the separation between the clouds actually grows until $6\, t_{cc}$ (in this case the swap-over occurs at $t > 10\, t_{cc}$). Fig. 4.6 shows the swap-over process occurring in

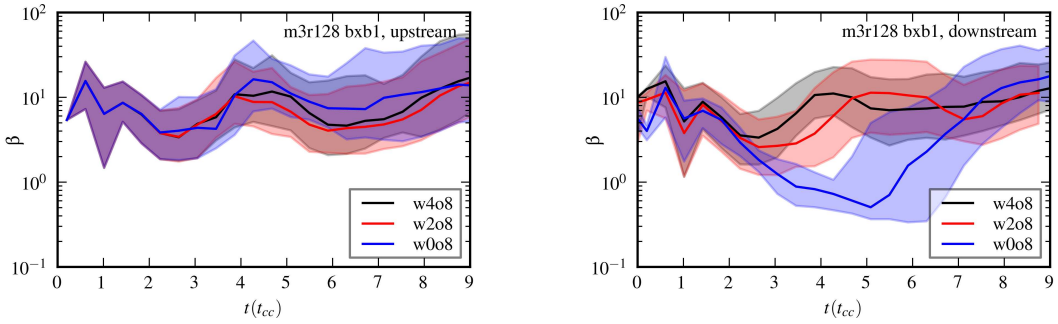

Figure 4.14: The time evolution of the β distributions for upstream (left panel) and downstream (right panel) clouds in R_{128} two-cloud simulations with parallel magnetic fields and preshock $\beta_0 = 1.13$. The initial cloud 'offset' is 8 while the initial cloud 'width' is varied. The solid line shows the median β value and the area between the 25th and 75th percentiles is shaded.

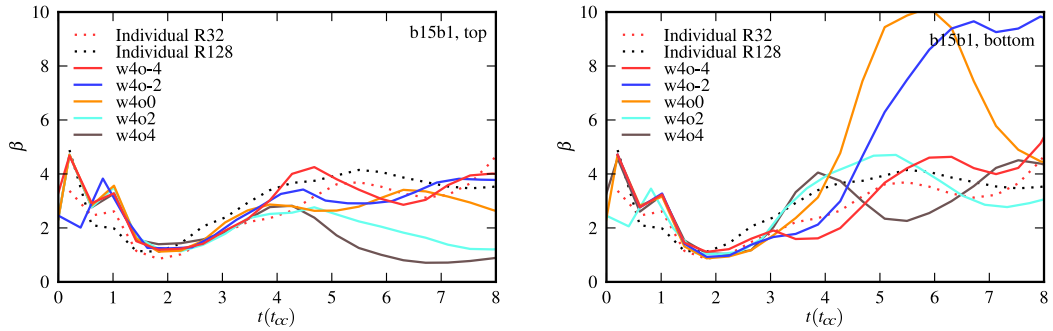

Figure 4.15: Evolution of the harmonic average of β in material from the 'top' cloud (left panel) and the 'bottom' cloud (right panel) in two-cloud simulations with an oblique magnetic field (where $\beta_0 = 1.13$ and $\theta_0 = 15°$). The initial cloud positions have a 'width' of $4\,r_{\rm cl}$ and varying 'offset'. The evolution of β in isolated clouds is also shown (for simulations with 32 (R_{32}) and 128 (R_{128}) cells per cloud radius).

simulation *w2o-8* at $t \approx 8\,t_{\rm cc}$ (here the 'bottom' cloud moves underneath and then behind the 'top' cloud).

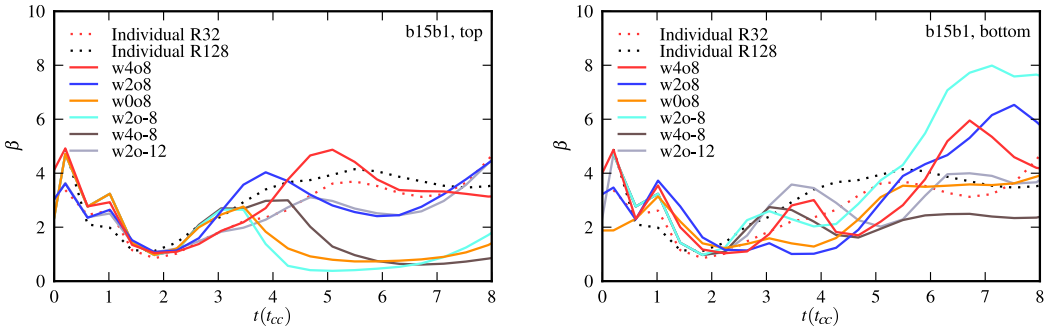

Figure 4.16: As Fig. 4.15 but for clouds in simulations with an initial 'offset' of $8\,r_{\rm cl}$ and varying 'width'. The upstream cloud is identified as the 'top' cloud in simulation *w0o8*.

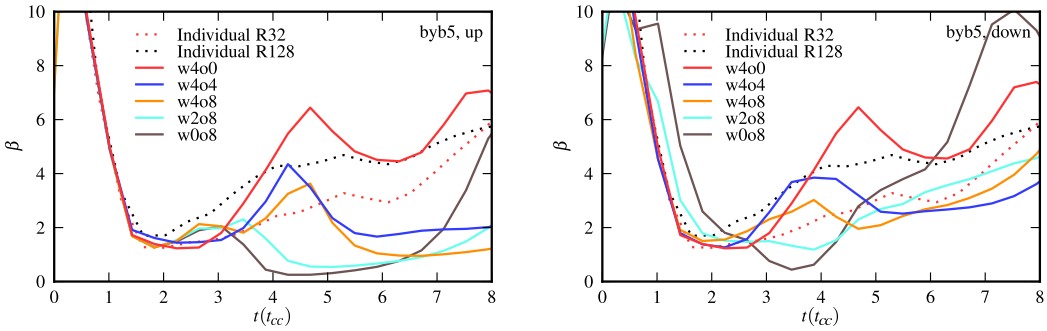

Figure 4.17: Evolution of the harmonic average of β in material from the upstream (left panel) and downstream (right panel) cloud in two-cloud simulations with a perpendicular magnetic field ($\beta_0 = 5.06$). The evolution of β in isolated clouds is also shown (for simulations with 32 (R_{32}) and 128 (R_{128}) cells per cloud radius).

4.3.2.5 The plasma β

Of the simulations performed, the parallel shock simulations with $\beta_0 = 1.13$ (i.e. models *bxb1*) have the highest post-shock β (~ 12, see Table 4.1). It is in these simulations that instabilities are least suppressed by the magnetic field. Simulations with single clouds reveal that the results are sensitive to resolution, with a convergence study indicating that of order 100 cells per cloud radius are needed for

accurate results (in keeping with previous work of adiabatic hydrodynamical shock-cloud interactions - see, e.g., Klein *et al.* 1994; Pittard *et al.* 2009). In contrast, the presence of additional clouds disturbs the flow such that longer wavelength instabilities play a more important role. This reduces the resolution requirements in multi-cloud simulations. However, in order to compare like-with-like, we perform the following analysis of β in the parallel shock simulations using resolution R_{128} for the multi-cloud simulations too.

We first study how the distribution of β in the simulations with a parallel shock changes as the initial positions of the clouds are varied. In each of the following figures we show the time evolution of the distribution of the plasma β of the cloud material (the distribution is calculated over all cells in the simulation behind the shock front but is weighted by the amount of cloud material in each cell). β changes with time as the cloud is first compressed, and then re-expands. At late times β should approach the value in the post-shock flow. This behaviour can be seen in Fig. 4.14.

We find that varying the initial cloud 'offset' has no real effect on the β distributions when the initial cloud 'width' is greater than the diameter of the clouds. In Fig. 4.14 we show how the evolution of β depends instead on the initial 'width' of the cloud distribution for simulations with $\beta_0 = 1.13$. We find that the upstream cloud is not affected in the *w2o8* simulation, but the growth of β is delayed by $1\,t_{\rm cc}$ in the downstream cloud (compare the red lines in the left and right panels of Fig. 4.14 between $3 \lesssim t/t_{\rm cc} \lesssim 5$). Note, though that this delay is not seen in the *bxb0.5* case where the magnetic field is more dominant.

In the *w0o8* case (see Fig. 4.2f), the downstream cloud falls inside the flux rope and β drops to ~ 0.5 in the downstream cloud until the clouds collide. The β

distribution of the upstream cloud is also affected in this case - β is generally slightly higher due to the increased pressure downstream. The same behaviour is seen if the magnetic field is made slightly stronger. For example, in simulations with $\beta_0 = 0.55$ (models *bxb0.5*) the minimum β is still around 0.5 in the downstream cloud, while the increase of the plasma β in the upstream cloud is even more prominent.

We find that simulations with an oblique magnetic field are much less sensitive to resolution, and we are able to use simulations with a resolution of 32 cells per cloud radius. We adopt the harmonic mean as the average for the β statistics in these simulations: it demonstrates good convergence because it is not influenced by a small number of cells with high β where the flow is poorly resolved. The harmonic mean is thus a good estimator for the 'typical' β value of cloud material, and it generally falls in between the 30^{th} and 50^{th} percentile values.

Figs. 4.15 and 4.16 show the evolution of the harmonic mean of β in material from the 'top' and 'bottom' clouds of various simulations. The 'top' cloud is the upstream one if the 'offset' is positive, and is the 'upfield' cloud in all simulations except *w2o-12* and *w2o-8*. These figures also show the variation of β in simulations with a single individual cloud. In Fig. 4.15 we see the effect of varying the 'offset' value of the initial cloud distribution while keeping the initial distribution 'width' fixed at a value of $4\,r_{\rm cl}$. In contrast, in Fig. 4.16 the initial distribution 'width' is varied while the 'offset' is kept at 8 or $12 r_{\rm cl}$.

These figures reveal that β is significantly reduced in the 'top' cloud when it is the upstream one (see models *w4o2* and *w4o4* in Fig. 4.15, and models *w4o-8*, *w2o-8* and *w0o8* in Fig. 4.16). In model *w2o-8* we see that $\beta < 1$ during the period $4 \lesssim t/t_{\rm cc} \lesssim 7$; Fig. 4.5 shows that the clouds collide at this time. In fact, the collision of the clouds is responsible for the low β values in the material of the top

cloud in all of these simulations, and also in simulation *w0o8* (where low β values occur in the upstream cloud). In contrast, we find that β in material in the 'bottom' cloud is similar to that in the isolated cloud or slightly higher.

When the 'top' cloud is the 'downstream' one, the harmonic mean of β in both of the clouds evolves similarly to the evolution of β in an isolated cloud. Exceptions to this behaviour occur only for the bottom cloud in simulations *w4o-2* and *w4o0* (see the right panel of Fig. 4.15) and simulation *w2o-8* (see the right panel of Fig. 4.16); in these cases the 'bottom' cloud reaches much higher β values. The reason for this difference is evident from Fig. 4.6, which reveals that in simulation *w2o-8* the 'bottom' cloud overtakes the 'top' cloud and becomes the 'downstream' cloud at the time when β starts growing. The same behaviour also occurs in the other two cases. For example, in simulation *w4o0* the bottom cloud crosses a line perpendicular to the upstream field lines passing through the 'top' cloud at this time. Finally, we note that although the clouds also pass each other in *w4o-4*, this happens at a later time and greater separation with the result that β does not grow as much in the bottom cloud.

Finally we study the evolution of β in simulations with a perpendicular magnetic field. The β in the post-shock flow of models *byb5* is 6.05. Since this is the same as in models *b15b1*, β in the shocked clouds varies in the range of 4–7 for the majority of cloud arrangements in simulations with these field values.

The 'upstream' clouds in simulations *byb5* correspond to 'upstream'-'top' clouds in the oblique simulations *b15b1* and thus all such clouds have reduced β values (see models *w4o4*, *w4o8*, *w2o8* and *w0o8* in the left panel of Fig. 4.17). We also find again that β in the downstream clouds evolves similarly to that in isolated clouds, and that only clouds that are shielded from the flow (such as the down-

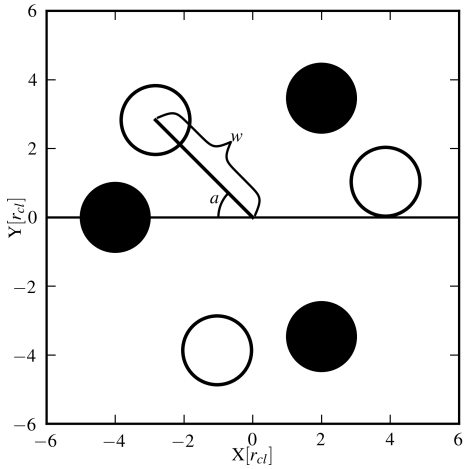

Figure 4.18: Illustrations of the cloud positions in three-cloud simulations. Two particular arrangements are shown: *s3w4a0* (with the clouds indicated by the filled circles) and *s3w4a45* (with the clouds indicated by the open circles).

stream clouds in simulations *w2o8* and *w0o8*) go through a phase of significantly reduced β (occurring at $t \approx 3$–$4\,t_{\rm cc}$ in these cases). Because the clouds in simulation *w4o0* are on the same field line, β increases as they mix. An increase in β is also seen in the downstream cloud of *w0o8* but further examination indicates that it is principally due to mixing from numerical diffusion as this behaviour is not seen at higher resolution. Other higher resolution results track the lower resolution results almost exactly.

4.3.3 Three-cloud interactions

We now investigate the MHD interaction of a shock with three closely spaced clouds which are arranged to form the vertices of an equilateral triangle (see Fig. 4.18). The centroid of the triangle is located at the origin of the computational grid and the exact arrangement is defined by the angle between the vector to the most upstream cloud and the (negative) x-axis and the length of this vector (so distribution

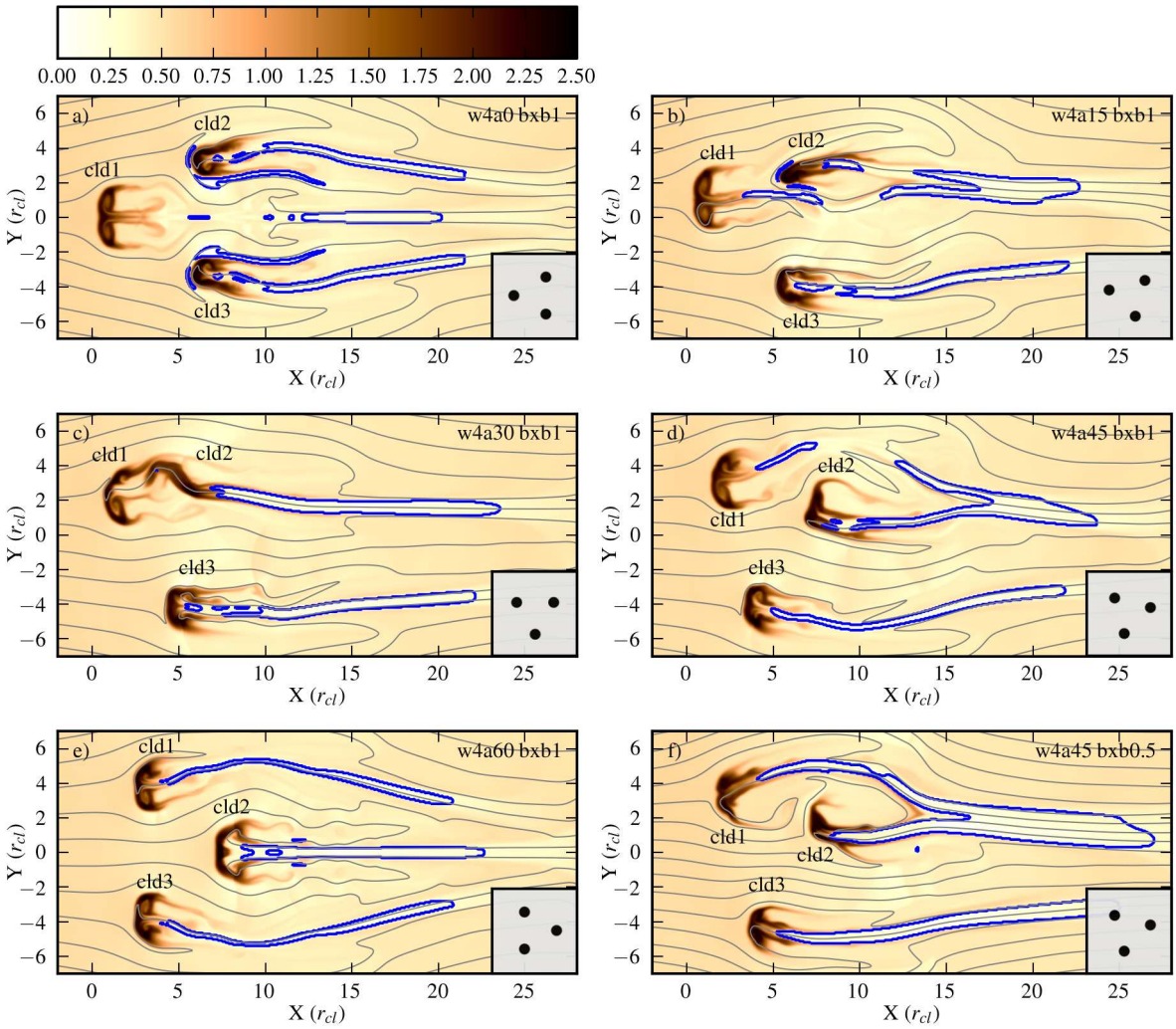

Figure 4.19: Snapshots at $t = 4\,t_{cc}$ of various three-cloud simulations with parallel magnetic fields ($\beta_0 = 1.13$, except in panel f where $\beta_0 = 0.55$). Individual clouds are labelled and the insert shows the initial cloud arrangement in each case. Only the orientation of the cloud arrangement is changed in these cases.

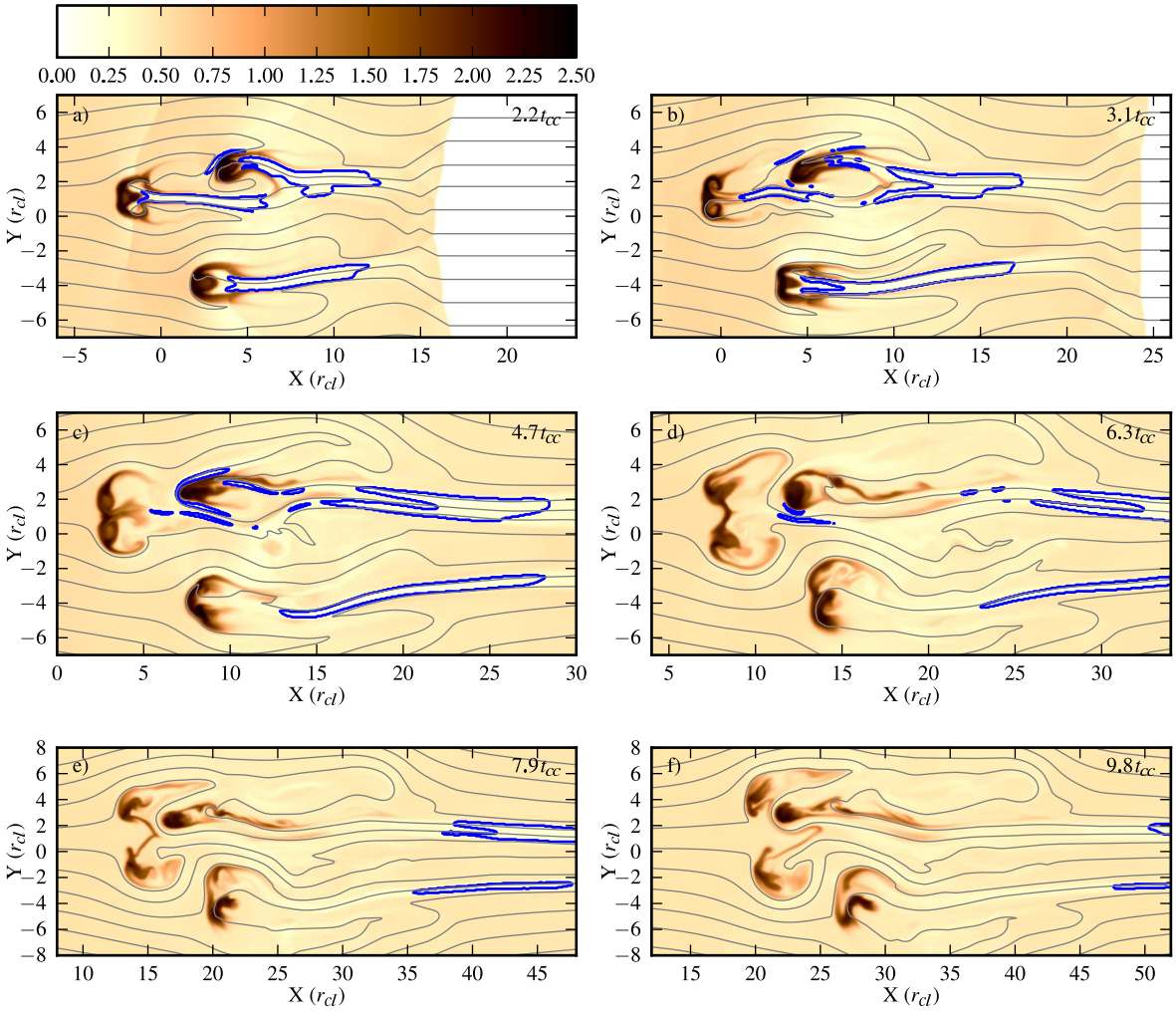

Figure 4.20: The time evolution of the three-cloud simulation *s3w4a15* with a parallel magnetic field ($\beta_0 = 1.13$). The logarithmic density and magnetic field evolution are shown at times $t = 2.2$, 3.1, 4.7, 6.3, 7.9 and 9.8 t_{cc}. The contour shows the 'flux rope' ($\beta < 1$ and $\rho|\mathbf{u}| < 0.5 \times \rho|\mathbf{u}|_{ps}$).

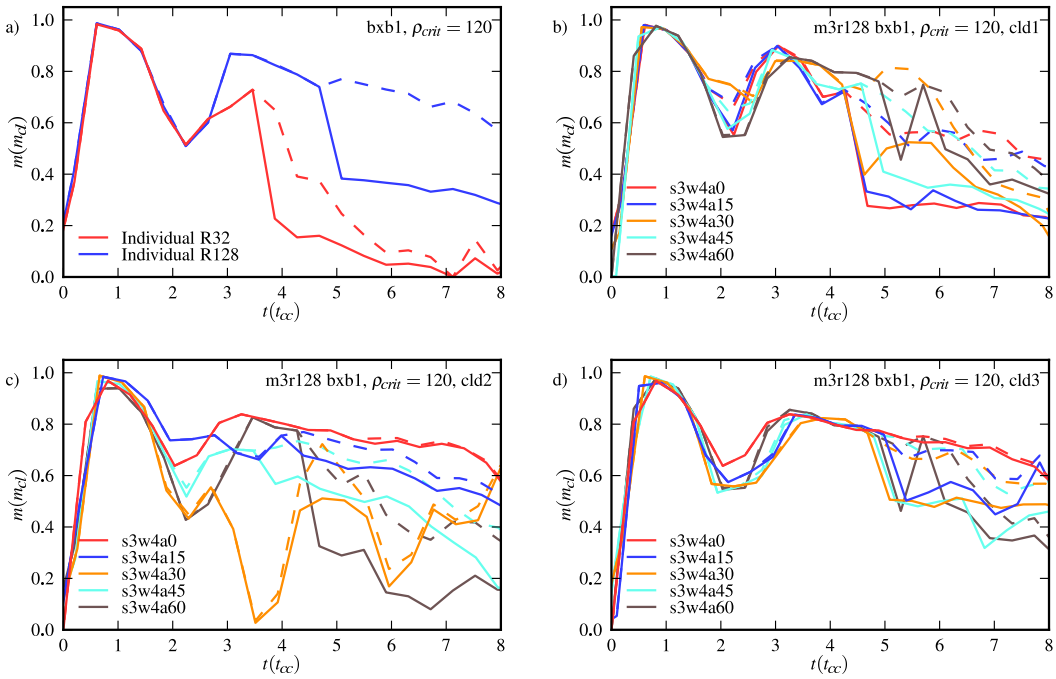

Figure 4.21: Evolution of the core mass (m, see text) for (a) single cloud simulations at two different resolutions, and for (b) cld1, (c) cld2 and (d) cld3 in high resolution three-cloud simulations. In each case the solid line represents the main fragment and the dashed line shows the sum of all fragments. The $t = 0$ time for each cloud starts when the shock first reaches the cloud.

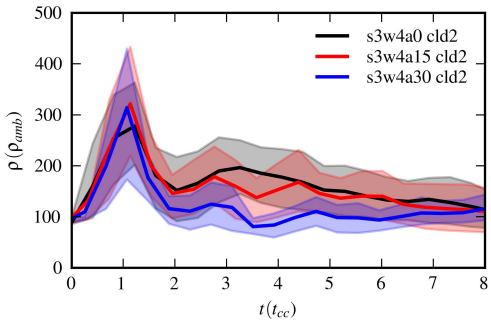

Figure 4.22: Evolution of the density (ρ) in cld2 in some of the three-cloud simulations. The average density within cld2 is shown by the solid line and the region between the 25th and 75th percentiles is shaded.

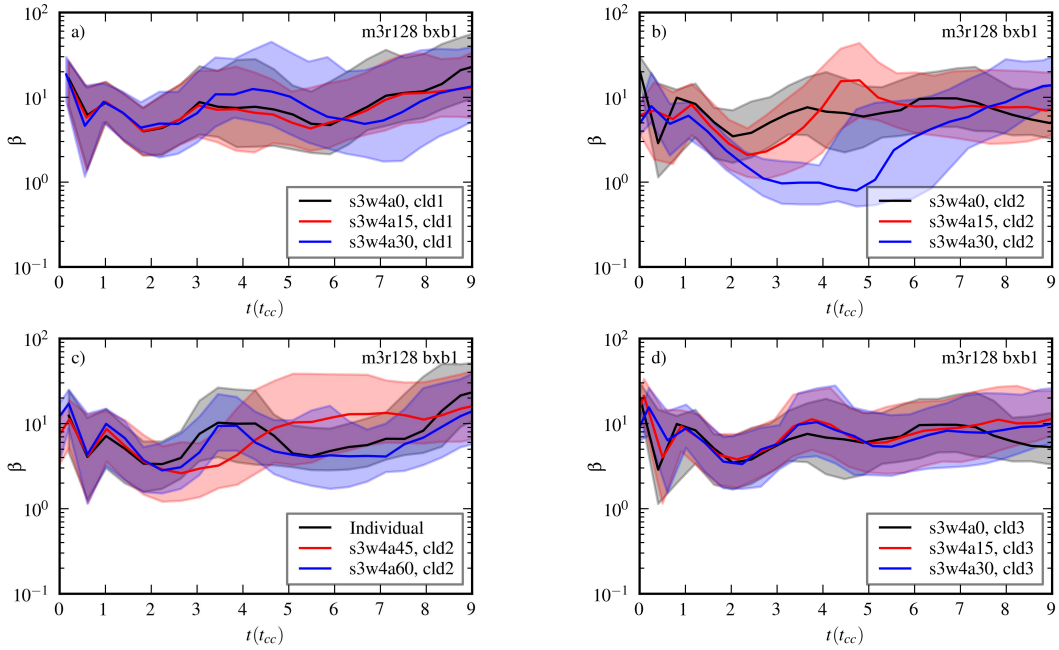

Figure 4.23: The time evolution of the β distributions for different clouds in high resolution (R_{128}) three-cloud simulations with parallel magnetic fields and a preshock $\beta = 1.13$. The solid line shows the median value and the area between the 25th and 75th percentiles is shaded.

w4a30 has the most upstream cloud located at $(x, y) = (-4\cos 30°, 4\sin 30°) = (-3.46, 2)$). The most upstream cloud is referred to as 'cld1'. The next cloud clockwise, referred to as 'cld2', will be the one that is behind (directly or with some lateral offset) 'cld1'. The final cloud, 'cld3', is then located off to the side.

A compact, *w4* arrangement gives a side length of $l = \sqrt{3} \times 4 = 6.93\, r_{\rm cl}$ for the equilateral triangle. If considered as part of a hexagonal lattice this distribution would give a mass ratio (the ratio of mass in the clouds to the intercloud mass) MR = 9.07. A slightly wider *w8* arrangement (not considered in this work) gives $l = \sqrt{3} \times 8 = 13.86\, r_{\rm cl}$ and MR = 2.12. The mass ratio can be increased by reducing w and by increasing the cloud density contrast, χ.

We now investigate the nature of the interaction with parallel, oblique and perpendicular shocks in turn.

4.3.3.1 Parallel shocks

The interaction of a shock with three-clouds can be thought of as being similar to a two-cloud scenario, but with the addition of a 'modifier' cloud. Fig. 4.19 shows the nature of the interaction for a relatively compact arrangement of clouds. When clouds are placed further apart the morphology of the interaction increasingly resembles either *w4a0* or *w4a60*, except when the orientation is such that the clouds line up.

As with the previous two-cloud simulations, the nature of the three-cloud interaction depends on the relative positioning of the clouds. In Fig. 4.19a), we see that the 'flux rope' from cld1 passes in between the two downstream clouds and completely detaches. In addition, an interesting low-β, low-momentum region forms near the inside 'wing' of the downstream clouds. Rotating the cloud distribution to break the lateral symmetry we observe that the 'flux ropes' of two of the clouds may merge (as seen in simulations *w4a15* and *w4a45* in Fig. 4.19b) and d). The merging of flux ropes was previously seen in the two-cloud simulation *w2o8* shown in Fig. 4.2e). The location of the third cloud influences the sections of 'flux rope' associated with individual clouds but the merged part looks the same. Finally, when cld2 falls directly into the 'flux rope' of cld1 (as seen in simulation *w4a30* in Fig. 4.19c), the resulting 'flux rope' appears very similar to that in the two-cloud simulation *w0o8* shown in Fig. 4.2f), but the morphology of cld2 is significantly changed by the presence of the third cloud.

The time evolution of simulation *w4a15* is shown in Fig. 4.20. In this simulation

the strongest interaction occurs between those clouds with the smallest difference in their lateral positions (cld1 and cld2 in this case). Compared to cld2, cld3 is able to retain a broadly symmetric structure for longer, with the only significant deviations by $t = 3\,t_{\rm cc}$ being to its tail. After this time, cld3 becomes increasingly asymmetric in appearance. At $t = 6\,t_{\rm cc}$, cld2 has a circular core and a tail of stripped material extending from its outside edge. Such a tail only occurs when a downstream cloud is in the 'wings' of an upstream cloud.

To better understand the nature of the interactions between clouds in the three-cloud simulations we now look at the evolution of the mass of the core region of each cloud and each cloud's density. We define cloud cores as circular regions with an average density $\langle\rho\rangle > \rho_{\rm crit} = 120\rho_{\rm amb}$ (i.e. a 20% increase on the initial cloud density). *Note that this definition differs from the one used in Chapter 3*. A different definition is required here as the diffusion is suppressed and in cells where the cloud material is present, it is always concentrated enough to dominate those cells. Fig. 4.21 shows the evolution of the core mass in single-cloud simulations and in the three-cloud simulations shown in Fig. 4.19. The core mass rises rapidly as each cloud is compressed and abruptly plateaus once 100% of the cloud material is above the density threshold. This takes roughly one cloud-crushing time-scale by definition. Subsequent re-expansion of each cloud causes the core mass to decrease (in the single cloud case the core mass decreases to $\approx 0.5\,m_{\rm cl}$ by $t \approx 2\,t_{\rm cc}$). In many cases the subsequent behaviour is oscillatory as the cloud cycles through phases of expansion and contraction, though a steady decline in the core mass is the dominant trend as material from the cloud mixes in with the ambient flow (ultimately the cloud density becomes equal to the post-shock density).

In many simulations the cloud fragments into multiple cores. When this hap-

pens the mass of the largest fragment is shown by the solid lines in Fig. 4.21 while the sum of the mass of all fragments is shown by the dashed lines. Any overlapping cores are merged into a single fragment. We find that this analysis is dependent on the resolution adopted in the simulations. As shown in Fig. 4.21a, a lower resolution simulation diverges from a higher resolution simulation at $t \approx 3\,t_{\rm cc}$. Therefore we only consider high resolution runs in this analysis (differences due to the resolution can be delayed by choosing a lower density threshold, $\rho_{\rm crit}$). In the high resolution single cloud case, the core splits into two fragments at $t \approx 5\,t_{\rm cc}$.

Since cld1 is not downstream of any other cloud, it evolves similarly to an isolated cloud and fragments at $t \approx 4.5\,t_{\rm cc}$ (see Fig. 4.21b). Fragmentation of cld1 is slightly suppressed in simulation *w4a60* because of the presence of the other clouds alongside. However, subsequent oscillations in the core mass of cld1 due to expansion and contraction of the cloud appear to be much weaker compared to the single cloud case, indicating that the presence of the other clouds is again being felt. At $t = 9\,t_{\rm cc}$, $\sim$0.4 $m_{\rm cl}$ remains in the combined fragments of cld1. The exception to this is simulation *w4a30*, where the interaction of cld1 with cld2 pushes the average density of cld1 down to $70\,\rho_{\rm amb}$ (i.e. below the density threshold for identification of material as 'core'). The average density of cld1 in the other simulations is $\approx$90 $\rho_{\rm amb}$ at this time, and for simulations with an isolated cloud it is $\approx$100 $\rho_{\rm amb}$.

Various types of interaction show up in the behaviour of the core mass of 'cld2'. Simulations *w4a0* and *w4a15* are noticeable for the large mass fraction which remains in the core and the lack of significant fragmentation. In both these simulations cld2 is on the 'outside' edge of the distribution, and the average density of cld2 is similar to that of the single-cloud case. In contrast, the average density of cld2 is lower (and thus there is less mass above threshold) in simulations *w4a45*

and *w4a60*. The cores also fragment in these cases. In these simulations cld2 is notable for being in the 'middle' of the cloud distributions. Fig. 4.19 shows that when cld2 is 'outside' it is longer and narrower, whereas when it is in the 'middle', it is wider and shorter.

Fig. 4.21 shows that the average core mass of cld3 at late times is similar to or slightly higher than that of an isolated cloud (note that the symmetry of simulation *w4a60* means that cld3 behaves identically to cld1, while the symmetry of simulation *w4a0* means that cld3 is identical to cld2). Very little fragmentation is seen in cld3 in any of the simulations, and in particular in simulation *w4a0* where cld2 is directly alongside it. In general the further downstream cld3 is, the more mass is contained in the core, though this variation is quite small and is somewhat time dependent.

Fig. 4.22 shows the evolution of the density in cld2 in three of the three-cloud simulations. We see that as various shocks pass through cld2 (the transmitted shock is the main one, but shocks also propagate inwards from the sides and back of the cloud), the average density increases by a factor of ∼3–4. Re-expansion starts after $t \approx 1\,t_{\rm cc}$ and the density drops reaching a local minimum at $t \approx 2\,t_{\rm cc}$. The density then increases slightly due to compression from the ram pressure of the flow as the cloud is accelerated downstream. The density steadily decreases from $t \approx 3\,t_{\rm cc}$ as the acceleration subsides and as material is stripped away. In simulation *s3w4a30*, cld2 lies in the 'flux rope' of cld1 and is largely shielded from the flow. As a consequence it does not experience a period of re-compression at $t \approx 3\,t_{\rm cc}$, but neither does it experience strong stripping by the flow. At $t \approx 4\,t_{\rm cc}$, cld1 collides with cld2 and the density of cld2 steadily increases up to $t = 9\,t_{\rm cc}$.

Fig. 4.23 shows that the evolution of β in the material of cld1 and cld3 is largely

independent of the cloud arrangement. However, this is not the case for cld2, where clear differences can be seen between simulations in panels b and c of Fig. 4.23. However, this is hardly surprising, since cld2 is variously located in the 'flux rope' of cld1 in simulation *w4a30*, in the 'wings' of cld1 in simulations *w4a15* and *w4a45*, in the 'outside' flow in simulation *w4a0*, and in the 'inside' flow in simulation *w4a60*. The presence of a third cloud appears to modify the behaviour seen in Fig. 4.14 - specifically β is higher when cld2 is between cld1 and cld3 (as in simulations *w4a45* and *w4a60*).

4.3.3.2 Oblique shocks

We now study the interaction of three-cloud distributions with an oblique shock ($\theta_0 = 15°$). Fig. 4.24 shows the resulting morphology at $t = 4\,t_{cc}$. An additional simulation with a negative orientation angle is also included (simulation *w4a-30*). In the *w4a-30* and *w4a0* simulations, the modifier cloud is cld2[1], but otherwise it is cld3. A two-stage process occurs: first, cld1 interacts (as in the two-cloud case) with the nearest cloud along the flow, then these clouds jointly interact with the third cloud. For instance, simulation *w4a-30* in Fig. 4.24a can be deconstructed as cld1 and cld3 interacting as in simulation *w0o8* in Fig. 4.5, and then the resulting combined 'clump' interacting with cld2 as in simulation *w4o-4* in Fig. 4.4. Similarly, simulation *w4a60* in Fig. 4.24f shows cld1 and cld2 interacting as in simulation *w4o4*, and then together interacting with cld3 as in simulation *w4o0* (compare Fig. 4.24f with Fig. 4.4b and c). The secondary interaction can also be categorized in terms of a 'width' and an 'offset'. In the three-cloud simulations studied, it appears that the appropriate width is the average 'width' between the combined clump

[1]From geometrical arguments we expect the switch to happen at an angle $a \approx 5°$.

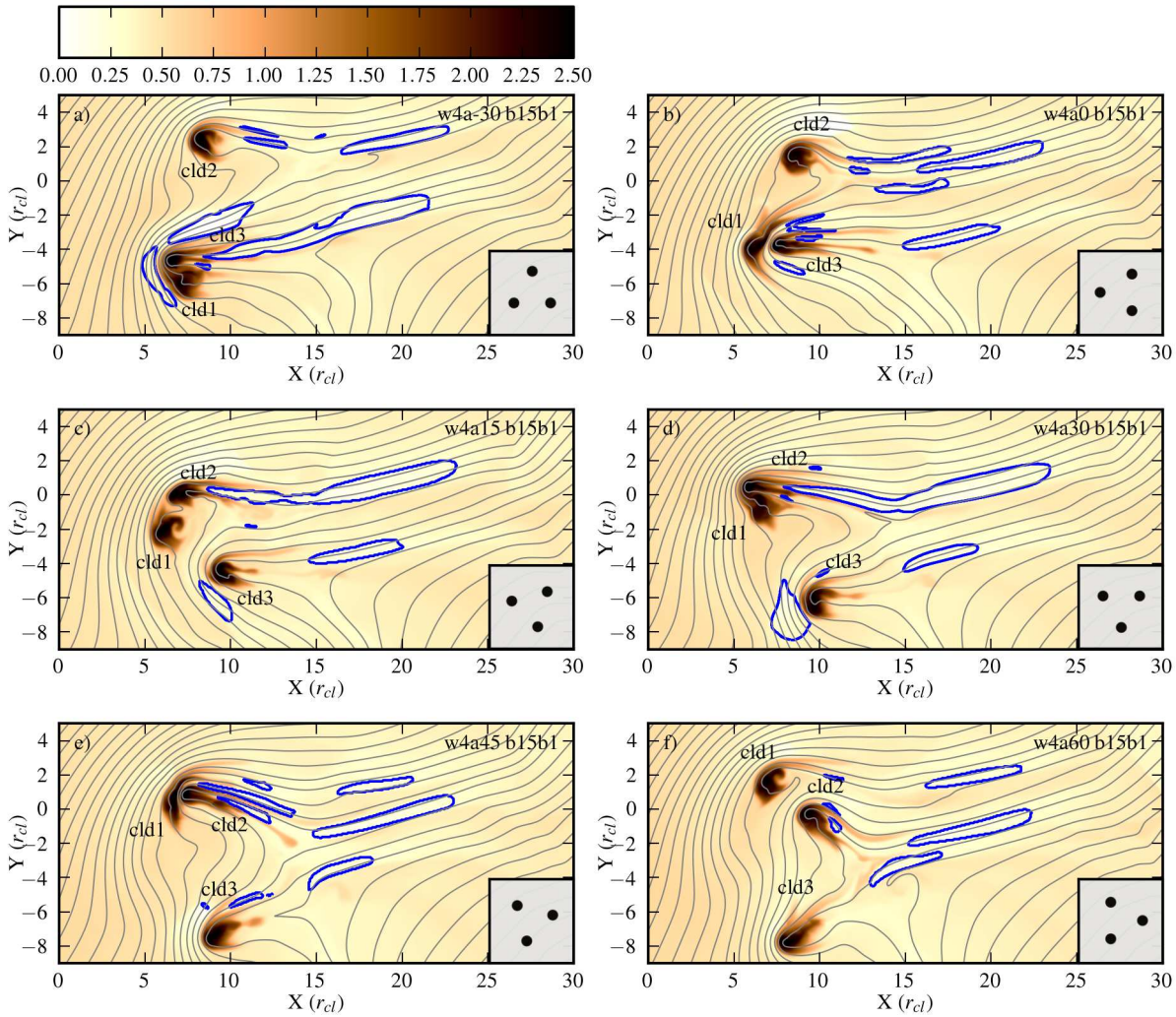

Figure 4.24: As Fig. 4.19 but for an oblique shock ($\theta_0 = 15°$, $\beta_0 = 1.13$). All snapshots are at $t = 4\,t_{cc}$.

and the third cloud, while the appropriate offset is between the more upstream of the two clouds interacting in the first stage and the third cloud with which they interact in the second stage[1]. Note that the secondary interaction has a greater effective 'width' than the two-cloud cases considered in Sec. 4.3.2. This means that the separation at closest approach is greater and that a secondary collision between

[1]So it is possible to make a priori estimates of these values.

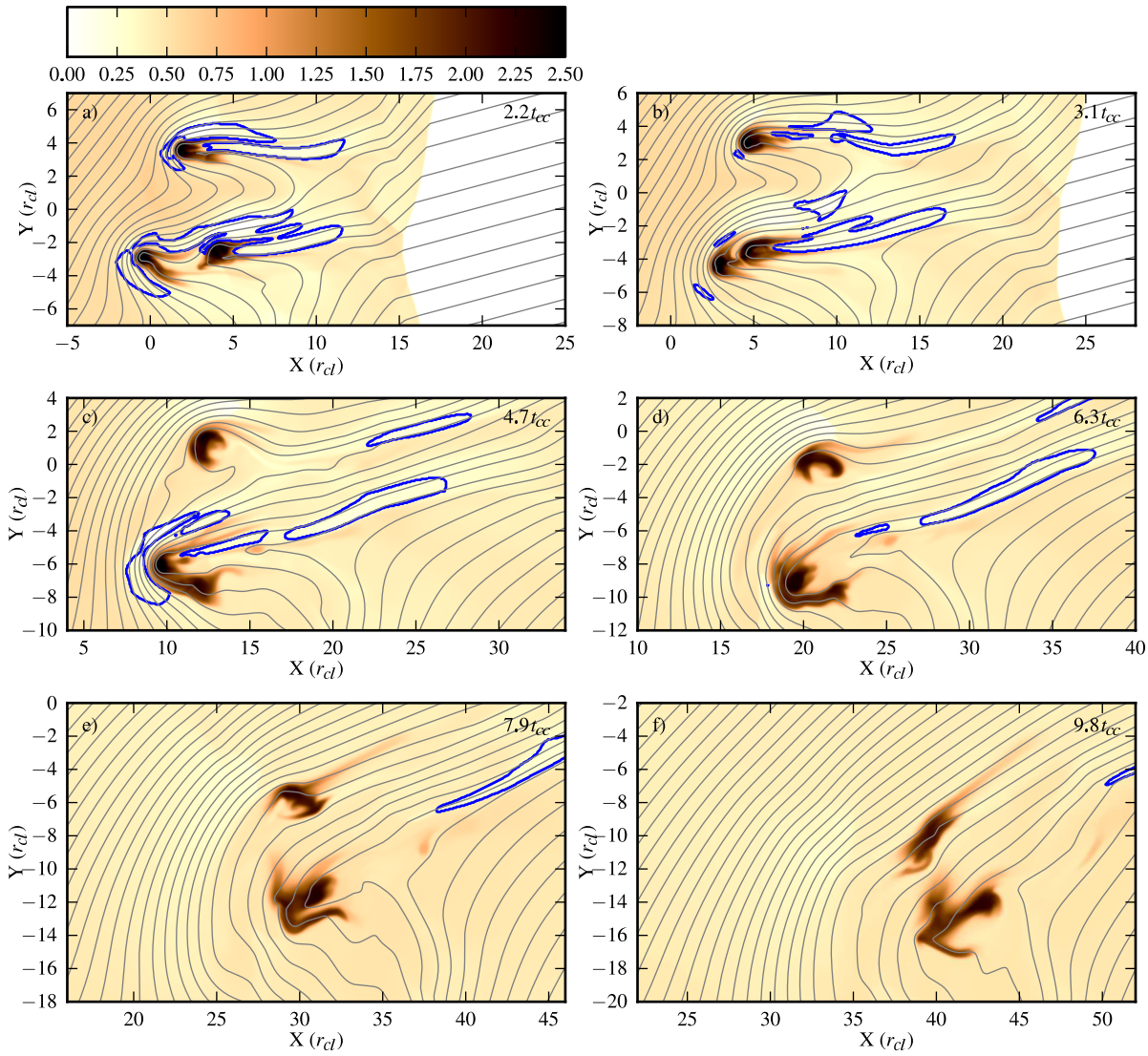

Figure 4.25: The time evolution of an oblique shock ($\theta_0 = 15°$, $\beta_0 = 1.13$) interacting with three-clouds (simulation *s3w4a-30*, $a = -30°$).

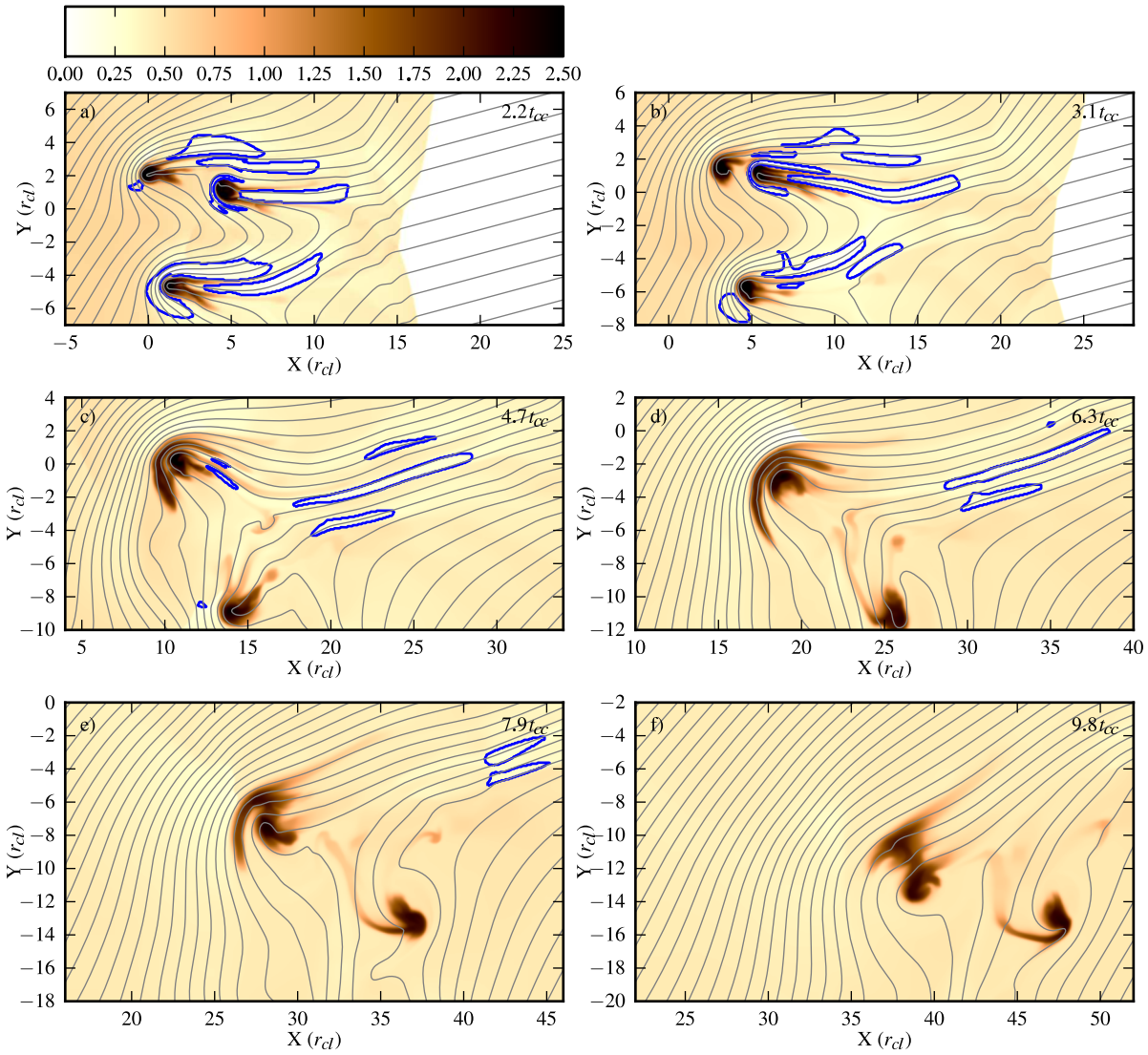

Figure 4.26: As Fig. 4.25 but for simulation *s3w4a45* ($\theta_0 = 15°$, $\beta_0 = 1.13$, $a = 45°$).

the combined clump and the third cloud does not occur. However, otherwise the morphologies are roughly equivalent.

Fig. 4.25 shows the time evolution of simulation *s3w4a-30* while Fig. 4.26 shows the time evolution of simulation *s3w4a45*. In simulation *s3w4a-30*, cld1 is initially at the bottom-left of the distribution, cld2 is at the top-right, and cld3 is at the

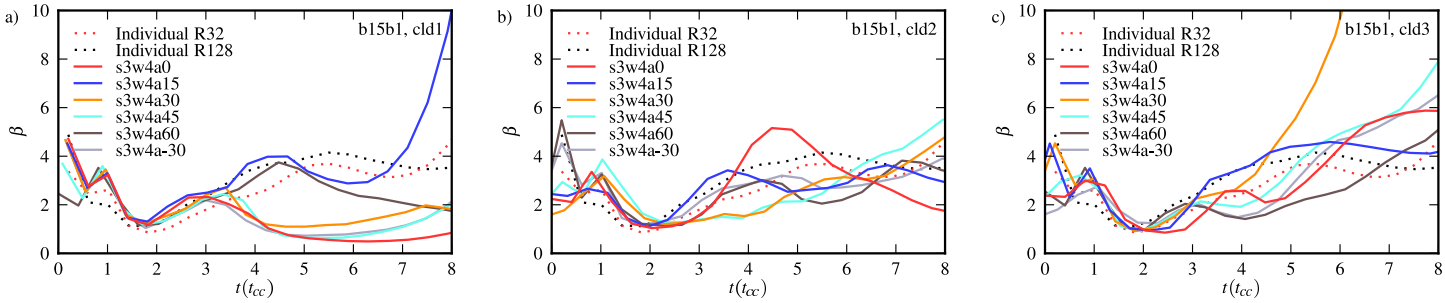

Figure 4.27: The evolution of the harmonic mean of β for three-cloud simulations with an oblique magnetic field. The left, middle and right panels show β for cld1, cld2 and cld3, respectively. The time axis is shifted appropriately for each cloud. The evolution of β in isolated clouds is also shown [for simulations with 32 (R_{32}) and 128 (R_{128}) cells per cloud radius].

bottom right (see also Fig. 4.24a). As the shock sweeps over, cld1 moves towards cld3 which is in the lee of cld1. cld1 engulfs cld3 by $t \sim 4\,t_{cc}$, and cld3 is then confined by the magnetic field threaded through cld1. In contrast, cld2 evolves in a relatively isolated way. The flow tries to force its way between cld1/3 and cld2, but the field lines between these two regions prevent this. In contrast, in simulation *s3w4a45* cld1 is initially at the top left of the distribution, cld2 is the most downstream cloud, and cld3 is at the bottom left (see also Fig. 4.24e). Fig. 4.26 shows that cld1 and cld2 interact first, and that cld1 engulfs cld2. Although cld3 is initially upstream of cld2, cld3 lies downfield. Thus as the interaction proceeds, the tension in the field lines created by the flow causes cld3 to accelerate downstream faster than the other clouds.

In the oblique field case cld1 often has very low β at late times (see Fig. 4.27). Low β's at late times were previously seen in the top cloud of the two-cloud simulations in Sec. 4.3.2 (see simulations *w4o-8*, *w2o-8* and *w0o8* in Fig. 4.16). In each case this is caused by the collision of the cloud with a cloud further down-

stream. Fig. 4.24 reveals that in the two cases where β stays higher (simulations *w4a15* and *w4a60*), cld1 has not collided with another cloud by $t = 4\,t_{\rm cc}$. In simulation *w4a15*, Fig. 4.24 shows cld1 about to squeeze between the two other clouds. cld1 proceeds to move into the 'shadow' of cld2, and β in cld1 rapidly grows after $t = 6.5\,t_{\rm cc}$. In simulation *w4a60*, cld1 and cld2 accelerate at a similar rate and do not collide (Fig. 4.24 shows these clouds still with significant separation at $t = 4\,t_{\rm cc}$). However, after $t = 4.5\,t_{\rm cc}$, as these clouds get close, β decreases in cld1.

The evolution of β in the other two clouds does not deviate much from the single-cloud case (see the middle and right panels of Fig. 4.27). The only noteworthy behaviour is that cld2 generally has a slightly lower β, while cld3 has a slightly higher β, at late times. β in cld2 is most different from the single-cloud case for simulation *w4a0* (β becomes very low by $t \gtrsim 7\,t_{\rm cc}$), while β in cld3 is most different in simulation *w4a30* (β becomes very large at $t \gtrsim 5\,t_{\rm cc}$).

4.3.3.3 Perpendicular shocks

In this section we study the interaction of a perpendicular shock with 3 closely spaced cylindrical clouds. Fig. 4.28 illustrates the range of morphologies which exist at $t = 4\,t_{\rm cc}$ from a variety of simulations. It reveals that collisions are common. The collisions increase the density of the downstream cloud of the pair and in some cases can last up to $t \sim 10\,t_{\rm cc}$ (cf. Fig. 4.29). In all cases the magnetic field in the oncoming flow is unable to pass between the clouds. It instead piles up at the upstream side and the field lines then bend around the clumpy region. Clouds either side of the centre of the region then behave like the 'top' cloud in the two-cloud oblique simulations (cf. Sec. 4.3.2.2).

Fig. 4.29 shows the time evolution of simulation *s3w4a15*. cld1 is initially accel-

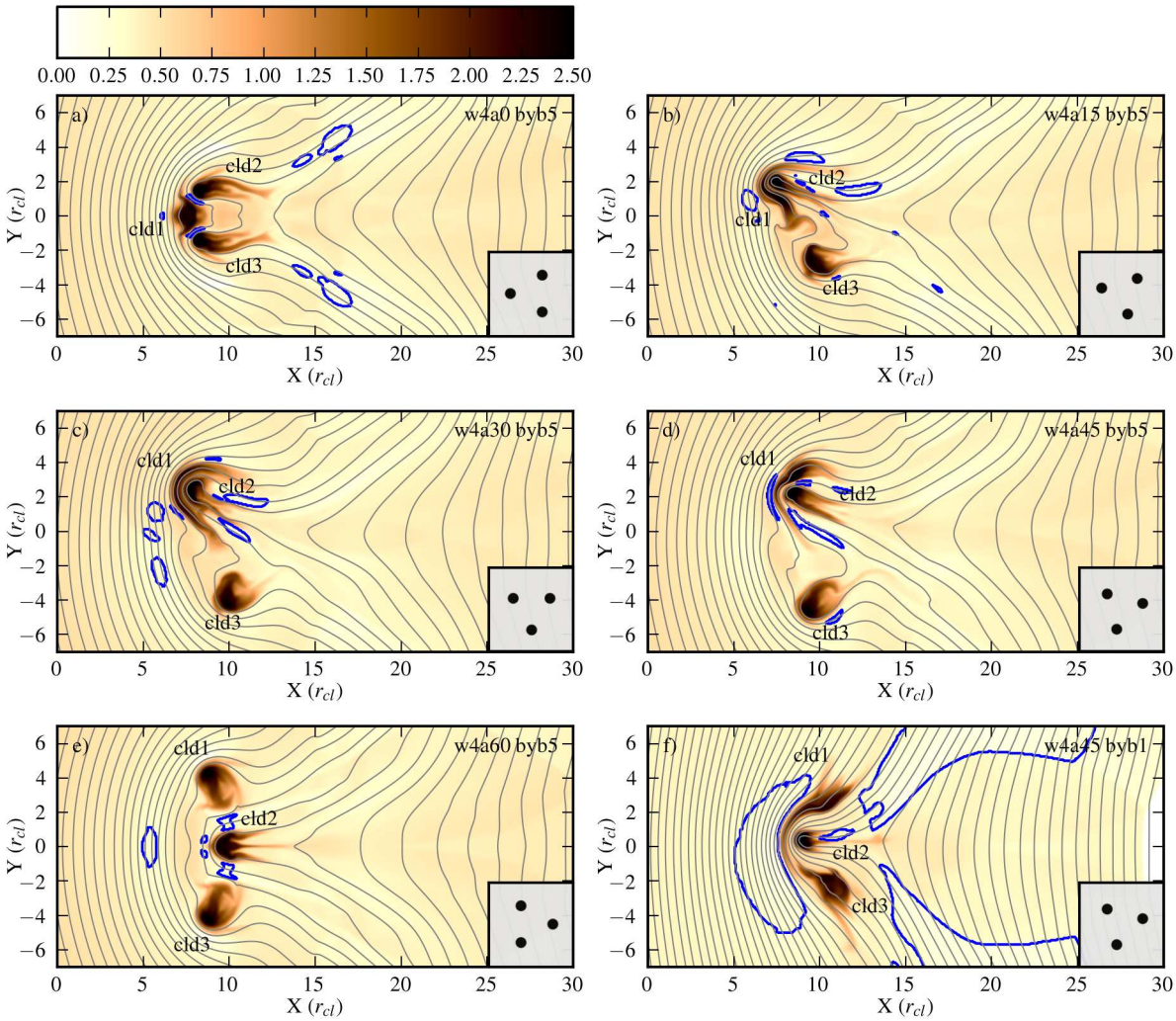

Figure 4.28: As Fig. 4.19 but for a perpendicular shock ($\beta_0 = 5.06$ except in panel f where $\beta_0 = 1.13$). All snapshots are at $t = 4\,t_{cc}$.

erated towards cld2 and cld3, and at $t = 4.6\,t_{cc}$ it appears to be poised to squeeze between them. However, the snapshot at $t = 6.3\,t_{cc}$ reveals that this does not happen. Instead, the field line that cld1 sits on is not able to force its way between cld2 and cld3, and cld1 ends up spreading along it while the field line instead wraps around cld2 and cld3. At the same time, cld2 and cld3 are forced together and mostly merge (they are on similar field lines). The level of mixing depends on the

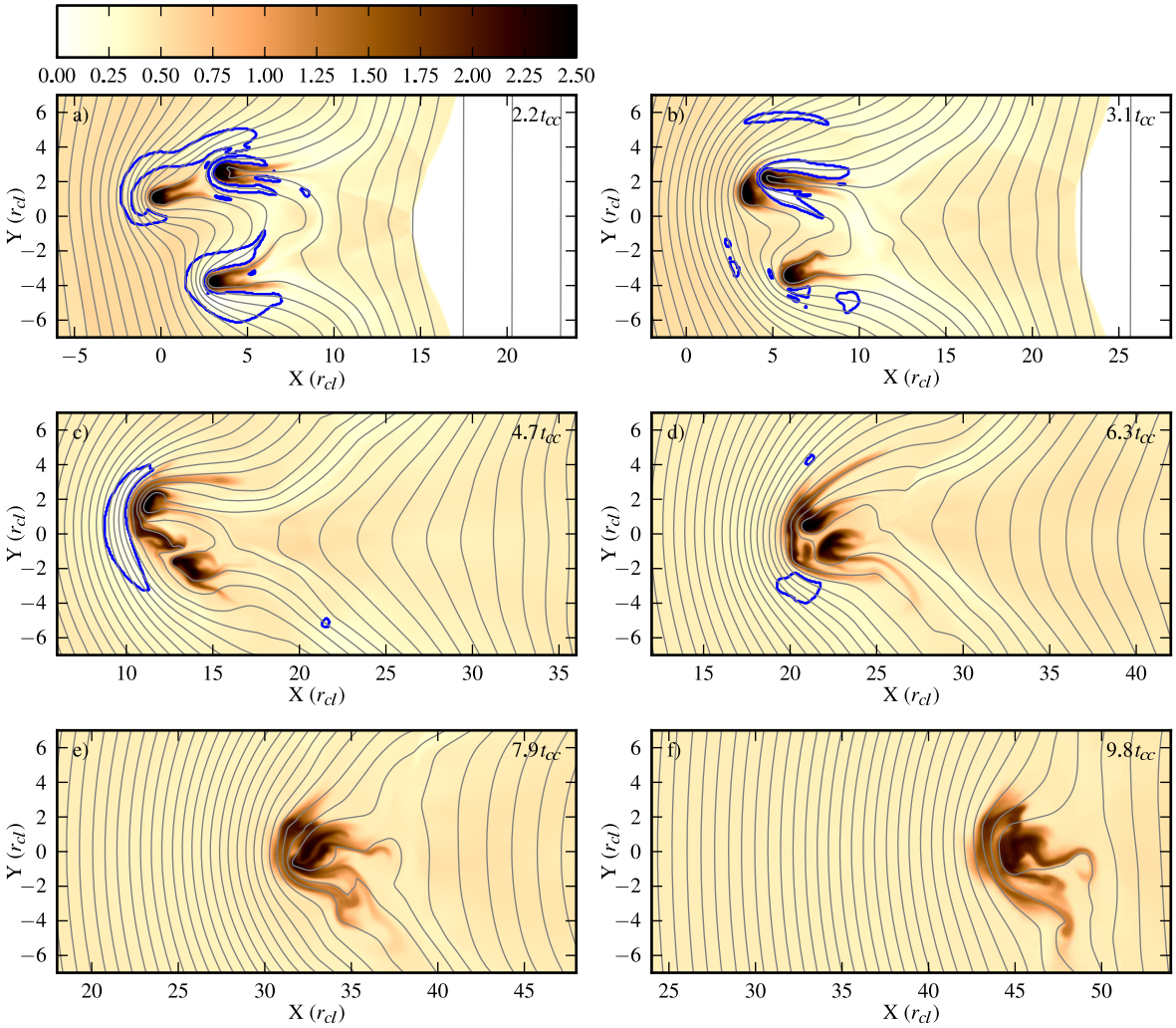

Figure 4.29: The time evolution of a perpendicular shock interacting with three clouds with $\beta_0 = 5.06$ (simulation *s3w4a15*).

field strength and the degree of diffusion of material across the field lines. The field lines straighten out at later times as the clouds are accelerated up to the flow speed of the post-shock gas. It is clear that the overall 'x'-size of the clumpy region is reduced by the field compression in this direction, while the 'y'-size is reduced by the diffusion of clouds along the field lines.

Fig. 4.30 shows the evolution of β in the material of cld1, cld2, and cld3 in

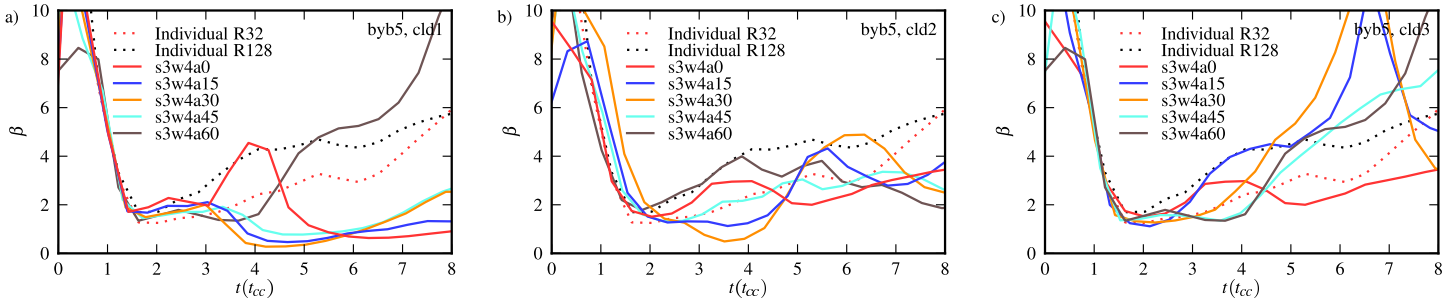

Figure 4.30: The evolution of the harmonic mean of β for three-cloud simulations with a perpendicular magnetic field. Panels (a), (b) and (c) show β for cld1, cld2 and cld3, respectively. The time axis is shifted appropriately for each cloud. The evolution of β in isolated clouds is also shown [for simulations with 32 (R_{32}) and 128 (R_{128}) cells per cloud radius].

simulations with a perpendicular field ($\beta_0 = 5.06$). In general, we see that β in cld1 is much lower than the isolated single cloud case, except for simulation *s3w4a60*. This simulation is notable because it is the only one in which cld1 is sufficiently on the 'outside' of the distribution that it does not collide with any of the other clouds (see Fig. 4.28). Fig. 4.30 also shows that the β in cld2 is similar to but generally lower than the isolated cloud case. β is most variable in simulation *s3w4a30* (in cld2 it is low at $t = 3.5 - 4\,t_{cc}$ when cld1 is compressing cld2, becomes noticeably higher at $t = 6\,t_{cc}$, and then drops again afterwards as it interacts strongly with cld3). The value of β in cld3 shows the most difference between simulations. For *s3w4a0* it stays low for most of the simulation time, but for simulations *s3w4a15* and *s3w4a30* β becomes very high at $t \approx 6.5\,t_{cc}$. Fig. 4.29 shows that in simulation *s3w4a15*, cld3 moves into the lee of cld1 at about this time (so is sheltered), but by $t = 7.9\,t_{cc}$ cld1 has collided with it, decreasing β once more.

4.4 Summary and conclusions

The results presented in Sec. 4.3 illustrate that the presence of nearby clouds modifies the evolution of a shocked cloud. In general, clouds on the same field lines are able to merge, even if they are quite widely separated. Conversely, clouds on different field lines tend to 'rebound' from each other if they are squeezed closely together. However, the details of the simulations are complicated. We now summarize the main results and attempt to draw generalities where possible, commenting on parallel, oblique and perpendicular shock interactions in turn.

In the case of a parallel shock, the shocked cloud needs to push aside field lines in order to expand laterally and this is made more difficult by a cloud alongside. Hence the expansion and fragmentation of the cloud is reduced. The downstream cloud is not very sensitive to the distance along the direction of the shock normal to the upstream cloud, at least for the range studied ('offsets' $\sim$1–8 $r_{\rm cl}$). Rather, for parallel shocks, the separation of clouds perpendicular to the shock normal (i.e. their 'width') largely determines their evolution. As the field lines disturbed by the upstream cloud advect downstream, they curl round and confine any downstream cloud separated by 'widths' $1-4\,r_{\rm cl}$. At 'widths' of $4\,r_{\rm cl}$ the evolution of clouds is analogous to the evolution of clouds alongside one another (i.e. with an 'offset'$\approx$ 0). At a 'width' of $2\,r_{\rm cl}$, the downstream cloud is confined and roughly circular, with mass stripping occurring along a tail from its outside edge. Such clouds are pushed towards the lower pressure region behind the upstream cloud and start expanding once in the lee. At negligible 'widths' a downstream cloud can fall in the 'flux rope' of the upstream cloud. While the initial shock compression of the downstream cloud is comparable to that of an isolated cloud, it is subsequently

shielded from the flow and is neither compressed nor accelerated significantly. After shock compression and re-expansion the properties of the downstream cloud are relatively constant until the upstream cloud ploughs into it (i.e. the evolution of a cloud in a flux rope is delayed until the upstream cloud reaches it).

In general, the presence of clouds downstream increases β in the upstream cloud via mechanical interaction, while clouds alongside decrease β by suppressing lateral expansion. By far the biggest effect is when a cloud is directly behind and in the 'flux rope' of an upstream cloud: in this case β in the downstream cloud can be significantly reduced for an extended period of time.

This basic behaviour also holds when a parallel shock interacts with three clouds, though the additional cloud modifies the morphology slightly. The additional cloud now allows a distinction to be made concerning whether the downstream cloud lies 'inside' or 'outside' with respect to the rest of the distribution (e.g., simulation *w4a15* versus simulation *w4a45*). An outside cloud is confined much as in the two-cloud simulations, but the field lines cannot curl as much around an inside cloud. The plasma β is generally higher in inside clouds, yet they are less confined than outside clouds.

The interaction of an oblique shock with clouds is a more general case than the specific cases of interactions of parallel or perpendicular shocks. With oblique shocks, as well as considering whether a cloud is upstream or downstream, one must also consider whether it is upfield or downfield. In two-cloud interactions we see some interesting dynamics where the upstream cloud accelerates past the downstream cloud, and then swings into its lee. The 'shielded' cloud then experiences reduced confinement forces and begins to diffuse, while the cloud more exposed to the oncoming flow experiences another period of compression. Clouds

are given much faster transverse motions than those interacting with parallel or perpendicular shocks. The plasma β in the upstream cloud can drop below unity for a duration of a few $t_{\rm cc}$ when it collides with the downstream cloud. The interaction of an oblique shock with three clouds shows the same type of behaviour, and can be understood in terms of the interaction of the most upstream cloud with its nearest neighbour, and then their joint interaction with the remaining cloud.

The interaction of a perpendicular shock with clouds is again a more specific case. If the clouds are side-by-side they have a chance of merging. We clearly see this in simulations where the clouds are separated with an initial 'width' of $4\,r_{\rm cl}$, but as the width is increased the clouds should eventually evolve as isolated clouds. We have not explored the transition between these regimes, but it will certainly depend on parameters such as M, χ and β_0. When the clouds have a non-zero 'offset' the fact that they exist on separate field lines prevents them from fully mixing. Nevertheless, the clouds tend to be driven towards each other much more strongly than when the shock is parallel or oblique. If the clouds have a small 'width' and larger 'offset' the upstream cloud tends to get driven into and then wraps around the downstream cloud. Like the oblique case, the plasma β in the upstream cloud can become less than unity when it collides with a downstream cloud. When three clouds are present, the most upstream or most downstream cloud may be prevented from moving between the other two clouds due to the tension in the field. Because the field lines also prevent the flow from passing between the clouds the magnetic field builds up on the upstream side and then bends around the clumpy region.

Previous work examining the MHD interaction of a shock with a single cloud found that the plasma β is low where the flow is compressed, rather than the magnetic field being turbulently amplified. The two-cloud and three-cloud interactions

presented in this work are more turbulent than single-cloud interactions due to the presence of neighbouring clouds, but low values of β are still not seen very often. When they are, it is again mostly due to the compression of the field by the flow, and is ultimately transient in nature. This highlights the difficulty of obtaining regions of low β (e.g., $\beta < 1$) in adiabatic simulations. To obtain such regions it is probably necessary to invoke cooling to reduce the thermal pressure (e.g., Vieser & Hensler 2007; van Loo *et al.* 2010). Johansson & Ziegler (2013) find that a weak perpendicular field ($\beta \sim 10^3$) is able to suppress conduction without limiting compression resulting in the highest density compressions of an individual cloud. Without considering the cooling, we find that moderate fields ($\beta = 5$) are effective at bringing several clouds together.

We note that the interaction of magnetized clouds has also been studied in solar physics, where Shen *et al.* (2012) modelled the propagation and collision of two coronal mass ejections (CMEs) in interplanetary space. The resulting structures and their evolution resemble some of the work shown in the present paper, though it is clear that additional complexities, such as magnetic reconnection in the neighbourhood of boundary layers (cf. Chian & Muñoz 2012), occur. Reconnection in turbulent flows is discussed in Lazarian (2014).

We now offer some thoughts on some important questions concerning the ISM. At this stage it is difficult to say anything about diffuse cloud lifetimes because the clouds in the simulation are 2D instead of 3D and some important physical processes, such as cooling and conduction, were not included. However, it is clear that the lifetimes are affected by the environment around the cloud, and specifically the presence of nearby clouds which can affect the flow and field lines. We have not considered specific observables in this work (such as emission maps), so it is unclear

what types of structures would actually be visible. We note that some other works which have focused on observables have considered high-velocity clouds (Henley, Kwak & Shelton 2012; Shelton, Kwak & Henley 2012), supernova remnants (e.g., Patnaude & Fesen 2005; Obergaulinger *et al.* 2014), and galactic winds (e.g., Marcolini *et al.* 2005). These works indicate that it is possible to gain some insights into some of the key parameters, such as the interstellar magnetic field, the Mach number of the shock, the properties of the clumpy medium, and the nature of the pressure sources. Insight into such parameters is most forthcoming, of course, when specific sources are modelled.

The present study has illustrated some of the complexity inherent in MHD interactions of a shock with multiple clouds, and attempts to lay some of the necessary foundations for understanding this problem. The role of the relative position is identified. The "offset" is not important in the parallel field case - the interaction can be determined from the "width" between the clouds. In the oblique field case the evolution of the cloud depends on the upfield/downfield distinction. Upstream, downfield clouds accelerate past downstream, upfield clouds, while vertical positions swap in most cases. The interaction between three clouds can be understood as two two-cloud interactions. Simulations with oblique and perpendicular fields lead to relatively compact cloud arrangements.

In future work we will build on the present study to examine the MHD interaction of a shock with many 10s and 100s of clouds. We will also extend this work to spherical as opposed to cylindrical clouds. The interaction could be quite different between these two cases because field lines will be able to slip past spherical clouds, which could significantly change the forces acting on the clouds. In addition, there could be interesting interactions between clouds whose field lines lie in

different planes. For instance, consider the interaction of a cloud in one plane with a second cloud in an adjacent parallel plane where there are different field lines in each plane. If the planes are far enough apart then the clouds should evolve independently (one plane might slip sideways relative to the other). However, the evolution may be markedly different when the planes are close enough together that pressure interactions occur between them.

Chapter 5

Additional MHD Simulations

5.1 Introduction

MHD simulations of shocks interacting with one, two and three clouds were presented in Chapter 4. That work laid the foundations to understand the variety of interactions between the clouds that would be present in a clumpy distribution. This Chapter builds upon it and presents the 2D interaction between a shock and magnetized clumpy regions in Sec. 5.3. Finite sized clumpy regions are investigated in Sec. 5.4. While a strong magnetic field, with magnetic pressure comparable to thermal pressure, significantly modifies the evolution of the system, even a weak field produces a noticeable effect as the interaction progresses (see also Johansson & Ziegler 2013) . Such simulations are presented in Sec. 5.5. 2D simulations are by necessity limited in their field geometries. Fully 3D simulations will therefore need to be considered in future work, but some initial comparisons are made in Sec. 5.6. Conclusions are presented in Sec. 5.7.

5.2 An MHD resolution test

We begin by presenting the resolution study that was the basis for choosing the numerical resolution and reliable statistical measures in other investigations of this Chapter and Chapter 4.

Unlike in the hydrodynamic case, a sub-grid turbulence model is not used in the MHD version of the code (see Sec. 2.5), potentially increasing the resolution requirements. However, the presence of a magnetic field can severely limit the development of instabilities. As seen in Shin, Stone & Snyder (2008), the flow is smoother and should be less sensitive to resolution.

Mac Low *et al.* (1994) found that in the parallel field case magnetic reconnection behind the cloud due to numeric diffusion leads to less magnetic energy at lower resolutions. Even between R_{50} and R_{100} the difference is significant. Other authors typically used of order 100 cells per cloud radius as in the hydrodynamic case (e.g. Shin, Stone & Snyder used R_{68} in their 3D simulations), although some authors compared their results to a single simulation at higher resolution to determine their reliability (e.g. Chapter 4 and Orlando *et al.* 2008).

5.2.1 Initial conditions

Two studies were performed, one with a single isolated cloud and another with a random distribution of clouds. The shock had a sonic Mach number, $M = 3$ and the clouds had a density contrast, $\chi = 100$. Three field orientations were used: i) a field parallel to the direction of shock propagation with a pre-shock $\beta = 1.13$, ii) an oblique field (initially at 15° to the shock normal) with a pre-shock $\beta = 1.13$, and iii) a perpendicular field with an initial $\beta = 5.06$. These simulations are referred

to as *bxb1*, *b15b1* and *byb5*, and their properties are summarized in Table 3.1.

The clumpy distribution consisted of 64 clouds in a region of $200\,r_{\rm cl} \times 100\,r_{\rm cl}$ giving a mass ratio, MR $= 1$, with periodic boundary conditions in y.

5.2.2 A single cloud resolution study

Other (hydrodynamic) resolution studies, such as Nakamura *et al.* (2006) and Pittard *et al.* (2009) compare the relative error measured at one or two points in the evolution to test for convergence. However, such a method is very sensitive to the selection of the time of the snapshot and can misrepresent the actual convergence in cases where different evolutionary tracks cross (e.g. Fig. 3.1). For this reason, where data over the entire evolution is available we choose to use a measure that compares evolutionary tracks rather than points. We define the Coefficient of Variation:

$$\mathrm{CV}(r) = \frac{\sqrt{\frac{1}{n}\sum_{i=1}^{n}(x_{r,i} - x_{R,i})^2}}{\bar{x}_R}, \tag{5.1}$$

where x_r denotes values at some resolution r, and x_R is the value at the reference resolution (usually the highest available). As the evolution is sampled at discrete points in time which may be slightly different between different simulations a spline interpolation is used to produce n uniformly spaced points between times $t_{\rm s}$ and $t_{\rm f}$. The CV is insensitive to n ($n = 100$ is used), but it can be very sensitive to the choice of $t_{\rm s}$ and $t_{\rm f}$. For the single cloud case, $t_{\rm s}$ was chosen to be the time the shock enters the cloud and $t_{\rm f} = t_{\rm s} + 9\,t_{\rm cc}$.

The coefficient of variation for various measures in shown in Fig. 5.1. The left column shows convergence in the cloud size perpendicular to the shock propagation

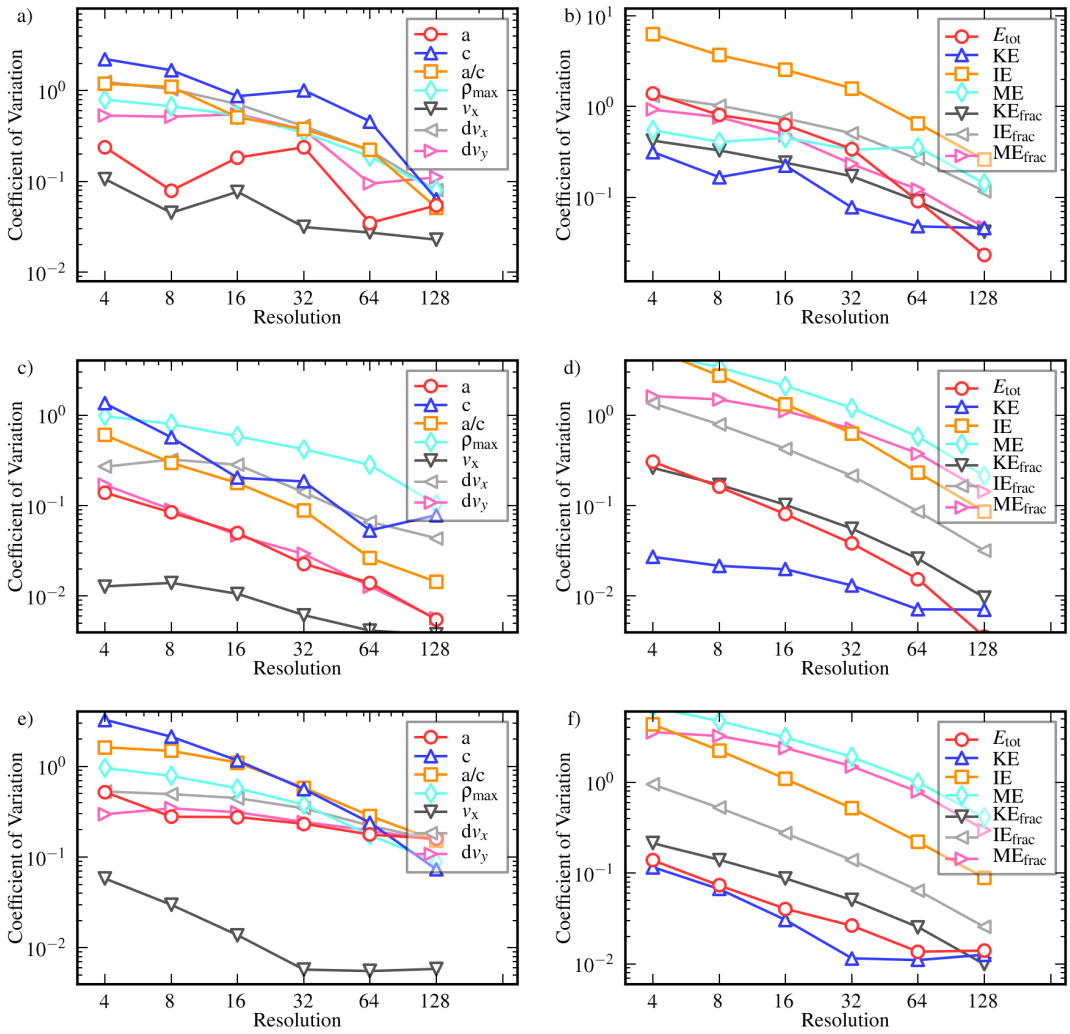

Figure 5.1: The coefficient of variation plotted against spatial resolution in single cloud simulations with parallel (top), oblique (middle) and perpendicular (bottom) magnetic fields. The left column shows convergence in various properties of the cloud structure while the right column shows the convergence in the total, kinetic, thermal and magnetic energies. The highest resolution (reference) simulation had a resolution of R_{256}.

(the y direction), a, the cloud size in the direction of shock propagation (the x direction), c, the cloud aspect ratio a/c, the cloud maximum density, ρ_{max}, the average cloud velocity in the x direction, v_{x}, the cloud velocity dispersion in the x direction, $\mathrm{d}v_{\mathrm{x}}$, and velocity dispersion in the y direction, $\mathrm{d}v_{\mathrm{y}}$. The right column shows the convergence in the total energy, E_{tot}, and its components: the kinetic (KE), the thermal (IE) and the magnetic (ME) energies, and the component energy fractions.

Even at a resolution of R_{128}, some differences compared to the R_{256} simulation arise at late times and the CV is generally quite high across all simulations and variables. A CV $\lesssim 0.1$ would indicate high accuracy, but only v_{x} and the related KE is truly well converged at lower resolutions. In the parallel field case all measures (except the ME) reach this threshold at R_{128}, showing that since the parallel field case is similar to the hydrodynamic case (Sec. 1.3.2.2) the hydrodynamic convergence criteria is also applicable to MHD simulations with parallel magnetic fields. A similar requirement also holds for other field orientations. However, different measures converge differently. The maximum density is naturally one of the worst converging measures and so is c, but the velocity dispersion converges somewhat better/earlier and the total energy of the cloud also converges well despite the large error in the ME.

Fig. 5.2 shows the evolution of the magnetic energy of the cloud material. The oblique and perpendicular cases show much higher magnetic energy at $2\,t_{\mathrm{cc}}$ for low resolution runs. This is caused by the diffusion of the cloud material, so that the magnetic energy of the cloud is summed up over a larger volume. However, the structure of the field is not affected and the same features in the evolution can

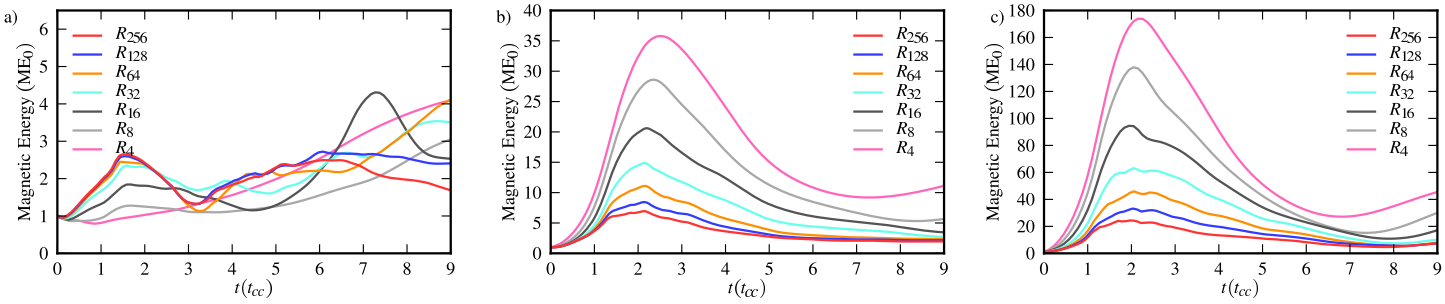

Figure 5.2: Evolution of the magnetic energy of the cloud normalized to the initial cloud magnetic energy in simulations with (a) parallel, (b) oblique and (c) perpendicular magnetic fields.

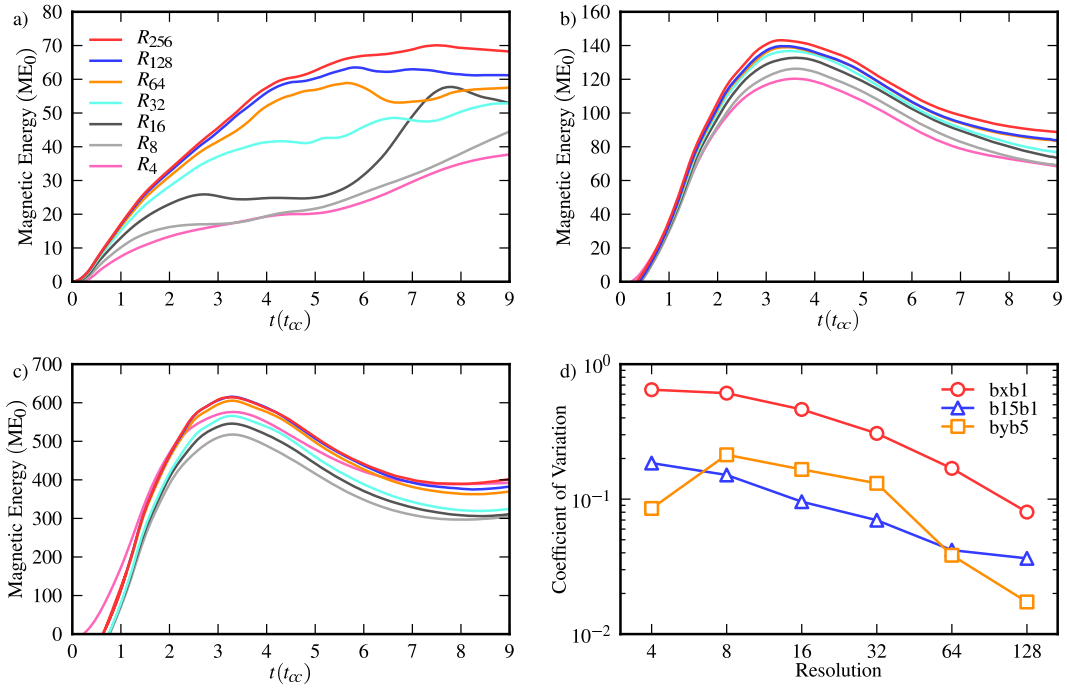

Figure 5.3: Evolution of excess magnetic energy on the grid normalized to initial cloud magnetic energy in simulations with (a) parallel, (b) oblique and (c) perpendicular magnetic fields. The coefficient of variation of the excess magnetic energy is shown in panel (d).

be clearly identified in all simulations above R_{32}. Furthermore, when the excess[1] magnetic energy of the entire grid is considered (see Fig. 5.3), we see that a lower resolution leads to a lower magnetic energy but the difference is small and insignificant above R_{32} (also confirmed by the CV as shown in Fig. 5.3d) for the oblique and perpendicular cases.

However, the parallel case is more complicated. The magnetic energy of the cloud diverges after 5.5 t_{cc} for R_{128} and a bit earlier for R_{64} although the numerical value remains close to the higher resolution results until 7 t_{cc} even at R_{32} (see Fig. 5.2a). However, the flux rope is not included in these results as it does not contain cloud material. In contrast, the excess magnetic energy shown in Fig. 5.3a includes the flux rope and can be compared to fig. 9 in Mac Low *et al.* (1994). In the two lowest resolution runs, R_4 and R_8, the magnetic energy increases much slower - presumably the maximum amount of magnetic reconnection is occurring in these simulations. A transitional behaviour is seen at R_{16} and a qualitative agreement is reached at higher resolutions although, as in Mac Low *et al.* lower resolutions underestimate the magnetic energy.

An important parameter, the plasma β, is plotted in Fig. 5.4. Values at two snapshots in time are compared between different resolutions and different types of average are considered. The arithmetic mean is not the most appropriate as, particularly at low resolution, β can grow without bound. This is partly negated by truncating the β distribution above 1000, but the arithmetic mean is still several times the median β. In contrast, the harmonic mean is biased towards the low values and is generally below the median.

[1]The excess magnetic energy is defined as the total magnetic energy in the grid minus the total if the cloud was not present, which accounts for the inflow of magnetic energy from the boundary conditions and for the change in the magnetic energy due to shock compression.

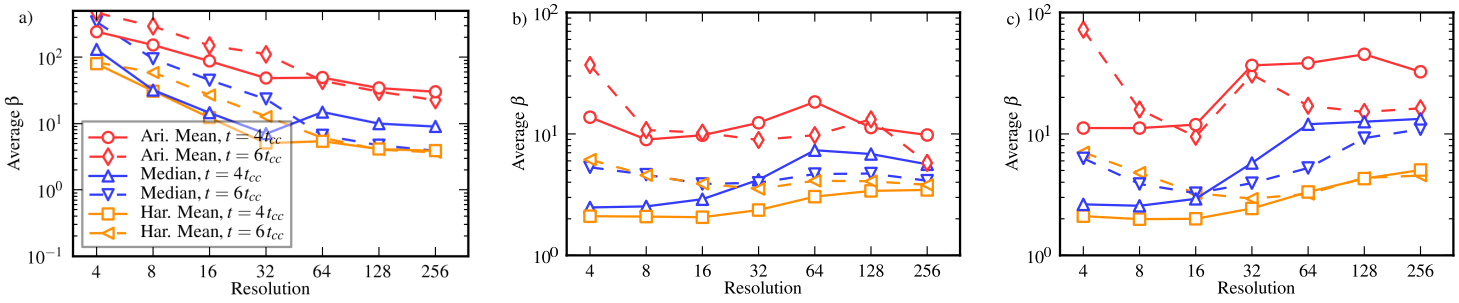

Figure 5.4: Average plasma β at different resolutions at $t = 4\,t_{cc}$ (sold lines) and $t = 6\,t_{cc}$ (dashed lines) for (a) parallel, (b) oblique and (c) perpendicular fields. The arithmetic mean, the median and the harmonic mean were used as three different types of average.

Finally, β distributions weighted by cloud mass at $t = 4\,t_{cc}$ at different resolutions are compared in Fig. 5.5. The effect of resolution in the parallel field case is to truncate the distribution at low β and to increase the amount of gas in high β bins. The R_{256} and R_{128} simulations are well matched, while lower resolutions start to show excess mass above $\beta = 20$. At the low β end R_{32} is truncated at $\beta = 0.7$, but this only affects a small fraction of the mass. More significantly, the R_{16} simulation is effectively truncated at $\beta = 5$. The oblique and perpendicular cases shows excess at high β but also in the vicinity of $\beta = 1$, presumably due to cloud material diffusing into $\beta \approx 1$ shocked gas.

5.2.3 A multiple cloud resolution study

In our multiple cloud resolution test we use the same field orientations and follow the evolution of two regions of clouds: the upstream region, *blk1*, located within the first $50\,r_{cl}$ and the downstream region, *blk3* located between $100\,r_{cl}$ and $150\,r_{cl}$ inside the clumpy region (the clumpy region is $200\,r_{cl}$ deep). Additionally, we also

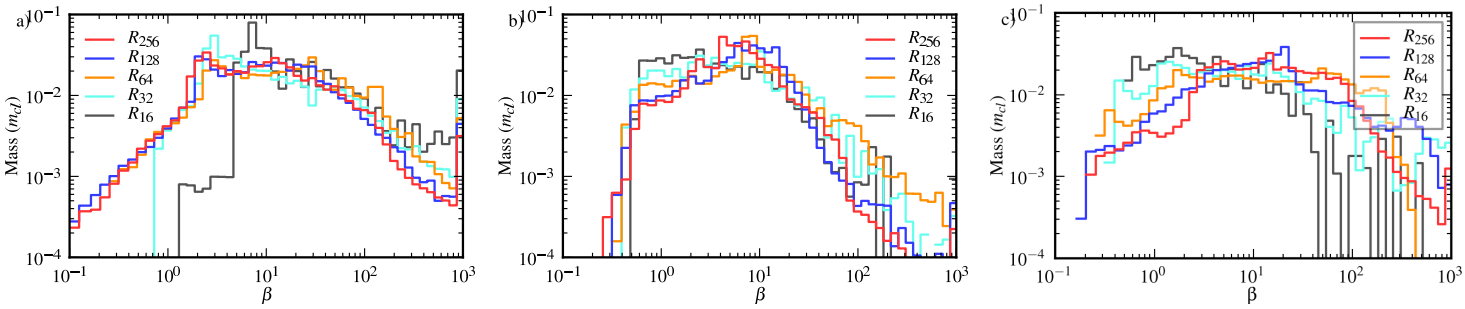

Figure 5.5: Histograms of cloud mass weighted β distributions at $t = 4\,t_{cc}$ for (a) parallel, (b) oblique and (c) perpendicular fields.

follow two individual clouds, *single1* and *single3*, in the upstream and downstream blocks respectively.

To calculate the Coefficient of Variation we identify the time when the shock enters the cloud as t_s and set $t_f = t_s + 9\,t_{cc}$ for individual clouds (i.e. the same as in the isolated cloud case in the previous section). For blocks of clouds, we set $t_s = t_{exit} - 3\,t_{cc}$ and $t_f = t_{exit} + 9\,t_{cc}$ where t_{exit} is the time when the shock leaves the relevant block of clouds. Figs. 5.6 and 5.7 show, as before, that the spatial diffusion of the cloud at lower resolutions leads to the largest errors in the average density, and in the internal and magnetic energies. In general, the difference between R_{32} and R_{64} in the multiple cloud simulations is comparable to the difference between R_{128} and R_{256} in the single cloud simulations, although CV $= 0.1$ still implies an error of the order of 10%. The bottom line, however, is that generally better convergence is obtained at lower resolutions in simulations with multiple clouds than in single cloud simulations.

Fig. 5.8 shows that the excess magnetic energy in the multiple-cloud simulations is well converged. Even at the lowest resolutions the accuracy is fairly high and unlike in the single cloud case, there is no split in the qualitative behaviour of the

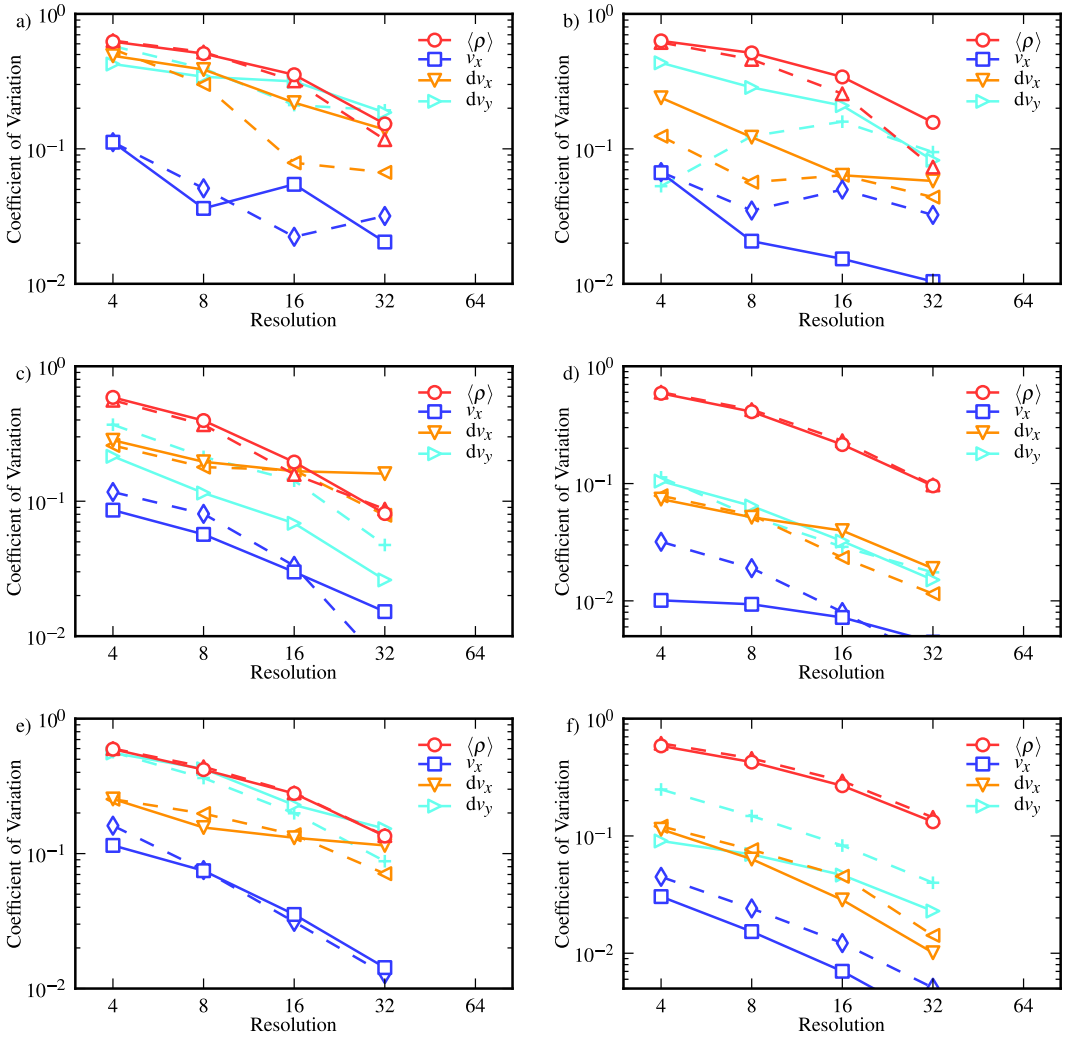

Figure 5.6: The coefficient of variation plotted against spatial resolution for individual clouds (left column) and blocks of clouds (right column) in multiple cloud simulations with parallel (top), oblique (middle) and perpendicular (bottom) magnetic fields. Solid lines refer to the cloud or block in the upstream region, while dashed lines refer to the cloud or block in the downstream region.

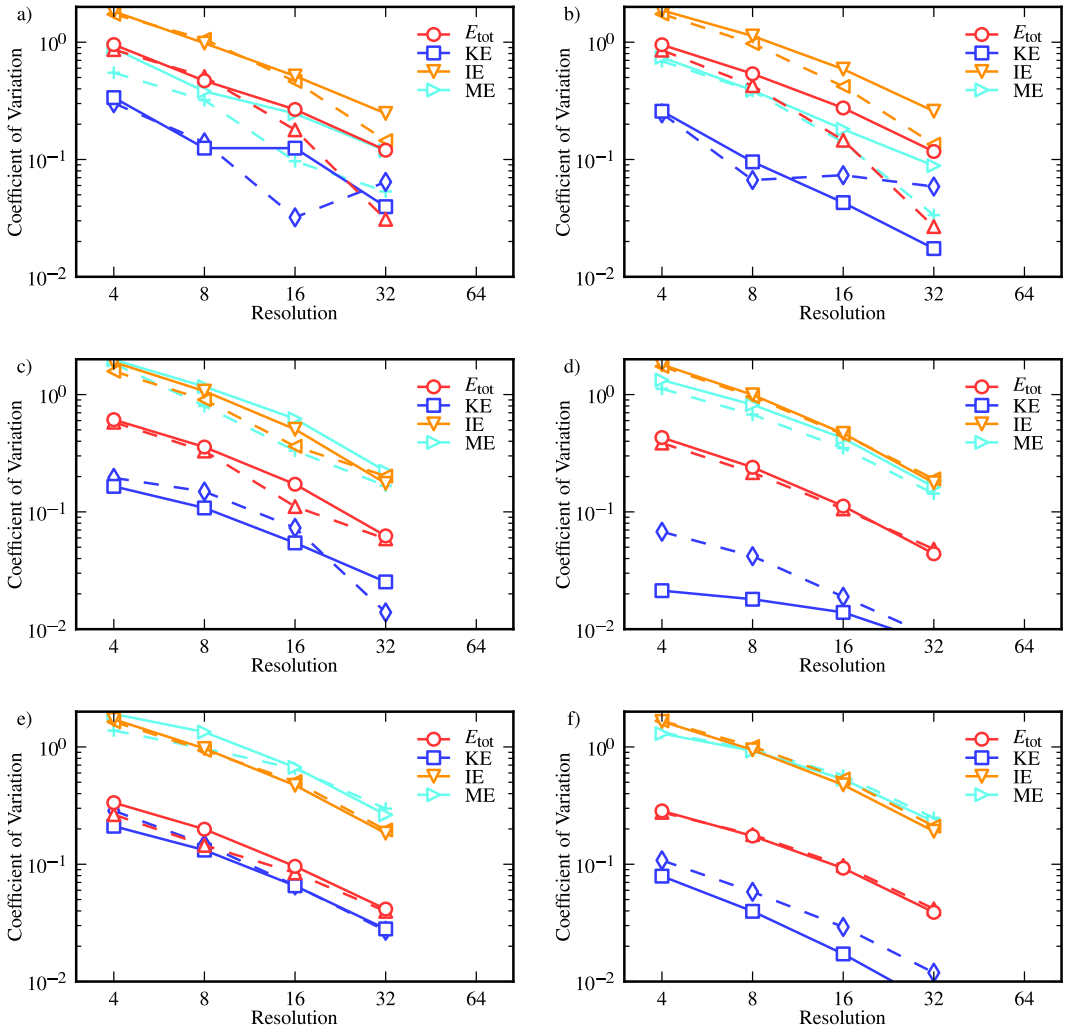

Figure 5.7: The coefficient of variation plotted against spatial resolution for individual clouds (left column) and blocks of clouds (right column) in multiple cloud simulations with parallel (top), oblique (middle) and perpendicular (bottom) magnetic fields. Solid lines refer to the cloud or block in the upstream region, while dashed lines refer to the cloud or block in the downstream region.

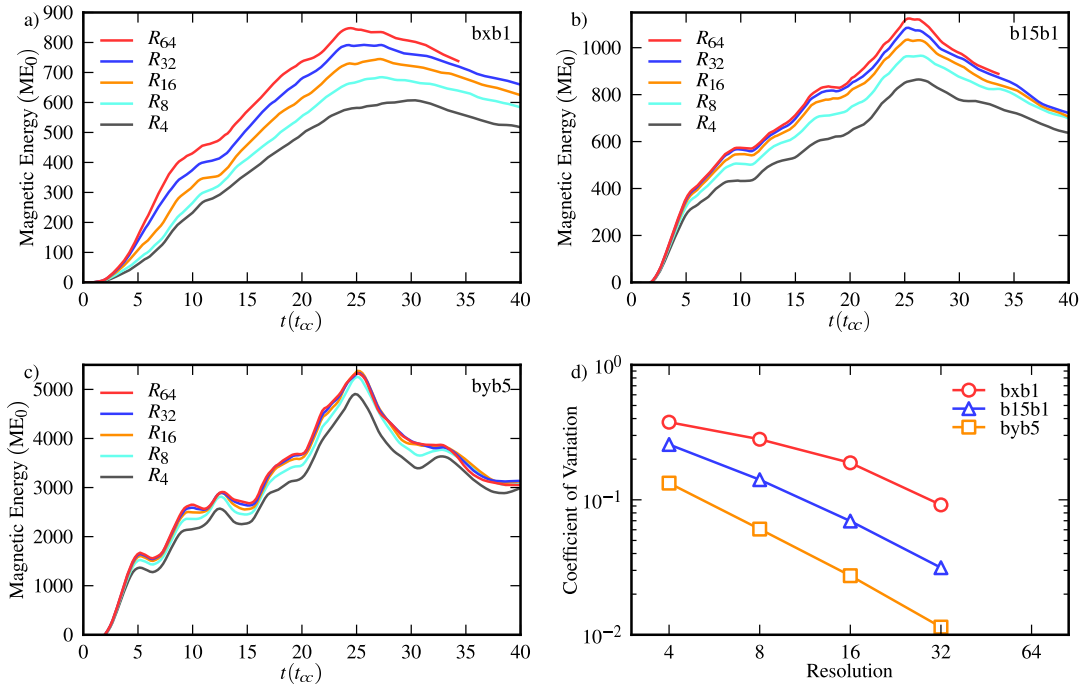

Figure 5.8: Evolution of the excess magnetic energy on the grid normalized to initial magnetic energy of a cloud in simulations with (a) parallel, (b) oblique and (c) perpendicular magnetic fields. The coefficient of variation is shown in panel (d). The maximum magnetic energy corresponds to the time when the shock leaves the clumpy region.

excess magnetic energy in the parallel field simulations.

A snapshot of the β distributions is given in Fig. 5.9. The R_{32} and R_{64} results are in close agreement when considered over a block of clouds. For individual clouds there is naturally more noise, but note how peaks on the distributions are slightly offset. The relative error in the average values of β (the harmonic mean and the median) are shown in Fig. 5.10. The parallel field case converges quickly but the relative error remains high. In contrast, the error in the oblique and perpendicular field cases is smaller, but the convergence is not so clear.

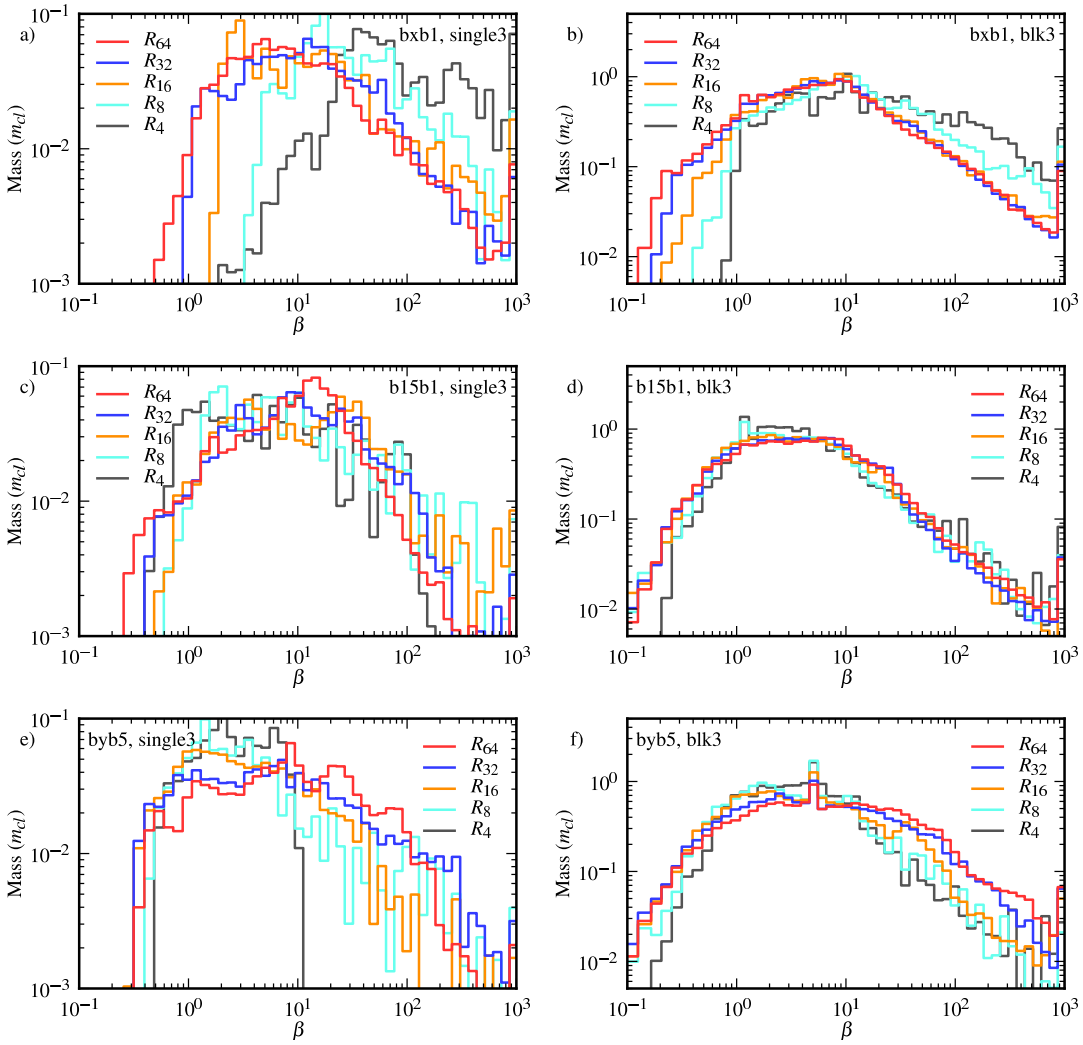

Figure 5.9: The distribution of the plasma β for an individual cloud in the downstream block (*single3*, left column), and for the downstream block as a whole (*blk3*, right column). For the individual cloud the distributions are shown at a time of $4\,t_{cc}$ after the shock hits the cloud. For the block the distributions are at the time when the shock leaves the block. The magnetic field orientation is parallel (top), oblique (middle) and perpendicular (bottom).

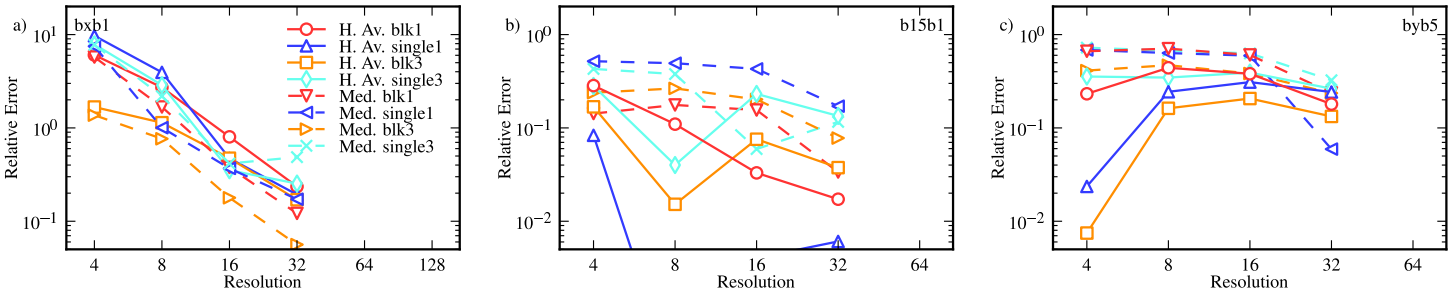

Figure 5.10: Relative error of the harmonic mean (solid lines) and the median (dashed lines) β in multi-cloud simulations with (a) parallel, (b) oblique and (c) perpendicular magnetic fields.

5.2.4 Conclusion

The previous two sections show that there are several differences in the numerical convergence, compared to the hydrodynamic case, when a strong magnetic field is present. In the hydrodynamic case the evolution is driven by the development of KH and RT instabilities, shorter wavelengths of which are suppressed due to numerical resolution, but longer wavelengths are more dynamically important. If the important wavelengths are unresolved the evolution is very different, but ∼100 cells per cloud radius is sufficient to resolve the important wavelengths and the solution is converged (Klein, McKee & Colella 1994). Convergence can be reached at lower resolution with a subgrid turbulence model (Pittard *et al.* 2009).

As shown by Mac Low *et al.* (1994) and Shin, Stone & Snyder (2008) the instabilities are suppressed by the magnetic field. The resolution effects manifest themselves as differences in the cloud diffusion (particularly across the field lines) and magnetic reconnection. Magnetic reconnection can be very strong at resolutions below R_{16} severely affecting the simulations, but at R_{32} and above the evolution is qualitatively similar. However, quantitative differences remain even at high res-

olutions. Although the error continues to decrease with increasing resolution we consider the simulations to be converged in a sense that the result is qualitatively the same across a large range of resolutions, there is no evidence to suggest that resolving a smaller lengthscale would introduce new, important processes.

In general it appears that a particular level of convergence can be reached at lower resolution (especially in simulations with a perpendicular field component - simulations with a parallel magnetic field instead share many similarities with purely hydrodynamic simulations and the requirement of 100 cells per cloud radius remains applicable). However, the rate of convergence is slower in MHD simulations and numerical differences remain even above R_{128}. This resolution testing also reveals that better convergence (at lower resolution) is obtained in simulations with multiple clouds than in single cloud simulations.

5.3 MHD shock interaction with a large number of clouds

This section combines the results of Chapters 3 and 4 by presenting simulations of a shock interacting with a distribution of a large number of magnetized clouds.

5.3.1 Initial conditions

The clumpy region occupied a region of $400\,r_{\rm cl} \times 100\,r_{\rm cl}$ and contained either 128, $\chi = 10^2$ clouds in the MR $= 1$ case (*chi2MR1*) or 492, $\chi = 10^2$ clouds in the MR $= 4$ case (*chi2MR4*). The same magnetic field arrangements were used as in Chapter 4, i.e. a parallel field orientation with $\beta_0 = 0.55$ (*bxb0.5*), an oblique

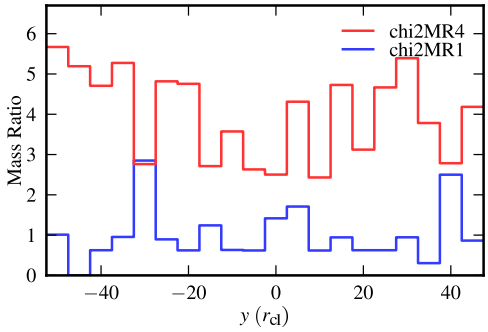

Figure 5.11: The 'regional' Mass Ratio (averaged across all x in the clumpy region) in $5\,r_{\rm cl}$ slices of the *chi2MR4* and *chi2MR1* cloud distributions.

field orientation with $\theta_0 = 15^\circ$ and $\beta_0 = 1.13$ (*b15b1*) and a perpendicular field orientation with $\beta_0 = 5.06$ (*byb5*). The sonic Mach number in these simulations is $M = 3$, while the Alfvénic Mach number, $M_a = 2.03$, 2.91 and 6.16 respectively. An additional oblique field arrangement, with $\theta_0 = 12^\circ$ and $\beta_0 = 1.1$ was chosen to be used with an $M = 10$, $M_a = 9.57$ shock, so that in the postshock medium $\theta_1 \approx 45^\circ$ (simulation *m10chi2MR4 b12b1*). Inflow/outflow boundary conditions were applied in the x direction, while periodic boundary conditions were used in the y direction in the majority of simulations. However, in some simulations (labelled *chi2MR4_finite*) the y boundary was moved $200\,r_{\rm cl}$ away from the clumpy medium and free inflow/outflow conditions were applied instead. The resolution of the most refined grid level was 32 cells per cloud radius (R_{32}).

5.3.2 Results

The distributions *chi2MR4* and *chi2MR1* consist of a random cloud distribution $100\,r_{\rm cl}$ deep repeated four times without an offset. This exaggerates inhomogeneities in the distribution so that there are $5\,r_{\rm cl}$ wide regions (slices) with 'regional' mass

ratios up to 5.8 in *chi2MR4* and up to 3 in *chi2MR1*. This variation is shown in Fig. 5.11.

Such inhomogeneities affect the evolution of the flow in the parallel field case. Fig. 5.12 shows that large-scale 'flux-ropes' form behind groups of clouds in simulation *m3chi2MR4 bxb0.5*. At $t = 28.5\,t_{\rm cc}$ one such rope can be seen at $y = -25$ which corresponds to a region of higher initial density, but the highest density region ($y \simeq -40$) is only beginning to form its 'flux-rope', so the relative positions of the clouds on local scales determine how quickly these 'flux-ropes' form.

At $t = 57.0\,t_{\rm cc}$ 4 ropes can be identified (marked with arrows on the right side). At $y = -40$, -25, 20 and 30 corresponding to four highest peaks in the MR distribution (the rope at $y = 20$ is probably the result of peak at $y = 15$ shifted due to expansion of the region at $y = 0$). The next highest peak at $y = 5$ does not form a large-scale 'flux-rope', although similar smaller scale features are visible in the close-up in Fig. 5.14.

The region at $y \sim 0$ has the lowest number of clouds, it protrudes the furthest downstream and also expands laterally, squeezing the 'flux-ropes'. Such structure remains even after the shock leaves the clumpy region.

As explained in Chapter 4 clouds inside the 'flux-rope' evolve very differently, even when compared to nearby clouds that fall just outside it. Such clouds are squeezed slightly from the sides, but otherwise are well shielded from the effects of the flow. Their evolution is driven by collisions with upstream clouds which create thin ($\sim 2\,r_{\rm cl}$) and long ($\sim 100\,r_{\rm cl}$) strings along which cloud remnants are distributed (seen particularly clearly in the middle panel of Fig. 5.12).

When the initial magnetic field is weaker, as in the $\beta_0 = 1.13$ case, such large-scale 'flux-ropes' do not form. The top panel of Fig. 5.13 shows that the cloud

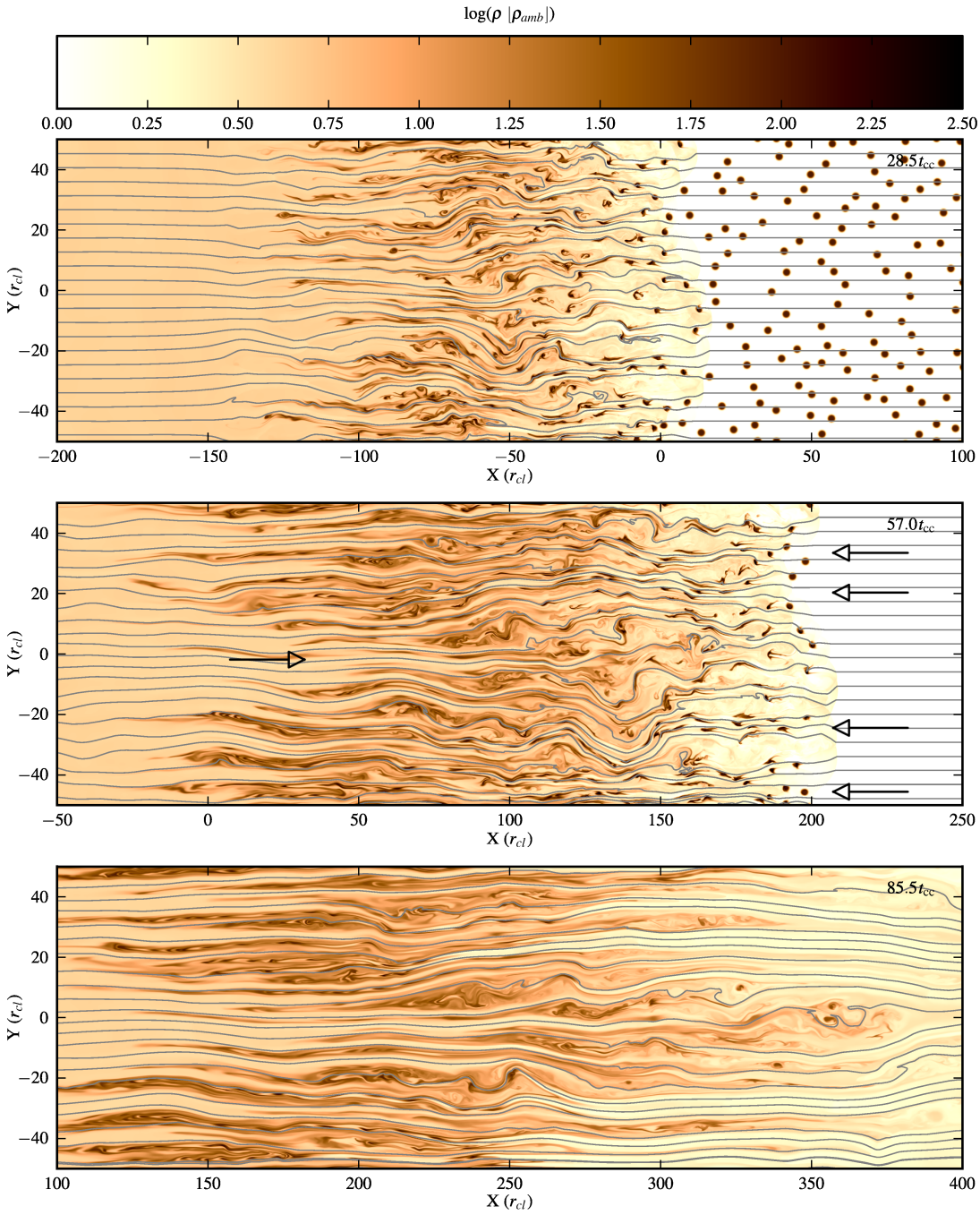

Figure 5.12: The evolution of the *M3chi2MR4* simulation with a parallel magnetic field and $\beta_0 = 0.55$. The snapshots shown are at times of 28.5 t_{cc}, 57.0 t_{cc} and 85.5 t_{cc} (top to bottom). The arrows on the right side point to the locations of the 'flux-ropes', the arrow on the left side points towards the expanded central region.

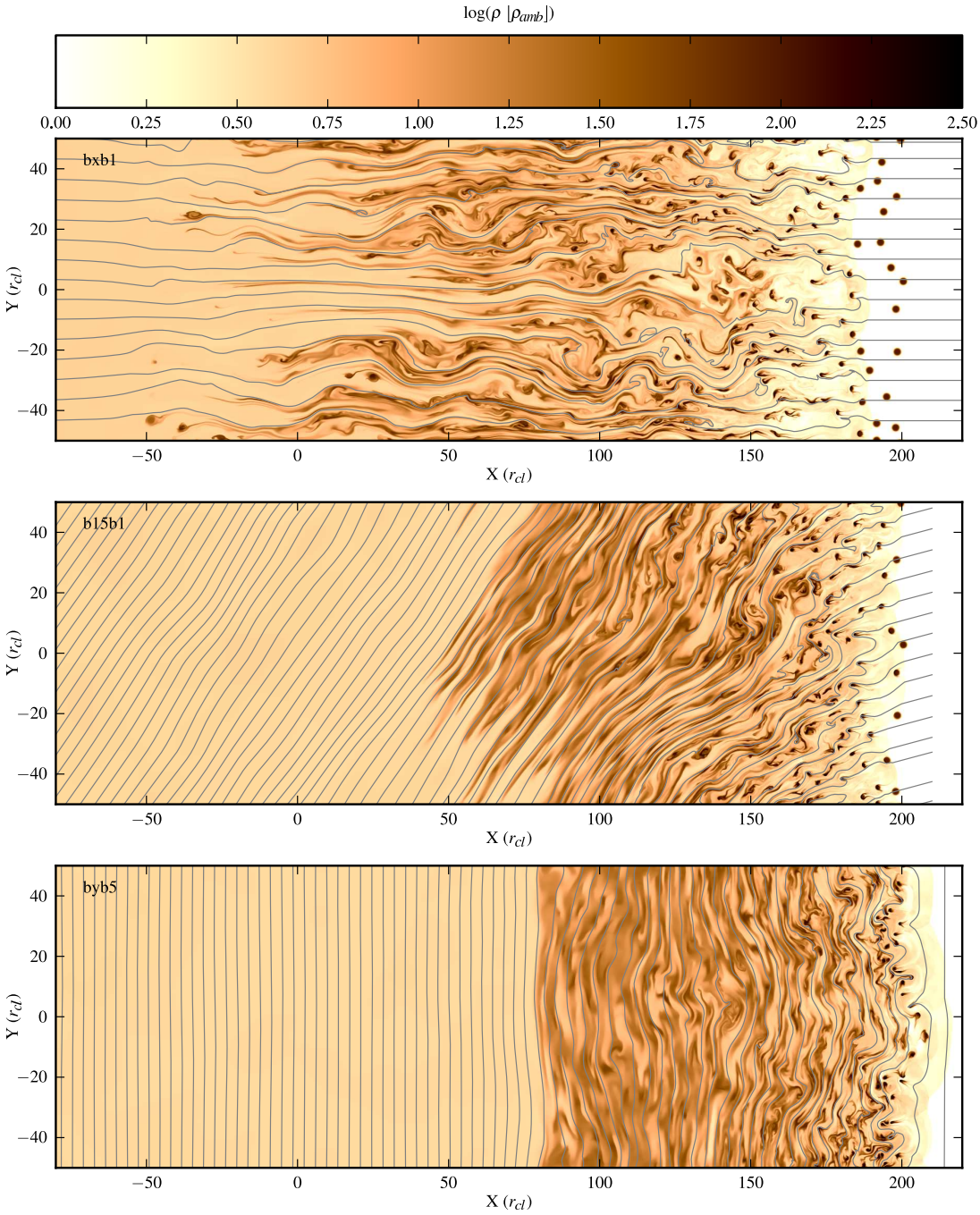

Figure 5.13: Morphology snapshots at a time when the shock leaves the clumpy region for *M3chi2MR4* simulations with an initial magnetic field which is parallel with $\beta_0 = 1.13$ (top), oblique with $\beta_0 = 1.13$ (middle) and perpendicular with $\beta_0 = 5.06$ (bottom). The times of the snapshots are 57.0 t_{cc}, 65.1 t_{cc} and 69.2 t_{cc} (top to bottom).

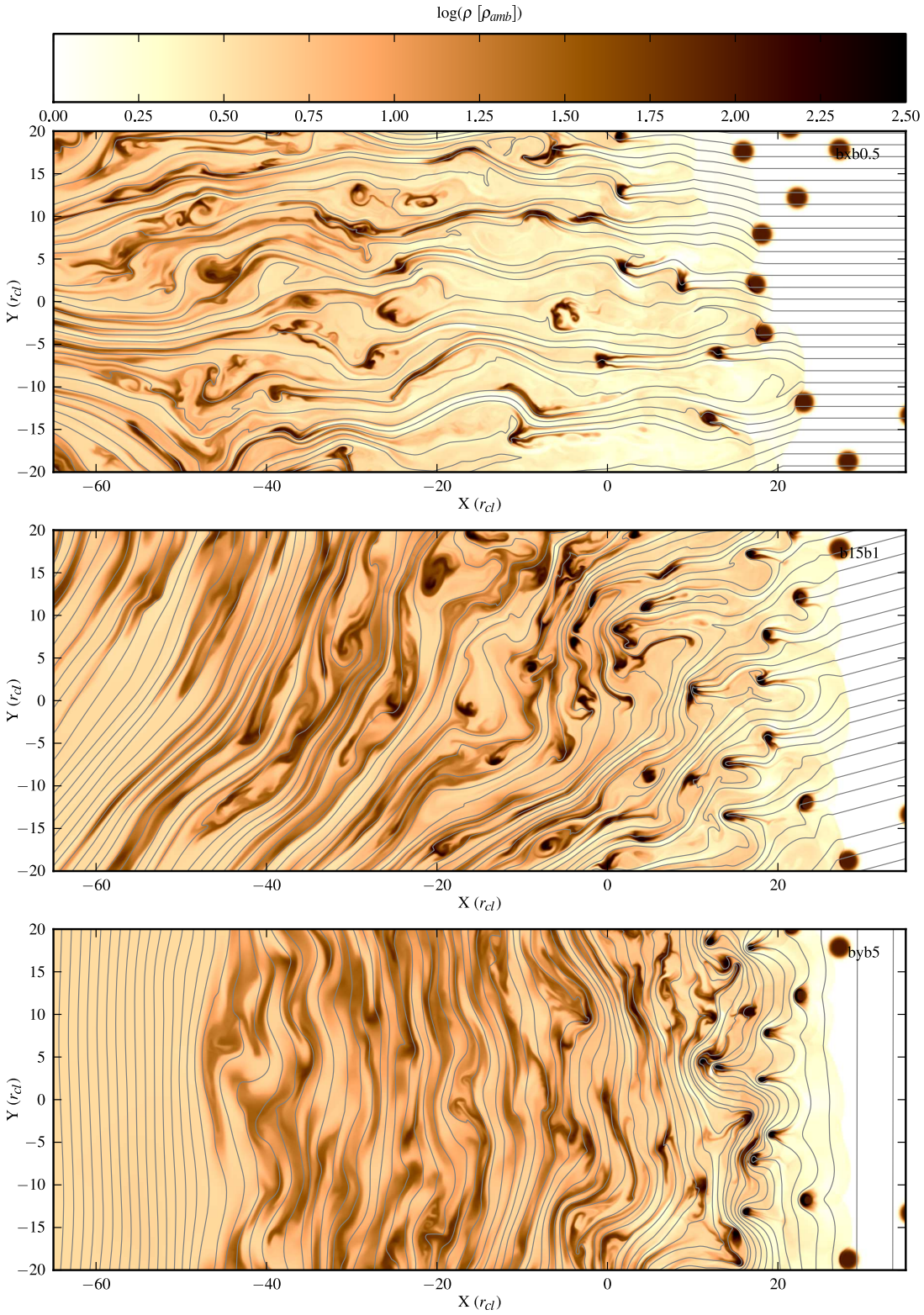

Figure 5.14: A close up of morphology snapshots at a time when the shock is halfway through the clumpy region for *M3chi2MR4* simulations with initial magnetic fields: parallel with $\beta_0 = 0.55$ (top), oblique with $\beta_0 = 1.13$ (middle) and perpendicular with $\beta_0 = 5.06$ (bottom) the times of snapshots are 29.3 t_{cc}, 35.8 t_{cc} and 37.9 t_{cc} (top to bottom).

evolution, particularly in the early stages, is more uniform across y. Only the $y = 0$ large-scale feature caused by lower local density remains.

Two large-scale 'flux-ropes' can be identified in the MR = 1 simulation shown in Fig. 5.15. They correspond to the two slices with MR > 2.5.

With perpendicular magnetic field the clouds can affect the flow further away via magnetic tension. The clouds accelerate faster and even overshoot the velocity of the post-shock flow causing oscillations in the 'shell'. Similarly, the shock reaches its 'steady state' (Chapter 3) velocity much earlier.

As seen in Chapter 4, oblique magnetic fields curve round an obstacle. Periodic boundary conditions limit this and a secondary restoring curve occurs. Individual clouds are focused where the field kinks, e.g. the $x = 150$, $y = 10$ region in the middle panel of Fig. 5.13 and the $x = 0$, $y = 10$ region in the middle panel of Fig. 5.14. When $M = 10$, the flow forces its way deep into the lower density $y = 0$ region (see Fig. 5.16).

Distributions of the plasma β are shown in Fig. 5.17 at two snapshots. The time of the snapshots corresponds to when the shock is at roughly $x = 100$ and $x = 300$. In simulation *bxb0.5* the values are very different in the 'flux-rope' and outside it, resulting in a flat distribution between $\beta = 0.5$ up to $\beta = 25$ for cloud material at the earlier time.

The excess magnetic energy (Fig. 5.18) increases very quickly in the first few t_{cc} after which it steadily increases while the shock is propagating through the clumpy region. An increase of the number of clouds by a factor of 4 leads to an increase in the maximum excess magnetic energy by a factor of 2.

The shapes of the excess magnetic energy curves are almost identical for the different initial magnetic field orientations and seem to only depend on the mass

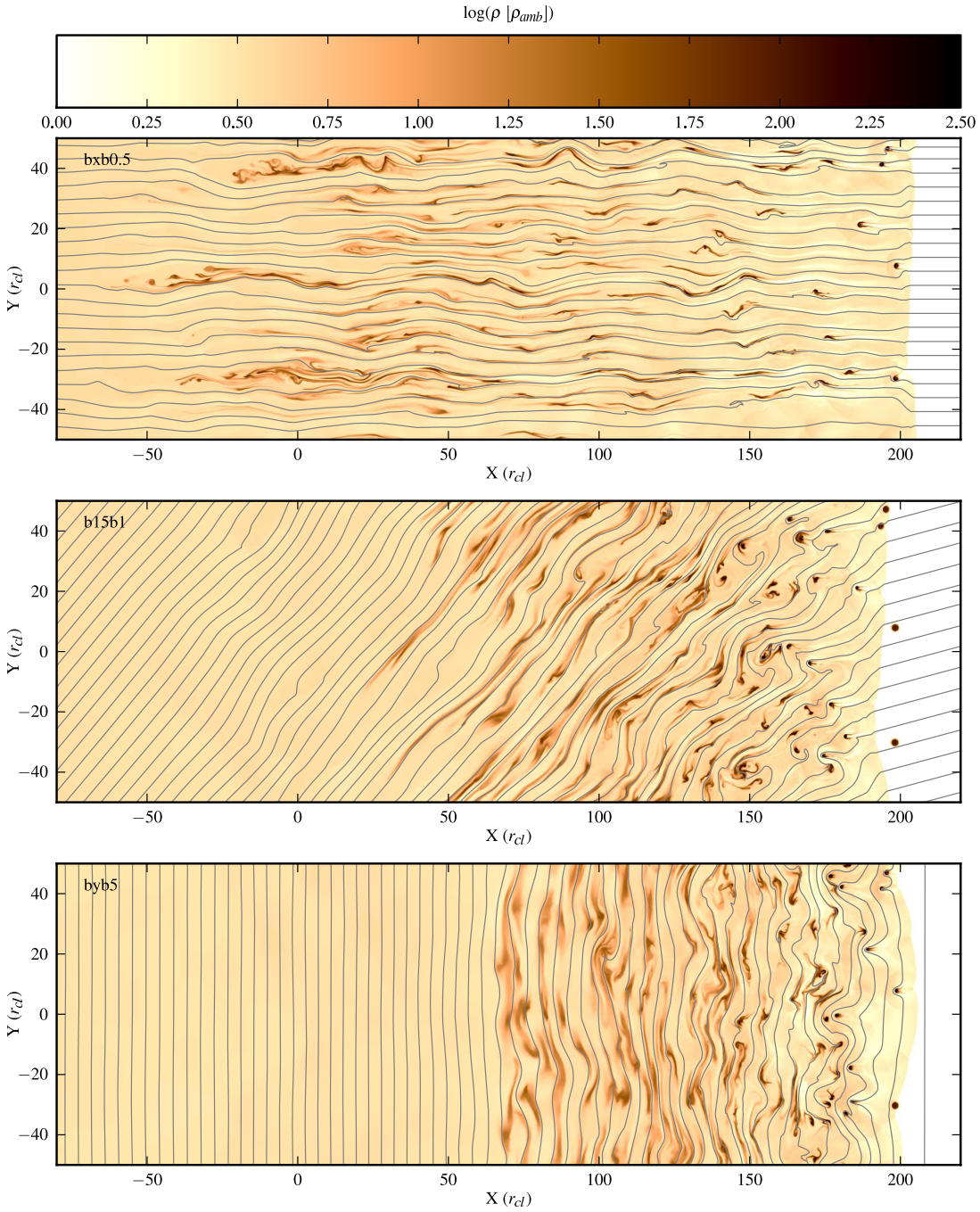

Figure 5.15: Morphology snapshots at a time when the shock leaves the clumpy region for *M3chi2MR1* simulations with an initial magnetic field which is parallel with $\beta_0 = 0.55$ (top), oblique with $\beta_0 = 1.13$ (middle) and perpendicular with $\beta_0 = 5.06$ (bottom). The times of the snapshots are $44.8\,t_{cc}$, $48.8\,t_{cc}$ and $50.5\,t_{cc}$ (top to bottom).

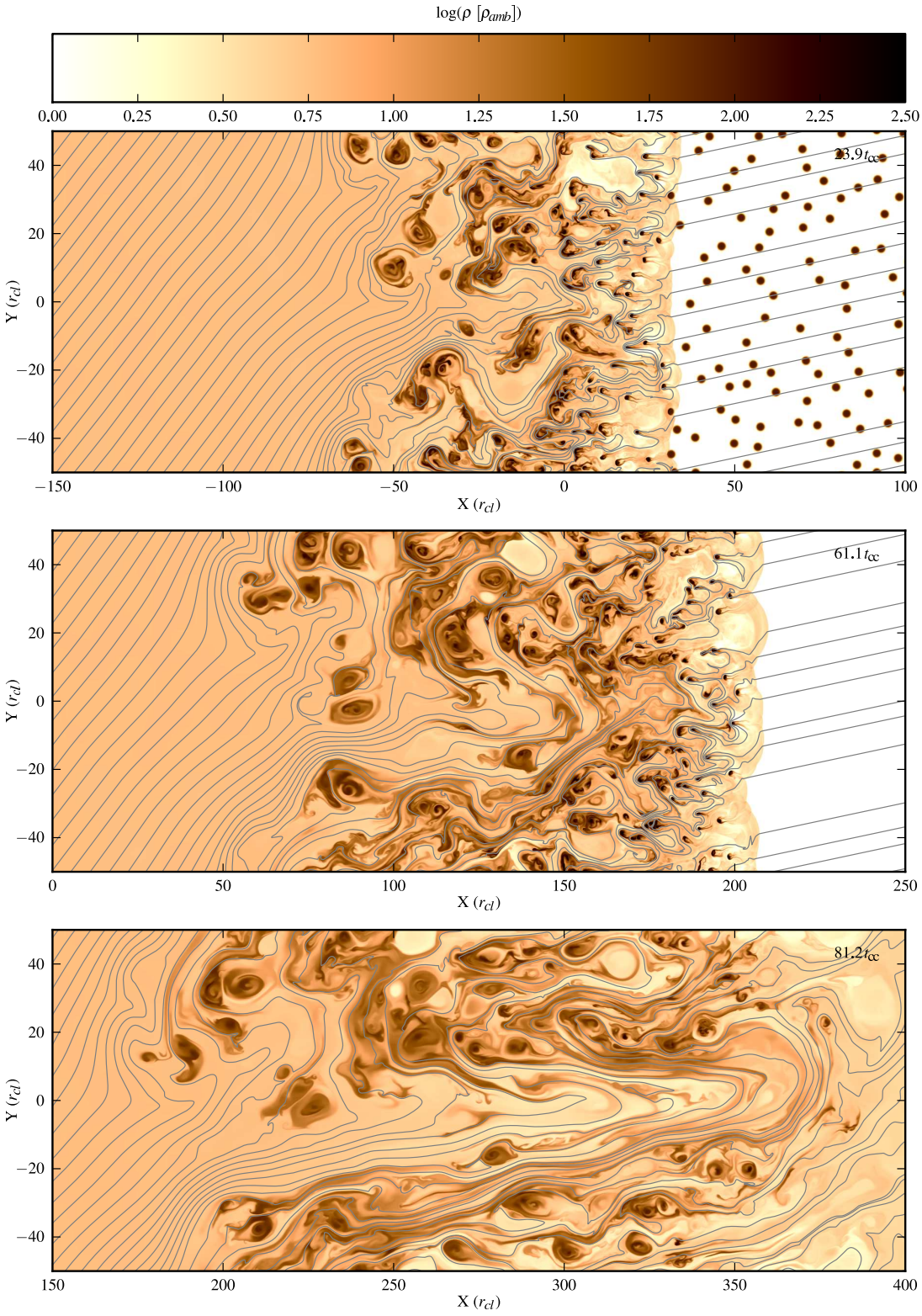

Figure 5.16: The evolution of the *M10chi2MR4* (Alfvénic Mach number, $M_a = 9.57$) simulation with an oblique magnetic field ($\theta_0 = 12°$) and $\beta_0 = 1.1$. Snapshots are shown at times 23.9 t_{cc}, 61.1 t_{cc} and 81.2 t_{cc} (top to bottom).

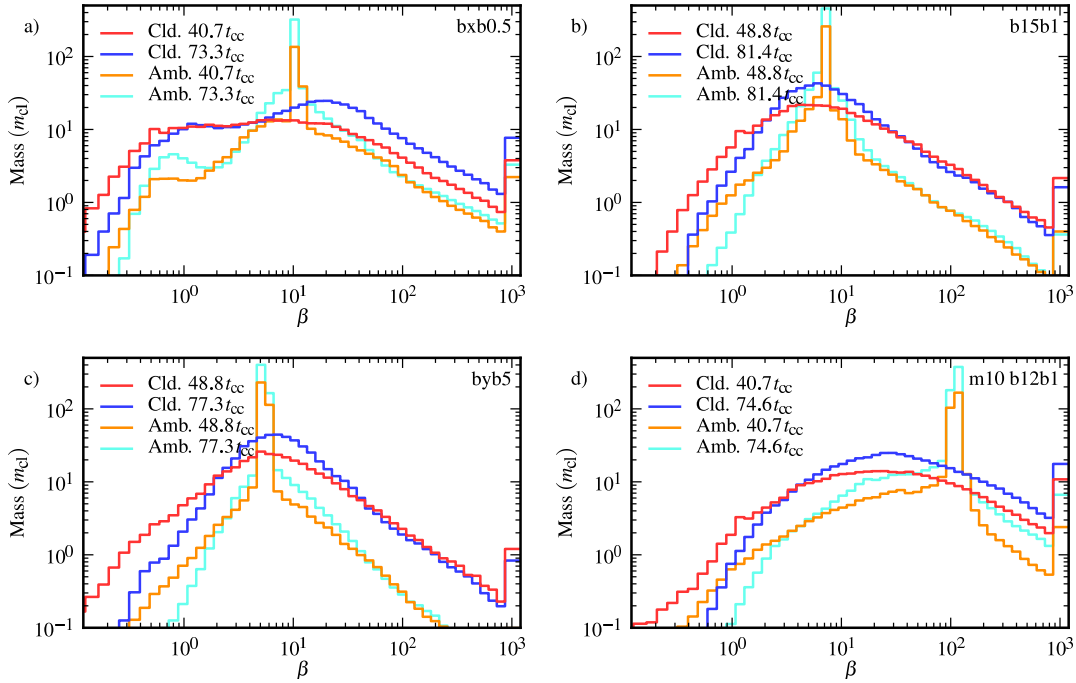

Figure 5.17: Distributions of the plasma β for cloud material and flow material in the region bounded by the forward and reverse global shocks in the *chi2MR4* distributions.

ratio of the cloud distribution and the Mach number (see Fig. 5.19). The maximum is reached at the same time for all three field orientations. The reasons for this are unclear at this stage. It is particularly perplexing as this means that the maximum is reached some $12\,t_{cc}$ *after* the shock leaves the clumpy medium in *M3chi2MR4 bxb0.5*, but $\sim$20 t_{cc} *before* such a time in *M3chi2MR1 byb5*.

5.4 Finite clumpy regions

Edge effects come into play if the clumpy region is finite in extent (i.e. without a periodic boundary condition). To investigate this we perform simulations with a

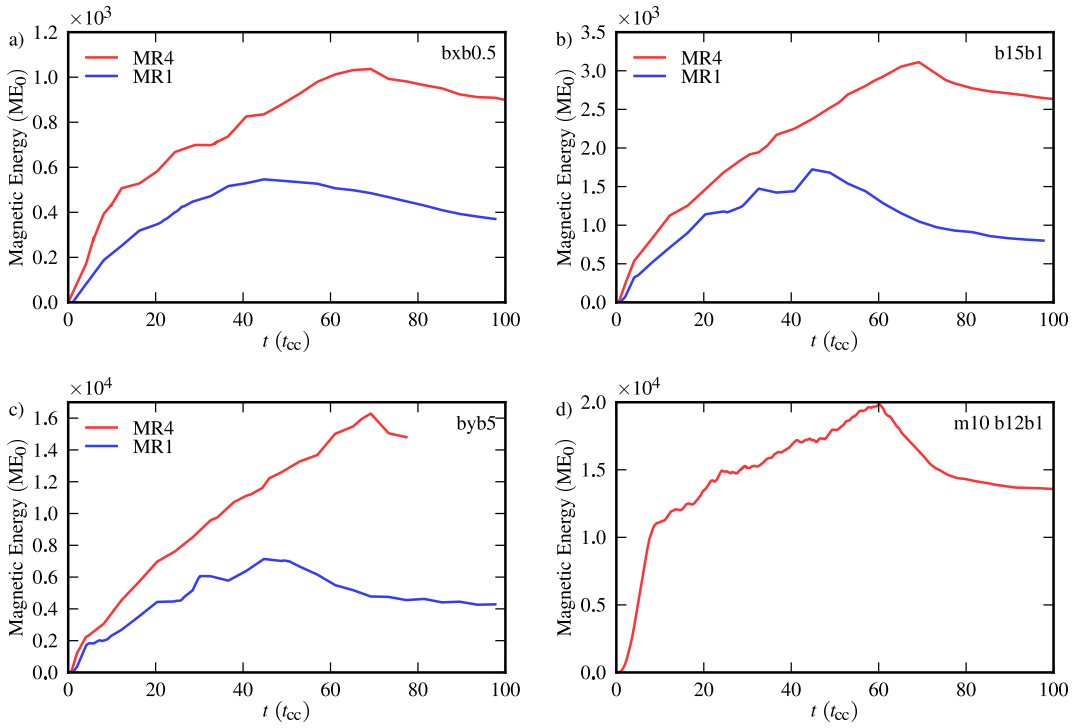

Figure 5.18: Evolution of the excess magnetic energy on the grid normalized to the initial magnetic energy of a single cloud for $M = 3$ simulations with (a) parallel, (b) oblique and (c) perpendicular magnetic fields and (d) for an $M = 10$ simulation with an oblique magnetic field.

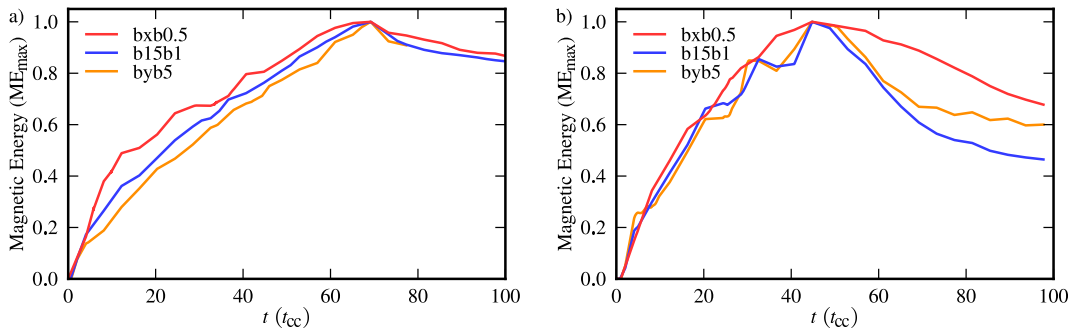

Figure 5.19: Evolution of excess magnetic energy on the grid normalized to the maximum excess magnetic energy that is achieved. The cloud distributions are (a) *chi2MR4* and (b) *chi2MR1*.

clumpy region extending from $x = \pm 200 r_{cl}$ and $y = \pm 50 r_{cl}$. Morphology snapshots of *chi2MR4* are shown in Fig. 5.20.

As the forward shock slows down as it propagates through the clumpy medium, the edge regions are overrun by the shock from the sides first. As this distribution has a depth to width ratio of 4 a rather large fraction of clouds experience the shock from the side. The direction of the shock relative to the field lines is different to that of the forward shock. In the parallel field case the side shock propagates perpendicular to the field lines and the early evolution of the edge clouds appears similar to the perpendicular field case in infinite clumpy regions. The side shock compresses the region, but it then rebounds downstream. This is seen spectacularly between $x = 25$ and $x = 0$ in the top panel of Fig. 5.20. The large scale 'flux-ropes' seen in the periodic case do not persist, but a similar distribution of cloud remnants along the field lines is seen, though the field lines are curved. The clouds in the very central region evolve slightly differently. The regular structure associated with the magnetic field is not as pronounced there, but it is unclear if this is because the local density there is lower (Fig. 5.11) or because it experiences a forward parallel shock rather than a perpendicular side shock.

The field wraps around the clumpy region in the oblique field case (see the middle panel of Fig. 5.20). The field is more parallel to the forward shock at the top (but perpendicular to the side shock) and more perpendicular at the bottom (but more parallel, yet still oblique, to the side shock). The field, shock and flow directions evolve in a complicated manner. For instance, most of the clouds at the top of the distribution initially experience a perpendicular shock but, soon after, the postshock flow changes to a nearly parallel direction, the field lines then curve and the morphology becomes that of the oblique field case.

In the perpendicular field case (see the bottom panel of Fig. 5.20), the side shock is oblique. The region is squeezed by a factor of nearly 3 (compare the width of the distrbution at $x = 50$ to its initial width), but afterwards expands along the field similarly to an individual cloud.

5.5 Weak magnetic fields

A weak magnetic field may prevent cloud destruction without inhibiting compression. While turbulence is strongly suppressed when $\beta \sim 1$ and field amplification occurs primarily in large scale compressive flows, in the weak field case, with $\beta \sim 1000$, turbulence can play a major role in modifying the field.

A three cloud arrangement *s3w4a15* (see Sec. 4.3.3) was used and three simulations were performed: *bxb565* (parallel field, $\beta_0 = 565$), *b15b1130* (oblique field, $\beta_0 = 1130$) and *byb5060* (perpendicular field, $\beta_0 = 5060$). Fig. 5.21 shows the density snapshots of these simulations at $t = 6.5\, t_{cc}$ and of corresponding low β simulations. Without suppression of turbulence and instabilities these simulations are much more sensitive to resolution. In this case R_{128} was used.

When the field is strong, the plasma β reaches its minimum values relatively early and increases as the cloud re-expands. However, the full distributions do not change much (see Fig. 5.22). In the weak field case the plasma β continues to decrease as turbulence develops and the magnetic field is amplified. The distribution of β becomes much wider, and eventually spans over four magnitudes in β. Very small cloud regions can achieve values of β as low as those in the strong field case although only ∼1% of the mass drops below $\beta = 1$ (Fig. 5.22).

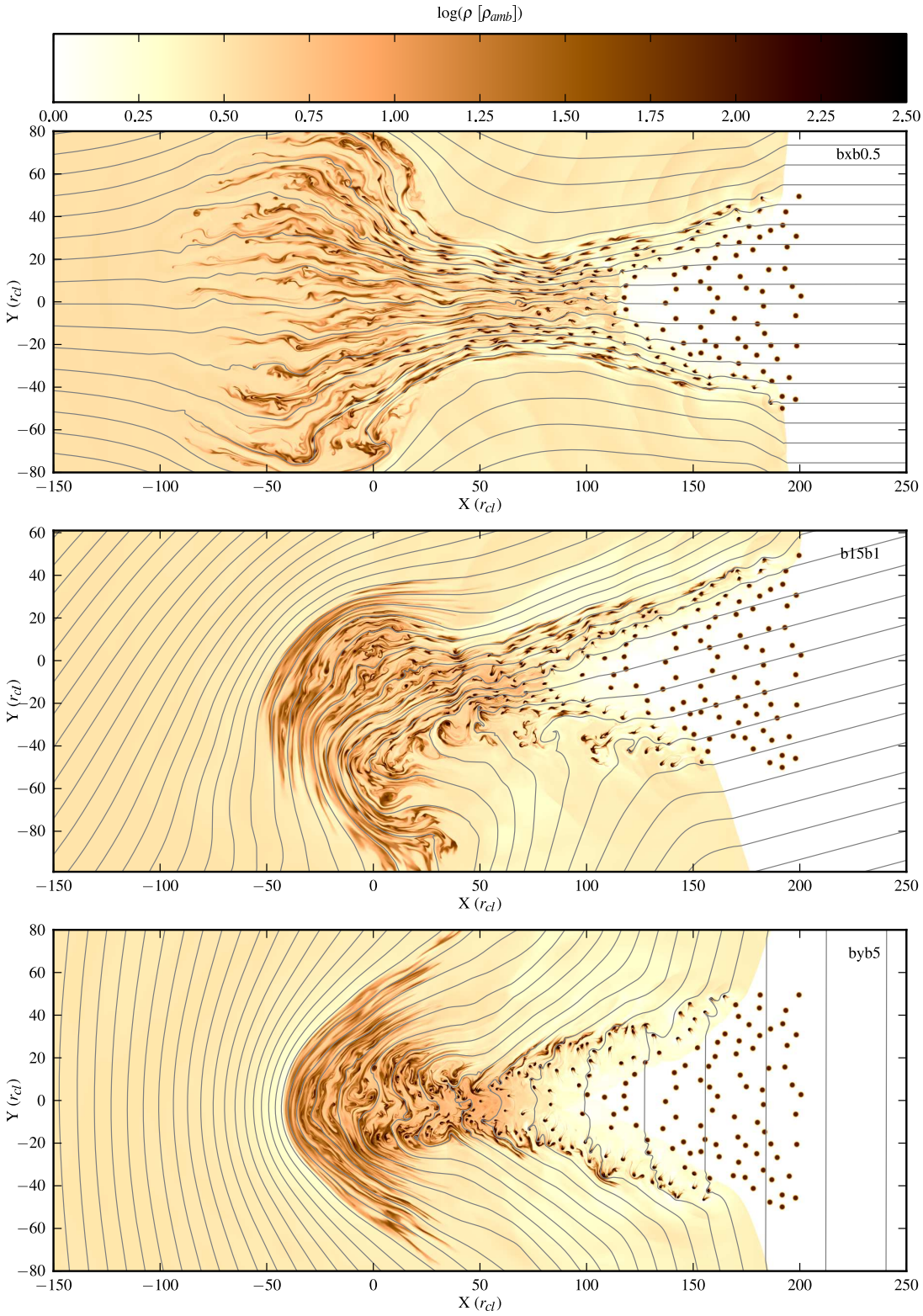

Figure 5.20: Morphology snapshots at $t = 40\,t_{cc}$ in *M3chi2MR4* finite region simulations with initial magnetic field orientation parallel with $\beta_0 = 0.55$ (top), oblique with $\beta_0 = 1.13$ (middle) and perpendicular with $\beta_0 = 5.06$ (bottom).

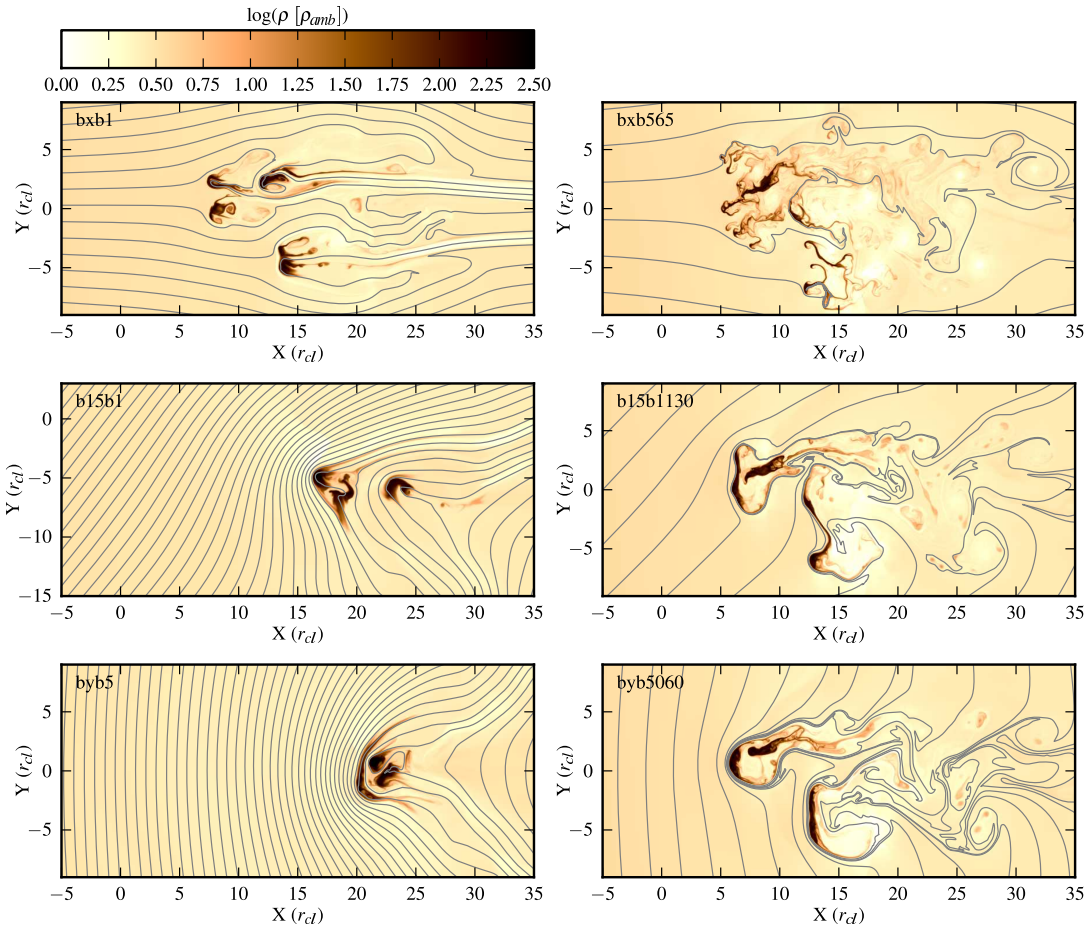

Figure 5.21: Morphology snapshots at $t = 6.5\, t_{cc}$ of strong field (left) and weak field (right) with parallel (top), oblique (middle) and perpendicular (bottom) magnetic fields. The initial cloud arrangement is *s3w4a15*. Weaker fields on the right side are represented by 10 times as many field lines as a same strength field would show on the left side.

5.6 3D simulations

Additional field morphologies are possible in 3D simulations. Oblique and perpendicular field lines are no longer forced to lie in the plane of the clouds. Furthermore, the field lines can slip around the clouds instead of being forced to wrap round them. For multiple cloud simulations this means that clouds are less likely

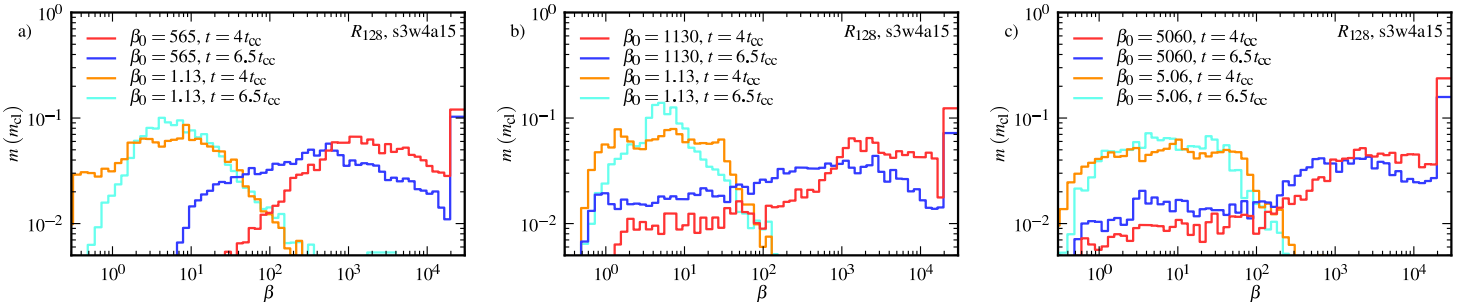

Figure 5.22: Distributions of the plasma β in region bounded by the forward and reverse shocks in strong field and weak field cases with (a) parallel, (b) oblique and (c) perpendicular magnetic fields.

to fall on the same field line (which is when the most dramatic effects were seen), there is less acceleration from the build up of magnetic pressure and the clouds are less likely to form tight groups blanketed by field lines. These effects are still possible, but perhaps not as inevitable as in 2D simulations.

The morphologies of 3D variants of *s3w4a15 b15b1* ($M = 3$, $M_a = 2.91$ and $\chi = 10^2$) are shown in Fig. 5.23. The resolution is R_{16} and the field is in the x–y plane. In the top panel the clouds and the field lie in the same plane and this can be directly compared to the 2D oblique field case (cf. Fig. 4.24c). The most upstream cloud appears to be engulfing 'cld2' more akin to *s3w4a45* in 2D (Fig. 4.24e). In the other two panels the clouds and the field are inclined by $\phi = 30°$ (middle panel) and $\phi = 90°$ (bottom panel). The interaction is less direct but the clouds still affect one another, for instance see how the 'tail' of 'cld1' snakes between the other two.

In the parallel field case the difference between 3D and 2D should be less although the probability that randomly distributed clouds lie on the same field line is smaller. Fig. 5.24 shows a volume rendering at $t = 4\,t_{cc}$ of the *s2w2o8* cloud arrangement (the clouds are located in the x–y plane). The general features can

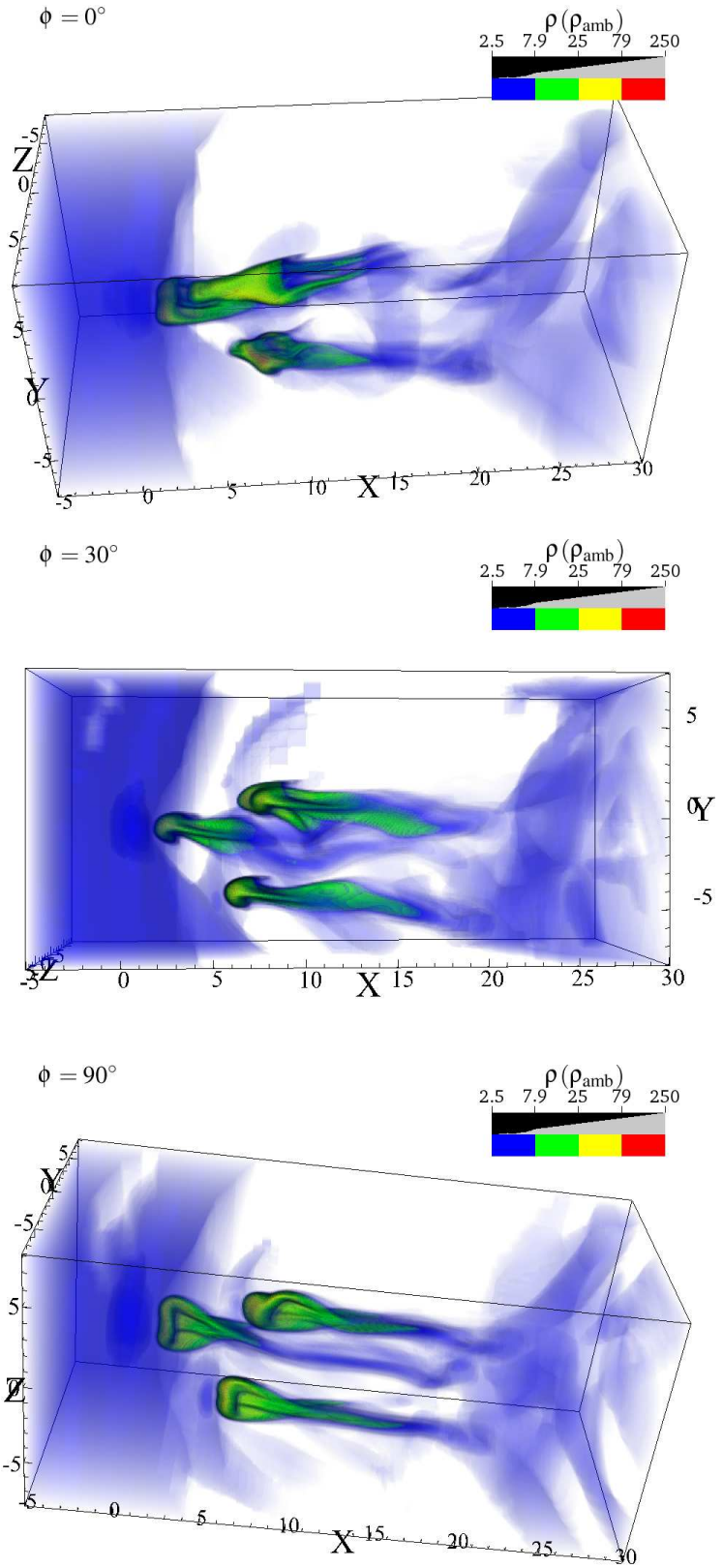

Figure 5.23: Volume rendering of the density in 3D oblique field simulations at $t = 4\,t_{cc}$. The field is in the x–y plane with $\beta_0 = 1.13$ and $\theta_0 = 15°$ (in the post-shock flow $\theta_1 \approx 45°$). The cloud arrangement is *s3w4a15*, the clouds are located in the $z = 0$ plane (top), $y = 0$ plane (bottom) and $\sin 30° y - \cos 30° z = 0$ plane (middle). For illustration purposes the cloud plane is inclined at roughly −60° to the observer.

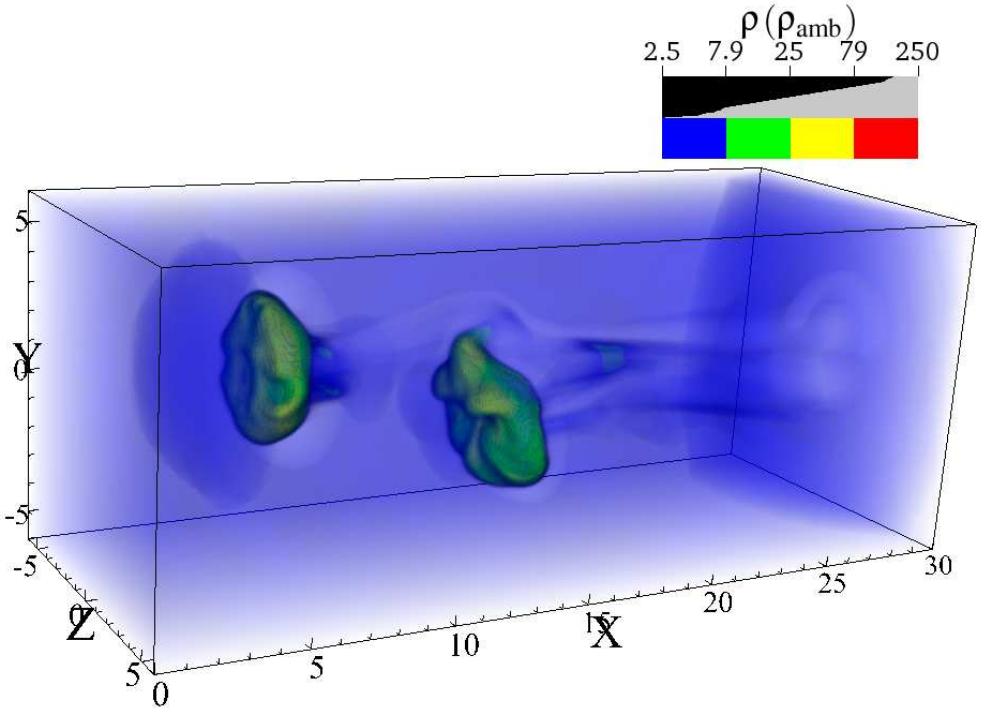

Figure 5.24: Volume rendering of density in 3D *s2w2o8* simulation at $t = 4\,t_{cc}$. The field is parallel to the direction of shock propagation (along the x-axis) and $\beta_0 = 1.13$ (*bxb1*).

be compared to the 2D simulation in Fig.4.2e. In this particular case it seems that unlike in the 2D case there is no mass stripping channel at $y \approx -2$. The downstream cloud is stripped more from the inside edge, somewhat similarly to the 2D simulation *s2w4o8* shown in Fig. 4.2d, suggesting that in 3D the field lines find it easier to move between the clouds.

Future work should examine the differences between the evolution of the individual clouds in the multi-cloud simulations compared to that in the single-cloud simulations, and to look for differences and similarities between 2D and 3D studies.

5.7 Conclusions

This Chapter has shown that the resolution requirements in MHD shock cloud interactions are slightly different than for the hydrodynamic case. Because instabilities and turbulence are suppressed by strong magnetic fields the condition that they are resolved at their dominant scales is not sufficient. Instead, we find that magnetic reconnection and diffusion across the field lines sets the minimum resolution requirements. We find that good qualitative agreement is reached at R_{32} but quantitative differences, although decreasing, remain even at R_{128}. In general we find somewhat lower resolution requirements in MHD simulations compared to purely hydrodynamic simulations, and lower requirements in multiple cloud simulations compared to single cloud simulations.

Insights gained from Chapter 4 on the evolution of several clouds can be applied to large clumpy regions containing tens or hundreds of clouds. In the parallel field case, the dominant criteria determining the cloud evolution is whether there is a cloud directly upstream. In a large clumpy region this is related to the total mass

in the slice of the region upstream of the cloud. The differences in this total mass as a function of position along the shock are amplified as the shock sweeps through the clumpy region and even nearby clouds can evolve very distinctly.

In the oblique case the field lines wrap around the clouds reducing their separation and often causing them to exchange relative positions. It is limited in the infinite regions but still, particularly in the stronger shock and higher post-shock β case multiple clumps of several clouds in close proximity are formed (Fig. 5.16).

When a region is not infinite, the shock enters it from the sides as well. The field orientation is relevant in the morphology of the region as a whole (it evolves a bit like a large individual cloud). However, individual clouds, particularly those towards the sides of the clumpy region, experience a range of different field–flow orientations.

In 3D simulations the field lines can slip around the clouds, and arrangements where two clouds are on the same field line are also less likely. This may limit the most extreme effects seen in the 2D cases and future studies will need to investigate these differences.

Finally, a weak magnetic field is interesting as it does not suppress the turbulence as much. Turbulent amplification can increase even a weak magnetic field to equipartition ($\beta \sim 1$) or even a little below (cf. Fig. 5.22). The studies of the turbulent magnetized ISM (e.g. Lemaster & Stone 2008) could benefit from studies of shock-cloud interactions with weak magnetic fields where the presence of clouds provides the driving mechanism for the turbulence (e.g. Inoue *et al.* 2009).

Chapter 6

Conclusions

6.1 Summary

This work has contributed to our understanding of the interaction between shocks and clouds by investigating how this interaction is modified by the presence of multiple clouds. A large parameter space was explored and a lot of complex interactions were observed, but some general features can be distilled out of it.

In Chapter 3 we have investigated the purely hydrodynamic interaction where the clumpy region is infinitely wide. Material stripped from the clouds 'mass-loads' the flow and leads to the formation of a dense shell. The average properties of the shell can be approximated by the interaction of a shock and a uniform (1D) density region where the density contrast of the uniform region is equal to the average density contrast in the clumpy region ($\chi_{\rm uniform} = {\rm MR} + 1$). It takes about a cloud destruction length, $L_{\rm CD}$, for individual clouds to be incorporated into the shell, and the differences between a uniform and a clumpy distribution are of that length-scale. For $\chi = 10^2$ clouds $L_{\rm CD}$ is much smaller than the assumed size of the clumpy

region, but for $\chi = 10^3$ clouds $L_{\rm CD}$ is comparable to the depth of the clumpy region and a shell does not form.

A 1D uniform region can also predict the maximum deceleration of the shock. A shock traversing the clumpy region decelerates, but when (if) a shell is formed a 'steady-state' begins. The shock velocity in the steady state matches that of the transmitted shock in the 1D simulation, but there is a caveat. From eq. 5.4 in Klein *et al.* (1994) we see that a shock transmitted into a higher density region slows down, but its Mach number remains the same or even increases because of the lower sound speed in the higher density medium. When there are discrete individual clouds the sound speed in the ambient medium remains high, so that a slowed down mass-loaded shock decreases in Mach number and can decay into a wave. This was seen in the simulation where the initial shock was weak, with a Mach number $M = 1.5$.

An interesting issue is the effect a turbulent mass-loaded flow has on the lifetimes of the clouds it encounters. In this work we have highlighted some pitfalls in trying to determine this. The resolution requirements are lower in multiple-cloud simulations as instabilities do not have to develop from small fluctuations when the flow is already turbulent. Additionally, clouds lose more mass to ablation in a 'mass-loaded' flow, which is less sensitive to resolution. This makes multiple-cloud simulations feasible as they can be performed at somewhat lower resolution, but an interaction with a 'clean' shock at the same resolution will be under-resolved, and thus a direct comparison at the same resolution will produce misleading conclusions.

After accounting for resolution effects, it appears that the predominant effect of the shell, when it is formed, is to homogenize the lifetimes. As the shell follows the

shock $\sim 1\, L_{\rm CD}$ behind, the clouds encounter it $\sim 1\, t_{\rm CD}$ after the shock passes. Even if the shock is slowed down, ablation in the shell ensures that clouds are destroyed in $\sim 1\, t_{\rm CD}$. Thus, clouds in the clumpy region are destroyed on a comparable time scale to single clouds.

However, a change in lifetime can be seen in clouds which are denser than the majority of their brethren. For example, when a few $\chi = 10^3$ clouds are seeded in a distribution of clouds where the dominant density ratio $\chi = 10^2$, it can be seen that those clouds which encounter a fully formed shell are destroyed faster than those which do not. However, the effect is not very strong, being perhaps of order of 10–20% in the cloud lifetimes. Some outliers in the destruction time are also seen and a more rigorous definition of the cloud lifetime will help to evaluate the difference in future work.

The addition of magnetic fields expands the parameter space further. Compared to the individual cloud case, the geometry of the problem is significantly modified by the relative arrangement of field and clouds. This is the first work to explore a variety of such interactions. In Chapter 4 the interactions were limited to two and three clouds and the effect of varying their relative positions was investigated.

In the parallel field case the presence of a neighbouring cloud alongside limits the expansion and fragmentation of the cloud. In order for the cloud to expand it has to push the field lines aside which is limited by any nearby cloud. The separation of the clouds along the direction of the flow is not so important, with the evolution primarily determined by the 'width' separating the clouds. For clouds separated along the flow direction, if the 'width' is large enough for the flow to pass between the clouds ($\sim 4\, r_{\rm cl}$), the evolution is similar to that occuring if the clouds were alongside one another. For a 'width' of $\sim 2\, r_{\rm cl}$ the flow deflected from

the upstream cloud passes the downstream cloud on the outside and the field lines curve around and confine it in a roughly circular shape. In such cases the downstream cloud is pushed towards the 'flux-rope' (i.e. the shielded region behind the upstream cloud). When two clouds are on the same field lines, the downstream cloud falls in the 'flux-rope'. It experiences an initial shock compression stage, but is neither compressed nor is accelerated as there is very little flow in the 'flux-rope'. The cloud re-expands along the field lines into an elongated shape, but further evolution is delayed until the upstream cloud collides into it. The evolution is significantly different for the perpendicular field case. Perpendicular field lines tend to drive clouds together as the field lines bend around them, although clouds can only merge if they lie on the same field lines to begin with.

The oblique field case is a more general one sharing some features with both the parallel and the perpendicular field cases. The evolution of a cloud not only depends on its relative position in the upstream–downstream direction, but also in the upfield–downfield direction. As the field lines bend around the two clouds, a downfield cloud is accelerated downstream more, while an upfield cloud experiences a greater transverse acceleration. In many cases the clouds swap relative positions (but of course, not the field lines they lie on). As one cloud moves into the lee of the other it is 'shielded' from the flow, the confining forces on it are reduced and it expands. Alternatively, when the cloud is suddenly exposed to the flow it experiences a second period of compression.

Adding a third cloud does not complicate things too much. In many cases two of the three clouds interact as before, while a more distant third cloud acts as a 'modifier'. In cases with an oblique field, as in cases with a perpendicular field, the clouds are driven towards each other. The three cloud interaction can thus

be often deconstructed as a two-step two-cloud interaction i.e., to start with two nearby clouds interact independently of the third, and then the resulting structure interacts with the third cloud.

In Sec. 5.3 we expanded this work to clumpy regions of infinite width. In one sense such a scenario is simpler than when there are only a few clouds as a strong field sets the global structure, but the field cannot wrap around the clumpy region as the region is infinite in extent. However, in an $M = 10$ oblique field simulation the field wraps around groups of 2 to 5 clouds creating clumps of several clouds (the relatively weaker field in this case is pushed around by the flow).

In the parallel field case large scale 'flux-ropes' form in regions where the average density directly upstream is relatively higher. The evolution of nearby clouds can then be very different depending on their location relative to the 'flux-rope'.

Finally, the interaction of a shock with large but finite clumpy regions is studied. The shock sweeps around the whole region driving shocks in from the sides, the orientations of which are different to the forward shock. The evolution of a cloud may then evolve through a whole set of field-flow orientations.

6.2 Future work

One important omission in this work was to ignore cooling effects. It can be shown that cooling behind shocks is very efficient for the typical conditions in the ISM, so much so that the isothermal equation of state is a common assumption. However, different regions cool at different rates and it is the balance between processes that confine and compress the clouds and ones that disperse them that determine their evolution. The work in this Thesis is focused on the dispersive effects and how the

presence of nearby clouds affect their evolution. Future work will have to include the cooling effects and study the balance between confinement and dispersive processes. For example, we see a large scale shell forming out of cloud material in hydrodynamic simulations. With strong cooling a shell may form through condensation of the swept up material, but the clouds would likely fragment and not be incorporated in it. With moderate cooling something similar to the shell may still form and then fragment, recycling the old clouds into new clouds. Fig. 6.1 indicates how cooling can affect the interaction of a shock with a group of clouds.

To improve the correspondence to the physical conditions the simulations should also be performed in 3D. Cylindrical clouds may not be that unphysical, considering the filamentary nature of the ISM, but the nature of instabilities and turbulence needs to be checked in 3D. Some preliminary MHD results were shown in Sec. 5.6. Hydrodynamic results also need to be checked in 3D, of which an example is shown in Fig. 6.2. However, because of computational cost the resolution is only R_{16}, which we have shown to be insufficient.

Including cooling/heating (and possibly thermal conduction) and performing 3D simulations allows specific objects to be modelled. Some recent work modelling the evolution of a supernova evolution and how it is affected by the morphology of the surrounding medium has been recently presented by Obergaulinger *et al.* (2014) and Zhou *et al.* (2011).

More abstract studies remain useful as well. Chapter 5 has shown how complicated the evolution of large finite regions can be, and the difficulties one faces in defining cloud lifetimes. It also shows how initially weak magnetic fields can be turbulently amplified. Simulations will need to remain simplified to isolate these effects and to better understand the processes at play.

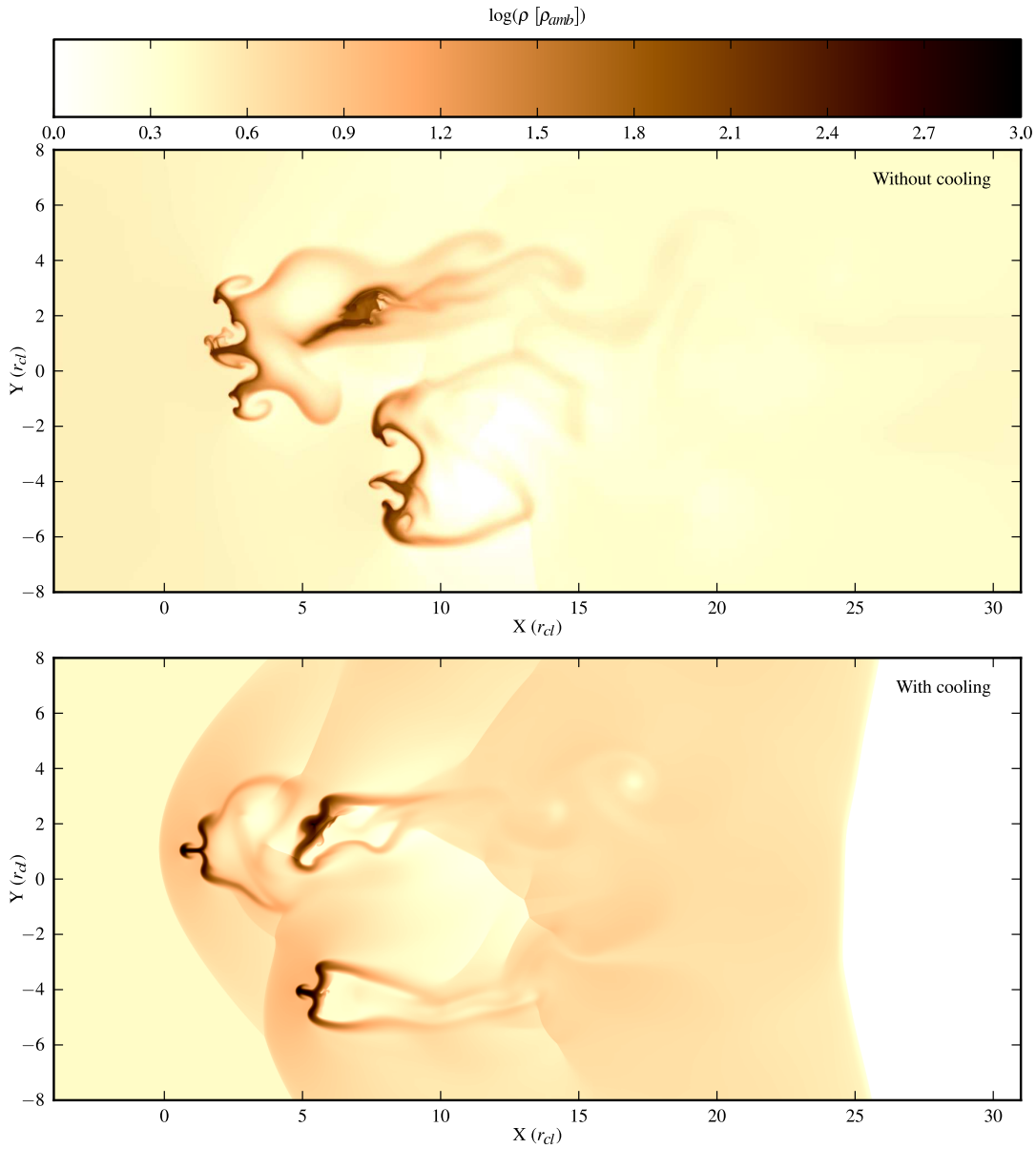

Figure 6.1: Morphology snapshots of a three cloud simulation without cooling (top) and with cooling (bottom). By using the cooling curve from Smith *et al.* (2008), $r_{\rm cl} = 5800\,{\rm AU}$, $n_{\rm amb} = 0.154\,{\rm cm}^{-3}$, $n_{\rm cl} = 10\,{\rm cm}^{-3}$ ($\chi = 65$) and $M = 3$ the cooling time for the shocked cloud is $t_{\rm cool} = 0.07\,t_{\rm cc}$. A heating rate, $\Gamma = 6.5 \times 10^{-27}\,{\rm erg\,s}^{-1}$, was used to maintain the unshocked medium stable at stable temperatures of $T = 10^4{\rm K}$ for the ambient medium and $T = 155{\rm K}$ for clouds.

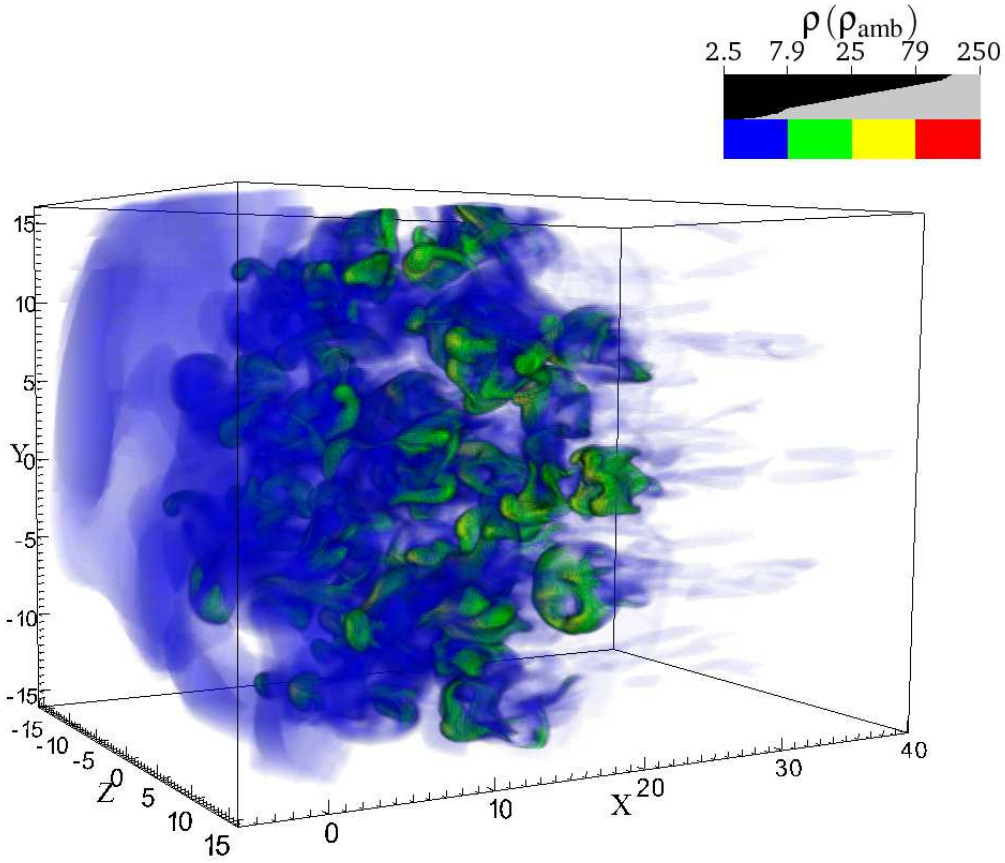

Figure 6.2: A 3D rendering of a simulation of a spherical clumpy region of radius $16\,r_{\rm cl}$ with 39 clouds. The time is $t = 8.1\,t_{\rm cc}$. $M = 3$, $\chi = 10^2$ and MR $= 1$.

6.3 Concluding remarks

In order to isolate the effects of a particular process some simplifications need to be made. This Thesis presented the first simulations with a large number of clouds which are able to significantly mass load the flow. It was not intended to be directly compared to observations but the generalizations that were drawn will aid the interpretation of future studies and in particular of future simulations.

In the last few years a number of very sophisticated simulations have been pre-

sented in the literature which are able to match observations very well. The wealth of physics included in these models makes untangling them almost as difficult as the real thing. Studies like the ones presented in this Thesis, that build from the bottom up exploring the parameter space at each step, will remain a valuable tool.

> I have a truly marvellous proof of this proposition which this margin is too narrow to contain.
>
> Pierre de Fermat, 1637

References

ADAMS, W.S. (1949). Observations of Interstellar H and k, Molecular Lines, and Radial Velocities in the Spectra of 300 O and B Stars. *ApJ*, **109**, 354.

AGER, M.A. (2009). *Magnetohydrodynamical Fragmentation*. Ph.D. thesis, University of Leeds.

ALŪZAS, R., PITTARD, J.M., HARTQUIST, T.W., FALLE, S.A.E.G. & LANGTON, R. (2012). Numerical simulations of shocks encountering clumpy regions. *MNRAS*, **425**, 2212–2227.

ALŪZAS, R., PITTARD, J.M., FALLE, S.A.E.G. & HARTQUIST, T.W. (2014). Numerical simulations of a shock interacting with multiple magnetized clouds. *MNRAS*, **444**, 971–993.

ALFVÉN, H. (1942). Remarks on the Rotation of a Magnetized Sphere with Application to Solar Rotation. *Arkiv for Astronomi*, **28**, 1–9.

ANATHPINDIKA, S. & BHATT, H.C. (2011). On the interaction of a thin, supersonic shell with a molecular cloud. *MNRAS*, **412**, 921–934.

ANATHPINDIKA, S.V. (2010). Collision between dissimilar clouds: stability of the bow-shock, and the formation of pre-stellar cores. *MNRAS*, **405**, 1431–1443.

ANDERSON, J.E. (1963). *Magnetohydrodynamic shock waves*.

AO, Y., HENKEL, C., MENTEN, K.M., REQUENA-TORRES, M.A., STANKE, T., MAUERSBERGER, R., AALTO, S., MÜHLE, S. & MANGUM, J. (2013). The thermal state of molecular clouds in the Galactic center: evidence for non-photon-driven heating. *A&A*, **550**, A135.

ARTHUR, S.J. & HENNEY, W.J. (1996). X-Rays from Mass-loaded Supernova Remnants in the Large Magellanic Cloud. *ApJ*, **457**, 752.

BAADE, W. & MINKOWSKI, R. (1954). Identification of the Radio Sources in Cassiopeia, Cygnus A, and Puppis A. *ApJ*, **119**, 206.

BAJAJA, E. & SHANE, W.W. (1982). High resolution HI observations of Messier 31. *A&AS*, **49**, 745–774.

BARNES, J.E., WOOD, K., HILL, A.S. & HAFFNER, L.M. (2014). Photoionization and heating of a supernova-driven turbulent interstellar medium. *MNRAS*, **440**, 3027–3035.

BECK, R. (2001). Galactic and Extragalactic Magnetic Fields. *Space Sci. Rev.*, **99**, 243–260.

BELL, A.R. (1978). The acceleration of cosmic rays in shock fronts. I. *MNRAS*, **182**, 147–156.

BERGIN, E.A., HARTMANN, L.W., RAYMOND, J.C. & BALLESTEROS-PAREDES, J. (2004). Molecular Cloud Formation behind Shock Waves. *ApJ*, **612**, 921–939.

BINNS, W.R., WIEDENBECK, M.E., ARNOULD, M., CUMMINGS, A.C., GEORGE, J.S., GORIELY, S., ISRAEL, M.H., LESKE, R.A., MEWALDT, R.A., MEYNET, G., SCOTT,

L.M., STONE, E.C. & VON ROSENVINGE, T.T. (2005). Cosmic-Ray Neon, Wolf-Rayet Stars, and the Superbubble Origin of Galactic Cosmic Rays. *ApJ*, **634**, 351–364.

BLITZ, L. (1990). The evolution of galactic giant molecular clouds. In L. Blitz, ed., *The Evolution of the Interstellar Medium*, vol. 12 of *Astronomical Society of the Pacific Conference Series*, 273–289.

BLITZ, L. & SPERGEL, D.N. (1991). Direct evidence for a bar at the Galactic center. *ApJ*, **379**, 631–638.

BLITZ, L., FUKUI, Y., KAWAMURA, A., LEROY, A., MIZUNO, N. & ROSOLOWSKY, E. (2007). Giant Molecular Clouds in Local Group Galaxies. *Protostars and Planets V*, 81–96.

BOFFETTA, G., CELANI, A. & VERGASSOLA, M. (2000). Inverse energy cascade in two-dimensional turbulence: Deviations from Gaussian behavior. *Phys. Rev. E*, **61**, 29.

BÖHM-VITENSE, E. (1992). *Introduction to stellar astrophysics. Volume 3. Stellar structure and evolution.*.

BOLATTO, A.D., WOLFIRE, M. & LEROY, A.K. (2013). The CO-to-H_2 Conversion Factor. *ARA&A*, **51**, 207–268.

BOVINO, S., SCHLEICHER, D.R.G. & GRASSI, T. (2014). Primordial star formation: relative impact of H_2 three-body rates and initial conditions. *A&A*, **561**, A13.

BRACKBILL, J.U. & BARNES, D.C. (1980). The effect of nonzero product of magnetic gradient and B on the numerical solution of the magnetohydrodynamic equations. *Journal of Computational Physics*, **35**, 426–430.

BROMM, V., COPPI, P.S. & LARSON, R.B. (2002). The Formation of the First Stars. I. The Primordial Star-forming Cloud. *ApJ*, **564**, 23–51.

BURSTEIN, D. (2003). Line-of-Sight Reddening Predictions: Zero Points, Accuracies, the Interstellar Medium, and the Stellar Populations of Elliptical Galaxies. *ApJ*, **126**, 1849–1860.

CASTOR, J., MCCRAY, R. & WEAVER, R. (1975a). Interstellar bubbles. *ApJL*, **200**, L107–L110.

CASTOR, J.I., ABBOTT, D.C. & KLEIN, R.I. (1975b). Radiation-driven winds in Of stars. *ApJ*, **195**, 157–174.

CHANDRASEKHAR, S. (1961). *Hydrodynamic and hydromagnetic stability*.

CHIAN, A.C.L. & MUÑOZ, P.R. (2012). Observation of magnetic reconnection at the turbulent leading edge of an interplanetary coronal mass ejection. In M. Faurobert, C. Fang & T. Corbard, eds., *EAS Publications Series*, vol. 55 of *EAS Publications Series*, 327–334.

CHU, Y.H. & KENNICUTT, R.C., JR. (1994). Kinematic structure of the 30 Doradus giant H II region. *ApJ*, **425**, 720–737.

CIOFFI, D.F., MCKEE, C.F. & BERTSCHINGER, E. (1988). Dynamics of radiative supernova remnants. *ApJ*, **334**, 252–265.

COMBES, F., YOUNG, L.M. & BUREAU, M. (2007). Molecular gas and star formation in the SAURON early-type galaxies. *MNRAS*, **377**, 1795–1807.

COOPER, J.L., BICKNELL, G.V., SUTHERLAND, R.S. & BLAND-HAWTHORN, J. (2008). Three-Dimensional Simulations of a Starburst-driven Galactic Wind. *ApJ*, **674**, 157–171.

COOPER, J.L., BICKNELL, G.V., SUTHERLAND, R.S. & BLAND-HAWTHORN, J. (2009). Starburst-Driven Galactic Winds: Filament Formation and Emission Processes. *ApJ*, **703**, 330–347.

CORBELLI, E., LORENZONI, S., WALTERBOS, R., BRAUN, R. & THILKER, D. (2010). A wide-field H I mosaic of Messier 31. II. The disk warp, rotation, and the dark matter halo. *A&A*, **511**, A89.

COWIE, L.L., MCKEE, C.F. & OSTRIKER, J.P. (1981). Supernova remnant revolution in an inhomogeneous medium. I - Numerical models. *ApJ*, **247**, 908–924.

COX, D.P. (2005). The Three-Phase Interstellar Medium Revisited. *ARA&A*, **43**, 337–385.

CRUTCHER, R.M. (2012). Magnetic Fields in Molecular Clouds. *ARA&A*, **50**, 29–63.

DALE, J.E. & BONNELL, I.A. (2012). Ionization-induced star formation - III. Effects of external triggering on the initial mass function in clusters. *MNRAS*, **422**, 1352–1362.

DALE, J.E., BONNELL, I.A. & WHITWORTH, A.P. (2007a). Ionization-induced star formation - I. The collect-and-collapse model. *MNRAS*, **375**, 1291–1298.

DALE, J.E., CLARK, P.C. & BONNELL, I.A. (2007b). Ionization-induced star formation - II. External irradiation of a turbulent molecular cloud. *MNRAS*, **377**, 535–544.

DALE, J.E., ERCOLANO, B. & BONNELL, I.A. (2012). Ionization-induced star formation - IV. Triggering in bound clusters. *MNRAS*, **427**, 2852–2865.

DALGARNO, A. (2006). Interstellar Chemistry Special Feature: The galactic cosmic ray ionization rate. *Proceedings of the National Academy of Science*, **103**, 12269–12273.

DALGARNO, A. & MCCRAY, R.A. (1972). Heating and Ionization of HI Regions. *ARA&A*, **10**, 375.

DAVIDSON, P.A. (2004). *Turbulence : an introduction for scientists and engineers*. Oxford University Press, Oxford, New York.

DAVIS, L., JR. & GREENSTEIN, J.L. (1951). The Polarization of Starlight by Aligned Dust Grains. *ApJ*, **114**, 206.

DEDNER, A., KEMM, F., KRÖNER, D., MUNZ, C.D., SCHNITZER, T. & WESENBERG, M. (2002). Hyperbolic Divergence Cleaning for the MHD Equations. *Journal of Computational Physics*, **175**, 645–673.

DIEHL, R., HALLOIN, H., KRETSCHMER, K., LICHTI, G.G., SCHÖNFELDER, V., STRONG, A.W., VON KIENLIN, A., WANG, W., JEAN, P., KNÖDLSEDER, J., ROQUES, J.P., WEIDENSPOINTNER, G., SCHANNE, S., HARTMANN, D.H., WINKLER, C. & WUNDERER, C. (2006). Radioactive ^{26}Al from massive stars in the Galaxy. *Nature*, **439**, 45–47.

DOMGÖRGEN, H. & MATHIS, J.S. (1994). The ionization of the diffuse ionized gas. *ApJ*, **428**, 647–653.

DOVE, J.B., SHULL, J.M. & FERRARA, A. (2000). The Escape of Ionizing Photons from OB Associations in Disk Galaxies: Radiation Transfer through Superbubbles. *ApJ*, **531**, 846–860.

DRAINE, B.T. (2000). Interstellar Grains. In P. Murdin, ed., *Encyclopedia of Astronomy and Astrophysics*.

DRAINE, B.T. (2003). Interstellar Dust Grains. *ARA&A*, **41**, 241–289.

DRAINE, B.T. (2011). *Physics of the Interstellar and Intergalactic Medium*.

DRAINE, B.T. & LI, A. (2007). Infrared Emission from Interstellar Dust. IV. The Silicate-Graphite-PAH Model in the Post-Spitzer Era. *ApJ*, **657**, 810–837.

DRURY, L.O.. (2012). Origin of cosmic rays. *Astroparticle Physics*, **39**, 52–60.

DRURY, L.O. (1983). An introduction to the theory of diffusive shock acceleration of energetic particles in tenuous plasmas. *Reports on Progress in Physics*, **46**, 973–1027.

DUARTE-CABRAL, A., DOBBS, C.L., PERETTO, N. & FULLER, G.A. (2011). Was a cloud-cloud collision the trigger of the recent star formation in Serpens? *A&A*, **528**, A50.

DULEY, W.W. (1996). The formation of H_2 by H-atom reaction with grain surfaces. *MNRAS*, **279**, 591–594.

DYSON, J. & WILLIAMS, D. (1997). *The Physics of the Interstellar Medium, Second Edition*.

DYSON, J.E. & HARTQUIST, T.W. (1987). Mass loaded astronomical flows. III - The structure of supernova remnants and the local soft X-ray background. *MNRAS*, **228**, 453–461.

DYSON, J.E., ARTHUR, S.J. & HARTQUIST, T.W. (2002). The evolution of mass loaded supernova remnants. I. Constant and Mach Number dependent mass injection rates. *A&A*, **390**, 1063–1074.

DYSON, J.E., PITTARD, J.M., MEABURN, J. & FALLE, S.A.E.G. (2006). The tails in the Helix Nebula NGC 7293. *A&A*, **457**, 561–567.

EBERT, R.W., MCCOMAS, D.J., ELLIOTT, H.A., FORSYTH, R.J. & GOSLING, J.T. (2009). Bulk properties of the slow and fast solar wind and interplanetary coronal mass ejections measured by ulysses: Three polar orbits of observations. *Journal of Geophysical Research: Space Physics*, **114**, n/a–n/a.

EFSTATHIOU, G. (2000). A model of supernova feedback in galaxy formation. *MNRAS*, **317**, 697–719.

EINFELDT, B. (1988). On Godunov-Type Methods for Gas Dynamics. *SIAM Journal on Numerical Analysis*, **25**, 294–318.

ELMEGREEN, B.G. (1982). The formation of giant cloud complexes by the Parker-Jeans instability. *ApJ*, **253**, 655–665.

ELMEGREEN, B.G. (1988). Magnetic cloud collision fronts. *ApJ*, **326**, 616–638.

ELMEGREEN, B.G. (1993). Formation of interstellar clouds and structure. In E.H. Levy & J.I. Lunine, eds., *Protostars and Planets III*, 97–124.

ELMEGREEN, B.G. (1998). Observations and Theory of Dynamical Triggers for Star Formation. In C.E. Woodward, J.M. Shull & H.A. Thronson Jr., eds., *Origins*, vol. 148 of *Astronomical Society of the Pacific Conference Series*, 150.

ELMEGREEN, B.G. & LADA, C.J. (1977). Sequential formation of subgroups in OB associations. *ApJ*, **214**, 725–741.

FABIAN, A.C. (2012). Observational Evidence of Active Galactic Nuclei Feedback. *ARA&A*, **50**, 455–489.

FALLE, S.A.E.G. (1994). The Effect of Turbulence on the Largescale Structure of Radio Jets. *MNRAS*, **269**, 607.

FALLE, S.A.E.G., KOMISSAROV, S.S. & JOARDER, P. (1998). A multidimensional upwind scheme for magnetohydrodynamics. *MNRAS*, **297**, 265–277.

FARHANG, A., KHOSROSHAHI, H.G., JAVADI, A. & VAN LOON, J. (2014). Probing the Local Bubble with Diffuse Interstellar Bands. In J. Cami & N.L.J. Cox, eds., *IAU Symposium*, vol. 297 of *IAU Symposium*, 84–88.

FERLAND, G.J., PORTER, R.L., VAN HOOF, P.A.M., WILLIAMS, R.J.R., ABEL, N.P., LYKINS, M.L., SHAW, G., HENNEY, W.J. & STANCIL, P.C. (2013). The 2013 Release of Cloudy. *Rev. Mex. Astron. Astr.*, **49**, 137–163.

FERMI, E. (1949). On the Origin of the Cosmic Radiation. *Physical Review*, **75**, 1169–1174.

FERRIÈRE, K. (2009). Interstellar magnetic fields in the Galactic center region. *A&A*, **505**, 1183–1198.

FERRIÈRE, K.M. (1999). Large-Scale Model of the Interstellar Medium, with New Constraints on the Hot Gas Component. In A.R. Taylor, T.L. Landecker & G. Joncas, eds., *New Perspectives on the Interstellar Medium*, vol. 168 of *Astronomical Society of the Pacific Conference Series*, 333.

FERRIÈRE, K.M. (2001). The interstellar environment of our galaxy. *Reviews of Modern Physics*, **73**, 1031–1066.

FIELD, G.B., GOLDSMITH, D.W. & HABING, H.J. (1969). Cosmic-Ray Heating of the Interstellar Gas. *ApJL*, **155**, L149.

FIELDS, B.D., HOCHMUTH, K.A. & ELLIS, J. (2005). Deep-Ocean Crusts as Telescopes: Using Live Radioisotopes to Probe Supernova Nucleosynthesis. *ApJ*, **621**, 902–907.

FLOWER, D.R., PINEAU DES FORÊTS, G. & WALMSLEY, C.M. (2007). The fractional ionization in dark molecular clouds. *A&A*, **474**, 923–930.

FRAGILE, P.C., MURRAY, S.D., ANNINOS, P. & VAN BREUGEL, W. (2004). Radiative Shock-induced Collapse of Intergalactic Clouds. *ApJ*, **604**, 74–87.

FRISCH, P.C., REDFIELD, S. & SLAVIN, J.D. (2011). The Interstellar Medium Surrounding the Sun. *ARA&A*, **49**, 237–279.

FUJIMOTO, Y., TASKER, E.J., WAKAYAMA, M. & HABE, A. (2014). Do giant molecular clouds care about the galactic structure? *MNRAS*, **439**, 936–953.

FUKUI, Y. & KAWAMURA, A. (2010). Molecular Clouds in Nearby Galaxies. *ARA&A*, **48**, 547–580.

GAENSLER, B.M., MADSEN, G.J., CHATTERJEE, S. & MAO, S.A. (2008). The Vertical Structure of Warm Ionised Gas in the Milky Way. *PASA*, **25**, 184–200.

GAHM, G.F., GRENMAN, T., FREDRIKSSON, S. & KRISTEN, H. (2007). Globulettes as Seeds of Brown Dwarfs and Free-Floating Planetary-Mass Objects. *ApJ*, **133**, 1795–1809.

GARCÍA-MARÍN, M., ECKART, A., WEISS, A., WITZEL, G., BREMER, M., ZAMANINASAB, M., MORRIS, M.R., SCHÖDEL, R., KUNNERIATH, D., NISHIYAMA, S., BAGANOFF, F., DOVČIAK, M., SABHA, N., DUSCHL, W.J., MOULTAKA, J., KARAS, V., NAJARRO, F., MUŽIĆ, K., STRAUBMEIER, C., VOGEL, S.N., KRIPS, M. & WIESEMEYER, H. (2011). Extended Submillimeter Emission of the Galactic Center and Near-infrared/submillimeter Variability of Its Supermassive Black Hole. *ApJ*, **738**, 158.

GAZOL, A., VÁZQUEZ-SEMADENI, E., SÁNCHEZ-SALCEDO, F.J. & SCALO, J. (2001). The Temperature Distribution in Turbulent Interstellar Gas. *ApJL*, **557**, L121–L124.

GENT, F.A., SHUKUROV, A., FLETCHER, A., SARSON, G.R. & MANTERE, M.J. (2013). The supernova-regulated ISM - I. The multiphase structure. *MNRAS*, **432**, 1396–1423.

GLASSGOLD, A.E. & LANGER, W.D. (1973). Heating of Molecular-Hydrogen Clouds by Cosmic Rays and X-Rays. *ApJ*, **186**, 859–888.

GLASSGOLD, A.E., GALLI, D. & PADOVANI, M. (2012). Cosmic-Ray and X-Ray Heating of Interstellar Clouds and Protoplanetary Disks. *ApJ*, **756**, 157.

GLOVER, S.C.O. & CLARK, P.C. (2014). Molecular cooling in the diffuse interstellar medium. *MNRAS*, **437**, 9–20.

GNEDIN, N.Y. & HOLLON, N. (2012). Cooling and Heating Functions of Photoionized Gas. *ApJS*, **202**, 13.

GOLDSMITH, P.F. (2001). Molecular Depletion and Thermal Balance in Dark Cloud Cores. *ApJ*, **557**, 736–746.

GOLDSMITH, P.F. & LANGER, W.D. (1978). Molecular cooling and thermal balance of dense interstellar clouds. *ApJ*, **222**, 881–895.

GOLDSMITH, P.F., LIS, D.C., LESTER, D.F. & HARVEY, P.M. (1992). High angular resolution far-infrared observations of Sagittarius B2. *ApJ*, **389**, 338–346.

GÓMEZ, G.C. & COX, D.P. (2004). Three-Dimensional Magnetohydrodynamic Modeling of the Gaseous Structure of the Galaxy: Description of the Simulations. *ApJ*, **615**, 744–757.

GONZALEZ-DELGADO, R.M., PEREZ, E., TENORIO-TAGLE, G., VILCHEZ, J.M., TERLEVICH, E., TERLEVICH, R., TELLES, E., RODRIGUEZ-ESPINOSA, J.M., MAS-HESSE, M., GARCIA-VARGAS, M.L., DIAZ, A.I., CEPA, J. & CASTANEDA, H. (1994). Violent star formation in NGC 2363. *ApJ*, **437**, 239–261.

GRAHAM, J.R., LEVENSON, N.A., HESTER, J.J., RAYMOND, J.C. & PETRE, R. (1994). An X-Ray and Optical Study of the Interaction of the Cygnus Loop Supernova Remnant with an Interstellar Cloud. In *American Astronomical Society Meeting Abstracts #184*, vol. 26 of *Bulletin of the American Astronomical Society*, 951.

GREGORI, G., MINIATI, F., RYU, D. & JONES, T.W. (2000). Three-dimensional Magnetohydrodynamic Numerical Simulations of Cloud-Wind Interactions. *ApJ*, **543**, 775–786.

GRENIER, I.A., CASANDJIAN, J.M. & TERRIER, R. (2005). Unveiling Extensive Clouds of Dark Gas in the Solar Neighborhood. *Science*, **307**, 1292–1295.

GREVESSE, N. & SAUVAL, A.J. (1998). Standard Solar Composition. *Space Sci. Rev.*, **85**, 161–174.

GRITSCHNEDER, M., BURKERT, A., NAAB, T. & WALCH, S. (2010). Detailed Numerical Simulations on the Formation of Pillars Around H II Regions. *ApJ*, **723**, 971–984.

GURNETT, D.A. & BHATTACHARJEE, A. (2005). *Introduction to Plasma Physics*.

HAN, J.L. & QIAO, G.J. (1994). The magnetic field in the disk of our Galaxy. *A&A*, **288**, 759–772.

HANJALIĆ, K. (1994). Advanced turbulence closure models: a view of current status and future prospects. *International Journal of Heat and Fluid Flow*, **15**, 178 – 203.

HANSEN, M. & OH, S.P. (2006). Lyman α radiative transfer in a multiphase medium. *MNRAS*, **367**, 979–1002.

HARPER-CLARK, E. & MURRAY, N. (2009). One-Dimensional Dynamical Models of the Carina Nebula Bubble. *ApJ*, **693**, 1696–1712.

HARTMANN, J. (1904). Investigations on the spectrum and orbit of delta Orionis. *ApJ*, **19**, 268–286.

HARTQUIST, T.W., DYSON, J.E., PETTINI, M. & SMITH, L.J. (1986). Mass-loaded astronomical flows. I - General principles and their application to RCW 58. *MNRAS*, **221**, 715–726.

HECKMAN, T.M., DAHLEM, M., LEHNERT, M.D., FABBIANO, G., GILMORE, D. & WALLER, W.H. (1995). An X-Ray and Optical Study of the Dwarf Galaxy NGC 1569: Evidence for a Starburst-driven Outflow. *ApJ*, **448**, 98.

HEILES, C. (2001). New Temperatures of Diffuse Interstellar Gas: Thermally Unstable Gas. *ApJL*, **551**, L105–L108.

HEILES, C. & TROLAND, T.H. (2003). The Millennium Arecibo 21 Centimeter Absorption-Line Survey. II. Properties of the Warm and Cold Neutral Media. *ApJ*, **586**, 1067–1093.

HENLEY, D.B., KWAK, K. & SHELTON, R.L. (2012). Simulations of High-velocity Clouds. II. Ablation from High-velocity Clouds as a Source of Low-velocity High Ions. *ApJ*, **753**, 58.

HENNEBELLE, P. & FALGARONE, E. (2012). Turbulent molecular clouds. *A&A Rev.*, **20**, 55.

HERBST, E. (1995). Chemistry in the Interstellar Medium. *Annu. Rev. Phys. Chem.*, **46**, 27–54.

HOANG, T. & LAZARIAN, A. (2008). Radiative torque alignment: essential physical processes. *MNRAS*, **388**, 117–143.

HOLLENBACH, D. & SALPETER, E.E. (1971). Surface Recombination of Hydrogen Molecules. *ApJ*, **163**, 155.

HOMEIER, N.L. & GALLAGHER, J.S. (1999). Kinematics and Structure of the Starburst Galaxy NGC 7673. *ApJ*, **522**, 199–208.

HORA, J.L., LATTER, W.B., SMITH, H.A. & MARENGO, M. (2006). Infrared Observations of the Helix Planetary Nebula. *ApJ*, **652**, 426–441.

HUANG, S. & GU, Q.S. (2009). Recent star-forming activity in local elliptical galaxies. *MNRAS*, **398**, 1651–1667.

INOUE, T., YAMAZAKI, R. & INUTSUKA, S.I. (2009). Turbulence and Magnetic Field Amplification in Supernova Remnants: Interactions Between a Strong Shock Wave and Multiphase Interstellar Medium. *ApJ*, **695**, 825–833.

INOUE, T., YAMAZAKI, R., INUTSUKA, S.I. & FUKUI, Y. (2012). Toward Understanding the Cosmic-Ray Acceleration at Young Supernova Remnants Interacting with Interstellar Clouds: Possible Applications to RX J1713.7-3946. *ApJ*, **744**, 71.

IZOTOV, Y.I., DYAK, A.B., CHAFFEE, F.H., FOLTZ, C.B., KNIAZEV, A.Y. & LIPOVETSKY, V.A. (1996). Spectrophotometry of Blue Compact Galaxies with Broad Emission Lines: Evidence for High-Velocity Gas Motion. *ApJ*, **458**, 524.

JANSSON, R. (2010). *The magnetic field of the Milky Way*. Ph.D. thesis, New York University.

JANSSON, R. & FARRAR, G.R. (2012). A New Model of the Galactic Magnetic Field. *ApJ*, **757**, 14.

JENKINS, E.B. (2013). The Fractional Ionization of the Warm Neutral Interstellar Medium. *ApJ*, **764**, 25.

JOHANSSON, E.P.G. & ZIEGLER, U. (2013). Radiative Interaction of Shocks with Small Interstellar Clouds as a Pre-stage to Star Formation. *ApJ*, **766**, 45.

JONES, F.C. (1994). A theoretical review of diffusive shock acceleration. *ApJS*, **90**, 561–565.

JONES, W. & LAUNDER, B. (1972). The prediction of laminarization with a two-equation model of turbulence. *International Journal of Heat and Mass Transfer*, **15**, 301 – 314.

JUN, B.I., JONES, T.W. & NORMAN, M.L. (1996). Interaction of Rayleigh-Taylor Fingers and Circumstellar Cloudlets in Young Supernova Remnants. *ApJL*, **468**, L59.

KALBERLA, P.M.W. & KERP, J. (2009). The Hi Distribution of the Milky Way. *ARA&A*, **47**, 27–61.

KANTROVITCH, A. & PETSCHEK, E., H (1966). MHD Characteristics and Shock Waves. In W.B. Kunkel, ed., *Plasma Physics in Theory and Application*.

KAPLAN, S.A. & PIKELNER, S.B. (1974). Large-scale dynamics of the interstellar medium. *ARA&A*, **12**, 113–133.

KLEIN, R.I., MCKEE, C.F. & COLELLA, P. (1994). On the hydrodynamic interaction of shock waves with interstellar clouds. 1: Nonradiative shocks in small clouds. *ApJ*, **420**, 213–236.

KLEIN, R.I., BUDIL, K.S., PERRY, T.S. & BACH, D.R. (2003). The Interaction of Supernova Remnants with Interstellar Clouds: Experiments on the Nova Laser. *ApJ*, **583**, 245–259.

KRAMIDA, A., RALCHENKO, Y., READER, J. & NIST ASD TEAM (2013). NIST Atomic Spectra Database (version 5.1). [Online; accessed 6-June-2014].

KRUIJSSEN, J.M.D. & LONGMORE, S.N. (2013). Comparing molecular gas across cosmic time-scales: the Milky Way as both a typical spiral galaxy and a high-redshift galaxy analogue. *MNRAS*, **435**, 2598–2603.

KRUIJSSEN, J.M.D., LONGMORE, S.N., ELMEGREEN, B.G., MURRAY, N., BALLY, J., TESTI, L. & KENNICUTT, R.C., JR. (2013). What controls star formation in the central 500 pc of the Galaxy? *ArXiv e-prints*.

KULKARNI, S.R. & HEILES, C. (1987). The atomic component. In D.J. Hollenbach & H.A. Thronson Jr., eds., *Interstellar Processes*, vol. 134 of *Astrophysics and Space Science Library*, 87–122.

KULSRUD, R.M. (2005). *Plasma physics for astrophysics*.

LAMERS, H.J.G.L.M. & CASSINELLI, J.P. (1999). *Introduction to Stellar Winds*.

LANDAU, L.D. & LIFSHITZ, E.M. (1987). *Fluid mechanics, 2nd ed.*

LARSON, R.B. (1981). Turbulence and star formation in molecular clouds. *MNRAS*, **194**, 809–826.

LAZARIAN, A. (2007). Tracing magnetic fields with aligned grains. *J. Quant. Spectrosc. Rad. Trans.*, **106**, 225–256.

LAZARIAN, A. (2013). Reconnection Diffusion, Star Formation, and Numerical Simulations. In N.V. Pogorelov, E. Audit & G.P. Zank, eds., *Numerical Modeling of Space Plasma Flows (ASTRONUM2012)*, vol. 474 of *Astronomical Society of the Pacific Conference Series*, 15.

LAZARIAN, A. (2014). Reconnection Diffusion in Turbulent Fluids and Its Implications for Star Formation. *Space Sci. Rev.*, **181**, 1–59.

LE BOURLOT, J., LE PETIT, F., PINTO, C., ROUEFF, E. & ROY, F. (2012). Surface chemistry in the interstellar medium. I. H_2 formation by Langmuir-Hinshelwood and Eley-Rideal mechanisms. *A&A*, **541**, A76.

LEMASTER, M.N. & STONE, J.M. (2008). Density Probability Distribution Functions in Supersonic Hydrodynamic and MHD Turbulence. *ApJL*, **682**, L97–L100.

LEVEQUE, R.J. (1998). Nonlinear Conservation Laws and Finite Volume Methods. In O. Steiner & A. Gautschy, eds., *Saas-Fee Advanced Course 27: Computational Methods for Astrophysical Fluid Flow.*, 1.

LI, S., FRANK, A. & BLACKMAN, E.G. (2013). Magnetohydrodynamic Shock-Clump Evolution with Self-contained Magnetic Fields. *ApJ*, **774**, 133.

LIN, C.C. & SHU, F.H. (1964). On the Spiral Structure of Disk Galaxies. *ApJ*, **140**, 646.

LONGMORE, S.N., RATHBORNE, J., BASTIAN, N., ALVES, J., ASCENSO, J., BALLY, J., TESTI, L., LONGMORE, A., BATTERSBY, C., BRESSERT, E., PURCELL, C., WALSH, A., JACKSON, J., FOSTER, J., MOLINARI, S., MEINGAST, S., AMORIM, A., LIMA, J., MARQUES, R., MOITINHO, A., PINHAO, J., REBORDAO, J. & SANTOS, F.D. (2012). G0.253 + 0.016: A Molecular Cloud Progenitor of an Arches-like Cluster. *ApJ*, **746**, 117.

LONGMORE, S.N., KRUIJSSEN, J.M.D., BALLY, J., OTT, J., TESTI, L., RATHBORNE, J., BASTIAN, N., BRESSERT, E., MOLINARI, S., BATTERSBY, C. & WALSH, A.J. (2013). Candidate super star cluster progenitor gas clouds possibly triggered by close passage to Sgr A*. *MNRAS*, **433**, L15–L19.

MAC LOW, M., MCKEE, C.F., KLEIN, R.I., STONE, J.M. & NORMAN, M.L. (1994). Shock interactions with magnetized interstellar clouds. 1: Steady shocks hitting nonradiative clouds. *ApJ*, **433**, 757–777.

MARCOLINI, A., STRICKLAND, D.K., D'ERCOLE, A., HECKMAN, T.M. & HOOPES, C.G. (2005). The dynamics and high-energy emission of conductive gas clouds in supernova-driven galactic superwinds. *MNRAS*, **362**, 626–648.

MARLOWE, A.T., HECKMAN, T.M., WYSE, R.F.G. & SCHOMMER, R. (1995). Observations of the impact of starbursts on the interstellar medium in dwarf galaxies. *ApJ*, **438**, 563–589.

MATHEWSON, D.S. & FORD, V.L. (1970). Polarization Observations of 1800 Stars. *MmRAS*, **74**, 139.

MATHIS, J.S. (1997). Composition and Size of Interstellar Dust. In Y.J. Pendleton, ed., *From Stardust to Planetesimals*, vol. 122 of *Astronomical Society of the Pacific Conference Series*, 87.

MATHIS, J.S., MEZGER, P.G. & PANAGIA, N. (1983). Interstellar radiation field and dust temperatures in the diffuse interstellar matter and in giant molecular clouds. *A&A*, **128**, 212–229.

MATSUURA, M., SPECK, A.K., SMITH, M.D., ZIJLSTRA, A.A., VITI, S., LOWE, K.T.E., REDMAN, M., WAREING, C.J. & LAGADEC, E. (2007). VLT/near-infrared integral field spectrometer observations of molecular hydrogen lines in the knots of the planetary nebula NGC 7293 (the Helix Nebula). *MNRAS*, **382**, 1447–1459.

McCray, R. (1983). Stellar winds and the interstellar medium. *Highlights of Astronomy*, **6**, 565–579.

McCray, R. & Kafatos, M. (1987). Supershells and propagating star formation. *ApJ*, **317**, 190–196.

McDowell, M.R.C. (1961). On the formation of H2 in H I regions. *The Observatory*, **81**, 240–243.

McKee, C.F. & Cowie, L.L. (1975). The interaction between the blast wave of a supernova remnant and interstellar clouds. *ApJ*, **195**, 715–725.

McKee, C.F. & Ostriker, E.C. (2007). Theory of Star Formation. *ARA&A*, **45**, 565–687.

McKee, C.F. & Ostriker, J.P. (1977). A theory of the interstellar medium - Three components regulated by supernova explosions in an inhomogeneous substrate. *ApJ*, **218**, 148–169.

Melioli, C., de Gouveia dal Pino, E.M. & Raga, A. (2005). Multidimensional hydrodynamical simulations of radiative cooling SNRs-clouds interactions: an application to starburst environments. *A&A*, **443**, 495–508.

Mellema, G., Kurk, J.D. & Röttgering, H.J.A. (2002). Evolution of clouds in radio galaxy cocoons. *A&A*, **395**, L13–L16.

Melnick, J., Tenorio-Tagle, G. & Terlevich, R. (1999). Supersonic gas motion in giant extragalactic HII regions. *MNRAS*, **302**, 677–683.

MENEGUZZI, M., AUDOUZE, J. & REEVES, H. (1971). The production of the elements Li, Be, B by galactic cosmic rays in space and its relation with stellar observations. *A&A*, **15**, 337–359.

MOLINARI, S., BALLY, J., NORIEGA-CRESPO, A., COMPIÈGNE, M., BERNARD, J.P., PARADIS, D., MARTIN, P., TESTI, L., BARLOW, M., MOORE, T., PLUME, R., SWINYARD, B., ZAVAGNO, A., CALZOLETTI, L., DI GIORGIO, A.M., ELIA, D., FAUSTINI, F., NATOLI, P., PESTALOZZI, M., PEZZUTO, S., PIACENTINI, F., POLENTA, G., POLYCHRONI, D., SCHISANO, E., TRAFICANTE, A., VENEZIANI, M., BATTERSBY, C., BURTON, M., CAREY, S., FUKUI, Y., LI, J.Z., LORD, S.D., MORGAN, L., MOTTE, F., SCHULLER, F., STRINGFELLOW, G.S., TAN, J.C., THOMPSON, M.A., WARD-THOMPSON, D., WHITE, G. & UMANA, G. (2011). A 100 pc Elliptical and Twisted Ring of Cold and Dense Molecular Clouds Revealed by Herschel Around the Galactic Center. *ApJL*, **735**, L33.

MOLINARI, S., BALLY, J., GLOVER, S., MOORE, T., NORIEGA-CRESPO, A., PLUME, R., TESTI, L., VÁZQUEZ-SEMADENI, E., ZAVAGNO, A., BERNARD, J.P. & MARTIN, P. (2014). The Milky Way as a Star Formation Engine. *ArXiv e-prints*.

MORRIS, M. & SERABYN, E. (1996). The Galactic Center Environment. *ARA&A*, **34**, 645–702.

MORTON, D.C. (1967). The Far-Ultraviolet Spectra of Six Stars in Orion. *ApJ*, **147**, 1017.

MOUSCHOVIAS, T.C. & PALEOLOGOU, E.V. (1979). The angular momentum problem and magnetic braking - an exact time-dependent solution. *ApJ*, **230**, 204–222.

NAKAMURA, F., MCKEE, C.F., KLEIN, R.I. & FISHER, R.T. (2006). On the Hydrodynamic Interaction of Shock Waves with Interstellar Clouds. II. The Effect of Smooth Cloud Boundaries on Cloud Destruction and Cloud Turbulence. *ApJS*, **164**, 477–505.

NESSYAHU, H. & TADMOR, E. (1990). Non-oscillatory Central Differencing for Hyperbolic Conservation Laws. *Journal of Computational Physics*, **87**, 408–463.

NUGIS, T. & LAMERS, H.J.G.L.M. (2000). Mass-loss rates of Wolf-Rayet stars as a function of stellar parameters. *A&A*, **360**, 227–244.

OBERGAULINGER, M., IYUDIN, A.F., MÜLLER, E. & SMOOT, G.F. (2014). Hydrodynamic simulations of the interaction of supernova shock waves with a clumpy environment: the case of the RX J0852.0-4622 (Vela Jr) supernova remnant. *MNRAS*, **437**, 976–993.

O'DELL, C.R., HENNEY, W.J. & FERLAND, G.J. (2005). A Multi-Instrument Study of the Helix Nebula Knots with the Hubble Space Telescope. *ApJ*, **130**, 172–187.

OLLING, R.P. & MERRIFIELD, M.R. (2000). Two measures of the shape of the dark halo of the Milky Way. *MNRAS*, **311**, 361–369.

OORT, J.H. (1951). Interaction of Nova and Supernova Shells With the Interstellar Medium. In *Problems of Cosmical Aerodynamics*, 118.

OPPENHEIMER, B.D. & DAVÉ, R. (2008). Mass, metal, and energy feedback in cosmological simulations. *MNRAS*, **387**, 577–600.

ORLANDO, S., PERES, G., REALE, F., BOCCHINO, F., ROSNER, R., PLEWA, T. & SIEGEL, A. (2005). Crushing of interstellar gas clouds in supernova remnants. I. The role of thermal conduction and radiative losses. *A&A*, **444**, 505–519.

ORLANDO, S., BOCCHINO, F., REALE, F., PERES, G. & PAGANO, P. (2008). The Importance of Magnetic-Field-Oriented Thermal Conduction in the Interaction of SNR Shocks with Interstellar Clouds. *ApJ*, **678**, 274–286.

OSTERBROCK, D.E. (1989). *Astrophysics of gaseous nebulae and active galactic nuclei*.

PALLA, F., SALPETER, E.E. & STAHLER, S.W. (1983). Primordial star formation - The role of molecular hydrogen. *ApJ*, **271**, 632–641.

PARKER, E.N. (1965). Dynamical Theory of the Solar Wind. *Space Sci. Rev.*, **4**, 666–708.

PARKER, E.N. (1966). The Dynamical State of the Interstellar Gas and Field. *ApJ*, **145**, 811.

PATNAUDE, D.J. & FESEN, R.A. (2005). Model Simulations of a Shock-Cloud Interaction in the Cygnus Loop. *ApJ*, **633**, 240–247.

PITTARD, J.M. (2011). Tails of the unexpected: the interaction of an isothermal shell with a cloud. *MNRAS*, **411**, L41–L45.

PITTARD, J.M. (2013). Self-sealing shells: blowouts and blisters on the surfaces of leaky wind-blown bubbles and supernova remnants. *MNRAS*, **435**, 3600–3613.

PITTARD, J.M., ARTHUR, S.J., DYSON, J.E., FALLE, S.A.E.G., HARTQUIST, T.W., KNIGHT, M.I. & PEXTON, M. (2003). The evolution of mass loaded supernova

remnants. II. Temperature dependent mass injection rates. *A&A*, **401**, 1027–1038.

PITTARD, J.M., DYSON, J.E., FALLE, S.A.E.G. & HARTQUIST, T.W. (2005). Dynamical and pressure structures in winds with multiple embedded evaporating clumps - I. Two-dimensional numerical simulations. *MNRAS*, **361**, 1077–1090.

PITTARD, J.M., FALLE, S.A.E.G., HARTQUIST, T.W. & DYSON, J.E. (2009). The turbulent destruction of clouds - I. A k-ϵ treatment of turbulence in 2D models of adiabatic shock-cloud interactions. *MNRAS*, **394**, 1351–1378, p09.

PITTARD, J.M., HARTQUIST, T.W. & FALLE, S.A.E.G. (2010). The turbulent destruction of clouds - II. Mach number dependence, mass-loss rates and tail formation. *MNRAS*, **405**, 821–838.

POLUDNENKO, A.Y., FRANK, A. & BLACKMAN, E.G. (2002). Hydrodynamic Interaction of Strong Shocks with Inhomogeneous Media. I. Adiabatic Case. *ApJ*, **576**, 832–848.

POLUDNENKO, A.Y., DANNENBERG, K.K., DRAKE, R.P., FRANK, A., KNAUER, J., MEYERHOFER, D.D., FURNISH, M., ASAY, J.R. & MITRAN, S. (2004). A Laboratory Investigation of Supersonic Clumpy Flows: Experimental Design and Theoretical Analysis. *ApJ*, **604**, 213–221.

QUIRK, J.J. (1994). A contribution to the great Riemann solver debate. *International Journal for Numerical Methods in Fluids*, **18**, 555–574.

RACHFORD, B.L., SNOW, T.P., TUMLINSON, J., SHULL, J.M., BLAIR, W.P., FERLET, R., FRIEDMAN, S.D., GRY, C., JENKINS, E.B., MORTON, D.C., SAVAGE, B.D., SONNEN-

TRUCKER, P., VIDAL-MADJAR, A., WELTY, D.E. & YORK, D.G. (2002). A Far Ultraviolet Spectroscopic Explorer Survey of Interstellar Molecular Hydrogen in Translucent Clouds. *ApJ*, **577**, 221–244.

RAGA, A.C., DE GOUVEIA DAL PINO, E.M., NORIEGA-CRESPO, A., MININNI, P.D. & VELÁZQUEZ, P.F. (2002). Jet/cloud collision, 3D gasdynamic simulations of HH 110. *A&A*, **392**, 267–276.

RAGA, A.C., CANTÓ, J. & RODRÍGUEZ, L.F. (2012). Analytic and numerical models for the expansion of a compact H II region. *MNRAS*, **419**, L39–L43.

RAND, R.J. & LYNE, A.G. (1994). New Rotation Measures of Distant Pulsars in the Inner Galaxy and Magnetic Field Reversals. *MNRAS*, **268**, 497.

REDFIELD, S. & LINSKY, J.L. (2004). The Structure of the Local Interstellar Medium. III. Temperature and Turbulence. *ApJ*, **613**, 1004–1022.

REYNOLDS, R.J. (1990). Faint optical line emission from the diffuse interstellar medium - Observations and implications. In S. Bowyer & C. Leinert, eds., *The Galactic and Extragalactic Background Radiation*, vol. 139 of *IAU Symposium*, 157–169.

ROBERTS, W.W. (1969). Large-Scale Shock Formation in Spiral Galaxies and its Implications on Star Formation. *ApJ*, **158**, 123.

ROGERS, H. & PITTARD, J.M. (2013). Feedback from winds and supernovae in massive stellar clusters - I. Hydrodynamics. *MNRAS*, **431**, 1337–1351.

ROSOLOWSKY, E., ENGARGIOLA, G., PLAMBECK, R. & BLITZ, L. (2003). Giant Molecular Clouds in M33. II. High-Resolution Observations. *ApJ*, **599**, 258–274.

ROY, J.R., AUBE, M., MCCALL, M.L. & DUFOUR, R.J. (1992). The origin of broad emission lines in the extragalactic giant H II region NGC 2363. *ApJ*, **386**, 498–505.

SALES, L.V., NAVARRO, J.F., SCHAYE, J., DALLA VECCHIA, C., SPRINGEL, V. & BOOTH, C.M. (2010). Feedback and the structure of simulated galaxies at redshift z= 2. *MNRAS*, **409**, 1541–1556.

SÁNCHEZ-SALCEDO, F.J., SAHA, K. & NARAYAN, C.A. (2008). The thickness of HI in galactic discs under MOdified Newtonian Dynamics: theory and application to the Galaxy. *MNRAS*, **385**, 1585–1596.

SANDFORD, M.T., II, WHITAKER, R.W. & KLEIN, R.I. (1982). Radiation-driven implosions in molecular clouds. *ApJ*, **260**, 183–201.

SEATON, M.J. (1959). Radiative recombination of hydrogenic ions. *MNRAS*, **119**, 81.

SEDOV, L.I. (1959). *Similarity and Dimensional Methods in Mechanics*.

SEIFRIED, D., SCHMIDT, W. & NIEMEYER, J.C. (2011). Forced turbulence in thermally bistable gas: a parameter study. *A&A*, **526**, A14+.

SGRO, A.G. (1975). The collision of a strong shock with a gas cloud - A model for Cassiopeia A. *ApJ*, **197**, 621–634.

SHELTON, R.L., KWAK, K. & HENLEY, D.B. (2012). Modeling the X-Rays Resulting from High-velocity Clouds. *ApJ*, **751**, 120.

SHEN, F., FENG, X. & WU, S.T. (2012). 3D MHD Numerical Study of Two CMEs' Evolution and Their Interaction. In N.V. Pogorelov, J.A. Font, E. Audit & G.P. Zank,

eds., *Numerical Modeling of Space Plasma Slows (ASTRONUM 2011)*, vol. 459 of *Astronomical Society of the Pacific Conference Series*, 247.

SHIN, M., STONE, J.M. & SNYDER, G.F. (2008). The Magnetohydrodynamics of Shock-Cloud Interaction in Three Dimensions. *ApJ*, **680**, 336–348.

SHOPBELL, P.L. & BLAND-HAWTHORN, J. (1998). The Asymmetric Wind in M82. *ApJ*, **493**, 129–153.

SHUKUROV, A., SARSON, G.R., NORDLUND, Å., GUDIKSEN, B. & BRANDENBURG, A. (2004). The effects of spiral arms on the multi-phase ISM. *Ap&SS*, **289**, 319–322.

SIDOLI, F., SMITH, L.J. & CROWTHER, P.A. (2006). The massive star population in the giant HII region Tol89 in NGC5398. *MNRAS*, **370**, 799–818.

SMITH, B., SIGURDSSON, S. & ABEL, T. (2008). Metal cooling in simulations of cosmic structure formation. *MNRAS*, **385**, 1443–1454.

SNOWDEN, S.L., EGGER, R., FINKBEINER, D.P., FREYBERG, M.J. & PLUCINSKY, P.P. (1998). Progress on Establishing the Spatial Distribution of Material Responsible for the 1 4 keV Soft X-Ray Diffuse Background Local and Halo Components. *ApJ*, **493**, 715.

SPITZER, L. (1978). *Physical processes in the interstellar medium*.

SPITZER, L., JR. (1956). On a Possible Interstellar Galactic Corona. *ApJ*, **124**, 20.

SPITZER, L., JR. & TOMASKO, M.G. (1968). Heating of H i Regions by Energetic Particles. *ApJ*, **152**, 971.

STAHLER, S.W. & PALLA, F. (2005). *The Formation of Stars*.

STEFFEN, W., GOMEZ, J.L., RAGA, A.C. & WILLIAMS, R.J.R. (1997). Jet-Cloud Interactions and the Brightening of the Narrow-Line Region in Seyfert Galaxies. *ApJL*, **491**, L73.

STERNBERG, A., HOFFMANN, T.L. & PAULDRACH, A.W.A. (2003). Ionizing Photon Emission Rates from O- and Early B-Type Stars and Clusters. *ApJ*, **599**, 1333–1343.

STONE, J.M. & NORMAN, M.L. (1992). The three-dimensional interaction of a supernova remnant with an interstellar cloud. *ApJL*, **390**, L17–L19.

STRICKLAND, D.K. & HECKMAN, T.M. (2009). Supernova Feedback Efficiency and Mass Loading in the Starburst and Galactic Superwind Exemplar M82. *ApJ*, **697**, 2030–2056.

STRÖMGREN, B. (1939). The Physical State of Interstellar Hydrogen. *ApJ*, **89**, 526.

STRONG, A.W., PORTER, T.A., DIGEL, S.W., JÓHANNESSON, G., MARTIN, P., MOSKALENKO, I.V., MURPHY, E.J. & ORLANDO, E. (2010). Global Cosmic-ray-related Luminosity and Energy Budget of the Milky Way. *ApJL*, **722**, L58–L63.

TAYLOR, G. (1950). The Formation of a Blast Wave by a Very Intense Explosion. I. Theoretical Discussion. *Proceedings of the Royal Society of London. Series A, Mathematical and Physical Sciences*, **201**, pp. 159–174.

TENORIO-TAGLE, G. (1979). The gas dynamics of H II regions. I - The champagne model. *A&A*, **71**, 59–65.

TIELENS, A.G.G.M. (2005). *The Physics and Chemistry of the Interstellar Medium*.

TORO, E.F. (2009). *Riemann Solvers and Numerical Methods for Fluid Dynamics: A Practical Introduction*. Springer, Berlin, 3rd edn.

TRIPP, T.M., MEIRING, J.D., PROCHASKA, J.X., WILLMER, C.N.A., HOWK, J.C., WERK, J.K., JENKINS, E.B., BOWEN, D.V., LEHNER, N., SEMBACH, K.R., THOM, C. & TUMLINSON, J. (2011). The Hidden Mass and Large Spatial Extent of a Post-Starburst Galaxy Outflow. *Science*, **334**, 952–.

TROLAND, T.H. & HEILES, C. (1986). Interstellar magnetic field strengths and gas densities Observational and theoretical perspectives. *ApJ*, **301**, 339–345.

TRUMPLER, R.J. (1930). Preliminary results on the distances, dimensions and space distribution of open star clusters. *Lick Observatory Bulletin*, **14**, 154–188.

TUMLINSON, J., THOM, C., WERK, J.K., PROCHASKA, J.X., TRIPP, T.M., WEINBERG, D.H., PEEPLES, M.S., O'MEARA, J.M., OPPENHEIMER, B.D., MEIRING, J.D., KATZ, N.S., DAVÉ, R., FORD, A.B. & SEMBACH, K.R. (2011). The Large, Oxygen-Rich Halos of Star-Forming Galaxies Are a Major Reservoir of Galactic Metals. *Science*, **334**, 948–.

URQUHART, J.S., FIGURA, C.C., MOORE, T.J.T., HOARE, M.G., LUMSDEN, S.L., MOTTRAM, J.C., THOMPSON, M.A. & OUDMAIJER, R.D. (2014). The RMS survey: galactic distribution of massive star formation. *MNRAS*, **437**, 1791–1807.

VAN DEN BERGH, S. (1971). Optical Studies of Cassiopeia a. III. Spectra of the Supernova Remnant. *ApJ*, **165**, 457.

VAN LOO, S., FALLE, S.A.E.G., HARTQUIST, T.W. & MOORE, T.J.T. (2007). Shock-triggered formation of magnetically-dominated clouds. *A&A*, **471**, 213–218.

VAN LOO, S., FALLE, S.A.E.G. & HARTQUIST, T.W. (2010). Shock-triggered formation of magnetically dominated clouds - II. Weak shock-cloud interaction in three dimensions. *MNRAS*, **406**, 1260–1268.

VEILLEUX, S. & BLAND-HAWTHORN, J. (1997). Artillery Shells over Circinus. *ApJL*, **479**, L105–L108.

VEILLEUX, S., CECIL, G. & BLAND-HAWTHORN, J. (2005). Galactic Winds. *ARA&A*, **43**, 769–826.

VIDALI, G. (2013). H2 Formation on Interstellar Grains. *Chemical Reviews*, **113**, 8762.

VIESER, W. & HENSLER, G. (2007). The evolution of interstellar clouds in a streaming hot plasma including heat conduction. *A&A*, **472**, 141–153.

WEINGARTNER, J.C. & DRAINE, B.T. (2001). Photoelectric Emission from Interstellar Dust: Grain Charging and Gas Heating. *ApJS*, **134**, 263–281.

WELSH, B.Y., LALLEMENT, R., VERGELY, J.L. & RAIMOND, S. (2010). New 3D gas density maps of NaI and CaII interstellar absorption within 300 pc. *A&A*, **510**, A54.

WESTMOQUETTE, M.S., EXTER, K.M., SMITH, L.J. & GALLAGHER, J.S. (2007a). Gemini GMOS/IFU spectroscopy of NGC 1569 - I. Mapping the properties of a young star cluster and its environment. *MNRAS*, **381**, 894–912.

WESTMOQUETTE, M.S., SMITH, L.J., GALLAGHER, J.S. & EXTER, K.M. (2007b). Gemini GMOS/integral field unit spectroscopy of NGC 1569 - II. Mapping the roots of the galactic outflow. *MNRAS*, **381**, 913–931.

WHITE, R.L. & LONG, K.S. (1991). Supernova remnant evolution in an interstellar medium with evaporating clouds. *ApJ*, **373**, 543–555.

WILLIAMS, R.J.R. & DYSON, J.E. (2002). Resolved shocks in clumpy media. *MNRAS*, **333**, 1–8.

WILSON, B.A., DAME, T.M., MASHEDER, M.R.W. & THADDEUS, P. (2005). A uniform CO survey of the molecular clouds in Orion and Monoceros. *A&A*, **430**, 523–539.

WOLFIRE, M.G., HOLLENBACH, D. & MCKEE, C.F. (2010). The Dark Molecular Gas. *ApJ*, **716**, 1191–1207.

WOLTJER, L. (1972). Supernova Remnants. *ARA&A*, **10**, 129.

XU, J. & STONE, J.M. (1995). The Hydrodynamics of Shock-Cloud Interactions in Three Dimensions. *ApJ*, **454**, 172.

YANG, H., CHU, Y.H., SKILLMAN, E.D. & TERLEVICH, R. (1996). The Violent Interstellar Medium of NGC 604. *ApJ*, **112**, 146.

YIRAK, K., FRANK, A. & CUNNINGHAM, A.J. (2010). Self-convergence of Radiatively Cooling Clumps in the Interstellar Medium. *ApJ*, **722**, 412–424.

YUSEF-ZADEH, F., COTTON, W., VITI, S., WARDLE, M. & ROYSTER, M. (2013a). Widespread Methanol Emission from the Galactic Center: The Role of Cosmic Rays. *ApJL*, **764**, L19.

YUSEF-ZADEH, F., HEWITT, J.W., WARDLE, M., TATISCHEFF, V., ROBERTS, D.A., COTTON, W., UCHIYAMA, H., NOBUKAWA, M., TSURU, T.G., HEINKE, C. & ROYSTER, M. (2013b). Interacting Cosmic Rays with Molecular Clouds: A Bremsstrahlung Origin of Diffuse High-energy Emission from the Inner $2^\circ \times 1^\circ$ of the Galactic Center. *ApJ*, **762**, 33.

ZHOU, X., MICELI, M., BOCCHINO, F., ORLANDO, S. & CHEN, Y. (2011). Unveiling the spatial structure of the overionized plasma in the supernova remnant W49B. *MNRAS*, **415**, 244–250.